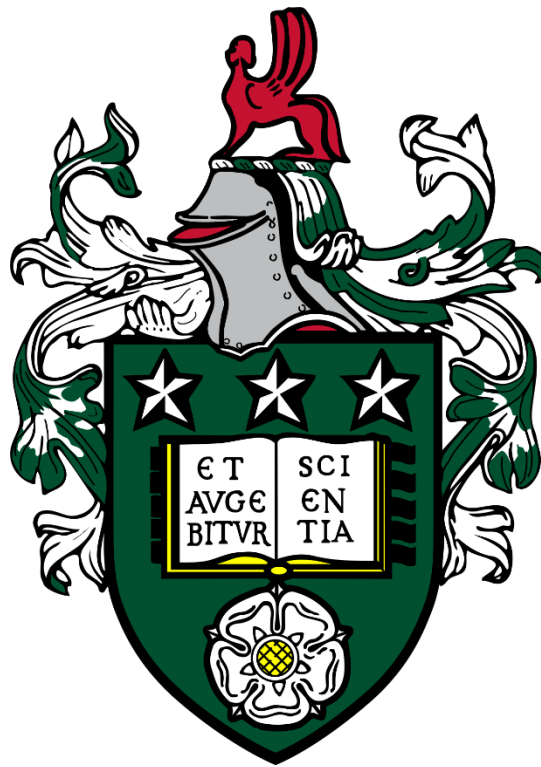


A hydrodynamic study on the soil removal mechanisms of liquid jets and sprays

by

Alistair James Rodgers



Submitted in accordance with the requirements for the degree of
Doctor of Philosophy

School of Mechanical Engineering, University of Leeds, United Kingdom

September 2019

Intellectual Property and Publication Statements

The candidate confirms that the work submitted is his own, except where work which has formed part of jointly authored publications has been included. The contribution of the candidate and the other authors to this work has been explicitly indicated below. The candidate confirms that appropriate credit has been given within the thesis where reference has been made to the work of others.

Chapters 3 and 4 contain theory and results published in a journal article in *Food and Bioproducts Processing* (Rodgers et al., 2019). The same work was also published in the conference proceedings of *Fouling and Cleaning in Food Processing 2018*, Lund University, Lund, Sweden.

This copy has been supplied on the understanding that it is copyright material and that no quotation from the thesis may be published without proper acknowledgement.

The right of Alistair James Rodgers to be identified as Author of this work has been asserted by him in accordance with the Copyright, Designs and Patents Act 1988.

Acknowledgements

I would like to thank my project supervisors; Professor Nik Kapur, Dr Greg de Boer, Gordon Scott and Professor Brent Murray for their continued guidance and advice throughout my research. Their support has been invaluable and I would not have been able to complete the work without them.

GlaxoSmithKline and The University of Leeds are gratefully acknowledged for funding the research. I would also like to thank technical staff at the university, in particular Mark Batchelor who was of great help with my experimental work.

A special mention also goes out to my parents, whose unwavering support throughout my time at university has helped me immeasurably. Finally; thank you to my peers Matthew Clarke and James Daghish who have helped make my time as a postgraduate researcher as enjoyable as it has been.

Abstract

This thesis presents a hydrodynamic study on the cleaning mechanisms of liquid jets and sprays used in batch cleaning processes in the pharmaceutical industry. By analysing an exemplar wash rack employed for cleaning-out-of-place (COP) on a pharmaceutical manufacturing facility, the flow rate distribution through the rack was predicted using the open source software EPANET. The flow rates obtained using this method were then applied to the design of experiments (DOE).

Two jet cases were considered; horizontal impingement on to a vertical wall and vertical impingement through a pipe. For the horizontal case, flow rates used were in the range $1 - 4 \text{ lmin}^{-1}$. Water temperatures were in the range $20 - 60 \text{ }^\circ\text{C}$ and soil layer thicknesses $0.19 - 1.9 \text{ mm}$. The soil used for horizontal experiments was white soft paraffin (WSP), an excipient commonly used in the manufacture of liquids, creams and ointments. Results from these experiments showed that cleaning occurred via a roll-up mechanism of WSP. Using an energy framework it was observed that cleaning efficiency decreased with time as the distance of the cleaning frontier from the impingement point of the jet increased. Cleaning beyond the drop point of WSP showed a significant increase in cleaning performance as phase transition occurred to mobile. For the vertical jet, the material cleaned was a gel. The primary failure mode was misalignment of the jet relative to the pipe, causing flow to miss the entrance to the pipe. Also residues were observed when the gel was preheated at $85 \text{ }^\circ\text{C}$ prior to cleaning. For the spray experiments, WSP was again used and the same flow conditions. Large residual films were observed at room temperature but again beyond the WSP drop point all material in contact with the flow was removed.

Computational simulations of single droplet impingement on to a wetted wall with contact angles varying from $0 - 83^\circ$ and a wall with a liquid film on the surface were also conducted using the computational fluid dynamics software COMSOL. This was intended to represent a constituent droplet of a spray and gauge its cleaning mechanism on a wall. Shear exerted on the wall was observed to significantly reduce with the presence of a liquid film on the surface.

Table of Contents

List of Figures	ix
List of Tables	xviii
Nomenclature	xix
1 Introduction	1
1.1 Context	1
1.2 Aims and objectives	2
1.3 Thesis structure	3
2 Literature Review	4
2.1 Costs and inefficiencies of cleaning in the pharmaceutical industry	4
2.2 Contaminants found in pharmaceutical product manufacture	4
2.3 Sinner’s Circle	5
2.3.1 Time.....	6
2.3.2 Action.....	6
2.3.2.1 Jets.....	6
2.3.2.1 Sprays.....	15
2.3.2.3 CIP technologies.....	39
2.3.3 Chemistry.....	41
2.3.4 Temperature.....	42
2.3.5 Beyond Sinner’s Circle.....	42
2.4 Pipe cleaning	43
2.5 Cleaning-out-of-place (COP)	43
2.6 Cleaning validation	45
2.6.1 Sampling techniques.....	46
2.6.2 Analysing cleaning validation samples.....	47
2.6.3 Acceptance criteria for cleanliness.....	48
2.6.4 Cleaning validation failure.....	49
2.7 Conclusions from the literature	49
2.7.1 Introduction to thesis.....	50
3 Method	51
3.1 Introduction	51
3.2 Wash rack characterisation	51
3.2.1 EPANET Model Components.....	51
3.2.1.1 Junctions.....	52
3.2.1.2 Reservoirs.....	52

3.2.1.3 Emitters	52
3.2.1.4 Pipes	52
3.2.1.5 Pumps	52
3.2.2 Flow-head formulation.....	53
3.2.3 Rack modelling.....	57
3.2.3.1 Nozzle characterisation	57
3.2.3.2 Pump/coupling characterisation	57
3.2.3.3 Rack 1	59
3.2.3.4 Rack 2	61
3.3 Horizontal jet apparatus	66
3.3.1 Test rig design.....	66
3.3.2 Design of experiments (DOE)	70
3.3.3 Material characterisation.....	71
3.3.3.1 Penetration tests.....	72
3.3.3.2 Contact angle measurement.....	73
3.4 Vertical jet apparatus	73
3.4.1 Test rig design.....	73
3.4.2 Design of experiments	75
3.4.3 Material characterisation.....	76
3.5 Spray apparatus	77
3.6 Image processing	78
3.7 Energy input calculations.....	78
3.8 Computational droplet simulations.....	79
3.8.1 Level set method.....	79
3.8.1.1 Conservative and non-conservative form	80
3.8.1.2 Initialising the level set function.....	80
3.8.1.3 Variables for geometric properties of the interface	80
3.8.1.4 Volume Force	81
3.8.1.5 Fluid properties	81
3.8.1.6 Boundary conditions.....	81
3.8.2 Finite element method.....	82
3.8.2 Droplet impingement model setup	83
3.8.2.1 Meshing the model	85
3.8.2.2 Boundary conditions.....	86
3.8.2.3 Interfacial thickness.....	86
3.8.2.4 Processing results	87

3.8.2.5 Mesh convergence	89
3.9 Computational jet simulations	96
3.9.1 Impinging jet model setup	97
3.10 Summary	99
4 Jet Results	100
4.1 Introduction	100
4.2 Horizontal jet impingement	100
4.2.1 Visualisation of soil removal	100
4.2.1.1 High flow, thin WSP layer	101
4.2.1.2 Medium flow, thin WSP layer	101
4.2.1.3 Low flow, thin WSP layer	103
4.2.1.4 High flow, medium WSP layer	103
4.2.1.5 Medium flow, medium WSP layer	104
4.2.1.6 Low flow, medium WSP layer	105
4.2.1.7 Thick WSP layer	105
4.2.2 Soil removal mechanism study	107
4.2.3 Effect of standoff distance	109
4.2.4 Effect of flow rate	110
4.2.5 Effect of WSP layer thickness	113
4.2.5.1 High flow	113
4.2.5.2 Medium flow	114
4.2.5.3 Low flow	114
4.2.6 Energy efficiency	115
4.2.7 Effect of water temperature	117
4.2.7.1 High flow, medium WSP layer	118
4.2.7.2 Medium flow, high WSP layer	119
4.2.7.3 Soil removal mechanism	120
4.3 Vertical jet impingement through pipe	122
4.3.1 Perfectly aligned jet	123
4.3.2 Misaligned jet	126
4.4 Rack optimisation study	128
4.5 Summary	130
5 Spray Results	132
5.1 Introduction	132
5.2 Visualisation of soil removal	132
5.2.1 High flow, thin WSP layer	132

5.2.2 Medium flow, thin WSP layer	134
5.2.3 Low flow, thin WSP layer	136
5.2.4 High flow, medium WSP layer	136
5.2.5 Medium flow, medium WSP layer	138
5.2.6 High flow, thick WSP layer	139
5.2.7 Medium flow, thick WSP layer	140
5.3 Residual film measurements	142
5.3.1 5 minutes cleaning.....	143
5.3.2 15 minutes cleaning.....	144
5.3.3 30 minutes cleaning.....	146
5.3.4 45 minutes cleaning.....	147
5.4 Effect of flow rate.....	148
5.4.1 Thin WSP layer	148
5.5 Effect of WSP thickness.....	152
5.5.1 High flow.....	152
5.5.2 Medium flow.....	153
5.6 Effect of standoff distance	154
5.7 Effect of water temperature.....	156
5.7.1 Medium flow, thin WSP layer, medium temperature	156
5.7.2 Medium flow, thin WSP layer, high temperature.....	158
5.8 Energy efficiency	161
5.9 Summary	163
6 Numerical Results.....	165
6.1 Introduction	165
6.2 Dry wall	165
6.2.1 Volume fraction of fluid time lapse images	165
6.2.1.1 0° contact angle.....	166
6.2.1.2 40° contact angle	168
6.2.2 Wall shear stress.....	170
6.3 Film on surface.....	173
6.3.1 Volume fraction of fluid time lapse images	173
6.3.1.1 Film thickness $h_0 = 0.05d$	173
6.3.1.2 Film thickness $h_0 = 0.15d$	174
6.3.2 Wall shear stress.....	176
6.4 Jet impingement.....	180
6.4.1 Jet velocity plots.....	180

6.4.2 Wall shear stress	181
6.4 Summary	185
7 Conclusions and Future Work	187
7.1 Introduction	187
7.2 Conclusions	187
7.2.1 Jet experiments	187
7.2.2 Spray experiments	188
7.2.3 Numerical modelling	188
7.2.4 Comparison of findings for jet and spray	189
7.2.5 Informing guidelines and application to site	189
7.3 Future work	190
Bibliography	192
Appendix A	i

List of Figures

Fig. 2. 1: Sinner's Circle for cleaning; Time, Action, Chemistry and Temperature.	5
Fig. 2. 2: Horizontal jet impinging on a vertical wall displaying the impingement point, O, radial flow zone, RFZ, the film jump and falling film. R_f is the radius of the film jump (Rodgers et al., 2019).	7
Fig. 2. 3: Effects of jet inclination on size and shape of cleaned area for inclination $\Phi = 45^\circ$, shown in the top half of the plot, and $\Phi = 90^\circ$, shown in the bottom half. S marks the source from which fluid flows radially outwards. Curves represent different times scaled at 1, 10 and 100 arbitrary units. Axes units are also arbitrary (Bhagat et al., 2017).	11
Fig. 2. 4: Schematic of jet breakup from coherent jet into droplet structure that impinges on wall (Recreated from Chee et al., 2019).	11
Fig. 2. 5: Schematic of Wilson et al. (2015) model of cleaning via a moving jet from left to right. w_c represents the width of the clean region, O the point of impingement, p the radial distance from impingement to the cleaning frontier, a_x the distance along the path of the jet, R_f the radial distance to the film jump and v_{jet} the velocity of the jet.	14
Fig. 2. 6: Predicted shape of cleaned region for moving jet. The continuous line represents the model from equation (2.5) and the square, triangular and circular points represent results from experiments. The dotted line is a circle of radius OX, p_w is the radial distance to the maximum cleaned width (Wilson et al., 2015).	15
Fig. 2. 7: Spray distributions: a) Flat fan, b) Hollow cone, c) Full cone (PNR, Accessed: 27/2/19).	16
Fig. 2. 8: Schematic of droplet disintegration for a liquid spray, the first image shows the point of impact of the droplet and the subsequent two images show the behaviour of the disintegration when K is $<$ or $>$ K_{crit} (Mundo et al., 1998).	17
Fig. 2. 9: Point of impact between droplet and wall (Rein, 1993).	19
Fig. 2. 10: Propagation of a shock wave into the drop after it impacted a solid surface, formation of an expansion wave and the onset of sideways jetting (Rein, 1993).	20
Fig. 2. 11: Droplet bouncing after impact (Rein, 1993).	21
Fig. 2. 12: Collision mechanisms for droplet impingement on liquid layer (Rein, 1993).	21
Fig. 2. 13: Jet from central cavity (Rein, 1993).	22
Fig. 2. 14: Droplet impingement behaviour for different angles of incidence and Weber number (Rein, 1993).	22
Fig. 2. 15: a) Droplet impingement on a dry surface, with no film layer present. The non-dimensional radius and height of the droplet are shown on the x and y-axis respectively	

b) Droplet impingement on a wetted surface with a film thickness approximately $\frac{1}{4}$ the radius of the droplet (Mundo et al., 1998).	23
Fig. 2. 16: Water droplet (dyed with ink) impact on a water layer. Droplet diameter $d = 1.9$ mm, fall height = 0.6 m. From left to left, time $t = 0.1$ ms, 1.9 ms, 11.4 ms, 25.6 ms, 74 ms and 113.8 ms after the first contact of the droplet and the layer (Wilkens, 1987).	25
Fig. 2. 17: Computational simulation of droplet impingement on to a liquid layer of the same properties as the droplet. Pressure distribution with time (Asadi and Passandideh-Fard, 2009).	26
Fig. 2. 18: Multiple droplet impingement: a) simultaneous, b) periodic (Moreira et al., 2010).	27
Fig. 2. 19: Multiple droplet impingement, periodic and spaced with angle of incidence for droplets (Moreira et al., 2010).	28
Fig. 2. 20: Effect of droplet spacing on droplet interaction a) $l_{\text{spacing}} = 0.8$ mm b) $l_{\text{spacing}} = 1.5$ mm.	29
Fig. 2. 21: Hydrodynamic regions upon periodic droplet impingement (Soriano et al., 2014).	29
Fig. 2. 22: Periodic droplet impingement and propagation of the crown (Zhang et al., 2016).	30
Fig. 2. 23: a) Top view, b) bottom view of periodic droplet impingement on translucent substrate, $We = 280$ (Zhang et al., 2016).	31
Fig. 2. 24: Experimental crown propagation images, $We = 443$ (Zhang et al., 2016). .	31
Fig. 2. 25: Experimental and numerical crown propagation images, $We = 280$ (Zhang et al., 2016).	32
Fig. 2. 26: Left: Experimental images of Cossali et al. (2004), Right: Computational simulations of Liang et al. (2018).	33
Fig. 2. 27: Interface between droplet impact evolution, For $We = 110$, $We = 443$ and $We = 693$. $\delta_f = 0.125$, $l_{\text{spacing}} = 1.5d$ (Cossali et al., 2004).	33
Fig. 2. 28: Time lapse of droplet impact on horizontal spacing, $l_{\text{spacing}} = 1.5d$ (left) vs $2.1d$ (right), $We = 800$, $Re = 100$, $\delta_f = 0.15$ and the liquid-gas density ratio, $\rho_T = 1000$ (Raman et al., 2015).	35
Fig. 2. 29: Schematic of biofilm removal process via impinging droplet (Cence et al. 2006).	37
Fig. 2. 30: Non-dimensional shear stress distribution on wall at various dimensionless times. Droplet velocity 50 ms^{-1} , four curves each represent a different droplet diameter shown in legend (Cence et al. 2006).	38

Fig. 2. 31: Non-dimensional shear stress versus dimensionless time. Legend shows water layer thickness, h_0 , to droplet radius, r , ratios (Cense et al. 2006)	39
Fig. 2. 32: Exemplar CIP nozzles: (a) static spray ball (b) rotary spray head (c) rotary jet head (Sørensen, Accessed: 7/1/19).....	40
Fig. 2. 33: a) Sinner's circle for tank CIP using static spray ball b) Sinner's circle for tank CIP using rotary jet head (Sørensen, Accessed: 7/1/19).....	41
Fig. 2. 34: a) Wash rack unloaded. Each pipe section can be seen leading to a nozzle on to which a component is loaded (b) Wash rack with disassembled components loaded on to jet/spray nozzles (c) Wash rack is loaded into washer via coupling (i), water is recirculated via sump (ii) rinse of the chamber is performed by rotating jet arm (iii) (Rodgers et al., 2019).	44
Fig. 3. 1: Coupling mechanism: Left: Female fitting on rack, right: male fitting in washer.	58
Fig. 3. 2: Assumed pump curve for Rack 1: Pressure drop ΔP vs flow rate Q	58
Fig. 3. 3: Left: Rack 1 unloaded. Each pipe section can be seen leading to a nozzle on to which a component is loaded. Right: Rack 1 with disassembled components loaded on to jet/spray nozzles (Rodgers et al. 2019).....	59
Fig. 3. 4: EPANET model of Rack 1: Lines represent pipe sections, circular nodes junctions, diamond nodes emitters, node 1 is a reservoir and the pump is that which connects nodes 1 and 2. A table of the discharge coefficients corresponding to each node can be found in Appendix A Table A1.	60
Fig. 3. 5: Bubble plot showing the distribution of flow rates in Rack 1 with each nozzle ID labelled. Flow rates proportional to nodal areas (blue), coupling left unfilled (Rodgers et al. 2019). Flow rate and percentage distribution data can be found in Table A2 in Appendix A.	60
Fig. 3. 6: Rack 2 loaded with disassembled parts from the production line.	61
Fig. 3. 7: Schematic of 4x4 pipe.	61
Fig. 3. 8: Flow rate Q vs square root of pressure drop ΔP from pipe interior to atmosphere. The gradients of each curve represent the discharge coefficient of the perforated pipe sections.	62
Fig. 3. 9: Exemplar spray ball used to model those on the rack (Delta Stainless Steel Ltd, Accessed: 5/3/19).	63
Fig. 3. 10: Flow rate Q vs square root of pressure drop ΔP from spray ball interior to atmosphere. The gradient of the line represents the discharge coefficient for the spray ball. Data accessed from Delta Stainless Steel Ltd (Accessed 5/3/19).	63

Fig. 3. 11: Nozzle discharge coefficient k for open pipe vs pipe diameter D (de Boer, 2014).	64
Fig. 3. 12: EPANET model of Rack 2: Lines represent pipe sections, circular nodes junctions, diamond nodes emitters, node 1 is a reservoir and the pump is that which connects nodes 1 and 2. Nozzle discharge coefficient data is available in Table A3 in Appendix A.	65
Fig. 3. 13: Bubble plot showing the distribution of flow rates in Rack 2 with each nozzle ID labelled. Flow rates proportional to nodal areas (blue), coupling left unfilled. Flow rate data and percentage distribution through nozzles can be found in Table A4 in Appendix A.	66
Fig. 3. 14: Top: Jet nozzle, bottom: footprint of horizontal 1 lmin^{-1} jet impinging on vertical Perspex wall. Key regions observed by Wilson et al. (2018) highlighted: rope, RFZ and falling film	67
Fig. 3. 15: Flow rate, Q , vs square root of pressure drop across the nozzle, ΔP for three repeat experiments.	68
Fig. 3. 16: a) Test rig schematic; the arrows represent the flow of water. The enclosure and wall are both made of Perspex to allow for easy observation and imaging from the camera. ΔP and Q represent pressure drop across the nozzle and flow rate respectively. b) Photograph of test apparatus with main components identified.....	69
Fig. 3. 17: Box Behnken DOE for 3 design variables: temperature, WSP thickness and flow rate.	71
Fig. 3. 18: Penetration test Force versus Distance plot (measured at 20°C) Error bars plotted using standard deviation.	72
Fig. 3. 19: Rack 2 position of filling needles (b) cleaned by vertically aligned impinging jets (a).	74
Fig. 3. 20: Vertically aligned jet test rig with key elements labelled.....	75
Fig. 3. 21: Shear Viscosity vs Shear Stress for gel (20°C).	76
Fig. 3. 22: cone PNR BCQ-1740-B1 spray nozzle (PNR, Accessed: 4/4/18).....	77
Fig. 3. 23: (a) Photograph of spray distribution from nozzle (b) surface droplet distribution (c) convex distribution of droplets on surface (PNR, Access: 4/4/18).	77
Fig. 3. 24: Example computational domain consisting of two phases, domain 1 and domain 2. The grey domain 1 is represented by $\Phi = 1$, the blue domain 2 is represented by $\Phi = 0$, the white interface is represented by $\Phi = 0.5$	79
Fig. 3. 25: COMSOL domain setup, wetted wall case.	83
Fig. 3. 26: Droplet impingement model with water film on the surface ($0.15d$ film thickness).	84

Fig. 3. 27: Interfacial thickness parameter, ϵ , control study: a) Default b) $\epsilon = 1 \times 10^{-5}$ m	87
Fig. 3. 28: Wall shear stress vs Position on the wall (Film thickness 0.15d).	88
Fig. 3. 29: Space averaged shear stress vs time (0.15d film thickness).	88
Fig. 3. 30: Mesh convergence study: coarse mesh (0.15d film thickness).	89
Fig. 3. 31: Mesh convergence study: most refined mesh (0.15d film thickness).	90
Fig. 3. 32: Mesh convergence study. Space and time averaged shear stress versus number of mesh elements.	91
Fig. 3. 33: Mesh 1: Level set function, Φ , along centre line ($r_{\text{wall}} = 0$), vs height along centre line, z (m). (Film thickness = 0.15d).	92
Fig. 3. 34: Zoomed in image of Fig. 3.33, with the location of $z = 0.25$ mm and $\Phi = 0.5$ highlighted. (Film thickness = 0.15d).	92
Fig. 3. 35: Mesh convergence: time corresponding to $z = 0.25$ mm, $\Phi = 0.5$, versus number of mesh elements (Film thickness = 0.15d).	93
Fig. 3. 36: Φ versus z : five contours before droplet impact to measure droplet diameter for convergence. From top to bottom: Mesh 1, Mesh 2, Mesh 3, Mesh 4.	95
Fig. 3. 37: Shear stress at $r_{\text{wall}} = 2d$ vs time (Mesh 3 and Mesh 4).	96
Fig. 3. 38: Single phase domain drawn in COMSOL, using coordinates of the film in the RFZ obtained from the equations of Bhagat and Wilson (2016).	98
Fig. 4. 1: Time lapse removal for 4 lmin ⁻¹ jet, 0.19 mm WSP thickness. Water temperature 20 °C (a) 3 s (b) 10s (c) 30 s (d) 300 s.	101
Fig. 4. 2: Time lapse removal for 2.5 lmin ⁻¹ jet, 0.19 mm WSP thickness, water temperature 20 °C (a) 3 s (b) 10s (c) 30 s (d) 300 s.	102
Fig. 4. 3: 300 s cleaning, 1 lmin ⁻¹ jet, 0.19 mm WSP thickness, water temperature 20 °C.	103
Fig. 4. 4: Time lapse removal for 4 lmin ⁻¹ jet, 0.95 mm WSP thickness, water temperature 20 °C (a) 3 s (b) 10s (c) 30 s (d) 300 s.	103
Fig. 4. 5: Time lapse removal for 2.5 lmin ⁻¹ jet, 0.95 mm WSP thickness, water temperature 20 °C (a) 3 s (b) 10s (c) 30 s (d) 300 s.	104
Fig. 4. 6: 300 s cleaning, 1 lmin ⁻¹ jet, 0.95 mm WSP thickness, water temperature 20 °C.	105
Fig. 4. 7: Time lapse removal for 4 lmin ⁻¹ jet and 1.9 mm WSP thickness (a) 3 s (b) 10s (c) 30 s (d) 300 s, water temperature 20 °C.	106
Fig. 4. 8: Time lapse removal for 2.5 lmin ⁻¹ jet and 1.9 mm WSP thickness (a) 3 s (b) 10s (c) 30 s (d) 300 s, water temperature 20 °C.	106

Fig. 4. 9: 300 s cleaning, 1 lmin ⁻¹ jet, 1.9 mm WSP thickness, water temperature 20 °C.	107
Fig. 4. 10: a) WSP ridge dye @ t = 1 min. b) Position of dye @ t = 3 min. c) Adhesive soil removal and build-up of the ridge of WSP on the perimeter of the clean area.....	108
Fig. 4. 11: Clean area versus time for each standoff distance, D (0.19 mm WSP thickness, 4 lmin ⁻¹ jet, water temperature 20°C).....	109
Fig. 4. 12: Clean Area versus Time for each flow rate (0.19 mm WSP thickness, water temperature 20 °C).	110
Fig. 4. 13: Horizontal jet impingement on vertical wall schematic.....	111
Fig. 4. 14: Clean area versus time (4 lmin ⁻¹ flow rate, water temperature 20 °C).....	113
Fig. 4. 15: Clean area versus time (2.5 lmin ⁻¹ flow rate, water temperature 20 °C)....	114
Fig. 4. 16: Clean area versus time (1 lmin ⁻¹ flow rate, water temperature 20 °C).	115
Fig. 4. 17: Area relative to final value at each time interval plotted against energy input to the cleaning process (0.19 mm WSP thickness, water temperature 20 °C).	116
Fig. 4. 18: Efficiency of WSP removal from surfaces expressed as clean area per energy (0.19 mm WSP thickness, water temperature 20 °C).	117
Fig. 4. 19: Clean area versus time (4 lmin ⁻¹ flow rate, 0.95 mm WSP thickness).	118
Fig. 4. 20: Clean area versus time (2.5 lmin ⁻¹ jet, 1.9 mm WSP thickness).	119
Fig. 4. 21: Time lapse of removal 1 lmin ⁻¹ jet, 0.95 mm WSP thickness, water temperature 60 °C. (a) 10 s. (b) 30 s. (c) 60 s. (d) 120 s. (e) Zoomed in region of clean area at long time 300 s.	121
Fig. 4. 22: Time lapse removal for 1 lmin ⁻¹ jet, 0.95 mm WSP thickness, water temperature 40 °C (a) 3 s (b) 10s (c) 30 s (d) 120 s.	121
Fig. 4. 23: Time lapse removal for 2.5 lmin ⁻¹ jet, 0.19 mm WSP thickness, water temperature 40 °C (a) 3 s (b) 10s (c) 30 s (d) 120 s.	122
Fig. 4. 24: Mass of water collected from exit to pipe versus time, perfectly aligned jet; fresh, baked and dried gel samples.	123
Fig. 4. 25: Removal of fouling deposit in pipe in 2 stages: 1(i) Needle initially full with gel ; 1(ii) water impinging on top of gel pushes fluid from pipe; 1(iii) water flow through pipe established; 2(i) residual film on wall surface which needs to be removed under shear to give clean walls 2(ii).	124
Fig. 4. 26: Mass flow rate versus Time for fresh, dried and baked samples.	125
Fig. 4. 27: Left: perfectly aligned jet, Right: misaligned jet (~2° angular displacement).	126
Fig. 4. 28: Mass of water collected from exit to pipe versus time, misaligned jet; fresh, baked and dried gel samples.	127

Fig. 4. 29: Bubble plot of flow distribution in Rack 2 after altering spray ball coefficients for improved flow distribution through the rack, coupling left unfilled.	130
Fig. 5. 1: Time lapse removal for 4 lmin ⁻¹ spray, 0.19 mm WSP thickness, water temperature 20 °C, 50 mm standoff (a) 30 s (b) 60s (c) 300 s (d) 600 s.	132
Fig. 5. 2a: Cleaned area close-up after one hour of cleaning: 4 lmin ⁻¹ spray, 0.19 mm WSP thickness, water temperature 20 °C, 50 mm standoff.	133
Fig. 5. 3: Time lapse removal for 2.5 lmin ⁻¹ spray, 0.19 mm WSP thickness, water temperature 20 °C, 50 mm standoff (a) 30 s (b) 60s (c) 300 s (d) 600 s.	134
Fig. 5. 4: Cleaned area close-up after one hour of cleaning: 2.5 lmin ⁻¹ spray, 0.19 mm WSP thickness, water temperature 20 °C, 50 mm standoff.	135
Fig. 5. 5: Cleaned area close-up after one hour of cleaning: 1 lmin ⁻¹ spray, 0.19 mm WSP thickness, water temperature 20 °C, 50 mm standoff.	136
Fig. 5. 6: Time lapse removal for 4 lmin ⁻¹ spray, 0.95 mm WSP thickness, water temperature 20 °C, 50 mm standoff (a) 30 s (b) 60s (c) 300 s (d) 600 s.	137
Fig. 5. 7: Cleaned area close-up after one hour of cleaning: 4 lmin ⁻¹ spray, 0.95 mm WSP thickness, water temperature 20 °C, 50 mm standoff.	137
Fig. 5. 8: Time lapse removal for 2.5 lmin ⁻¹ spray, 0.95 mm WSP thickness, water temperature 20 °C, 50 mm standoff (a) 30 s (b) 60s (c) 300 s (d) 600 s.	138
Fig. 5. 9: Cleaned area close-up after one hour of cleaning: 2.5 lmin ⁻¹ spray, 0.95 mm WSP thickness, water temperature 20 °C, 50 mm standoff.	139
Fig. 5. 10: Time lapse removal for 4 lmin ⁻¹ spray, 1.9 mm WSP thickness, water temperature 20 °C, 50 mm standoff (a) 300 s (b) 600 s.	139
Fig. 5. 11: Cleaned area close-up after one hour of cleaning: 4 lmin ⁻¹ spray, 1.9 mm WSP thickness, water temperature 20 °C, 50 mm standoff.	140
Fig. 5. 12: Time lapse removal for 2.5 lmin ⁻¹ spray, 1.9 mm WSP thickness, water temperature 20 °C, 50 mm standoff (a) 300 s (b) 600 s.	140
Fig. 5. 13: Cleaned area close-up after one hour of cleaning: 2.5 lmin ⁻¹ spray, 1.9 mm WSP thickness, water temperature 20 °C, 50 mm standoff.	141
Fig. 5. 14: Left (a) Sample plate on test rig. Right (b) Sample plate mounted on to X-Y table.	142
Fig. 5. 15: Left (a) 5 minutes cleaning sample. Right (b) 5 minutes cleaning CTS	143
Fig. 5. 16: Close-up of highlighted region in 5.15b.	144
Fig. 5. 17: Left (a) 15 minutes cleaning sample. Right (b) 15 minutes cleaning CTS	144
Fig. 5. 18: Close-up of highlighted region.	145
Fig. 5. 19: Left (a) 30 minutes cleaning sample. Right (b) 30 minutes cleaning CTS.	146

Fig. 5. 20: Close-up of highlighted region.	147
Fig. 5. 21: Left (a) 45 minutes cleaning sample. Right (b) 45 minutes CTS.	147
Fig. 5. 22: Close-up of highlighted region.	148
Fig. 5. 23: Cleaned Area versus Time for each flow rate (0.19 mm WSP thickness, water temperature 20 °C, 50 mm standoff) The red, green and blue lines represent the impingement areas from the cone of the spray for the 1, 2.5 and 4 lmin ⁻¹ sprays respectively.....	149
Fig. 5. 24: Full cone spray impingement on clean vertical wall a) side view b) front view.	150
Fig. 5. 25: Spray soil removal mechanism schematic.	151
Fig. 5. 26: Cleaned area versus time (4 l min ⁻¹ flow rate, water temperature 20 °C, 50 mm standoff).....	153
Fig. 5. 27: Cleaned area versus time (2.5 l min ⁻¹ flow rate, 20 °C, 50 mm standoff). .	153
Fig. 5. 28: Time lapse removal for 2.5 lmin ⁻¹ spray, 0.19 mm WSP thickness, water temperature 20 °C, 125 mm standoff (a) 30 s (b) 60 s (c) 300 s (d) 600 s.....	155
Fig. 5. 29: Cleaned area close-up after one hour of cleaning: 2.5 lmin ⁻¹ spray, 0.19 mm WSP thickness, water temperature 20 °C, 125 mm standoff.	155
Fig. 5. 30: Time lapse removal for 2.5 lmin ⁻¹ spray, 0.19 mm WSP thickness, water temperature 40 °C, 50 mm standoff (a) 10 s (b) 30 s (c) 60 s (d) 120 s.....	157
Fig. 5. 31: Left: long-time (300 s) clean area close-up (2.5 lmin ⁻¹ spray, 0.19 mm WSP thickness, water temperature 40 °C), Right: long-time cleaned area close-up (2.5 lmin ⁻¹ spray, 0.19 mm WSP thickness, water temperature 20°C).....	157
Fig. 5. 32: Time lapse removal for 2.5 lmin ⁻¹ spray, 0.19 mm WSP thickness, water temperature 60 °C, 50 mm standoff (a) 10 s (b) 30s (c) 60 s (d) 120 s.....	158
Fig. 5. 33: Long-time (300 s) clean area close up (2.5 lmin ⁻¹ spray, 0.19 mm WSP thickness, water temperature 60 °C).	159
Fig. 5. 34: Clean area versus time, 2.5 lmin ⁻¹ spray, 0.19 mm WSP thickness, water temperature 20 °C, 40 °C and 60 °C (50 mm standoff).	159
Fig. 5. 35: Time lapse removal for 1 lmin ⁻¹ spray, 0.95 mm WSP thickness, water temperature 40 °C, 50 mm standoff (a) 10 s (b) 30 s (c) 60 s (d) 120 s.....	160
Fig. 5. 36: Long-time (300 s) clean area close up (1 lmin ⁻¹ spray, 0.95 mm WSP thickness, water temperature 40 °C).	161
Fig. 5. 37: Area relative to long-time value at each time plotted against energy input to the cleaning process (0.19 mm WSP thickness, water temperature 20 °C).	161
Fig. 5. 38: Clean Area versus Energy, 2.5 lmin ⁻¹ jet and spray, 1.9 mm WSP thickness, water temperature 60 °C.....	162

Fig. 6. 1: Volume fraction of fluid time lapse, 0° wetted wall. (a) $t = 0$ ms, (b) $t = 3$ ms, (c) $t = 3.6$ ms, (d) $t = 4.1$ ms. (e) $t = 4.7$ ms and (f) $t = 15$ ms.	166
Fig. 6. 2: Volume fraction of fluid time lapse, 40° wetted wall. (a) $t = 3.6$ ms, (b) $t = 4.1$ ms, (c) $t = 4.7$ ms, (d) $t = 7.2$ ms and (e) $t = 15$ ms.	168
Fig. 6. 3: Volume fraction of fluid time lapse, 40° wetted wall. (a) $t = 3.6$ ms, (b) $t = 4.1$ ms, (c) $t = 4.7$ ms, (d) $t = 5.1$ ms and (e) $t = 15$ ms.	169
Fig. 6. 4: Wall shear stress for each $\theta = 0^\circ, 20^\circ, 40^\circ, 60^\circ$ and 83° , $r_{\text{wall}} = 0$	170
Fig. 6. 5: Wall shear stress for each contact angle, $\theta = 0^\circ, 20^\circ, 40^\circ, 60^\circ, 83^\circ$, $r_{\text{wall}} = d$	171
Fig. 6. 6: Wall shear stress for the $\theta = 0^\circ, 20^\circ$. $r_{\text{wall}} = 2d$	172
Fig. 6. 7: Volume fraction of fluid time lapse, film thickness = $0.05d$ (a) $t = 3.6$ ms, (b) $t = 4.1$ ms, (c) $t = 4.7$ ms and (d) $t = 15$ ms.	173
Fig. 6. 8: Volume fraction of fluid time lapse, film thickness = $0.15d$. (a) $t = 3.6$ ms, (b) $t = 4.1$ ms, (c) $t = 5.1$ ms, (d) $t = 15$ ms.	175
Fig. 6. 9: Volume fraction of fluid time lapse, film thickness = d . (a) $t = 3$ ms, (b) $t = 3.6$ ms, (c) $t = 4.1$ ms, (d) $t = 15$ ms	176
Fig. 6. 10: Wall shear stress versus time: no film (0° contact angle), film thickness $h_0 = 0.05d, 0.15d, 0.25d$ and $0.5d$. $r_{\text{wall}} = 0$	177
Fig. 6. 11: Wall shear stress versus time: no film (0° contact angle), film thickness $h_0 = 0.05d, 0.15d, 0.25d$ and $0.5d$. $r_{\text{wall}} = d$	178
Fig. 6. 12: Wall shear stress versus time: no film (0° contact angle), film thickness $h_0 = 0.05d, 0.15d, 0.25d$ and $0.5d$. $r_{\text{wall}} = 2d$	179
Fig. 6. 13: Wall shear stress versus time: film thickness $h_0 = 0.05d, 0.15d, 0.25d$ and $0.5d$. $r_{\text{wall}} = 3d$	179
Fig. 6. 14: Jet impingement COMSOL model: Surface velocity magnitude.....	180
Fig. 6. 15: Jet impingement: 3D Surface velocity magnitude.....	181
Fig. 6. 16: Wall shear stress vs radial position on wall. COMSOL model compared with literature	182
Fig. 6. 17: Wall shear stress vs radial position on wall.....	183
Fig. 6. 18: Wall shear stress versus radial position on wall.....	184

List of Tables

Table 2.1: Critical process parameters and quality attributes of a typical cleaning system (LeBlanc et al., 2012).....	44
Table 3.1: COMSOL model parameters.....	85
Table 3. 2: Mesh convergence study: Mesh IDs and number of elements.....	90
Table 4.1: Jet flow rate and corresponding impingement force.....	112
Table 7. 1: Key comparisons for jet and spray.....	189
Table A.1: Nozzle discharge coefficients (Rack 1).....	i
Table A.2: Nozzle flow rate data (Rack 1) and % total flow with/without coupling discharge.....	ii
Table A.3: Nozzle discharge coefficients (Rack 2).....	iii
Table A.4: Nozzle flow rate data (Rack 2) and % total flow.	iv

Nomenclature

Roman

a	Acceleration (ms^{-2})
a_x	Moving jet cleaning frontier (m)
c_s	Droplet shockwave velocity (ms^{-1})
d	Droplet diameter (mm)
$d_{c,\text{base}}$	Droplet crown base diameter (mm)
$d^*_{c,\text{base}}$	Droplet crown base diameter/droplet diameter
d_{avg}	Average cleaned area diameter (mm)
d_{jet}	Jet diameter (mm)
D	Nozzle standoff distance (mm)
D_j	Pipe diameter in EPANET (mm)
dm	EPANET nodal demand (ls^{-1})
el	EPANET nodal elevation (m)
f	Droplet frequency (Hz)
f_j	Friction factor in EPANET
F	Volume force (Nm^{-3})
F_x	Horizontal jet impingement force (N)
g	Acceleration due to gravity (ms^{-2})
H	Head loss (mH ₂ O)
h_{rj}	Roughness height in EPANET (mm)
h_0	Film thickness (mm)
k	Nozzle discharge coefficient ($\text{lmin}^{-1}\text{Pa}^{-0.5}$)
K_c	Droplet breakup threshold parameter
$K_{c,\text{wet}}$	Droplet breakup threshold parameter (wetted surface)
L	Jet length (m)
L_c	Characteristic length scale (mm)
L_j	Pipe length in EPANET (m)
L_R	Length scale of roughness (mm)
L_{spacing}	Horizontal droplet spacing (mm)

\dot{m}	Mass flow rate (kgs^{-1})
N_f	Number of fixed head nodes in EPANET
N_j	Number of variable head nodes in EPANET
N_p	Number of pipes in EPANET
O	Jet impingement point
Oh	Ohnesorge Number
P	Pressure (Pa)
p	Jet momentum (kgms^{-1})
p_c	Radial distance to moving jet cleaning frontier (m)
p_w	Radial distance to maximum moving jet cleaned width (m)
ΔP	Pressure drop across orifice (Pa)
Q	Flow rate (lmin^{-1})
Q _{eff}	Effective flow rate (lmin^{-1})
r_j	Resistance factor in EPANET
r_{wall}	Co-ordinate on wall (mm)
R	Maximum wall length in droplet simulations (mm)
R_f	Radial distance from jet impingement point to film jump (mm)
r	Droplet radius (mm)
Re	Reynolds Number
R_{ND}	Film thickness/roughness amplitude
S	Splatter fraction
t^*	Non-dimensional time
u	Velocity (ms^{-1})
u_{jet}	Impinging jet velocity (ms^{-1})
u_d	Initial droplet velocity (ms^{-1})
v_d	Droplet velocity (ms^{-1})
v_{jet}	Dynamic jet horizontal component of velocity (ms^{-1})
We	Weber Number
w_c	Moving jet cleaned width (mm)
z	Height in COMSOL domain (mm)

Greek

α	Spray angle ($^{\circ}$)
α_{jet}	Moving jet discharge parameter (m^5s^{-1})
β	Level set method initialisation parameter
γ	Shear rate (s^{-1})
∂	Film thickness/droplet diameter
ϵ	Level set method interfacial thickness parameter
κ	Interfacial curvature
μ	Viscosity (Pa.s)
μ_T	Turbulent viscosity (Pa.s)
η	Dynamic viscosity (Pa.s)
ρ	Density (kgm^{-3})
σ	Surface tension (Nm^{-1})
θ	Contact angle ($^{\circ}$)
θ_c	Moving jet angle between a_x and p_c ($^{\circ}$)
\varnothing	Level set function
τ_{ci}	Normalised time scale between consecutive droplet impacts
τ_{wall}	Wall shear stress (Pa)
$\tau_{avg,rwall}$	Space averaged wall shear stress (Pa)
$\tau_{avg,t}$	Time and space averaged wall shear stress (Pa)

Abbreviations

COP	Cleaning-out-of-place
CIP	Cleaning-in-place
CTS	Confocal thickness sensor
GMP	Good manufacturing practice
cGMP	Current good manufacturing practice
MACO	Maximum allowable carry-over
PDE	Partial differential equation
RFZ	Radial flow zone
TACT	Time Action Chemistry Temperature

WSP White soft paraffin

Chapter 1

Introduction

1.1 Context

The cleaning of production equipment is a significant yet frequently overlooked aspect of the batch manufacturing cycle. With batch cleaning, control is required to manage residues between batches of product, particularly when multiple products are made using the same equipment (Lakshmana Prabu et al., 2010). With batch processing, equipment is commonly disassembled into its constituent parts which are then loaded onto a washing rack for cleaning-out-of-place (COP) (PMTTC, 2015). Each washing rack comprises a series of pipes and nozzles through which a mixture of (often heated) water and surfactant passes. The nozzles are positioned such that the fluid flow cleans the loaded components via a jet or spray. This is in contrast to the counterpart cleaning-in-place (CIP), where cleaning is done in situ with no disassembly of production equipment.

Batch processing is prevalent within pharmaceutical manufacture where the active pharmaceutical ingredient is manipulated into a dose form suitable for human use e.g. creams and ointments. Within this sector, after the cleaning process has taken place, the parts are inspected and must meet cleanliness acceptance criteria with limits for cleaning validation, as established by the manufacturer and a regulatory body. A visually clean criterion, whereby after inspection the part appears clean to the naked eye, is a minimum requirement for acceptance and is limited by the Food and Drug Administration (FDA) to use between batches of the same product, in other cases it must be used in conjunction with other criteria (FDA, 1993). In 1992 the FDA instituted an important alert to a bulk pharmaceutical manufacturer that was manufacturing a potent steroid product in the same equipment that was used for production of non-steroidal products. This was considered a potential for cross-contamination that could pose a serious threat to the public. The FDA deemed the manufacturer's cleaning validation inadequate since they were looking only for evidence of the absence of the previous compound in each batch. There was however evidence from sampling of rinse water that residual by-products and degradants from the previous process were present in batches (FDA, 1993). Other regulatory bodies in the pharmaceutical industry include the Medicines and Healthcare Products Regulatory Agency (MHRA) and the European Medicines Agency (EMA).

While regulations and guidelines vary from country to country, they are designed to ensure the safety, efficiency and security of the pharmaceutical product being manufactured. Good practice is used to identify common failures and the cleaning

process amended to address these (PMTc, 2015). This can be a source of inefficiency to a manufacturer since additional maintenance costs and costs due to production loss are incurred, whilst there is also a detrimental impact to a company's reputation. In the event of products cross-contaminated from previous batches having to be recalled, incurred costs include product rehabilitation costs, recall costs and costs of interruption to business. Shewale et al. (2014) valued this to be 49% of the total recall cost. Between 2001 and 2014 the FDA reported more than 1,984 recalls in the pharmaceutical industry with more than \$700 million manufacturer's penalties and billions more lost in revenue (Shewale et al., 2014).

This research addresses batch cleaning of components where COP is frequently used. Here parts are removed from the process equipment and loaded onto racks which incorporate a series of nozzles, before undergoing a series of distinct cleaning operations. This work studies hydrodynamic cleaning from a wash rack into two distinct phases: (i) the distribution of the flow within the rack to the formation of jets/sprays at the nozzle, (ii) the interaction of the fluid with the substrate. The work is novel in its approach as it is applied to wash racks used in the pharmaceutical industry, which have not been studied in great detail. In addition, the soil used for experiments is an excipient commonly used in the manufacture of pharmaceuticals and an energy framework has been adopted to evaluate the efficiency of different cleaning procedures, for both jets and sprays. The output from the research can be utilised and applied directly to industry and whilst the primary focus is on COP, certain aspects of the research will be applicable to CIP, particularly the study of water temperature and its affect on the rheology of the soil and subsequent cleaning efficacy.

1.2 Aims and objectives

The aim of this research is to ultimately provide guidance to the pharmaceutical industry to improve flow conditions used in batch cleaning processes, for greater cleaning efficiency, and gain a more detailed understanding of the cleaning mechanisms of liquid jets and sprays. The objectives of the research are as follows:

1. Model the flow distribution through wash racks and replicate the flow conditions delivered to the nozzles experimentally.
2. Perform a range of experiments under different flow conditions, representative of those used in industry, to develop an understanding of cleaning via jets and sprays.
3. Conduct a mechanistic study to gauge the soil removal mechanisms involved for jet cleaning.

4. Model droplet impingement on to a soil layer computationally to gauge the soil removal mechanisms involved in spray cleaning.
5. Draw conclusions from the research and apply to industry.

1.3 Thesis structure

Chapter 2 comprises a literature review which outlines cleaning demands and challenges in industry, with a particular focus on cleaning in the pharmaceutical industry with which this research is primarily concerned. Chapter 3 details the methods used in completing the research, including the design of a test rig used for experimentation and methods for supporting computational work. Chapters 4, 5 and 6 contain results gathered computationally and experimentally via jets and sprays. Chapter 7 discusses the results shown in previous chapters and describes how the findings are pertinent to industry and how this research can ultimately be applied in industry to take steps towards optimal cleaning. Finally, Chapter 8 summarises the thesis and its conclusions, and presents the future work that remains to continue the research further.

Chapter 2

Literature Review

2.1 Costs and inefficiencies of cleaning in the pharmaceutical industry

Cleaning of production equipment is ubiquitous in the pharmaceutical industry. Fouling is a major problem and frequent cleaning, often daily, is required. Fouling deposits can endanger hygienic operation as well as lowering the efficiency of the plant. Cleaning is also necessary at plant changeover before processing of another product starts (Palabiyik et al., 2014). Issues such as cross-contamination of products, separation of products in flexible manufacturing operations, microbial impacts on hygiene, batch integrity and traceability are extremely important. Cleanliness includes chemical and biological aspects, usually at the microscale (Wilson, 2005). The need for frequent cleaning means that there is an increase in resource consumption and longer down time on plant, where production comes to a halt. It is therefore important to increase the efficiency of cleaning processes employed in industry, which can take up to 30% of total working time of the machine or facility in question (Fuchs et al., 2019). The need to ensure product safety and purity means that cleaning protocols are commonly overdesigned, but the damage to a brand's image arising from product recall due to contamination is so detrimental that there is little incentive to experiment with safety margins (Fryer and Asteriadou, 2009). In addition to the negative impact on a brand's image due to recall, there are large financial implications to a company. These include product rehabilitation costs, recall costs and costs of the aforementioned interruption to business, which recalling from Chapter 1 were estimated to be 49% of total recall cost by Shewale et al. (2014).

2.2 Contaminants found in pharmaceutical product manufacture

There are three main contributors to the contamination commonly found in pharmaceutical production equipment.

1. The primary cause can be attributed to cross contamination with active ingredients, whereby high levels of residual ingredients from a previous batch of produce contaminate the subsequent batch. There is also the potential of synergistic interactions between pharmacologically active chemicals being a real concern (Lakshmana Prabu et al., 2010).
2. Contamination with unintended materials or compounds is another potential form of vessel contamination. The routine use, maintenance and cleaning of the vessels leads to potential contamination. This is due to regular contact with lubricants,

chemical cleaning agents and cleaning tools for example (Lakshmana Prabu et al., 2010).

3. Microbiological contamination is another possibility since conditions in the vessel for maintenance, cleaning and storage may provide an ideal environment for adventitious microorganisms to proliferate (Lakshmana Prabu et al., 2010).

2.3 Sinner's Circle

Cleaning as a process has been described as a mixture of four factors which combine to form the quadrants of Sinner's circle (see Fig. 2.1); **T**ime, **A**ction, **C**hemistry and **T**emperature (Sinner, 1959). Together they form the TACT cleaning parameters that are required to be controlled in any cleaning process, whether manual, semi-automated or automated.

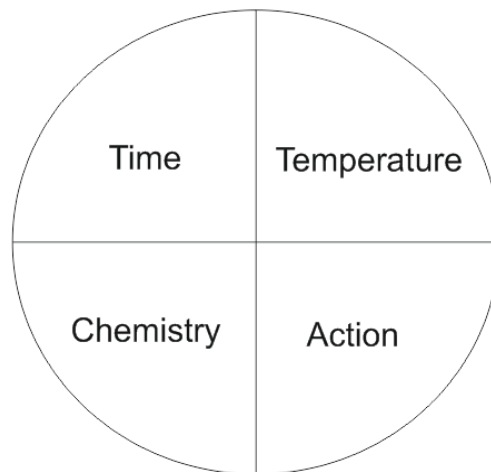


Fig. 2. 1: Sinner's Circle for cleaning; Time, Action, Chemistry and Temperature.

Changes in one TACT parameter will cause a commensurate increase or decrease in the other parameters. The correct balance of parameters is determined by the nature of the soil and the surface being cleaned (Lodhi et al., 2014). Whilst cleaning can be achieved manually whereby equipment is cleaned directly by a trained operator, in most cases cleaning processes are automated (LeBlanc et al., 2012). In the pharmaceutical industry, large production equipment such as mixing vessels are commonly cleaned by cleaning-in-place (CIP) operations, whereby it is cleaned in-situ with no disassembly. (PMTTC, 2015). Aqueous solutions are circulated through units to remove residual films, by a combination of thermodynamics (i.e. temperature, dissolution), mechanics (hydraulic action of the flow) and chemistry (surfactants, detergents, dispersants and reactive agents) (Wilson et al., 2015).

2.3.1 Time

Time is defined as the length of time for the cycle step. In the pharmaceutical industry production operations are typically based on operating 24 hours a day, 7 days a week. CIP operations typically comprise of an 8 hour turn around, from dirty to clean, in this daily cycle. The majority of this time is for heating and cooling, but CIP time is important in determining the number of CIP systems required. For a static spray ball for example, complete wetting of a tank interior wall can be achieved in 30-90s, based on a flow rate of approximately $50 - 70 \text{ lmin}^{-1}$ and 1.7 bar (Greene, 2003). Factory acceptance tasks are put in place to test the effectiveness of spray balls typically used in CIP, using a Riboflavin coverage test. What this does is to ensure that the vessel internals are thoroughly wetted by the spray but does not ensure the tank will be cleaned by the CIP system. The Riboflavin test works by spraying a dilute Riboflavin solution on to the vessel internals, allowing it to dry. The spray will then be activated to remove the residue. After the desired time interval, the tank is inspected with a UV light to determine if the Riboflavin has been completely removed. If the Riboflavin removal is insufficient the nozzle and flow rate will be adapted and the tests repeated (Greene, 2003). A safety factor is added since removal of different soils may require more time for different removal mechanisms to take place. Typically, this is 2-3 on the test time and the same time used for all steps in the CIP cycle. Based on six cleaning steps of 5 minutes each, with allowance for set-up, air blows, heating and chemical additions, the time taken to clean a circuit containing a major flow path (tank) and a few minor flow paths (dip pipe or transfer line) is about 90 minutes (Greene, 2003).

2.3.2 Action

Action is the mechanism used to deliver the cleaning agent (LeBlanc et al., 2012). Cleaning requires bond rupture at fouling-equipment interfaces and mechanical action is often used to achieve this. Techniques available achieve this by direct or indirect application of shear or normal forces. This is commonly achieved using liquid jets or sprays (Wilson, 2005).

2.3.2.1 Jets

Liquid jets are widely used in cleaning operations to remove layers of soil from the internal and external surfaces of process equipment. They offer several advantages over simple 'fill and soak' strategies in employing smaller volumes of liquid and generally requiring less time (Wang et al., 2015). The jets can be created by fixed or rotating nozzles. Liquid water is usually used but other solvents and surfactants can be added to improve the efficiency of the soil removal.

Jet impingement perpendicular to wall

To better understand the hydrodynamics of cleaning, Wilson et al. (2012, 2014) considered the impingement of a jet on a vertical wall. Experimentally they observed three key regions (see Fig. 2.2) - (i) the radial flow zone (RFZ) where a thin, fast moving layer of fluid exerts a shear stress on the surface, (ii) a rope like jump which bounds the RFZ, termed the film jump and (iii) a falling film that drains from the film jump. Drosos et al. (2004) described how the flow in the falling film develops from an initially uniform liquid layer with a smooth surface, to a complex state in which two-dimensional waves first appear, eventually developing further downstream into larger three-dimensional waves.

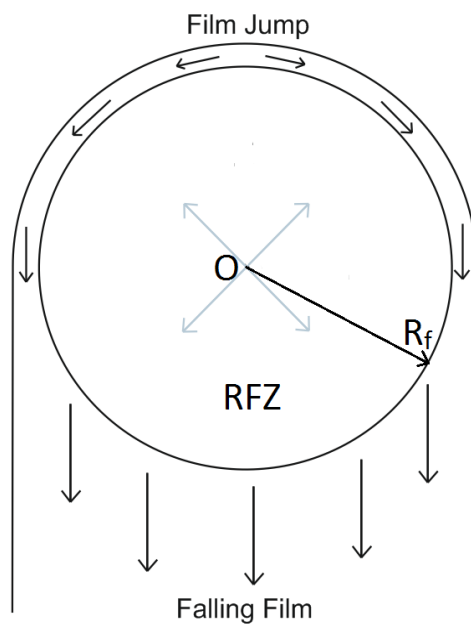


Fig. 2. 2: Horizontal jet impinging on a vertical wall displaying the impingement point, O, radial flow zone, RFZ, the film jump and falling film. R_f is the radius of the film jump (Rodgers et al., 2019).

In addition to considering the hydrodynamics, the behaviour of the soil removal was also considered, with three identified mechanisms that can often occur in parallel with each other:

- i. Dissolution, where the jetted fluid solvates the product.
- ii. Erosion, where the jet causes the product to be broken down due to hydrodynamic forces.
- iii. Soaking, whereby when the soil is insoluble and prolonged contact with the solvent promotes a change in the microstructure of the layer such that one of the previous mechanisms can occur. This is the predominant mechanism in the falling film due to the shear stress exerted on the wall being lower in this region.

The radius of the location of the film jump of a horizontal jet can be reasonably predicted by equation 2.1, derived empirically by Wilson et al. (2014). Note that this is for a clean surface with no soil layer present.

$$R_f = 0.276 \left[\frac{\dot{m}}{\eta \rho \sigma (1 - \cos \theta)} \right]^{\frac{1}{4}} \quad (2.1)$$

Where R_f is the radial distance from the impingement point to the film jump, \dot{m} is the mass flow rate, η is the liquid dynamic viscosity, ρ is its density, σ is the gas-liquid surface tension and θ is the contact angle between the substrate and the impinging liquid (Wilson et al., 2014).

When a vertical jet impinges on a horizontal wall, the flow behaviour changes as the effects of gravity are no longer noticeable. Again a RFZ forms as the liquid flows radially outwards from the impingement point, up to the formation of a jump in the film where the film depth increases. The flow pattern is symmetric and there is no falling film. The highest shear stresses are generated at the boundary of the radial flow zone and the film jump, beyond this boundary the shear stress on the wall is relatively low (Wilson et al., 2014).

Bhagat and Wilson (2016) described the RFZ in three distinct zones; boundary layer formation (BLF), laminar to turbulent transition (LTT) and turbulent. They went on to define the location on the wall at which the transition between each zone occurs, as a function of the jet diameter and jet Reynolds number. The Reynolds number, Re , is a dimensionless number used in fluid mechanics which defines the ratio of inertial to viscous forces in a flow regime, given by equation 2.2.

$$Re = \frac{\rho u L_c}{\eta} = \frac{\text{inertial forces}}{\text{viscous forces}} \quad (2.2)$$

Where ρ is the fluid density, u is velocity, L_c is the characteristic length scale and η is the dynamic viscosity. The expressions for the locations of zone transitions were described for the BLF – LTT and LTT – turbulent by equations 2.3 and 2.4 respectively.

$$\frac{r_{wall}}{d_{jet}} = 0.24 Re_{jet}^{1/3} \quad (2.3)$$

$$\frac{r_{wall}}{d_{jet}} = 0.2964 Re_{jet}^{1/3} \quad (2.4)$$

Where r_{wall} is the coordinate on the wall, d_{jet} is the diameter of the jet and Re_{jet} is the jet Reynolds number. At any particular point on the wall the behaviour of the flow could then be identified. Bhagat and Wilson (2016) also developed an expression for the height of

the film in the RFZ, h_0 , as a function of r_{wall} , d_{jet} and Re_{jet} . Equations 2.5, 2.6 and 2.7 describe h_0 in the BLF, LTT and turbulent zones respectively.

$$\frac{h_0}{d_{jet}} = 0.125 \left(\frac{d_{jet}}{r_{wall}} \right) + \frac{1.06}{\sqrt{Re_{jet}}} \left(\frac{r_{wall}}{d_{jet}} \right)^{0.5} \quad (2.5)$$

$$\frac{h_0}{d_{jet}} = \frac{3.792}{Re_{jet}} \left(\frac{r_{wall}}{d_{jet}} \right)^2 + 0.1975 \left(\frac{d_{jet}}{r_{wall}} \right) \quad (2.6)$$

$$\frac{h_0}{d_{jet}} = \frac{0.0209}{Re_{jet}} \left(\frac{r_{wall}}{d_{jet}} \right)^{1.25} + (0.296 - 0.001356 Re_{jet}^{0.5}) \left(\frac{d_{jet}}{r_{wall}} \right) \quad (2.7)$$

From this, knowing the jet geometry and flow conditions, i.e. Re_{jet} , the profile of the RFZ could be predicted.

Various works in the literature formulated expressions for the shear stress exerted on the wall, τ_{wall} , by an impinging jet, an important parameter from a cleaning perspective since adhesive removal of a soil is achieved by exerting a shear force on the substrate. Yeckel and Middleman (1987) studied the removal of an oil layer by a water jet impinging perpendicularly downwards on to a horizontal plate. They defined the wall shear stress using a two-zone model, assuming a turbulent film throughout the entire RFZ. Equation 2.9 describes the shear stress on the wall beyond the point where the turbulent boundary layer reaches the free surface and 2.8 is used before then. The point at which the turbulent boundary layer reaches the free surface is given by $1.84r_{wall} Re_{jet}^{1/9}$.

$$\tau_{wall} = 0.0397 \frac{\rho u_{jet}^2}{2} \left(\frac{2r_{wall}}{d_{jet}} \right)^{-0.2} Re_{jet}^{-0.2} \quad (2.8)$$

$$\tau_{wall} = 30.3 \frac{\rho u_{jet}^2}{2} \left(\frac{2r_{wall}}{d_{jet}} \right)^{0.25} \frac{Re_{jet}^{0.25}}{\left[\left(\frac{2r_{wall}}{d_{jet}} \right)^{2.25} + 27.24 Re_{jet}^{0.25} \right]^2} \quad (2.9)$$

Where u_{jet} is the perpendicular impinging jet velocity. Liu et al. (1991) described the wall shear stress in the BLF and LTT zones as 2.10 and 2.11 respectively.

$$\tau_{wall} = \eta \frac{1.5u_{jet}}{2.679} \sqrt{\frac{r_{wall} d_{jet}}{Re_{jet}}} \quad (2.10)$$

$$\tau_{wall} = \eta \frac{0.3u_{jet}}{r_{wall} \left(\frac{5.147}{Re_{jet}} \left(\frac{r_{wall}}{d_{jet}} \right)^2 + 0.1713 \left(\frac{d_{jet}}{r_{wall}} \right) \right)} \quad (2.11)$$

Where η is the impinging liquid dynamic viscosity. Bhagat and Wilson (2016) developed the equations 2.12, 2.13 and 2.14 for the wall shear stress in the BLF, LTT and turbulent

zones respectively. In the latter the shear stress is calculated with the assumption of a Blasius boundary layer

$$\tau_{wall} = \eta \frac{u_{jet}}{2.12 \sqrt{\frac{\eta r_{wall}}{\rho u_{jet}}}} \quad (2.12)$$

$$\tau_{wall} = \eta \frac{u_{jet}}{4r_{wall} \left(\frac{3.792}{Re_{jet}} \left(\frac{r_{wall}}{d_{jet}} \right)^2 + 0.1975 \left(\frac{d_{jet}}{r_{wall}} \right) \right)^2} \quad (2.13)$$

$$\tau_{wall} = \frac{0.0478\rho}{Re_{jet}^{0.25}} \left(\frac{u_{jet}}{\frac{0.167}{Re_{jet}^{0.25}} \left(\frac{r_{wall}}{d_{jet}} \right)^{2.25} + (2.37 - 0.0108 Re_{jet}^{0.5})} \right)^2 \quad (2.14)$$

In many CIP applications, liquid jets are generated by rotating nozzles or spray balls, in which case the jet is dynamic as opposed to the static case previously discussed. In large vessels such as some of those used in pharmaceutical manufacture, coherent jets may leave the nozzle as coherent but due to the distance required to travel to the walls of the vessel the jet can atomise and impinge as a series of droplets. At longer standoff distances gravity will also cause the jet to droop from a horizontal trajectory and impingement becomes inclined. Rotation of the nozzle will also generate a curved jet, in which case cleaning models become more complex (Bhagat et al., 2017).

Jet impingement inclined to wall

Bhagat et al. (2017) studied the effects of the inclination of a jet relative to a horizontal surface on the size and shape of the area cleaned. Fig. 2.3 shows a comparison between a jet inclined at 45° and 90° to the horizontal surface. For the same impingement point, S, the effect of jet inclination to the surface is shown in Fig. 2.3. The top half of the graph shown shows a 45° inclination, compared to a perpendicular jet in the bottom half. For arbitrary units of time, 1, 10 and 100, the footprints of the jet at those times are shown in the figure. The 45° jet is noticeably elongated than the perpendicular jet, wetting a greater length but less width than the perpendicular jet.

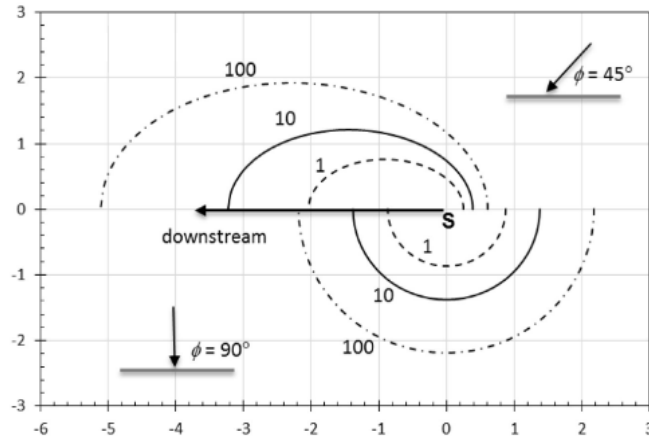


Fig. 2. 3: Effects of jet inclination on size and shape of cleaned area for inclination $\phi = 45^\circ$, shown in the top half of the plot, and $\phi = 90^\circ$, shown in the bottom half. S marks the source from which fluid flows radially outwards. Curves represent different times scaled at 1, 10 and 100 arbitrary units. Axes units are also arbitrary (Bhagat et al., 2017).

Large standoff distance between jet and wall

Much of the research into liquid jet impingement has been conducted at small standoff distances which have not been scaled up to typical standoff distances seen in industrial CIP applications, where large mixing vessels are cleaned. In this scenario due to the large distance between the nozzle and the wall, the jet droops from a true line and disintegrates from a coherent jet into a droplet structure (see Fig. 2.4).

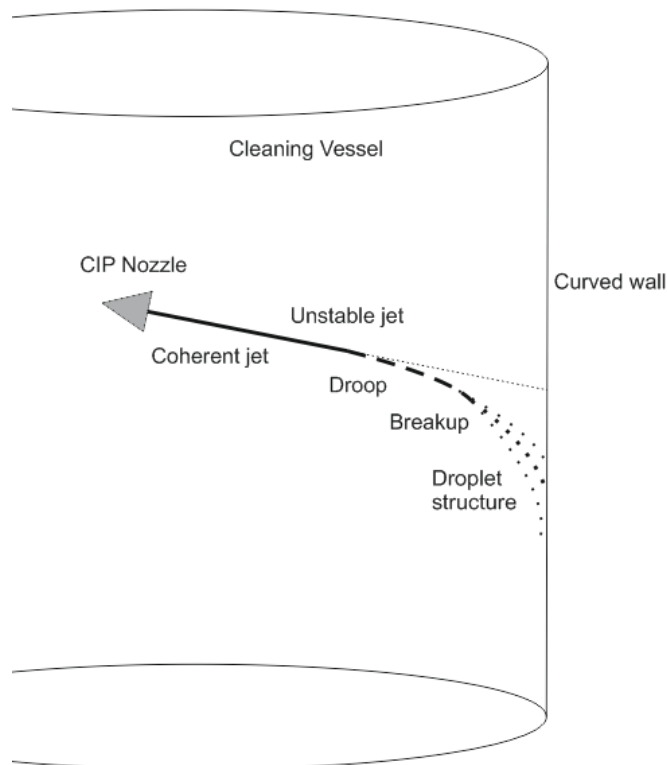


Fig. 2. 4: Schematic of jet breakup from coherent jet into droplet structure that impinges on wall (Recreated from Chee et al., 2019).

Rayleigh (1879) showed that jet breakup is due to hydrodynamic instability. He demonstrated that a coherent jet is unstable due to perturbations in the stream. Disturbances in wavelengths grow with time and distance from the nozzle exit, promoted by the interaction between the liquid and ambient gas, and when these become larger than the jet circumference the jet is unstable. Grant and Middleman (1966) observed that breakup time decreased with increasing velocity; this corresponds to an increase in the rate of growth of a disturbance with increasing velocity i.e. the jet becomes less stable as velocity is increased.

Fuchs et al. (2019) found experimentally that for $Re_{jet} = 32000$ and $Re_{jet} = 80000$, the primary jet breakup length was 0.27 m and 0.63 m respectively. Tafreshi and Pourdeyhimi (2003) suggested jet breakup is also very reliant on nozzle geometry. When jet breakup occurs the energy and momentum imparted on a surface for cleaning is subsequently reduced (Feldung Damjkaer et al., 2017). With increasing jet lengths, up to 2490 mm, those that had experienced breakup (Feldung Damjkaer et al., 2017) exhibited a smaller film jump radius on a clean surface than the model of Wilson et al. (2014) predicted for the same flow conditions. Contrary to this trend however for a different nozzle diameter, at some point the RFZ was larger at the maximum jet length than lower jet lengths. This means the effective cleaning area in this case was increased for a broken-up jet. For easier to clean soils this could be utilised for improved cleaning performance, however more difficult to clean soils require a more coherent jet. At higher flow rates more splatter was observed at the location of jet impingement, resulting in a lower flow rate of liquid and subsequent momentum flow in the RFZ. Wang et al. (2013) quantified the effects of splatter from short jets ($L = 50$ mm). They defined an effective volumetric flow rate in the falling film, accounting for splatter, given by equation 2.15.

$$Q_{eff} = Q (1 - S) \quad (2.15)$$

Where Q_{eff} ($lmin^{-1}$) is the effective volumetric flow rate in the falling film, Q ($lmin^{-1}$) is the volumetric flow rate of the impinging jet and S is the dimensionless splatter fraction. Chee et al. (2019) investigated how the splatter fraction for a jet varied for longer jet lengths up to 1 m. They found that for shorter jets, where $L < 300$ mm, S was dominated by Re_{jet} which saw an almost linear increase with increasing Re in the regime $Re > 13000$. For longer jets, where $L > 300$ mm, S became independent of Re and strongly dependent on L . For the longest jets S approached 0.4, indicating that a significant fraction of the flow delivered by the jet did not appear in the falling film. Splatter was not determined solely by jet breakup, for longer jets the value of S did not change significantly when the jet was breaking up into droplets. Chee et al. (2019) proposed that splatter is attributed to

momentum of drops formed as the jet breaks up and whether this is enough for rebound to occur. They also suggested that it is related to the stability of the film and rope surrounding the RFZ, and whether surface tension is strong enough to prevent these shedding droplets. Studying the effect on the shape of the RFZ, Chee et al. (2019) found that for a range of Q_{eff} values the height of the RFZ above impingement, Z , compared to the half-width at impingement, R , followed the relationship $Z \sim 4R/5$, demonstrating the influence of gravity on the steady state RFZ shape for long jets.

Jet impingement on a curved wall

The effect of wall curvature was also investigated by Chee et al. (2019). In reality, cleaning operations in industry will often be on curved walls as opposed to the frequently studied flat surfaces. They found that flow patterns generated by impinging jets on cylindrical target walls were similar to those observed on flat walls, namely the formation of a RFZ near the impingement point, a film jump above this and a rope like boundary that confines the falling liquid. For vertical cylinders, at low flow rates in the regime $4200 < Re < 21000$, R and Z were insensitive to curvature. As the flow rates increased, R became more sensitive to curvature and decreased as curvature increased. The results showed that splatter increased at higher curvatures, reducing Q_{eff} and subsequently R . Horizontal cylinders exhibited a very similar behaviour at low flow rates while a decrease with curvature for both R and Z was observed at higher flow rates, attributed to splatter. Horizontal cylinders exhibited a noticeably higher splashback than in the vertical cylinders. For wall curvatures of up to 20 m^{-1} , cleaning performance was seen to be remarkably similar, agreeing with the small effect observed in the flow patterns on a clean surface. This suggests that using a flat surface is a valid assumption in this regime.

Moving jets

Wilson et al. (2015) studied the effects of a moving jet on the removal of a soil layer. In the model presented in Fig. 2.5 the jet impingement is assumed to be stationary and the soil layer moves from right to left. In their experiments their jet moved from left to right and the soil layer remained static, creating the same relative velocity. The experimental results they obtained showed a good agreement with the cleaned region predicted by their model.

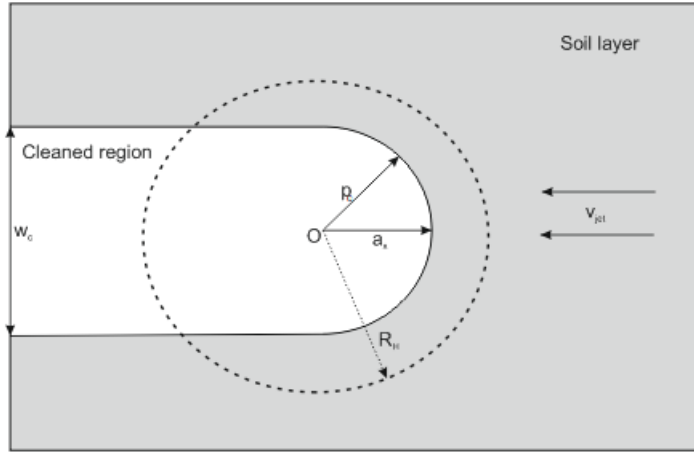


Fig. 2. 5: Schematic of Wilson et al. (2015) model of cleaning via a moving jet from left to right. w_c represents the width of the clean region, O the point of impingement, p the radial distance from impingement to the cleaning frontier, a_x the distance along the path of the jet, R_f the radial distance to the film jump and v_{jet} the velocity of the jet.

Here they assume that the velocity of the liquid in the RFZ is much greater than the velocity of the oncoming soil layer, such that the soil is effectively static in relation to the jet. The rate of removal is then determined by the radial distance from the impingement point. The leading frontier of the cleaned region is not a circular arc but curved. The cleaning frontier is assumed to lie within the radial flow zone which extends to the film jump, R_f . Point X, located at a_x , is a stationary point and the rate of cleaning, $\frac{da_x}{dt}$, is equal to the rate at which material is convected towards this point, v_{jet} . v_{jet} is given by $\frac{\alpha_{jet}}{a_x^4}$, where α_{jet} (m^5s^{-1}) is a constant that describes the discharge of fluid from and relative motion of the nozzle. The curve of the frontier can be defined by equation 2.16.

$$\frac{dp_c}{d\theta_c} = \frac{\alpha_{jet}}{v_{jet}p_c^3 \sin\theta_c} - \frac{p_c}{\tan\theta_c} \quad (2.16)$$

Where θ_c is the angle between a_x and the p_c . Integrating with respect to θ_c allows the shape of the curve to be derived. The shape of the cleaning frontier relative to impingement point, O , is obtained by calculating $x = p_c \cos\theta_c$ and $y = p_c \sin\theta_c$ and is plotted in dimensionless form (x/a_x , y/a_x) in Fig. 2.6. The cleaned width is then given by equation 2.17.

$$w_c = 2 \times 1.47a_x = 2.94\alpha_{jet}^{0.25} \quad (2.17)$$

The resulting plot of the predicted clean region is given in Fig. 2.6, also marked on the plot is the experimental data obtained by Wilson et al. (2015).

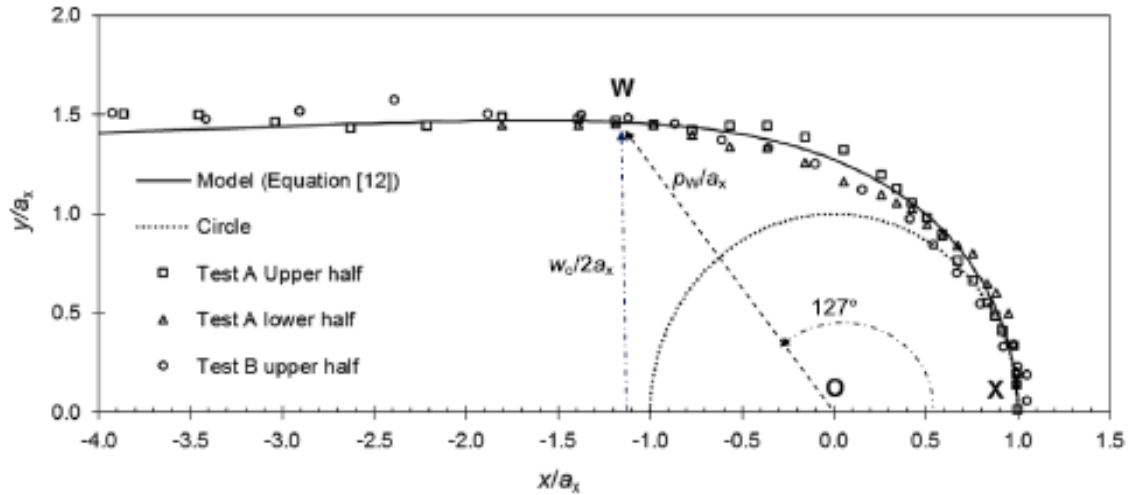


Fig. 2. 6: Predicted shape of cleaned region for moving jet. The continuous line represents the model from equation (2.5) and the square, triangular and circular points represent results from experiments. The dotted line is a circle of radius OX , p_w is the radial distance to the maximum cleaned width (Wilson et al., 2015).

A maximum in w_c occurs at point W , where $y/a_x = 1.47$, $\theta = 127^\circ$, $x/a_x = -1.11$ and $p_w/a_x = 1.84$. The narrower front at larger θ_c is not observed experimentally, since as the jet moves this region will already have been cleaned by the jet upstream and once cleaned will not be re-soiled (Wilson et al., 2015).

2.3.2.1 Sprays

Liquid sprays are an alternative form of imparting mechanical action on to a surface to be cleaned. Despite being less widely used than liquid jets in cleaning applications, it is important to understand the fluid mechanics of spray impacts with surfaces for improved understanding of the processes in which they are used.

Spray types and their applications

Liquid sprays come in three primary designs; flat fan, full cone and hollow cone. The spray angle can be altered between different kinds of nozzle. The spray distributions for each design are shown in Fig. 2.7.

i. Flat fan

Flat fan nozzles are typically used for high-pressure washing applications (~20 – 200 bar) such as car washing, since the droplets are concentrated into a narrow stream analogous to a fan. Flat fans are also widely used when precision impact on intricate parts is required due to the concentrated nature of the droplets. Other applications include cooling and applying lubricating oils (PNR, Accessed: 27/2/19)

ii. Hollow cone

Hollow cone nozzles concentrate spray droplets on the outer surface of the cone, with no droplets distributed on the inside of the spray pattern. The turbulence design of hollow cone nozzles uses a tangential injection of liquid into the nozzle chamber, generating a centrifugal force and creating a hollow cone pattern. Very wide spray angles are achievable compared to other designs and they are widely used in industrial applications (PNR, Accessed: 27/2/19).

iii. *Full cone*

Full cone nozzles distribute the droplets across the entire cone and are popular for cooling applications but are diverse and can be adapted for a wide range of uses (PNR, Accessed: 27/2/19).



Fig. 2. 7: Spray distributions: a) Flat fan, b) Hollow cone, c) Full cone (PNR, Accessed: 27/2/19).

Droplet impingement on to solid surfaces

A spray can be considered an accumulation of droplets, when a spray is directed on to a surface the interaction between the fluid and the surface can be simplified by considering a single droplet impinging on the surface. The impingement of spray droplets on to surfaces is a well-studied phenomenon in nature and technical applications, e.g. rain droplets on window glasses and paint sprays on cars. However, the prediction of wall impingement appears to be rather complex because there are so many influencing factors. The outcome of the impingement is governed by the properties of the fluid, namely viscosity, surface tension, density and droplet diameter. Furthermore, surface roughness, thickness of liquid wall film and ambient temperature are also very important (Mundo et al., 1998). In the case of low impingement momentum normal to the wall, the droplet appears to spread out on the surface and forms a liquid film. In the case of high impingement momentum, the droplet forms a conical sheet arising from the surface, assuming the shape of a crown. This crown then disintegrates through the appearance

of rim jets or circumferential ligaments into secondary droplets (Mundo et al., 1998). The study of Mundo et al. (1998) found that a large fraction of droplets near the wall were generated through atomisation after impact of the primary droplets. With increasing velocity and momentum of the primary droplets, the number of these droplets increased and their size decreased. Moreira et al. (2010) state that splash of a droplet occurs when inertial forces overcome capillary effects, a criterion which can be written as 2.18.

$$\rho v_d^2 > \frac{\sigma}{d\sqrt{Re}} \quad (2.18)$$

Where v_d is the droplet velocity, ρ its density, σ the surface tension of the liquid/gas interface, d the droplet diameter and Re the Reynolds number using the normal component of velocity to the wall on to which the droplet impinges.

Fig. 2.8 shows schematics of a single droplet impinging on a surface, showing the two observed behaviours of the droplet after impact, complete deposition and partial re-atomisation.

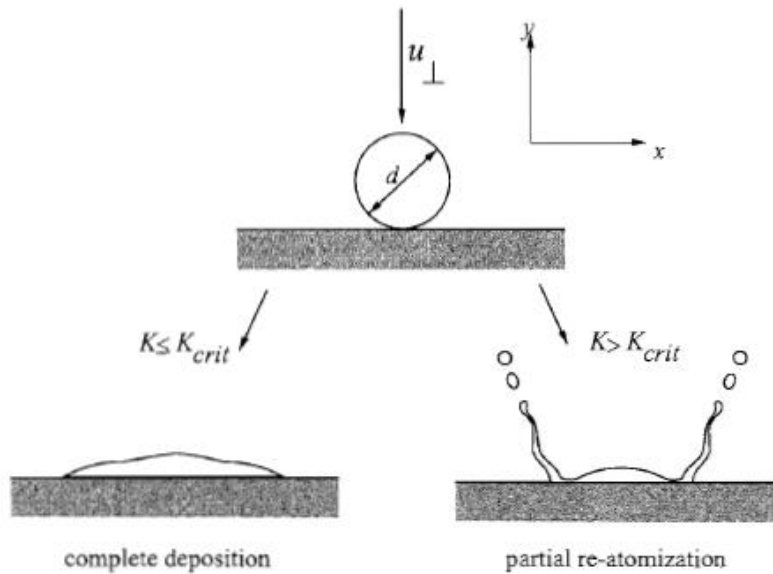


Fig. 2. 8: Schematic of droplet disintegration for a liquid spray, the first image shows the point of impact of the droplet and the subsequent two images show the behaviour of the disintegration when K is $<$ or $>$ K_{crit} (Mundo et al., 1998).

The schematic shows the approaching droplet with diameter d and velocity normal to the wall, u . Here a non-dimensional parameter, K , is introduced. K is proportional to the Reynolds number and Ohnesorge number of the impinging droplet. The Ohnesorge number is given by equation 2.19.

$$Oh = \frac{\eta}{\sqrt{\rho\sigma d}} = \frac{\sqrt{We}}{Re} = \frac{\text{viscous forces}}{\sqrt{\text{inertia} \times \text{surface tension}}} \quad (2.19)$$

Where η is the fluid viscosity, ρ is the density, d is the droplet diameter, σ is the surface tension, Re is the Reynolds number and We is the Weber number, a dimensionless number which is the ratio of kinetic energy on impact to surface energy (Mundo et al., 1998). The Weber number is given by equation 2.20.

$$We = \frac{\rho v_d^2 d}{\sigma} \quad (2.20)$$

K can then be given by equation 2.21.

$$K = Oh \cdot Re^{1.25} \quad (2.21)$$

A critical value of K , K_c , occurs where if K exceeds this the droplet exhibits complete deposition into a liquid film that forms on the surface. Above K 's critical value, the aforementioned crown shape film arises around the point of impingement. Due to its divergence the film becomes thinner at its upper rim and finally disintegrates into ligaments and droplets. Axisymmetric and concentric waves on the surface of the film enhance the disintegration process (Mundo et al., 1998). The critical value, K_c , was first defined by Stow and Hadfield (1981), given by 2.22.

$$K_c = A \cdot Oh^a \cdot We^b \quad (2.22)$$

Where A , a and b are experimentally derived dimensionless constants. Stow and Hadfield proposed these to be 1, -0.37 and 1 respectively. Mundo et al. suggested they were equal to 1, -0.4 and 1 respectively.

Whilst droplets are in most cases assumed to be spherical in shape, they are however subject to deviations from a true sphere. Many are rendered slightly ellipsoidal due to aerodynamic forces acting on the droplet and droplet oscillations may also cause deviation from a spherical shape, thus the phase of the oscillation at the moment of impact may be relevant. Oscillation of a drop is attributed to flow within the drop. An internal flow can be generated by the friction between a moving drop and fluid surrounding it, this leads to an internal circulation which results in a drag reduction. Circulation within the droplet depends very much on the cleanliness of the liquid surface, the presence of surfactants can shield the interior of the droplet which prohibits any circulation (Rein, 1993).

Rein (1993) considered the initial phase at the point of impact with the surface. Upon impact the droplet experiences an increase in pressure equal to the water hammer pressure $\rho c v_d$, where ρ and c are the density and sound speed in the liquid respectively and v_d is the impact velocity of the droplet. Even for low impact velocities the pressure

rise can be significant. The initial contact between the droplet and the wall is considered point-like, as shown in Fig. 2.9.

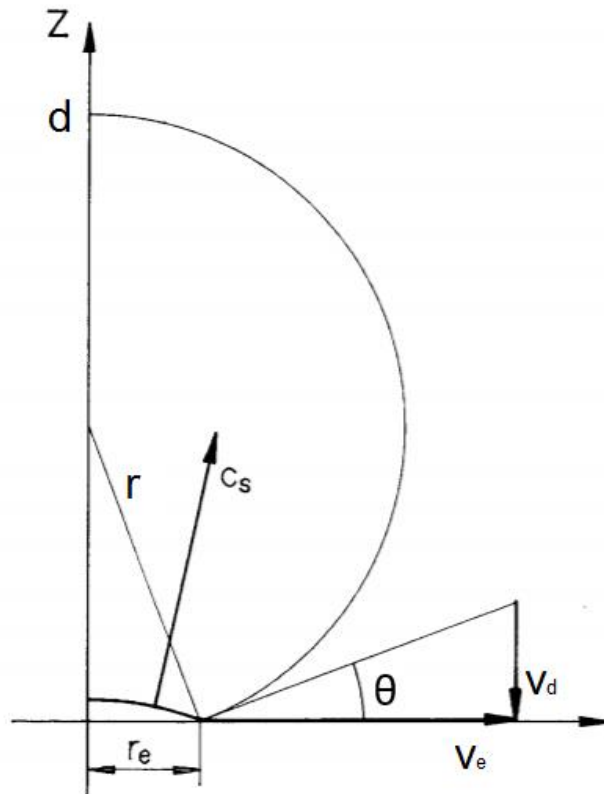


Fig. 2. 9: Point of impact between droplet and wall (Rein, 1993).

Upon impingement, a contact zone r_e develops and the contact edge moves outward with velocity v_e . Initially this velocity is supersonic with respect to both the sound speed in the liquid and the speeds of the dilatational and shear waves in the solid wall. As the drop further approaches the wall, the contact angle θ increases and the contact edge velocity increases. A shock wave is formed and propagates inside the drop with velocity c_s which is of the same order of magnitude as c . Provided that $v_d > c_s \sin \theta$, the shock remains attached to the contact edge and the liquid ahead of the drop is not disturbed by the impact. When the contact angle exceeds a critical value given by $\theta_c = \sin^{-1}(v_d/c_s)$, the shock separates from the contact edge and moves up the undisturbed surface of the drop. The compressed liquid is no longer enclosed by the shock and the wall and sideways jetting of fluid becomes possible. The propagation of the wave into the drop is shown schematically in Fig. 2.10.

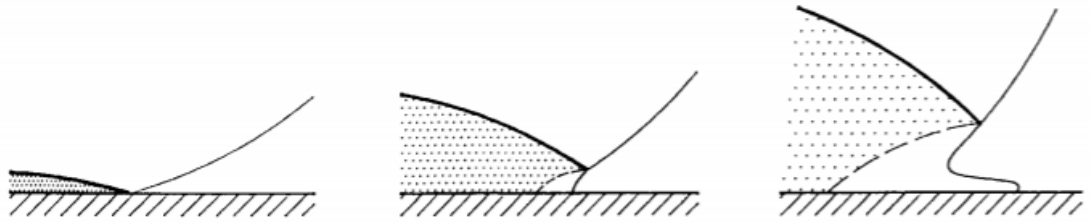


Fig. 2. 10: Propagation of a shock wave into the drop after it impacted a solid surface, formation of an expansion wave and the onset of sideways jetting (Rein, 1993).

In the limit of low-speed impacts the critical contact radius becomes very small, i.e. the radius where the shock overtakes the contact edge. In the low-speed case jetting begins at a contact radius that is larger than the critical contact radius for jetting. For high-speed impacts the jet velocity observed is much larger. Jets with velocities much greater than the impact velocity are observed, in the high-speed case jet velocity exceeds the impact speed by approximately an order of magnitude, whilst at low speeds the jet velocity is approximately twice that of the impact velocity. The jetting flow is either the initial phase of a spreading motion of the droplet on the surface, or it results in splashing. In the spreading case the outcome of the impact is a liquid lamella that shrinks and eventually assumes its equilibrium shape, whereas for splashing the drop disintegrates into many smaller droplets (Rein, 1993).

During the initial stage of impact the drop is merely deformed and compressed at its base, thus surface tension forces and viscosity of the liquid do not enter the scenario at that early stage. The surrounding gas is also of minor importance, causing a minor ellipsoidal shape of the drop. The wall is usually assumed to be rigid, which is a valid approximation provided impact velocity is not too high. The governing parameters on droplet behaviour upon impact are density, compressibility, impact velocity and radius of the drop (Rein, 1993).

Spreading occurs when the lamella expands very quickly and reaches a maximum radius within a short time. The kinetic and surface energy of the drop are dissipated by viscous processes in the thin sheet of liquid and transformed into additional surface energy. Eventually the drop assumes its equilibrium shape on the surface. In some cases the recoil of the lamella may cause the drop to separate from the surface and is a possible mechanism for drops to bounce off the surface after impact (see Fig. 2.11).

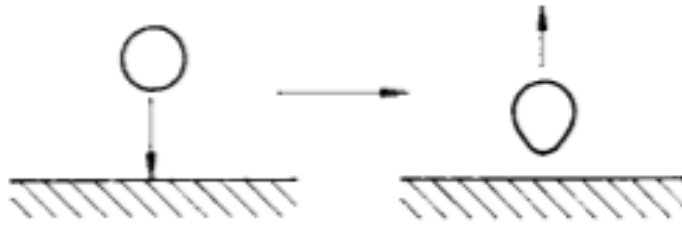


Fig. 2. 11: Droplet bouncing after impact (Rein, 1993).

Droplet impingement on to liquid layers

The impingement of droplets on to liquid layers was also considered by Rein (1993). Four regimes of droplet collision were proposed; floating, bouncing, coalescence and splashing. These are shown schematically in Fig. 2.12.

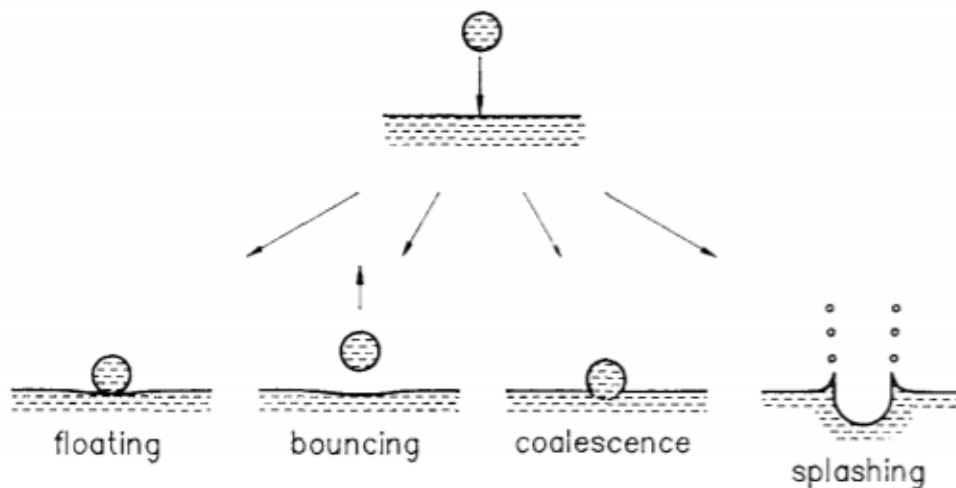


Fig. 2. 12: Collision mechanisms for droplet impingement on liquid layer (Rein, 1993).

In some cases, after impact, a droplet floats on the surface for several seconds and then disappears. In the case of coalescence the drop disappears quickly into the target liquid and the impacted surface is hardly disturbed, practically no secondary droplets are produced. In the case of splashing the liquid surface is greatly disturbed. The formation of a liquid column that rises out of the centre of the crater formed after impact, above the original surface of the target liquid is characteristic of splashing. Contrary to impingement on a solid surface, secondary droplets do not have to be formed in order to create a splash. A hemispherical cavity with a radius that can be an order of magnitude greater

than the drop radius is formed. At the circumference of the cavity a liquid sheet, termed a crown, rises above the original liquid level. The sheet of liquid may close above the cavity forming a bubble. When the cavity collapses a central jet rises out of the centre of the cavity, shown in Fig. 2.13. Secondary droplets are usually produced in splashing, these are shed from the rim of the crown and the tip of the jet.

When drops bounce off a liquid layer a contact can temporarily be formed between the liquids, the reflected drop may be smaller than the impinging one. This is also termed partial coalescence. The experiments of Ching et al. (1984) saw no bouncing of single droplets, only when the droplets impinged sequentially in a stream. It was suggested that disturbances on the liquid surface produced by preceding droplets are important for

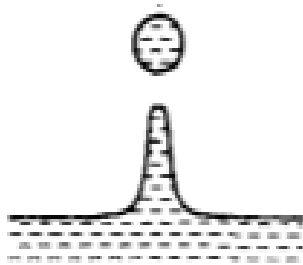


Fig. 2. 13: Jet from central cavity (Rein, 1993).

bouncing to occur and with single drops most of the energy is lost in forming a crater in the liquid layer, leaving insufficient energy for bounce. However, Rodriguez et al. (1985) observed single drops bouncing, provided the Weber number was small enough. The angle of incidence of the impinging droplet was found to have a large impact on the behaviour of the droplet. Jayaratne and Mason (1964) performed a study where this incidence

angle was varied and found that alternating zones exist where drops either bounce from the layer or coalesce. When impact velocity is increased the zones of coalescence are diminished and splashing becomes more likely. Fig. 2.14 shows a plot of Weber number vs incidence angle and the zones for different mechanisms are highlighted. Note that the transition to splashing occurs when the Weber number is further increased.

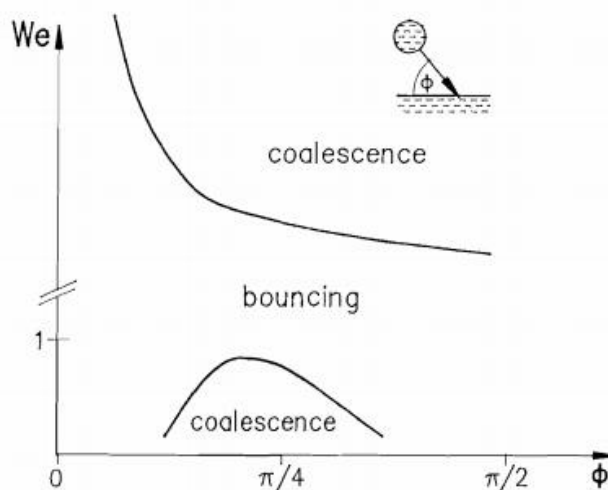


Fig. 2. 14: Droplet impingement behaviour for different angles of incidence and Weber number (Rein, 1993).

The presence of a liquid film on the surface decreases the critical value of K aforementioned by Mundo et al. (1998), since the film leads to a redirection of the outflowing fluid underneath the droplet in a direction normal to the wall. This phenomenon can be observed in Figure 2.15.

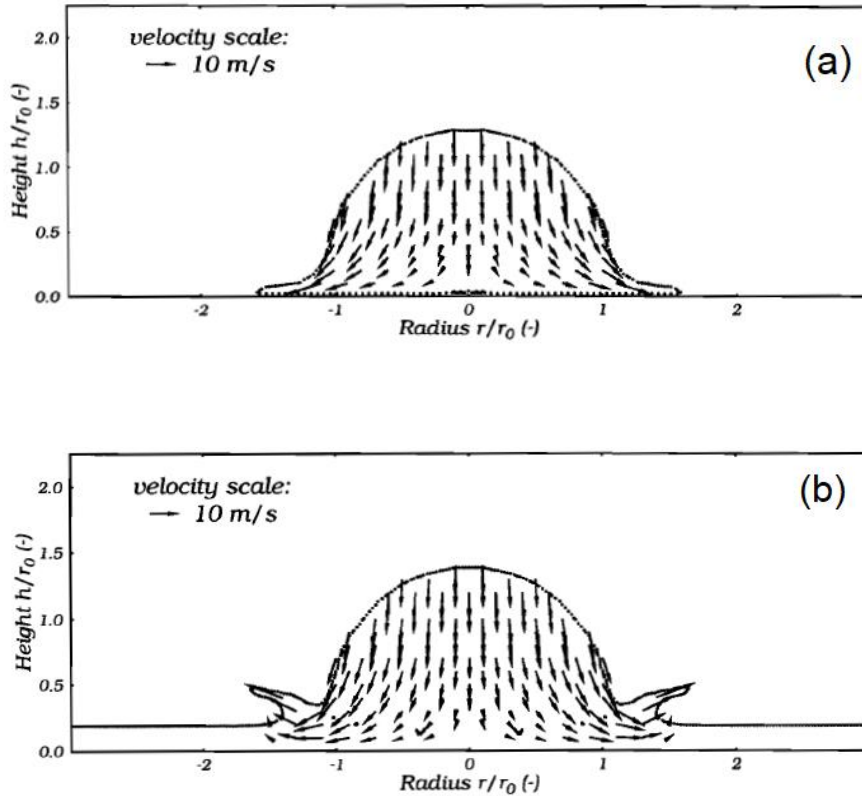


Fig. 2. 15: **a)** Droplet impingement on a dry surface, with no film layer present. The non-dimensional radius and height of the droplet are shown on the x and y-axis respectively **b)** Droplet impingement on a wetted surface with a film thickness approximately $\frac{1}{4}$ the radius of the droplet (Mundo et al., 1998).

Figure 2.15b shows that the presence of a liquid film on the surface causes the droplet to form the crown shape as the film directs the outflowing fluid normal to the wall. At the same velocity scale as Figure 2.15a on the other hand the droplet behaves as it should below the critical value of K and forms a liquid film on the surface. An increase in surface roughness also has the effect of significantly reducing the value of K (Mundo et al., 1998).

Moreira et al. (2010) suggested that, depending on wettability of the surface by the liquid film, crown splash may result in dewetting of the surface as the liquid sheet lifts. Other influencing parameters are surface topography, surface temperature, impaction angle of the droplet and the properties of the liquid film. Tropea and Morengo (1999) proposed that the depth of the liquid film influences droplet impaction, depending on the ratio of film thickness to droplet diameter $\delta_f = h_0/d$ and the non-dimensional ratio of film thickness

to roughness amplitude, R_{ND} . The length scale of roughness, L_R , is introduced. The four categories of impacts onto wetted surfaces were considered:

- Very thin film ($L_R/d < \delta_f < 3R_{ND}^{0.16}$): droplet behaviour is dependent on surface topography.
- Thin film ($3R_{ND}^{0.16} < \delta_f < 1.5$): dependence on droplet behaviour on surface topography becomes weaker.
- Thick film ($1.5 < \delta_f < 4$): droplet impact is no longer dependent on surface topography but only on the film thickness.
- Deep pool ($\delta_f > 4$): impact is dependent on neither surface topography or film thickness.

Moreira et al. (2010) observed that crown splash is less likely to occur when δ_f increases for thin films, but the opposite occurs for $\delta_f > 1.5$. Wang et al. (2002) developed a set of criteria for $K_{c,wet}$, the droplet disintegration limit for a wetted surface, adapted from that of equation 2.22 taking surface wetting into account. For varying film thickness to droplet diameter (h_0/d), δ_f , $K_{c,wet}$ is given by the set of equations 2.23.

$$K_{c,wet} = We_c = 450 \quad \text{for } \partial_f \leq 0.1$$

$$K_{c,wet} = We_c = 1043.8 + 232.6\partial_f^{-1} \quad \text{for } 0.1 < \partial_f \leq 1 \quad (2.23)$$

$$K_{c,wet} = We_c = 1043.8 + 232.6\partial_f^{-1} - 1094.4\partial_f^{-2} + 1576.4\partial_f^{-3} \quad \text{for } \partial_f > 1$$

Where We_c is the critical Weber number for prompt splash. Using 2.20 this can be rearranged to calculate the critical impact velocity required for splash on a wall wetted with a liquid film.

Wilkins (1987) showed the different stages of splashing using a high-speed camera and a water droplet dyed with ink impinging on a deep pool of water. The images from the experiment are presented in Fig. 2.16.

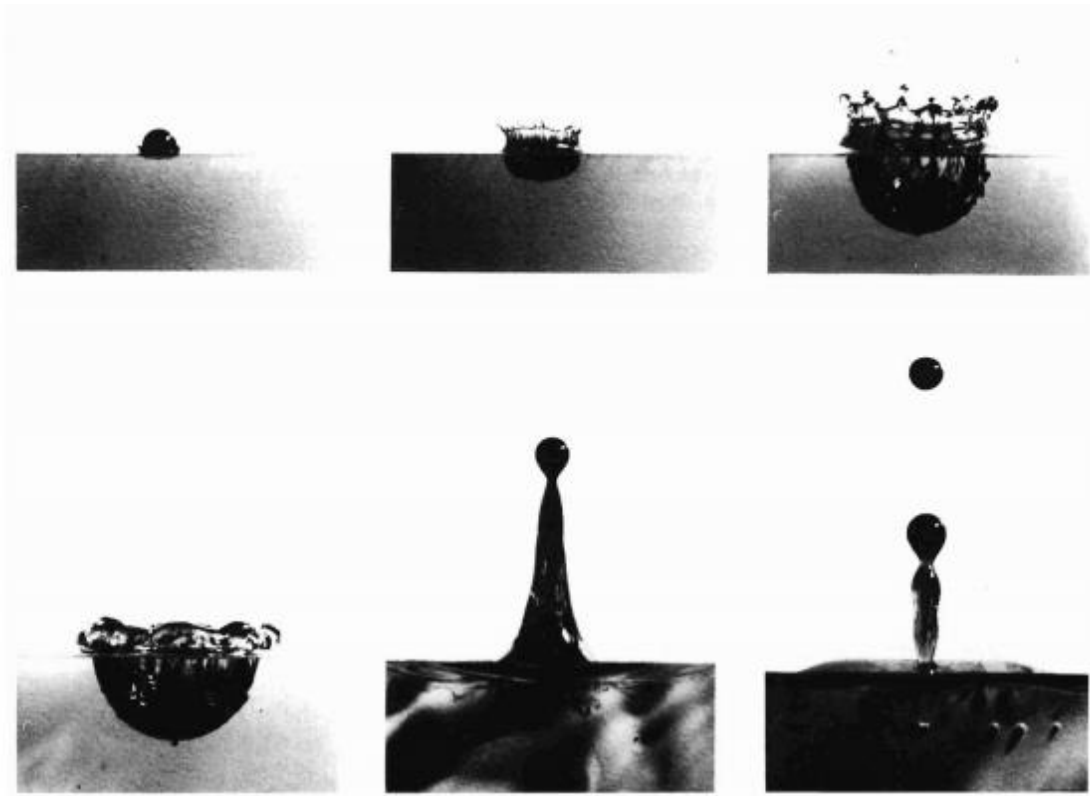


Fig. 2. 16: Water droplet (dyed with ink) impact on a water layer. Droplet diameter $d = 1.9$ mm, fall height = 0.6 m. From left to left, time $t = 0.1$ ms, 1.9 ms, 11.4 ms, 25.6 ms, 74 ms and 113.8 ms after the first contact of the droplet and the layer (Wilkens, 1987).

Splashing first occurs when the droplet coalesces with the liquid layer and a thin film of target liquid is ejected upward at the periphery of the drop. A cavity is then formed in the layer and this expands to form a crater of hemispherical shape. The droplet then deforms and lines the walls of the crater. A sheet of liquid is raised above the original surface and forms the crown shape discussed by Mundo et al. (1998). The sheet becomes unstable and smaller secondary droplets are shed from its rim. The crown is primarily composed of target liquid and some of the droplet liquid that lines the cavity. The crown and crater eventually collapse and a central jet is emitted from the layer and drops may form from the tip of the jet (Rein, 1993).

Asadi and Passandideh-Fard (2009) computationally modelled the impingement of a droplet impinging on to a liquid layer of the same properties using the volume of fluid method in an axisymmetric coordinate system. Their model assumes a perfectly spherical droplet, of diameter $d = 4.2$ mm, impact velocity $v_d = 5.1$ ms⁻¹ and the liquid layer thickness, $h_o = 2.1$ mm. The material properties were based on a water-glycerol solution of density $\rho = 1200$ kgm⁻³, viscosity $\eta = 0.02$ Pa.s and surface tension $\sigma = 0.07$

Nm^{-1} . A plot of the pressure distribution within the droplet and the layer during impact is shown in Fig. 2.17.

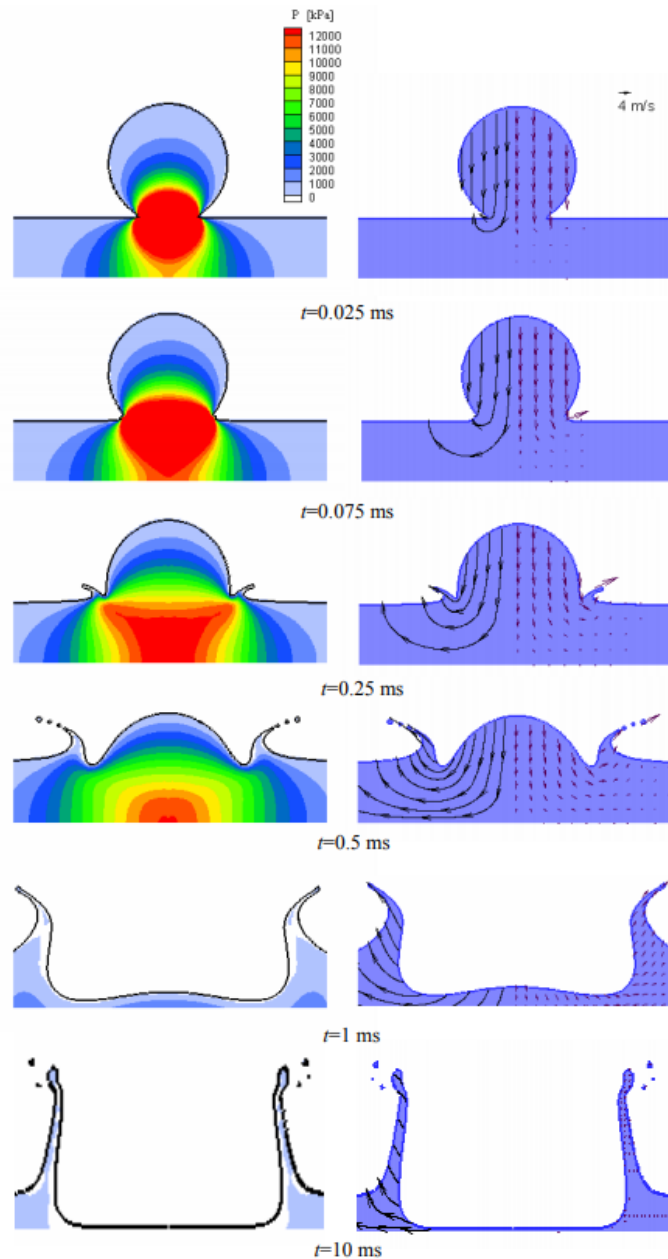


Fig. 2. 17: Computational simulation of droplet impingement on to a liquid layer of the same properties as the droplet. Pressure distribution with time (Asadi and Passandideh-Fard, 2009).

The pressure upon impact is at its peak, due to the sudden stagnation of the droplet giving rise to water hammer pressure. The contact area between the droplet and the layer increases as the droplet coalesces to the layer and the pressure is dissipated across the layer. Sideways jetting of the droplet, observed by Rein et al. (1993), occurs

at 0.075 ms after impact. A crater in the layer then develops and the crown forms, with droplets shedding from its rim. The pressure drops considerably after the formation of the crown and once the crown has subsided into the surrounding layer, the pressure decreases to the reference pressure which is assumed to be zero in the simulation (Asadi and Passandideh-Fard, 2009).

Despite single droplet impingements providing an understanding of the mechanisms involved in spray impingement, interactions occur between droplets in a spray which produce hydrodynamic structures that differ from those observed in the single droplet case. As such a spray is not simply a summation of individual droplets. It is therefore important to consider the case of multiple droplets impinging on the surface to understand the interactions between droplets (Moreira et al., 2010). Two primary cases can be considered, multiple simultaneous impingements and multiple periodic impingements. The two cases are depicted schematically in Fig. 2.18. The combination of both cases, prevalent in a spray structure, is shown in Fig. 2.19, demonstrating the complexity of modelling spray impacts on to surfaces.

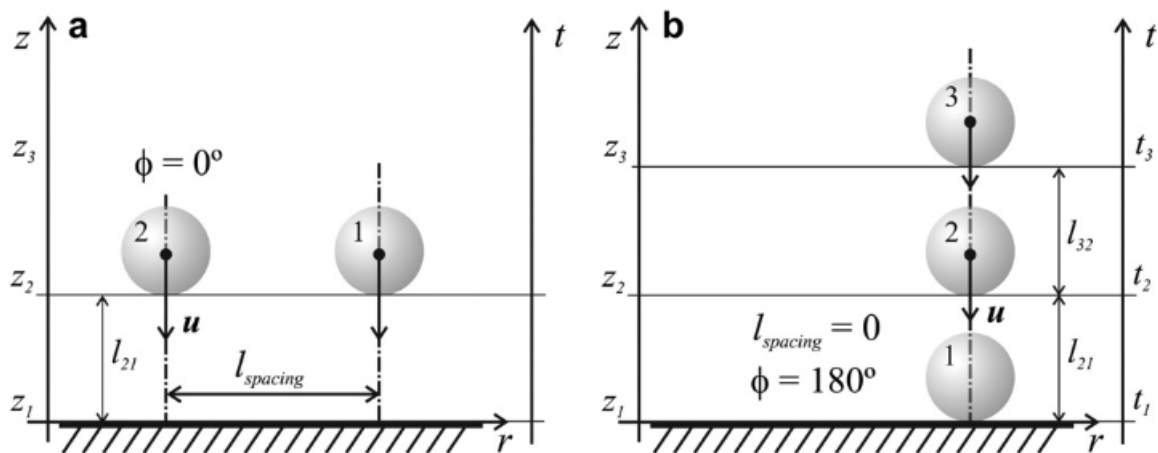


Fig. 2. 18: Multiple droplet impingement: a) simultaneous, b) periodic (Moreira et al., 2010).

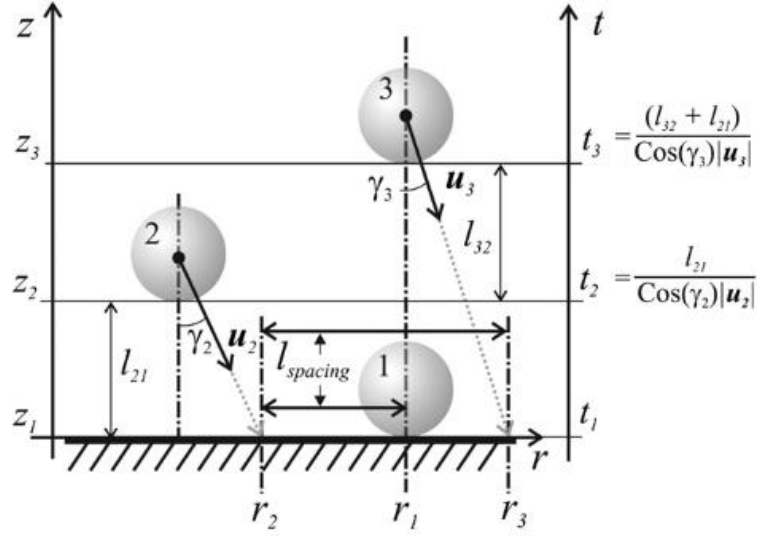


Fig. 2. 19: Multiple droplet impingement, periodic and spaced with angle of incidence for droplets (Moreira et al., 2010).

The length scale, l_{spacing} , corresponds to the horizontal space between droplets, given by $r_{i+1} - r_i$. The normalised time scale between consecutive impacts, τ_{ci} , can be expressed as 2.24.

$$\tau_{ci} = \frac{t_{i+1} - t_i}{t_{i+2} - t_i} = \frac{l_{i+1,i}}{l_{i+1,i} + l_{i+2,i+1}} \frac{u_{i+2} \cos(\gamma_{i+2})}{u_{i+1} \cos(\gamma_{i+1})} \quad (2.24)$$

Where u is the velocity of the droplet, γ is the angle of impact, i corresponds to the droplet impinging on the wall and $(i+1)$ and $(i+2)$ are the droplets that subsequently impinge. The phase difference of the consecutive droplet impingements, Φ , is expressed as $2\pi\tau_{ci}$.

Periodic droplet impingement on solid surface

Mechanisms of sprays impacting on surfaces are still not well understood due to the vast number of physical variables and complexities of sprays. To reduce the number of variables it is desirable to consider single and multiple streams of mono-dispersed droplets (Soriano et al. 2014). The experiments of Soriano et al. (2014) studied single streams and triple streams of droplets of a specifically engineered fluid known as HFE-7100, with a density of 1520 kgm^{-3} (3M, Accessed: 25/2/19) on to a thin Indium Tin Oxide layer. Droplet diameters were in the range $0.22 - 0.29 \text{ mm}$, droplet velocities in the range $1.8 - 4.4 \text{ ms}^{-1}$, impingement frequencies in the range $2730 - 13500 \text{ Hz}$ and spacing between droplets, l_{spacing} , between $0.4 - 1.5 \text{ mm}$. Fig. 2.20 compares the interaction between 0.009 lmin^{-1} , 7200 Hz droplets for a) $l_{\text{spacing}} = 0.8 \text{ mm}$ and b) $l_{\text{spacing}} = 1.5 \text{ mm}$.

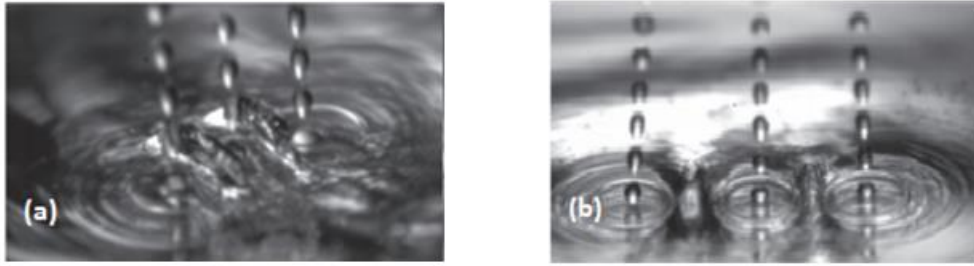


Fig. 2. 20: Effect of droplet spacing on droplet interaction **a)** $l_{\text{spacing}} = 0.8 \text{ mm}$ **b)** $l_{\text{spacing}} = 1.5 \text{ mm}$.

Splashing was observed between adjacent impinging droplet streams at an impact spacing of 0.8 mm, however smooth radial spreading of liquid film on the surface was observed at 1.5 mm spacing. At 1.5 mm spacing the craters created by the droplets have time to fully develop and this is optimal as the liquid achieves maximum contact with the substrate (Soriano et al., 2014). The craters created by the impinging droplets were studied in more detail and the hydrodynamic regions of interest were highlighted, as shown in Fig. 2.21.

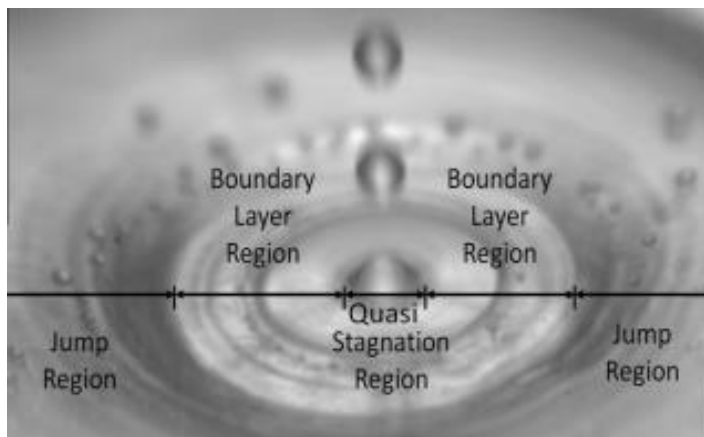


Fig. 2. 21: Hydrodynamic regions upon periodic droplet impingement (Soriano et al., 2014).

The crater is broken down into three primary regions of interest; the quasi stagnation region, the point at which the droplet impinges the surface and stagnates; the boundary layer region, where the boundary layers grow periodically upon impingement of each droplet and the jump region, in which a hydraulic jump forms in the liquid on the surface (Soriano et al., 2014). The spreading of liquid on the surface arising from periodic drops is noticeably similar to that of a coherent jet, whereby a thin liquid layer moves out radially (RFZ) to a jump in thickness in the liquid, i.e. the film/hydraulic jump. Fig. 2.22 shows a schematic of periodic droplet impingement and subsequent propagation of the crown.

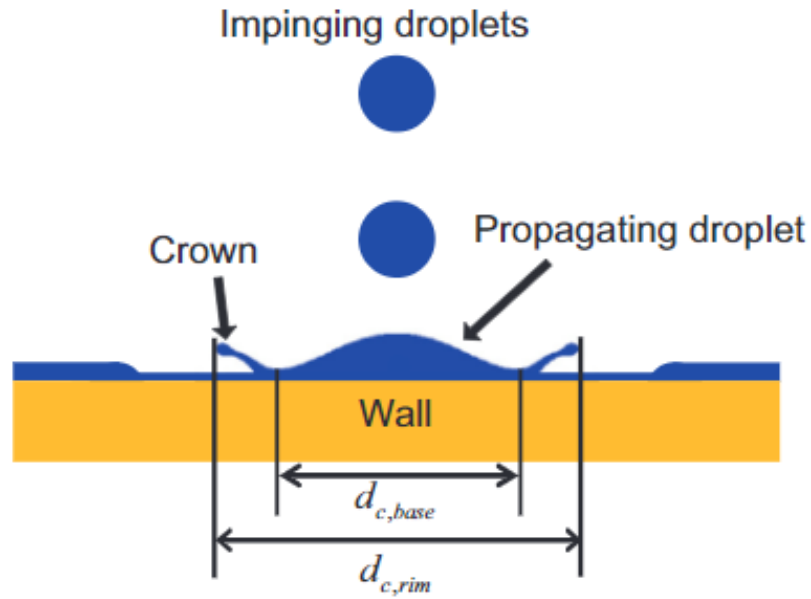


Fig. 2. 22: Periodic droplet impingement and propagation of the crown (Zhang et al., 2016).

Rieber and Frohn (1999) proposed a formula for the non-dimensional width of $d_{c,base}$, $d_{c,base}^*$, which is given by $d_{c,base}/d$, the diameter of the impinging droplets. The formula is given by 2.25.

$$d_{c,base}^* = \left[\frac{\sqrt{2}u_d^{1/2}}{6^{1/4}h_0^{1/4}\pi^{1/2}d^{1/4}f^{1/2}} \right] (t^*)^{1/2} \quad (2.25)$$

Where u_d is the impingement velocity of the droplets, h_0 is the unperturbed liquid film thickness, f is the frequency of the impinging droplets and t^* is the non-dimensional time, given by $2\pi ft$.

Zhang et al. (2016) studied the hydrodynamics, both experimentally and numerically, of a droplet train of HFE-7100 on a pre-wetted solid surface and they were particularly interested in disintegration of the droplet and crown propagation. Flow rates in their experiments were varied from $0.0028 - 0.0038 \text{ lmin}^{-1}$, frequencies $6000 - 7200 \text{ Hz}$, droplet diameters $0.24 - 0.26 \text{ mm}$, droplet spacings $0.54 - 0.62 \text{ mm}$, droplet velocities $3.23 - 4.45 \text{ ms}^{-1}$ and Weber numbers $280 - 575$. Fig. 2.23 shows a top and bottom view of the periodic droplet impingement on a translucent substrate.

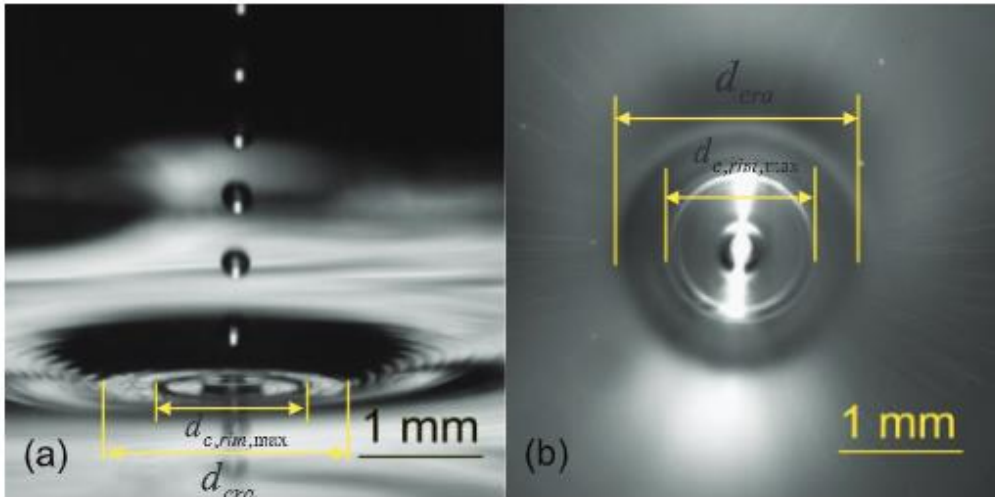


Fig. 2. 23: **a)** Top view, **b)** bottom view of periodic droplet impingement on translucent substrate, $We = 280$ (Zhang et al., 2016).

Fig. 2.23 shows how the droplet induced crown propagates radially outward until it reaches a maximum diameter, denoted in a) by $d_{c,rim,max}$, corresponding to the inner ring. After the crown reaches the maximum diameter, the liquid continues flowing radially outward however the velocity of the fluid decreases. A hydraulic jump forms, originating at d_{cra} , the crater diameter. This is because of lower fluid inertia and surface tension. Zhang et al. (2016) observed that the crater diameter and maximum crown rim diameter increased with droplet Weber number. Fig. 2.24 shows a time lapse of the periodic droplet impingement from the experiments of Zhang et al. (2016) and propagation of the crown.

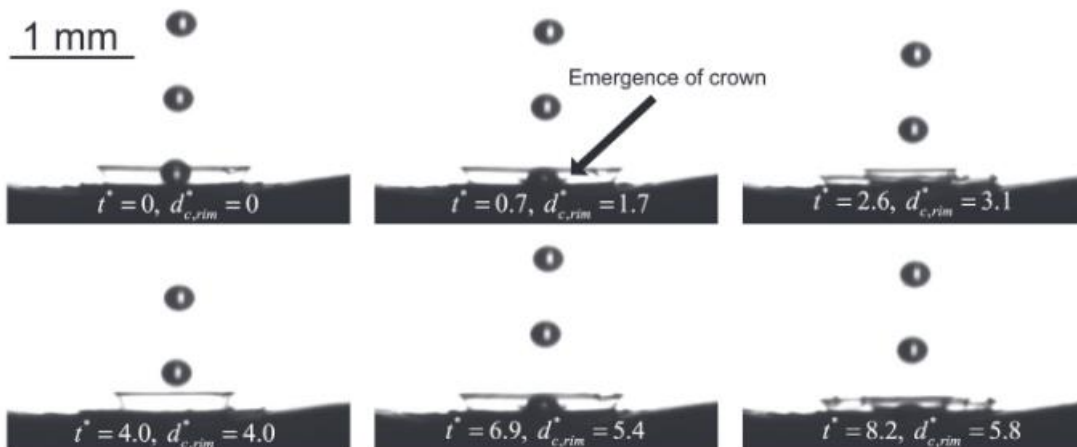


Fig. 2. 24: Experimental crown propagation images, $We = 443$ (Zhang et al., 2016).

Non-dimensional time $t^* = 0$ is defined by the moment when a droplet just touches the film. Radial propagation of the crown begins at $t^* = 0.7$ and continues to a maximum value $d_{c,rim}^* = 5.8$ at $t^* = 8.2$. Irregularity of the crown shape may occur if K_{wet} is exceeded and splashing occurs. Zhang et al. (2016) also studied the case numerically in ANSYS Fluent. The volume of fluid (VOF) method was employed, to capture the interface between the air and HFE-7100 liquid. A 2D axisymmetric laminar solver was used in the simulation, which was able to accurately capture the behaviour of the droplets for low Weber numbers. At high Weber numbers where splashing occurred in the experiments, a 3D solver was required to capture the splashing of the crown rim. Fig. 2.25 shows the agreement between the experimental and numerical data.

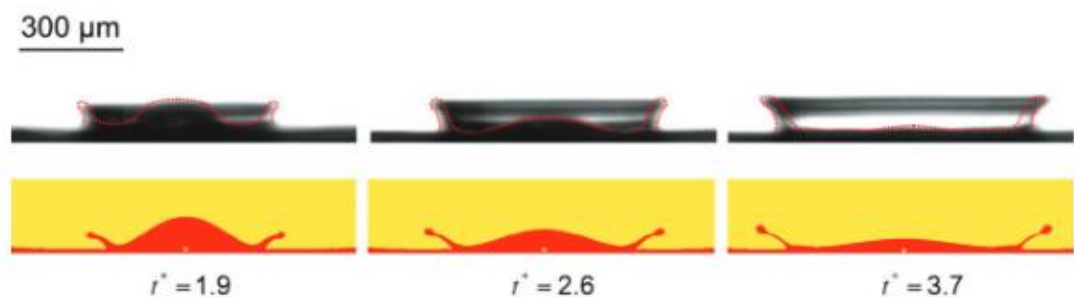


Fig. 2. 25: Experimental and numerical crown propagation images, $We = 280$ (Zhang et al., 2016).

Fig. 2.25 shows how there was a reasonable agreement between the experimental results and numerical simulations, particularly at $t^* = 1.9$. For $t^* \geq 2.6$ the disparity between the two results becomes more apparent.

Simultaneous droplet impingement on liquid layer

Liang et al. (2018) created a computational model to predict the behaviour of multiple droplets simultaneously impacting on to a liquid film. The level set and volume of fluid method was used, with water as the fluid in both the droplet and the layer, drop diameter $d = 2$ mm, the horizontal spacing, $l_{spacing}$, between droplets is in the range 2 - 4.84 mm and the non-dimensional film thickness, δ_f , is in the range 0.125 – 0.5. Fig. 2.26 shows the results of their model compared to experimentally obtained results by Cossali et al. (2004) which were under the same conditions.

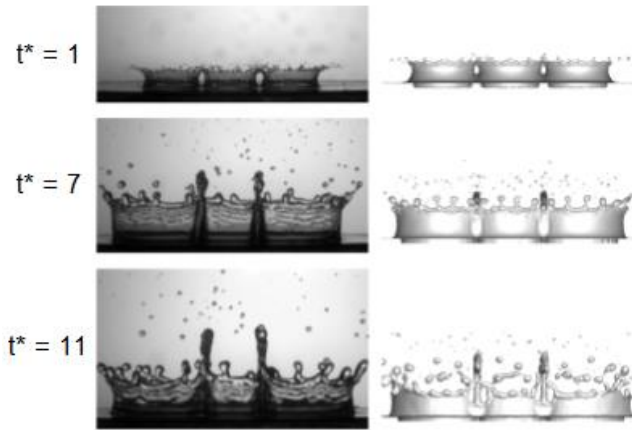


Fig. 2. 26: Left: Experimental images of Cossali et al. (2004), Right: Computational simulations of Liang et al. (2018).

For both cases $We = 520$, $l_{spacing} = 4.84\text{mm}$ and $\delta_f = 0.194$. Splashing is observed in both cases and the numerical results show a very accurate match to the experimental. The splashing was particularly well captured using a random disturbance subjected to Gaussian distribution. At non dimensional time, $t^* = 1$, three separate crowns are formed, adjacent of which begin to interact with each other. At $t^* = 7$, an upward rising liquid central sheet is produced due to the collision of adjacent crowns. Many fingering structures are generated on the rim of the crowns, which eject numerous secondary droplets. At $t^* = 11$ the evolution of the central sheet height increases continuously, which is greater than the height of the separate crowns. Fig. 2.27 shows the evolution of the interface between three simultaneously impinging droplets, for three different cases; $We = 110$, $We = 443$ and $We = 693$.

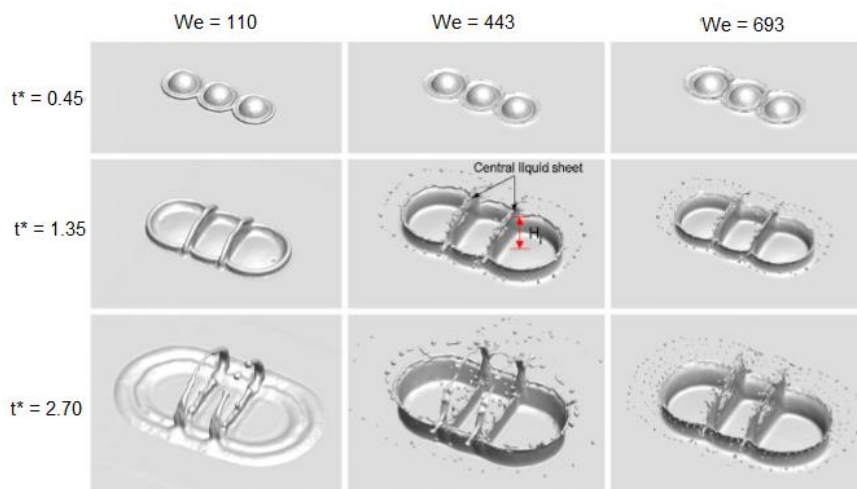


Fig. 2. 27: Interface between droplet impact evolution, For $We = 110$, $We = 443$ and $We = 693$. $\delta_f = 0.125$, $l_{spacing} = 1.5d$ (Cossali et al., 2004).

The central liquid sheet can be observed in each case. For the low impingement momentum case of $We = 110$, the no separate crowns are formed and no secondary droplets are detached from the crown rims. The central liquid sheet does however rupture into several larger droplets due to the effects of surface tension. Cossali et al. (2004) predicted a splashing threshold of $We = 200$ without consideration of other parameters. For $We = 110$, at $t^* = 2.7$, the droplets coalesce with the liquid film to form two surface waves propagating radially. For $We = 443$, the intermediate impingement momentum case, the separation of secondary droplets from the crown rim is observed at $t^* = 1.35$, caused by instability effects. The central sheet is also torn due to continuous extension with fixed liquid mass, which induces rupturing of the sheet. At $t^* = 2.7$ the sheet ruptures entirely and breaks into many secondary droplets. For $We = 693$, a relatively high impingement momentum, a number of secondary droplets can be observed after impact, of much smaller size than for $We = 443$. It can be deduced that increasing We increases the number of secondary droplets produced after impingement, but the size of the secondary droplets decreases. The evolution of droplet behaviour after impact is therefore completely different to a single droplet case. The formation and subsequent rupturing of the central liquid sheet lowers the threshold for splashing. There are at least five origins for the secondary droplets, including ejecta splashing in the droplet-film neck region at the early stage, splashing at separate crown rims, final crown breakup at the later stage, splashing at the rim of the central liquid sheet and breakup of the central sheet. The latter two are unique features of simultaneous droplet impingement, whilst the former is also observed in single droplet impacts.

Raman et al. (2015) presented a numerical study on the dynamic behaviour of two droplets impinging simultaneously on to a liquid film. The Lattice-Boltzmann method was employed to compute the simulation. A study on the effect of horizontal spacing of the droplets on the formation of the central liquid sheet was conducted and presented in Fig. 2.28.

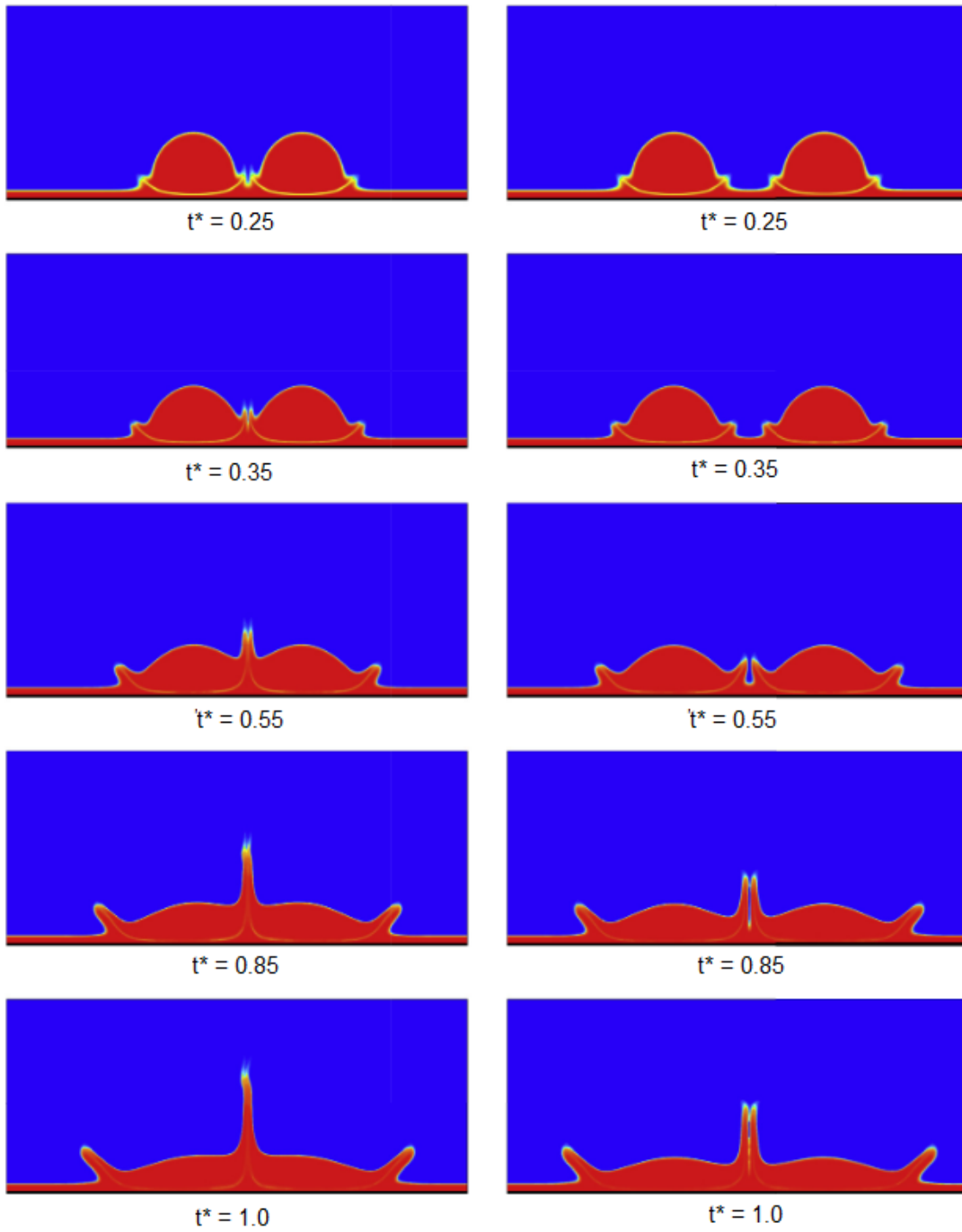


Fig. 2.28: Time lapse of droplet impact on horizontal spacing, $l_{\text{spacing}} = 1.5d$ (left) vs $2.1d$ (right), $We = 800$, $Re = 100$, $\delta_i = 0.15$ and the liquid-gas density ratio, $\rho_T = 1000$ (Raman et al., 2015).

Fig. 2.28 shows the time lapse on the evolution of the central liquid sheet formation for two spacings, with $l_{\text{spacing}} = 1.5d$ on the left and $2.1d$ on the right. After the impact occurs at $t^* = 0.25$, two small rims form on the periphery of the droplet-film contact region. These

grow radially outwards forming a crown with increasing radius and height. The two rims propagate towards each other and form the central uprising sheet. This is formed by the collision and coalescence of the two rims formed by the impinging droplets. The time taken for the central sheet to rise is prolonged with increased droplet spacing since the propagation distance for the rims to meet is further. There also appears to be entrapment of air in the sheet in the 2.1d spacing case, which Raman et al. (2016) suggest may be a result of using a 2D geometry. The height of the central sheet is larger for the shorter spacing of the droplets. Raman et al. (2016) also conducted a study of film thickness on the surface on the effect of the central sheet formed by the two impinging droplets. They observed that for small film thicknesses ($\delta_f = 0.1 - 0.2$) increasing the film thickness increased the height of the central sheet. For thicker films ($\delta_f = 0.5 - 1.5$) an opposite trend was observed, noting that an increase in film thickness caused a decrease in the height of the central sheet. They attributed this to impact energy of the droplet dissipating throughout the film at a higher rate than a thin film, thus the two central rims from the droplets having lower energy and thus rising to lower heights.

Moreira et al. (2010) observed that for simultaneous impacts, where $l_{\text{spacing}} > 0$, interaction occurs between spreading lamellas, forming asymmetric uprising sheets of fluid. In a complete wetting system, where each spreading lamella forms a crown, the interaction arises between the uprising crowns. Barnes et al. (1999) suggested that for $l_{\text{spacing}} < 2d$, there is insufficient time for crown formation before interaction occurs, whilst for $l_{\text{spacing}} < d$, droplets coalesce. The height of the sheets was said to mainly depend on drop spacing and the interaction phase Φ . They said that for $\Phi = 0^\circ$, the maximum sheet height occurred at $l_{\text{spacing}} = 2d$, and for $\Phi = 180^\circ$ at $l_{\text{spacing}} = 2.5d$.

Droplet cleaning

The impingement of droplets can be used for removal of soils from a surface, as they are in spray cleaning applications. The removal of a biofilm from a surface using an impinging droplet was studied by Cense et al. (2006). A monodisperse droplet stream was set up experimentally to impinge on to a biofilm approximately 60 – 80 μm thick. They described the removal process in two stages, penetration and growth, shown schematically in Fig. 2.29.

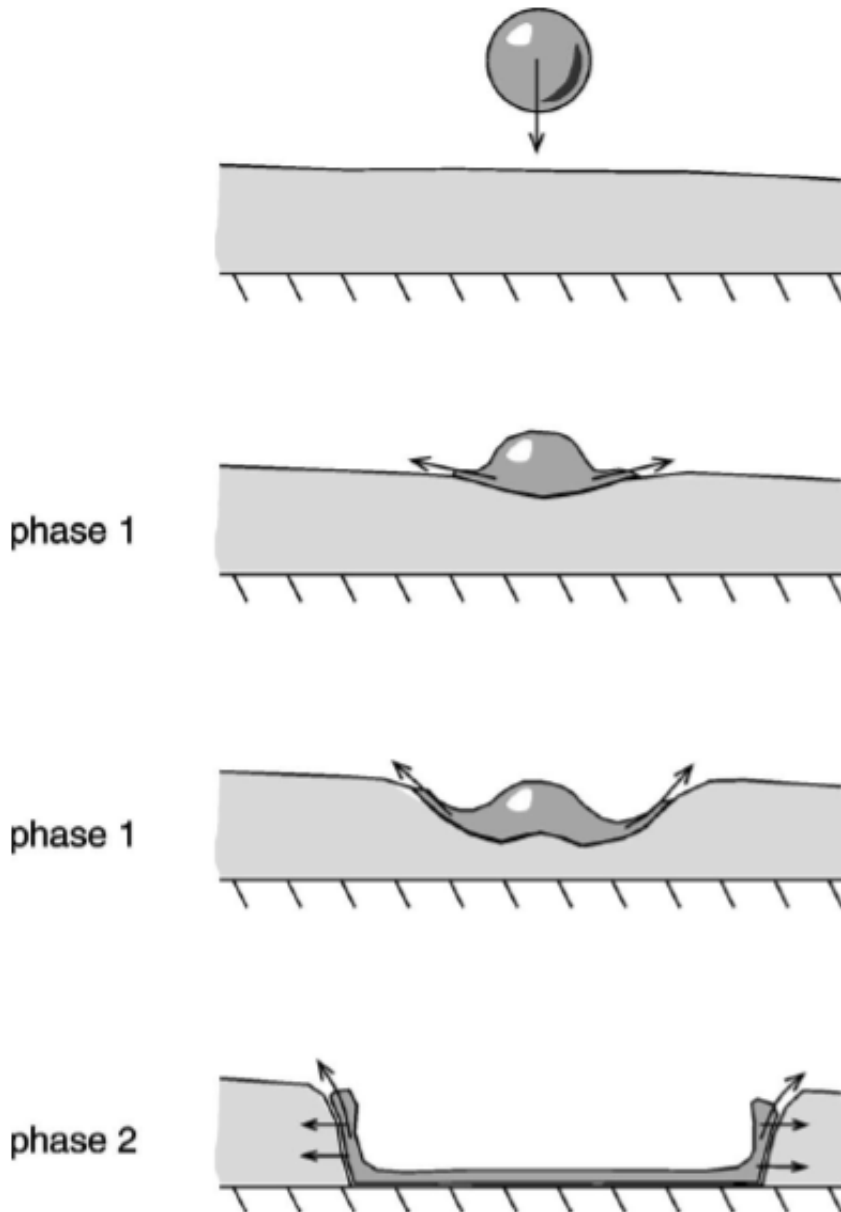


Fig. 2. 29: Schematic of biofilm removal process via impinging droplet (Cence et al. 2006).

As Fig. 2.29 shows, the droplet penetrates the layer in the first phase and the second phase is the process in which the existing hole in the biofilm grows. A critical velocity was proposed by Cence et al. (2006) which was the minimum velocity required for penetration of the film. The top layer required critical velocities of approximately 15 ms^{-1} and critical velocities were found to be inversely proportional to droplet diameter. Penetration required exposure to the droplet stream of approximately 10 s. The critical number of droplets required for penetration to occur was inversely proportional to droplet velocity for all the diameters under study (20 – 200 μm).

Cense et al. (2006) also performed numerical simulations of droplet impacts on to a dry wall. They measured the shear stress exerted on the wall for different droplet diameters and plotted this against the position on the wall. The resulting plot is shown in Fig. 2.30.

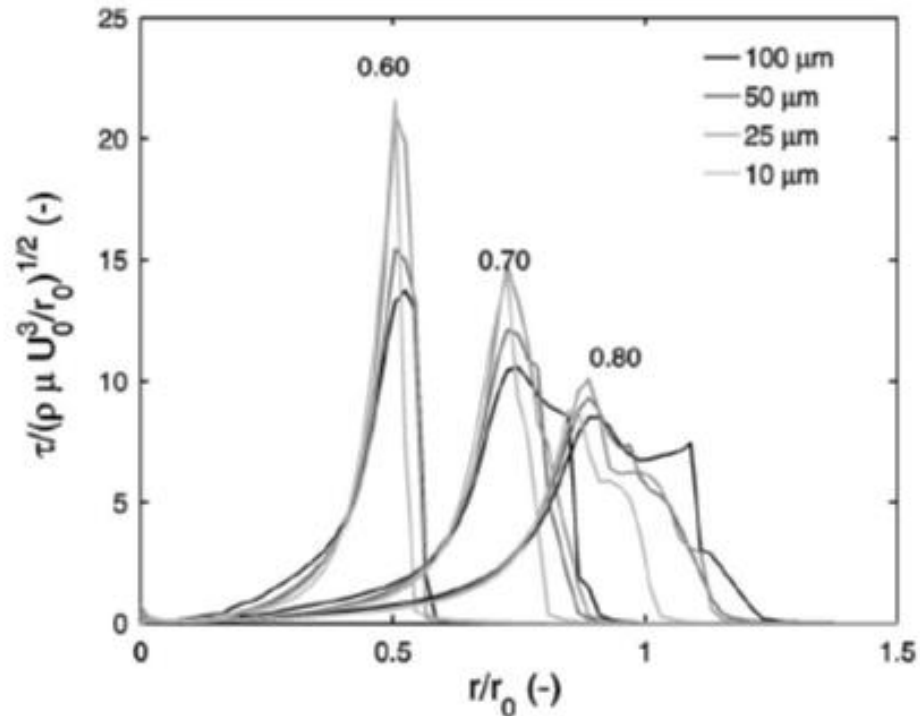


Fig. 2. 30: Non-dimensional shear stress distribution on wall at various dimensionless times. Droplet velocity 50 ms^{-1} , four curves each represent a different droplet diameter shown in legend (Cense et al. 2006).

Here the non-dimensional shear stress is given by the expression $\tau_{\text{wall}} / (\rho \eta v_d^3 / r)^{1/2}$ which is plotted against position on the wall, expressed in dimensionless form given by r_{wall} / r . Each set of curves are at various non-dimensional times, 0.6, 0.7 and 0.8, and represent different droplet diameters shown in the legend. It can be observed that after its initial impact the droplet exerts a large peak in shear stress on the wall at approximately $r_{\text{wall}} / r = 0.5$. The peak value decreases as the droplet diameter is increased. As the time in the simulation is increased the droplet exerts a shear stress further down the wall and the magnitude decreases for each diameter with increasing distance along the wall. Cense et al. (2006) also conducted numerical studies of droplet impacts on to a wall with a thin liquid film on the surface. This was studied due to the fact that in reality previous droplet impacts leave a thin layer on the surface. Fig. 2.31 shows a plot of dimensionless wall shear stress versus dimensionless time, for varying water layer thickness to droplet radius ratios.

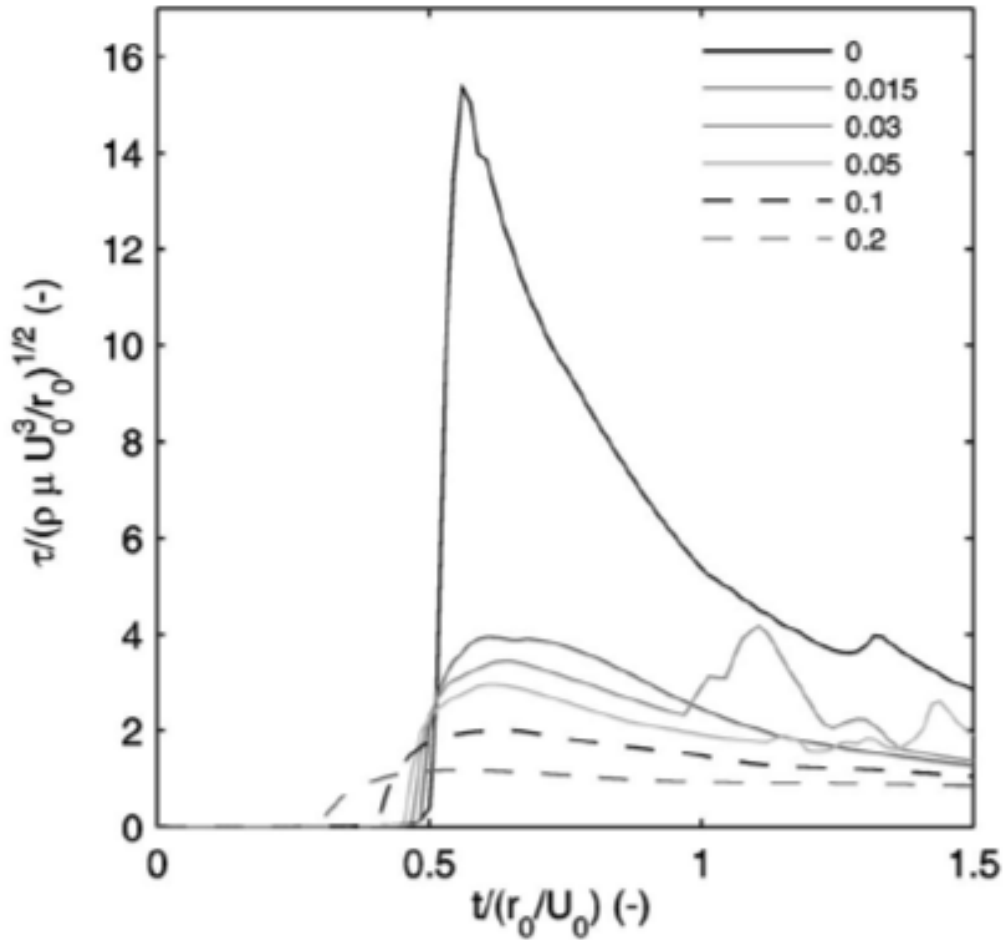


Fig. 2.31: Non-dimensional shear stress versus dimensionless time. Legend shows water layer thickness, h_0 , to droplet radius, r , ratios (Cense et al. 2006)

Fig. 2.31 shows that on a dry wall, $h_0/r = 0$, the spike in shear stress is considerably larger (~ 15) than when a liquid film is on the surface. When a liquid film is present the energy from the droplet is partially absorbed and Fig. 2.31 shows that as the film thickness is increased, the peak shear stress on the wall decreases. For the thickest film under study, $h_0/r = 0.2$, the peak dimensionless shear stress on the wall is approximately 1.

2.3.2.3 CIP technologies

Three primary technologies exist in the pharmaceutical industry for creating mechanical action on internal walls of production equipment for cleaning soiled surfaces, shown in Fig. 2.32 (Sørensen, Accessed: 7/1/19).



Fig. 2. 32: Exemplar CIP nozzles: (a) static spray ball (b) rotary spray head (c) rotary jet head (Sørensen, Accessed: 7/1/19).

i. Static spray ball

Contrary to what its name suggests, the spray ball is in fact a series of jets as opposed to the conventional atomised droplet structure one might associate with a spray. A static spray ball disperses the cleaning fluid through each perforated hole in the exemplar spray ball shown in Fig. 2.32a. For CIP, the spray ball is lowered into the tank where it remains in a fixed location. A liquid jet protrudes from each perforated hole which impinges on to a fixed location on the tank surface. As each jet impinges on the surface, they create an area where the impact force and shear stress are active. After impact the jets form a falling film of cleaning fluid, which generate shear stress on the interior walls of the tank in an uneven pattern (Sørensen, Accessed: 7/1/19).

ii. Rotary spray head

In contrast to the static spray ball, the rotary spray head is a dynamic cleaning device. The flow of the cleaning fluid released from the spray head causes the head to rotate. This creates a swirling movement, which enables the fluid to hit the tank surface with an impact force greater than that created by the static spray ball. An exemplar rotary spray head is shown in Fig. 2.32b. The pulsating force and impact created provide a combination of shear stress and variable falling film of cleaning fluid that covers all the internal surfaces of the tank. Due to the greater forces exerted on the walls the cleaning time required to achieve the desired cleanliness is reduced relative to the static spray ball (Sørensen, Accessed: 7/1/19).

iii. Rotary jet head

The rotary jet head is considered the most effective of the three automated tank CIP technologies currently employed in the pharmaceutical industry, an example of which is shown in Fig. 2.32c. This is because it creates the highest impact force and shear stress

on the wall. The jet head consists of between one and four cleaning nozzles, each of which disperses the cleaning fluid through a well-defined jet. The head rotates at a predefined velocity to provide a full 360° indexed cleaning pattern. The tank interior surfaces are fully wetted after a specified cleaning time which is dictated by the rotational velocity, the configuration of the head and the tank geometry. The impact force and coverage of the interior surface create a footprint that is much larger and wall shear stress far higher than those created by a static spray ball and rotary spray head. The cleaning in the case of the rotary jet head is dominated by the impact force of the jet. The comparison of the Sinner's circle to that of the static spray ball is shown in Fig. 2.33.

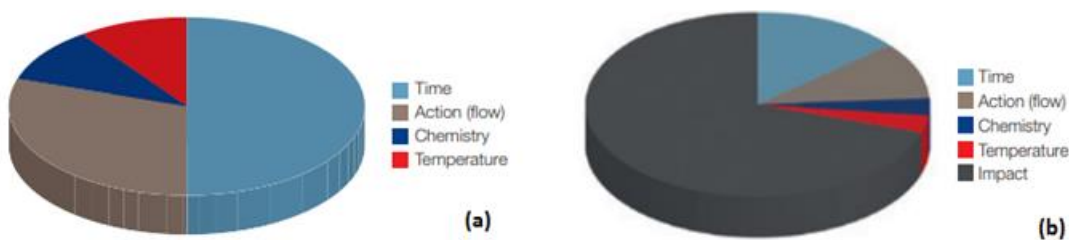


Fig. 2.33: a) Sinner's circle for tank CIP using static spray ball b) Sinner's circle for tank CIP using rotary jet head (Sørensen, Accessed: 7/1/19).

A rotary jet head has been found to reduce cleaning time by up to 70% and reduce fluid consumption by up to 90% relative to the static spray ball technology (Sørensen, Accessed: 7/1/19). The reduction in time and fluid consumption required comes at the expense of the additional energy costs incurred in rotating the jet arm. A trade-off must be conducted to optimise the CIP process.

2.3.3 Chemistry

In most industrial applications, water used for cleaning will contain a surfactant which is responsible for the chemical action in the cleaning process. A surfactant, the contraction of the term surface-acting-agent, is a substance that, when present at low concentration in a system has the property of adsorbing onto the surfaces or interfaces of the system and altering the surface or interfacial free energies of those surfaces (or interfaces). The term interface indicates a boundary between two immiscible phases, the term surface denotes an interface where one phase is a gas, usually air. Surfactants can operate independently or in aggregate form called micelles (Rosen and Kunjappu, 2012).

Different surfactant soil removal mechanisms can be classified according to the type of soil removed. Solid, inorganic (particulate) soils are removed via a wetting mechanism which lowers adhesion between the soil and substrate surface (Cox, 1986). Liquid (oily) soils are generally removed through a 'roll-up' mechanism. The mechanism of oily soil

removal by aqueous surfactants has been described as a succession of three steps (Chateau et al., 2004):

- i. Transport of the surfactants within the aqueous phase onto the substrate and soil surface.
- ii. Penetration of surfactant molecules into the soil, leading to a rolling-up for liquid soils, and to a decrease in adhesion energy for solid soils.
- iii. Transport and dispersion of the dislocated soil.

Surfactants are available in concentrated forms that are diluted and used in cleaning cycles. Surfactant concentrations directly affect the performance of the cleaning process. Selection of the cleaning agent should consider various aspects, including the soil type and ease of removal. If the concentration of surfactant is too high for a relatively easy to clean soil, this may result in excessive rinsing required to fully remove it from the vessel. Concentrations should be optimised therefore for different cleaning processes (LeBlanc et al., 2012).

2.3.4 Temperature

The optimal temperature range will vary for different steps of the cleaning process (LeBlanc et al., 2012). If proteins are present, any pre-rinse is done at ambient temperature to remove as much protein as possible without denaturation. Subsequent washes are conducted at much higher temperatures, up to 90°C in some cases to change the phase of the soil and increase its mobility, thus assisting in cleaning. Raising temperature is typically done via a sanitary steam-heated shell and tube heat exchanger (Greene, 2003).

2.3.5 Beyond Sinner's Circle

Encapsulated within Sinner's Circle is the shape and roughness of the surface, the rheology of the product to be cleaned, the choice of surfactant and the nature of the interaction of the spray or jet with the product, for example miscible or immiscible. Fryer and Asteriadou (2009) categorised cleaning problems in terms of cost and complexity of the soil by classifying them as (i) viscoelastic or viscoplastic fluids such as yoghurt that can be rinsed from a surface with water; (ii) microbial and gel-like films which require both water and a chemical agent; (iii) solid-like cohesive foulants that require mostly chemical removal. Within the pharmaceutical sector, many active pharmaceutical ingredients (API) are concentrated into dose forms that are applied dermatologically. These include steroidal creams, typically a two-phase oil-in-water emulsion, and ointments, which are single phase, often petroleum-based solutions. Cleaning was also classified by Fryer and Asteriadou (2009) in terms of the cleaning mechanisms which

can be employed for a given system. They suggested that cleaning must first overcome cohesive forces that bind the material together and secondly adhesive forces between the deposit and the surface. This can be done by fluid action alone (fluid mechanical removal) or through a combination of fluid and chemical mechanisms (diffusion-reaction removal). With the latter, cleaning involves diffusion of the chemical to and/or into the deposit and a physicochemical reaction that transforms the deposit to a removable form.

2.4 Pipe cleaning

For pipe sections where an impinging jet or spray would not achieve effective coverage of the walls, CIP is often achieved by pushing a piston like object through the pipe to clean the walls. This is known as 'pigging'. The technique is widely used in the pharmaceutical industry, as well as the hydrocarbon recovery, processing and food industries (Quarini, 2002). Conventional pigs are limited to use in relatively simple geometries, typically uniform pipes with constant diameter and they find it difficult to negotiate bends or changes in cross-sectional area. For complex geometry pipes, a variation of this method known as 'ice pigging' can be used. In this method the pig is made of a slurry of crushed ice that is flushed through the pipe network. The slurry scrapes the interior walls as it moves through the pipe and removes soil from them, flushing it out in the process. The ice pig can negotiate very complex geometries such as heat exchangers and never gets stuck in the system. With the ice pig being made of water it also has considerable environmental benefits (Quarini, 2002).

2.5 Cleaning-out-of-place (COP)

Smaller, more intricate, equipment items and portable process equipment that are difficult to clean as installed are often disassembled and transported to a designated cleaning or wash area where the cleaning procedure is performed, either manually or automated. The downside to COP processes is that the opportunity for cross contamination arises when equipment is being transferred to the designated area. COP systems typically consist of dishwasher type cabinets, where the disassembled equipment is loaded on to a wash rack, then put inside the cabinet and cleaned (LeBlanc et al., 2012). A typical wash rack employed in cleaning components is shown in Fig. 2.34. The rack is coupled to a pump which distributes flow through the hollow structure to the nozzles. The nozzles are positioned to impinge on components to remove any soil. Custom racks are used to ensure the cleaning of a component is uniform from batch to batch and thereby allowing a validated process to be established. The principle of poka-yoke (Shimbun, 1988) is often employed to minimise operator error around loading racks to ensure specific parts sits in the same location (in relation to the jet) each time it is cleaned.



Fig. 2. 34: **a)** Wash rack unloaded. Each pipe section can be seen leading to a nozzle on to which a component is loaded **(b)** Wash rack with disassembled components loaded on to jet/spray nozzles **(c)** Wash rack is loaded into washer via coupling (i), water is recirculated via sump (ii) rinse of the chamber is performed by rotating jet arm (iii) (Rodgers et al., 2019).

2.6 Cleaning process design

The design of a cleaning process begins with consideration of critical process parameters and critical quality attributes of the cleaning system. These are outlined in Table 2.1 (LeBlanc et al., 2012).

Table 2.1: Critical process parameters and quality attributes of a typical cleaning system (LeBlanc et al., 2012).

Critical Process Parameters	Critical Quality Attributes
<ul style="list-style-type: none"> • Process temperature • Process pressure • Process flow • Process time • Cleaning agent concentration • Dirty hold time • Clean hold conditions 	<ul style="list-style-type: none"> • Visual detection or limits • Cleaning agent residues • Product residues • Microbiological residue limits • Drainability/drying • Conductivity/resistivity

Cleaning processes typically involve multiple steps. Each step has a function and a set of parameters that are controlled within defined ranges to ensure the most effective removal of soil. The four common steps are outlined below.

- i. Vacuum or pre rinse – removes readily soluble and/or non-adhering residues. This helps to reduce the soil load prior to washing.
- ii. Wash with cleaning solution – removes soluble and dried residues, solubilisation of soils by degradation, heat and/or wetting with detergents.
- iii. Rinse – removes suspended or solubilised soils and, when applicable, the cleaning solution. This step may involve a series of pulse rinses, with the final rinse often consisting of a higher grade of solvent. Pre rinse, wash and rinse cycles are typically performed at a flow rate of approximately 0.9 – 1.4 lmin⁻¹ per square foot of internal surface (McLaughlin and Zisman, 2005).
- iv. Dry - removes water and other solvents. This can be achieved with air or nitrogen flow by heat. It was informed from site that drying cycles are typically performed at approximately 85 °C.

2.6 Cleaning validation

Cleaning validation plays an important role in reducing the possibility of product contamination from pharmaceutical equipment. It demonstrates that the cleaning process adequately and consistently removes product residues, process residues and environmental contaminants from the manufacturing equipment in order for it to be safely used in the manufacture of subsequent products. The importance of risk analyses in the selection of cleaning processes and their validation cannot be underestimated. This includes traditional risk analysis based on effects of product quality on patients, as well as business risk considerations such as steps taken to minimise lost product from contamination (LeBlanc et al., 2012). All equipment in the pharmaceutical industry, regardless of size, must meet government standards for cleanliness. These standards are referred to as Good Manufacturing Practice (GMP), or more recently, Current Good Manufacturing Practice (cGMP) (McLaughlin and Zisman, 2005). GMP is usually communicated through direct exchanges between personnel who represent regulatory authorities and representatives of companies. A subject matter expert is delegated to represent the inspected party, who can provide a high-level overview of all aspects of cleaning validation and competently relay this to the inspecting party (PMTTC, 2015).

Cleaning validation for a specific cleaner involves testing for acceptable residues on pharmaceutical manufacturing surfaces. This includes:

- i. Identifying residues
- ii. Selecting a residue detection method
- iii. Selecting a sampling method
- iv. Setting residue acceptance criteria
- v. Validating residue detection methods
- vi. Conducting recovery studies
- vii. Writing procedures and training operators

This procedure is used to document acceptable residues three or more times and then a monitoring program can be put in place (McLaughlin and Zisman, 2005).

2.6.1 Sampling techniques

A number of sampling methods are available and commonly used in industry. The validation protocol should clearly define sampling locations and methods, ensuring the most difficult areas to clean are sampled and the number and location of swabs/rinse volumes is sufficient to represent the equipment and contents in question (PMTTC, 2015).

- i. Visual Inspection – is an intuitive method in cases where other sampling techniques result in a maximum acceptable residue which would be visibly detectable. Its primary advantages are that it is a quick detection method and it is a direct method for process contacting surfaces to verify that no visible residues, foreign objects or extraneous matter are present. Hand-held UV light sources may be used to enhance visibility where applicable. When visual inspection is the direct method, the visual limit of detection must be established through visual detection studies (PMTTC, 2015).
- ii. Swab sampling – is generally the preferred method for sampling for cleaning validation. Subject to operator training the method is relatively consistent. The most difficult areas to clean must be sampled and the number and location of swabs taken should again be sufficient to represent the equipment. The solvent used to saturate the swab should be chosen such that it provides adequate stability and solubility for the residues of interest. The procedure involves wiping the surfaces with a swab to remove residues from the surface. Firms may train the operator to use the same amount and direction of strokes of the swab to ensure consistency. Personnel carrying out the swabbing must be qualified and re-qualified on a regular basis (PMTTC, 2015)
- iii. Rinse sampling – Sampling and testing of rinse samples for residual active ingredients is a commonly adopted method to evaluate cleanliness. This is in many cases a convenient method to use and requires control of the solvent used for rinsing, the contact time and the mixing involved. Rinse samples are typically used to sample

difficult areas to reach, swab sampling is preferred where available. It should be ensured that the rinse volume is sufficient to cover all equipment surfaces and that the rinse samples adequately represent the contents. The rinse solution is then analysed for the target residue (PMTTC, 2015). The primary disadvantage of this method is that, analogous to washing a dirty pot, the contaminant may not be soluble or may still be physically occluded in the equipment. When washing a pot one does not look at the rinse water to determine if it is clean, one looks at the pot (Lakshmana Prabu et al., 2010).

2.6.2 Analysing cleaning validation samples

There are many analytical techniques available that can be used in cleaning validation. The appropriate analytical tool for a particular job depends on the specifications or parameters to be measured. The limit should always be set prior to the analysis tool selection. Analytical tools can be categorised as specific and non-specific. A specific method detects unique compounds in the presence of potential contaminants. Non-specific methods detect any compound that produces a certain response, i.e. pH and conductivity (Lakshmana Prabu et al., 2010)

The most common analytical tools are as follows:

- i. High pressure liquid chromatography (HPLC) – specific method and is the method of choice for cleaning validation where the active ingredient is well characterised (PMTTC, 2015). HPLC instruments can be found in almost every pharmaceutical company. HPLC uses a variety of detectors, including UV, fluorescence, electrochemical, refractive index, conductivity and many others. These are for the determination of surfactants in concentrated products (Lakshmana Prabu et al., 2010).
- ii. Conductivity – non-specific method that has been applied to the analysis of inorganic molecules which result in ionic species when dissolved in water. The method is not generally used for the analysis of swab or rinse samples but can be found in parts washers where the cycle is terminated when a certain conductivity is reached. A criticism of this method is that the system “cleans until clean”, resulting in variable and non-standard cycles (PMTTC, 2015).
- iii. Capillary electrophoresis - can be used for many different types of analysis; separation, detection and determination of sodium lauryl sulphate in cationic, anionic and non-ionic surfactants (Lakshmana Prabu et al., 2010).
- iv. Total organic carbon (TOC) – a non-specific method that looks for residual carbon molecules. The source of the carbon is not determined which arguably means that

the system detects potential residue from numerous sources such as the active ingredients and detergent (PMTTC, 2015).

- v. Ion chromatography – can be used for analysis of inorganic, organic and surfactants present in the cleaners. Most cleaners contain sodium and/or potassium. The ion chromatography detection technique of suppressed conductivity is more sensitive to potassium ions than to sodium ions. Very low levels of cleaning agents can also be detected using this technique (Lakshmana Prabu et al., 2010).
- vi. Thin layer chromatography (TLC) – widely used for qualitative determination of surfactants (Lakshmana Prabu et al., 2010).
- vii. Atomic absorption spectroscopy – used for determination of inorganic contaminants (Lakshmana Prabu et al., 2010).
- viii. Bioluminescence – useful for biologicals (Lakshmana Prabu et al., 2010).
- ix. Fourier transform infrared (FT-IR) spectroscopy– in the mid-IR range is a more sensitive technique than most for detecting low concentrations of organic compounds. Mid-IR grazing-angle spectroscopy is the most sensitive optical absorption technique available for measuring low chemical concentrations on reflective surfaces such as metals. The primary advantage of FT-IR spectroscopy is that fibre-optic cables that transmit the mid-IR range have made it possible to put probes into production equipment for in situ analysis, whereas conventional spectroscopic techniques require materials to be placed inside the spectrometer's sample compartment (Mehta et al., 2002).
- x. Contact angle measurement – a variation of surface energy testing, contact angle measurement is the measure of the relationship of the surface energy of a surface and the interfacial tension of the liquid on the surface, whereby the liquid droplet will have a characteristic contact angle between the surface and the edge of the droplet when it stabilises on the surface. This can be used to determine cleanliness because the properties of various contaminated surfaces are reflected by different contact angles (McLaughlin and Zisman, 2005).
- xi. Fluorescence measurement – UV light can be directed on to a contaminated surface and the contaminant is excited to a new frequency and emitted from the surface as fluorescent radiation. The fluorescence from the surface can then be measured via a photo diode and this is directly proportional to the level of contamination on the surface when compared to a 'clean' control sample.

2.6.3 Acceptance criteria for cleanliness

Once the cleaning process has taken place, the parts are inspected and must meet cleanliness acceptance criteria with limits for cleaning validation established by the

manufacturer and a regulatory body. Said criteria include (Lakshmana Prabu et al., 2010);

- i. Visually clean; whereby after inspection the part appears clean to the naked eye. This is a minimum requirement for acceptance and is limited by the Food and Drug Administration (FDA) to use between lots of the same product, in other cases it must be used in conjunction with other criteria (FDA, 1993).
- ii. Swab tests; in which the contaminant must not typically exceed a concentration of 10 parts per million in the subsequent batch, although this may vary for specific products.
- iii. Dose criterion, where typically no more than 0.1% of minimum daily dose of any product will appear in the maximum daily dose of another. Again for certain products this limit may differ.
- iv. Health based limits; determine that no more than the acceptable daily exposure of the product being cleaned appears in the maximum daily dose of the next product being manufactured. The limit is the amount of active substance that a person can be exposed to as a contaminant in another product without experiencing any adverse health effects (PMTTC, 2015).
- v. Maximum Allowable Carry-Over (MACO), where the limits for carryover of product residues are based on the aforementioned health-based limits. The health-based values are then put into the following formula (2.26) to derive the MACO.

$$\text{MACO}_{A \rightarrow B} = \frac{\text{Health based value} \times \text{SBS}_B}{\text{max DD}_B} \quad (2.26)$$

Where $\text{MACO}_{A \rightarrow B}$ is the MACO from product A in product B, maxDD is the maximum daily dose of product B, SBS_B is the smallest batch size of product B (LeBlanc et al. 2012).

2.6.4 Cleaning validation failure

In the event that the remaining residue fails the acceptance test, the cleaning method is not considered to be validated. In this case the cleaning method should either be amended to be more effective and then have the amended method validated; or dedicated equipment should be used for at least the part of the process which cannot be successfully cleaned (PMTTC, 2015).

2.7 Conclusions from the literature

In this chapter a literature review of the cleaning process in manufacturing, particularly of pharmaceuticals, has been presented. The requirement for cleaning has been

highlighted as well as the detrimental effect to companies in the industry if cleaning does not meet cleanliness criteria set out by regulatory bodies. The validation of cleaning processes employed in the industry has been researched in detail, including sampling and testing of cleaned equipment to see if the process has satisfied acceptance criteria. Cleaning methods have been researched, including CIP and COP processes, and particular emphasis has been placed on the fluid mechanics of jet and spray impingement on surfaces.

The literature review has provided a good understanding of cleaning in the pharmaceutical industry, however there are noticeable gaps in the literature. Whilst CIP processes, such as tank cleaning, have been researched in great detail, there remains very little on COP processes. Little is understood about washing racks and how the flow conditions imparted on to surfaces compares to those experienced in CIP. Whilst cleaning using liquid jets has been explored in thorough detail, there is little on the counterpart spray. The literature review delved into single droplets impinging on solid and liquid targets and a useful understanding of the behaviour of droplets after impact was obtained. Periodic and simultaneous impingements were also explored to replicate more closely the behaviour of a spray and again this provided a useful insight into droplet interactions with the surface. However, the literature did not study droplet impingement from a cleaning perspective, and no emphasis was shown on the mechanisms of a spray, or series of droplets, removing a soil from a substrate.

2.7.1 Introduction to thesis

The research presented that follows aims to target the gaps observed in the literature in order to develop a more detailed understanding of COP processes in the pharmaceutical industry. An emphasis will be placed on wash racks typically used in COP. The flow distribution on these racks and the subsequent cleaning performance of the parts placed on them will be studied. Both cleaning via jets and sprays will be explored, experimentally and numerically, from a predominantly hydrodynamic perspective. Whilst the effects of temperature will be explored, the cleaning solution used will be surfactant free. This primarily was due to time limitations on the research and future research can address this area.

Chapter 3

Method

3.1 Introduction

This chapter will discuss the characterisation of the wash racks under study and how the design of the apparatus was matched experimentally for both the jet and spray modes of operation. The test rig design used for experiments and the material selection will be discussed and the method for processing of results detailed. Finally, the method for computational simulations in support of the spray soil removal mechanism study will be outlined.

3.2 Wash rack characterisation

Two exemplar wash racks were under study, 'Rack 1' and 'Rack 2', both of which were operational on a pharmaceutical manufacturing site. Described next is a method for describing the flow network from the pump, through the racks and to the nozzles in order to better understand: (i) the overall flow distribution; and (ii) the ranges of flow rate from jets on a suitable washing rack. This is undertaken as a way to evoke hydrodynamic studies of the individual jet-surface interaction in the correct parameter space and as a design methodology for analysing wash racks.

Fluid flow through the wash racks was modelled by application of the conservation of mass and momentum under steady-state, incompressible and isoviscous conditions. The water-surfactant mixture present in the wash racks was assumed to have the same properties of water at standard operating conditions. For the distribution studies, a pipe network approach was used to predict flow distribution, utilising the open source software EPANET (United States Environmental Protection Agency, 2016). EPANET is designed to perform extended period simulation of hydraulic and water quality behaviour within pressurised pipe networks. A network consists of pipes, nodes (pipe junctions), pumps, valves and storage tanks or reservoirs. EPANET tracks the flow of water in each pipe, the pressure at each node and the height of water in each tank (Rossman, 2000).

3.2.1 EPANET Model Components

EPANET models water distribution systems as a series of links connecting nodes. Links include pipes, pumps and control valves. Nodes are represented by junctions, tanks and reservoirs. Together they form a network and the flow through the network can be calculated to represent the water distribution system being studied (Rossman, 2000).

3.2.1.1 Junctions

Junctions are points in the network that join links together, where water either enters or leaves the network. The input data for junction nodes are the elevation of each node above a reference point and the demand of water, the rate at which water leaves the network. After the simulation is run, the output results for junctions are the hydraulic head and the pressure (Rossman, 2000).

3.2.1.2 Reservoirs

Reservoirs are nodes and they represent an external source of infinite water supply to the network. The input required to the reservoir is the hydraulic head which, under no pressure, is equal to the surface elevation of the reservoir. Since the reservoir is a boundary of the network, its head is independent of what happens inside the network, therefore no output data is produced (Rossman, 2000).

3.2.1.3 Emitters

Emitters represent nozzles or orifices that discharge water from the network to the atmosphere. The flow rate through an emitter is related to the pressure drop across it via equation 3.1.

$$Q = k\Delta P^{0.5} \quad (3.1)$$

Where Q is the flow rate through the nozzle, k is the discharge coefficient, which is primarily governed by the nozzle geometry, and ΔP is the pressure drop from the nozzle to the atmosphere. The input for emitters is solely the discharge coefficient and the outputs are the pressure drop and flow rate through it (Rossman, 2000).

3.2.1.4 Pipes

Pipes are links that deliver water between points in the network. EPANET assumes that all pipes are flooded at any one time. Flow travels from high to low hydraulic head. The input parameters for pipes are the beginning and end nodes of the pipe, the pipe diameter, pipe length and roughness (used to determine head loss). The outputs for pipes include flow rate, flow velocity and head loss (Rossman, 2000).

3.2.1.5 Pumps

Pumps are links that impart energy to a fluid thereby raising its hydraulic head (Rossman, 2000). The input parameters for a pump are the start and end nodes and its pump curve. The pump curve represents the relationship between the head and flow rate that a pump can deliver at its nominal speed setting. The user must input a set of corresponding head and flow rate values into EPANET create the pump curve, either from a manufacturer's

data sheet or obtained experimentally. The output parameters from the pump are the flow rate and head (Rossman, 2000).

3.2.2 Flow-head formulation

EPANET is based on the Bernoulli approximation, which equates the static and dynamic pressure at a particular point in the pipe to another, and flow continuity which facilitates equations to be derived relating each node in the flow network, the resulting matrix problem is solved using a variant of the Newton-Raphson method known as the gradient method (Todini and Pilati 1988). The approach employed assumes frictionless pipe sections to simplify the model specification with tests carried out to show this was a reasonable assumption for the racks under study. Todini and Pilati (1988) presented a flow-head formulation to solve the flow in the pipes of a water distribution system and the head at each node in the system. There are three types of governing equations for flow and head in a network of pipes:

1. Continuity of flow at each node
2. Head loss – flow relationship for each pipe
3. Conservation of energy for each loop and the paths, each comprising a network of pipes (Simpson and Elhay, 2008).

Consider a water distribution network of pipes and junctions/nodes in which the system has N_p pipes, N_j variable-head nodes and N_f fixed-head nodes, assuming that the network is completely connected. The vectors of unknowns in the network are:

- $\mathbf{q} = (Q_1, Q_2, \dots, Q_{N_p})^T$, where Q_j is the flow through the j^{th} pipe.
- $\mathbf{h} = (H_1, H_2, \dots, H_{N_j})^T$, where H_i is the head for the i^{th} node.

The demands and elevations at each node are known and defined as:

- $\mathbf{dm} = (DM_1, DM_2, \dots, DM_{N_i})^T$, where DM_i is the demand at the i^{th} node.
- $\mathbf{el} = (z_1, z_2, \dots, z_{N_i})^T$, where z_i is the elevation at the i^{th} node.

Continuity for each of the variable head nodes in the network yields 3.2.

$$\sum_{i=1}^{N_{pi}} Q_i + DM_i = 0 \quad \text{for } i = 1, 2, \dots, N_j \quad (3.2)$$

where N_{pi} is the number of pipes connected to node i .

The head loss equation is given by equation 3.3 for each pipe in the network connecting nodes i and k .

$$H_i - H_k = r_i Q_j |Q_j| \quad \text{for } j = 1, 2, \dots, N_p \quad (3.3)$$

where r_j is the resistance factor, given by equation 3.4.

$$r_j = \frac{8f_j L_j}{\pi^2 g D_j^5} \quad (3.4)$$

where L_j is the pipe length, g is acceleration due to gravity and D_j is the internal pipe diameter. The friction factor can then be calculated using equation 3.5 (Simpson et al., 2008).

$$f_j = \frac{1.325}{\left[\ln \left(\frac{h_{r_j}}{3.7D_j} + \frac{5.74}{Re^{0.9}} \right) \right]^2} \quad (3.5)$$

Where h_{r_j} is the roughness height, for the stainless-steel pipes used in the wash racks under study this is typically in the range of 1 μm (Lee et al., 2012) and Re is the Reynolds number for the flow in the pipe. Using the roughness height of 1 μm and the known pipe geometry and flow conditions, the friction factor could be calculated. For the smallest diameter pipe in the network, which would yield the worst-case scenario friction factor, the friction factor for this pipe was calculated using equation 3.5 to be 0.023. Given that this is still a very small value, despite being worst-case, it was deemed valid to carry forward the assumption of frictionless pipes in the EPANET models.

Todini and Pilati (1988) defined two topology matrices to describe the network. The first is the unknown head node incidence matrix $A1$, with dimensions $N_p \times N_j$, such that:

- $A1(j, i) = -1$ if the flow in pipe j enters node i ,
- $A1(j, i) = 0$ if pipe j does not connect to node i ,
- $A1(j, i) = 1$ if the flow in pipe j leaves node i .

The $A1$ matrix takes the form of 3.6.

$$\mathbf{A1} = \begin{pmatrix} -1 & 1 & \dots & \dots & 0 & 0 \\ 0 & -1 & \dots & \dots & 0 & 0 \\ \dots & \dots & \dots & \dots & \dots & \dots \\ \dots & \dots & \dots & \dots & \dots & \dots \\ 0 & 0 & \dots & \dots & -1 & 0 \\ 0 & 0 & \dots & \dots & 1 & -1 \end{pmatrix} \quad (3.6)$$

Each row in $A1$ represents a pipe and contains either 2 numbers, -1 and +1, representing the end nodes of the pipe or one number, -1 or +1, if the other end of the pipe is a fixed head node (e.g. a reservoir). Consider the first row of $A1$ (3.6), the '-1' means that pipe 1 (row 1) is connected to node 1 whilst the '+1' means that the other end of the pipe is connected to node 2. In row 2 (pipe 2), the pipe is connected to node 2 and since all other elements in the row are zero, it is connected to a fixed head node (row 1) and node

2 (row 2). All other numbers in column 2 must therefore be zero (Simpson and Elhay, 2008).

The other topology matrix is the fixed head node incidence matrix with dimensions $N_p \times N_f$ which contains -1 if the flow from a pipe enters a fixed head node and +1 if flow from a pipe leaves a reservoir. The matrix is labelled A_2 and can be written in the form of 3.7.

$$\mathbf{A}_2 = \begin{pmatrix} 1 & 0 \\ 0 & 0 \\ \dots & \dots \\ \dots & \dots \\ 0 & 1 \\ 0 & 0 \end{pmatrix} \quad (3.7)$$

Each column must have at least one entry, +1 or -1. In 3.7, the network has two fixed head nodes. The first entry in A_2 means that pipe 1, row 1, is connected to reservoir, column 1, with a flow leaving the reservoir. The entry +1 in column 2 means that pipe $N_p - 1$ is connected to reservoir 2 (Simpson and Elhay, 2008).

From equation 3.1, continuity for all pipes in the network can be written in matrix form. Shown in 3.8.

$$\mathbf{A}_1^T \mathbf{q} + \mathbf{d}\mathbf{m} = 0 = f_2(\mathbf{q}, \mathbf{h}) \quad (3.8)$$

where the LHS of 3.8 is denoted by the function $f_2(\mathbf{q}, \mathbf{h})$. The head loss equations from 3.3 can be rewritten as 3.9.

$$r_i Q_j |Q_j| - (H_i - H_k) = 0 \quad (3.9)$$

A diagonal matrix, G , of size $N_p \times N_p$ is introduced, shown in 3.10.

$$\mathbf{G} = \begin{pmatrix} r_1 |Q_1| & 1 & \dots & \dots & 0 & 0 \\ 0 & r_2 |Q_2| & \dots & \dots & 0 & 0 \\ \dots & \dots & \dots & \dots & \dots & \dots \\ \dots & \dots & \dots & \dots & \dots & \dots \\ 0 & 0 & \dots & \dots & r_{N_p-1} |Q_{N_p-1}| & 0 \\ 0 & 0 & \dots & \dots & 0 & r_{N_p} |Q_{N_p}| \end{pmatrix} \quad (3.10)$$

The non-linearity in the system occurs due to the fact G is dependent on the unknown flows in vector \mathbf{q} . 3.9 can be rewritten in matrix form, shown in equation 3.11. This considers the presence of fixed head nodes (Simpson and Elhay, 2008).

$$\mathbf{G}\mathbf{q} - \mathbf{A}_1\mathbf{h} - \mathbf{A}_2[\mathbf{e}\mathbf{l}] = 0 = f_1(\mathbf{q}, \mathbf{h}) \quad (3.11)$$

Where $[\mathbf{e}\mathbf{l}]$ is a vector of the reservoir or fixed head nodes. The two sets of matrix equations in 3.8 and 3.11 can then be rewritten in block matrix form, shown by 3.12.

$$f(\mathbf{q}, \mathbf{h}) = \begin{pmatrix} \mathbf{G} & -\mathbf{A1} \\ -\mathbf{A1}^T & 0 \end{pmatrix} \begin{pmatrix} \mathbf{q} \\ \mathbf{h} \end{pmatrix} - \begin{pmatrix} \mathbf{A2}[\mathbf{e}l] \\ \mathbf{d}m \end{pmatrix} = 0 \quad (3.12)$$

The first matrix on the LHS of 3.12 shows the partitioning of a $N_p + N_j$ square matrix into a 2x2 block matrix. The first matrix may be exploited as it is symmetric. The only non-constant values in this matrix are the diagonal elements of G. A Newton iterative solution to the set of non-linear equations in 3.12 can be formulated in terms of Taylor's series expansion and linearization as 3.13:

$$\mathbf{J} \begin{pmatrix} \frac{\partial \mathbf{q}}{\partial \mathbf{h}} \end{pmatrix} = \begin{pmatrix} -f_1 \\ -f_2 \end{pmatrix} \quad (3.13)$$

which can be rewritten as 3.14:

$$\begin{pmatrix} \frac{\partial \mathbf{q}}{\partial \mathbf{h}} \end{pmatrix} = \mathbf{J}^{-1} \begin{pmatrix} -f_1 \\ -f_2 \end{pmatrix} \quad (3.14)$$

so long as the Jacobian is invertible. The derivative of the first matrix on the LHS can be multiplied by the vector $(\mathbf{q}^T, \mathbf{h}^T)^T$ of 3.12 to form the Jacobian shown in 3.14. The diagonal nature of G is exploited with only the diagonal elements of the Gq matrix changing upon differentiation, so computation of the Jacobian becomes straightforward (Simpson and Elhay, 2008). Rewriting 3.12 as 3.15:

$$f(\mathbf{q}, \mathbf{h}) = \begin{pmatrix} \mathbf{Gq} & -\mathbf{A1h} \\ -\mathbf{A1}^T \mathbf{q} & 0 \end{pmatrix} - \begin{pmatrix} \mathbf{A2} \\ \mathbf{d}m \end{pmatrix} = 0 \quad (3.15)$$

The derivatives of the diagonal elements of Gq assume that r is constant. Friction factors depend on flow however, they are updated at the end of each iteration. The derivatives can be written as 3.16.

$$\frac{d}{dQ_j} (r_j Q_j |Q_j|^{n-1}) = r_j n |Q_j|^{n-1} \quad \text{for } Q_j \neq 0 \quad (3.16)$$

The terms in the matrix containing A2 in 3.15 are independent of q and h, therefore the Jacobian matrix for 3.15 becomes 3.17.

$$\mathbf{J} = \begin{pmatrix} n\mathbf{G} & -\mathbf{A1} \\ -\mathbf{A1}^T & 0 \end{pmatrix} \quad (3.17)$$

Todini and Pilati (1988) show an analytic expression for the inverse of J where the inverse of nG, denoted by \mathbf{D}^{-1} , is easy to compute for a diagonal matrix. It has terms $1/(nr_j |Q_j|)$ at each location along the diagonal. Assuming the head loss exponent, n, is the same for each pipe the Jacobian can be written as 3.18 (Simpson and Elhay, 2008).

$$\mathbf{J}^{-1} = \begin{pmatrix} \mathbf{D} - \mathbf{DA1}(\mathbf{A1}^T \mathbf{DA1})^{-1} \mathbf{A1}^T \mathbf{D} & -\mathbf{DA1}(\mathbf{A1}^T \mathbf{DA1})^{-1} \\ -(\mathbf{A1}^T \mathbf{DA1})^{-1} \mathbf{A1}^T \mathbf{D} & -n(\mathbf{A1}^T \mathbf{DA1})^{-1} \end{pmatrix} \quad (3.18)$$

The reformulation allows a two-stage solution process for each iteration. One for the flows and the other for the heads. Substituting 3.18, 3.8 and 3.11 into 3.13 and simplifying gives the two-step Todini and Pilati (1988) algorithm to solve, at each iteration, the heads (3.19) and discharges (3.20).

$$h^{k+1} = (\mathbf{A1nG}^{-1}\mathbf{A1}^T)^{-1}[\mathbf{A1}^T n(q^k - \mathbf{G}^{-1}\mathbf{A2}[eI]) - (\mathbf{A1}^T q^k + \mathbf{dm})] \quad (3.19)$$

$$q^{k+1} = \left(1 - \frac{1}{n}\right) q^k + \mathbf{G}^{-1} \frac{1}{n} (\mathbf{A1}h^{k+1} + \mathbf{A2}[eI]) \quad (3.20)$$

where $n = 2$ for the Todini and Pilati formulation. Equation 3.19 depends on an initial guess of the flows, it is common to use 0.305 ms^{-1} (Rossman, 2000) to compute flows in all pipes.

3.2.3 Rack modelling

Using the theory discussed, the rack was idealised and modelled in EPANET in order to compute the flow distributions through both Rack 1 and Rack 2.

3.2.3.1 Nozzle characterisation

Each nozzle on the wash rack was characterised by defining the discharge coefficient k ($\text{l min}^{-1}\text{Pa}^{-0.5}$) based on a measured flow rate Q (l min^{-1}) versus pressure drop ΔP (Pa) relationship. The model defining the discharge coefficient is described by equation 3.1, in order to determine k for a specific nozzle, a hydraulics bench circuit was set up to allow control of the volumetric flow through the nozzle. A digital manometer was used to give the pressure difference over the nozzle for a range of flow rates. Subsequently the square root of the pressure drop was plotted against the flow rates with the gradient of the linear regression corresponding to k (Rossman, 2000). Manufacturers do sometimes provide this data for nozzles in data sheets however it is not always possible to find this information for all nozzle types, additionally it is often the case that nozzles are made in-house and the discharge coefficients are not known. A comparison between manufacturer data and experiments performed in a laboratory gave a typical difference of ~5-7%, between values of k .

3.2.3.2 Pump/coupling characterisation

In order to model the flow through the coupling the characteristics of the pump are required; either from a manufacturer's data sheet or through experimentation, plotting the pressure drop across the pump against the flow rate through it. Once the pump curve is obtained it can be related to that which is delivered to the rack by varying the discharge coefficient of the coupling until the pressure downstream matched that measured in situ. Together the pump and coupling form a delivery curve for the wash rack model. The

coupling is a self-cleaning mechanism, whereby flow discharged through the coupling ensures no soil builds up on the interlocking section. An exemplar coupling mechanism is shown in Fig. 3.1.



Fig. 3. 1: Coupling mechanism: Left: Female fitting on rack, right: male fitting in washer.

Fig. 3.1 shows the coupling mechanism on an exemplar wash rack on site. The image on the left shows the female fitting on the wash rack itself, with the main feed protruding behind it. On the right of Fig. 3.1 the male fitting in the washer is depicted. Once inserted into the wash rack, the rack is locked into the washer via a spring-loaded mechanism. There is a gap for leakage to occur for self-cleaning purposes as previously described. An assessment was made to include the pump curve, allowing the self-cleaning flow through the coupling to be estimated. However, the pump data of the commercial rack and losses internal to the washer piping before the coupling was not known to be 100% accurate. The pump curve for the analysis, obtained from a manufacturer's data sheet is shown in Fig. 3.2.

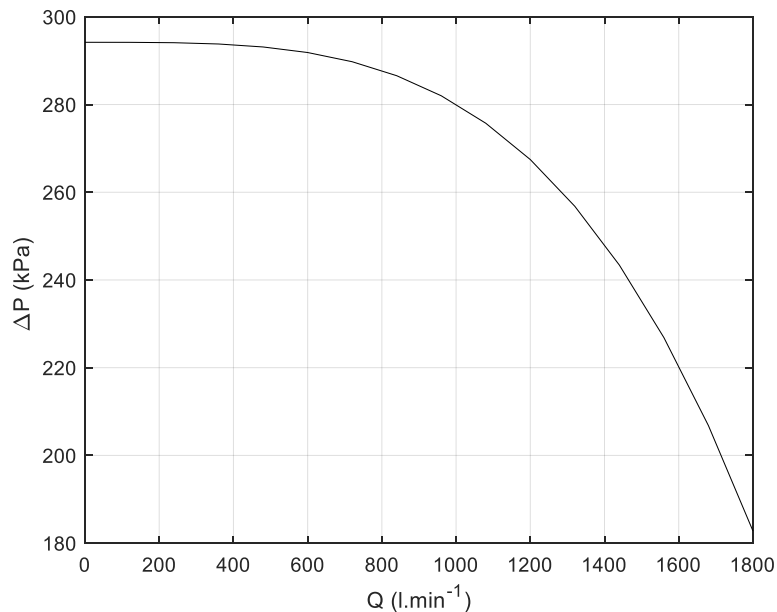


Fig. 3. 2: Assumed pump curve for Rack 1: Pressure drop ΔP vs flow rate Q .

3.2.3.3 Rack 1

Rack 1 is shown both unloaded and loaded with components disassembled from the production line in Fig. 3.3.

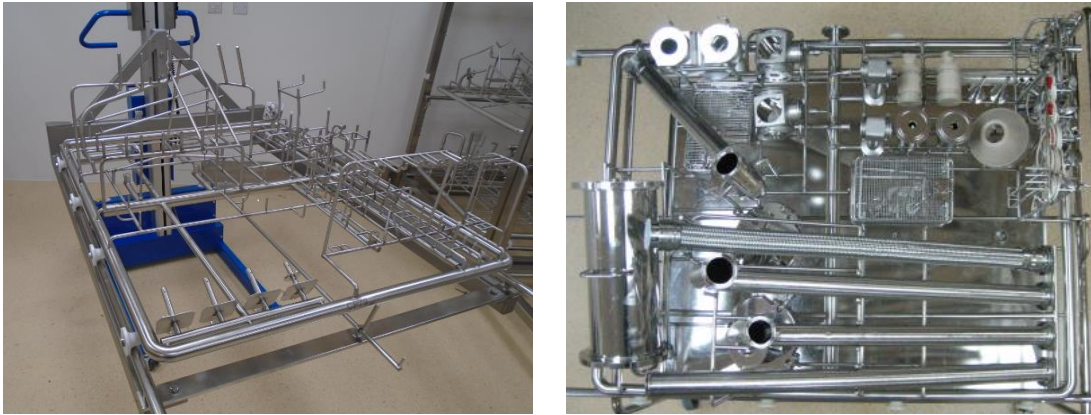


Fig. 3. 3: Left: Rack 1 unloaded. Each pipe section can be seen leading to a nozzle on to which a component is loaded. Right: Rack 1 with disassembled components loaded on to jet/spray nozzles (Rodgers et al. 2019).

Measurements of Rack 1 were taken on site to map out the flow network in EPANET. The diameter, length and connectivity of each pipe was applied to the model. Each pipe section was assumed to be frictionless, as aforementioned, to simplify the model specification, with tests carried out to show this was a reasonable assumption for this rack (de Boer, 2014). The discharge coefficients for each nozzle on the rack were obtained from a manufacturer's data sheet and applied to the model. The idealised flow network created in EPANET is shown in Fig. 3.4. For reference the size of the pipe sections were specified as follows: the main feed was 40 mm in diameter; and all sections protruding from the main feed were 22 mm in diameter. The length of the main feed, from nodes 1 – 73 was 940 mm.

Node 2 in the network represents the coupling that connects the rack to the pump, which is shown in Fig. 3.4 as the connection between the coupling and node 1 (the reservoir). The pump curve of Fig. 3.2 was applied to the model. It was known for Rack 1 that the pressure downstream of the coupling was 140 kPa, which was determined in-situ on site during quality assurance processes. Equating the pressure downstream to this in the EPANET model allowed the subsequent flow through the rack to be calculated. The subsequent flow distribution is shown in the bubble plot of Fig. 3.5.

Flow rate data for each nozzle can be found in Table A2. The flow rate range used for experiments was extracted from the data generated above and will later be discussed in 3.3.2.

3.2.3.4 Rack 2

The second exemplar wash rack under study, Rack 2, was also modelled in EPANET to compute the flow distribution through the rack. The loaded rack is shown in Fig. 3.6.

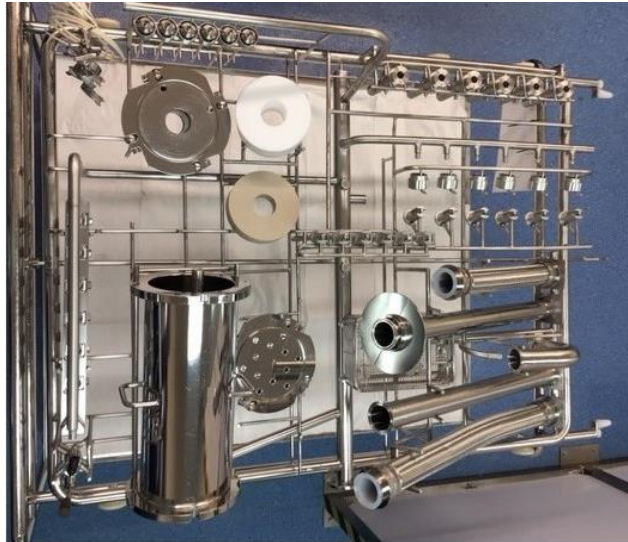


Fig. 3. 6: Rack 2 loaded with disassembled parts from the production line.

Following the same procedure as for Rack 1, measurements were taken on site to map out the position of nozzles and assign pipe dimensions and pump characteristics to the EPANET model. Several pipes on Rack 2 however were perforated such that flow exits along the length of the pipe to clean the interior walls of elongated sections such as those that can be seen in Fig. 3.6. The holes on the perforated pipe sections were measured to be 1.5mm in diameter and four were drilled around the circumference of each pipe, separated 90° apart. Three different variations of perforations were observed; 4 lots of 4, 6 lots of 4 and 7 lots of 4 holes, all equally spaced. For future reference these are denoted by 4x4, 6x4 and 7x4 respectively. A schematic of the 4x4 hole perforated pipe section is shown in Fig. 3.7.

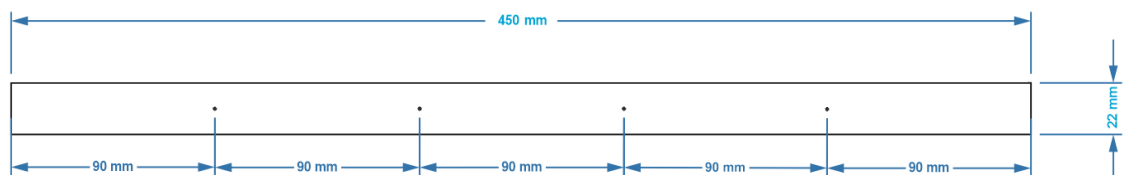


Fig. 3. 7: Schematic of 4x4 pipe.

The 4x4 pipe was a 450 mm section of 22 mm outer diameter, with a wall thickness of 1 mm. 4 lots of holes were drilled around the circumference of the pipe 90° apart, meaning the view of Fig. 3.7 is the same for each side of the pipe. The circumferential holes were spaced 90 mm apart along the centre line of the length of the pipe.

Since the perforation represented a source of external flow from the pipe network this needed to be added to EPANET to ensure accuracy of the flow distribution. Steel pipe was ordered and cut to replicate the perforated pipes on the rack in the laboratory. The pipes were then sealed at the downstream end and connected to a hydraulics bench, where the flow rate through them was increased and the pressure drop between the pipe interior and the atmosphere was measured via a manometer probe positioned through the sealed end. By plotting the flow rate against the square root of the pressure drop, the discharge coefficient of the perforated pipe sections could then be calculated by taking the gradient of each line. The coefficients were then applied to the EPANET model by assigning the coefficient to a single point on the centre of the respective pipe section through which all the flow is assumed to be discharged. Fig. 3.8 shows the discharge coefficient curves for each type of perforated pipe.

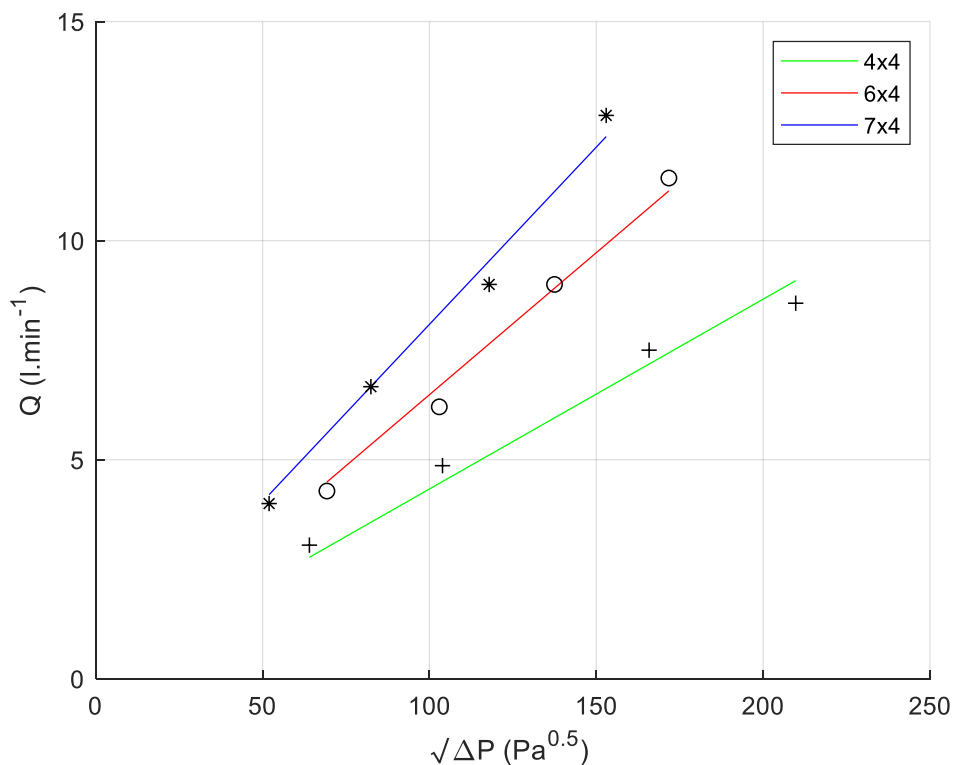


Fig. 3. 8: Flow rate Q vs square root of pressure drop $\sqrt{\Delta P}$ from pipe interior to atmosphere. The gradients of each curve represent the discharge coefficient of the perforated pipe sections.

The discharge coefficients for the 4x4, 6x4 and 7x4 perforated pipes were calculated to be $0.043 \text{ lmin}^{-1}\text{Pa}^{-0.5}$, $0.065 \text{ lmin}^{-1}\text{Pa}^{-0.5}$ and $0.081 \text{ lmin}^{-1}\text{Pa}^{-0.5}$ respectively. As well as the discharge coefficients for the perforated pipes being an unknown, certain spray balls on Rack 2 were made in house and as such there was no discharge data accessible, nor were they available for experimentation. To mitigate for this an approximation of the



Fig. 3. 9: Exemplar spray ball used to model those on the rack (Delta Stainless Steel Ltd, Accessed: 5/3/19).

discharge coefficient for the spray balls was made to apply to the EPANET model. Firstly, measurements of each holes on the spray ball were taken and the number of holes counted. An exemplar spray ball was then considered with the same diameter of holes as the spray balls on the rack, whose flow rate and pressure data were accessed online (Delta Stainless

Steel Ltd, Accessed: 5/3/19). The exemplar spray ball from which the data was taken is shown in Fig. 3.9.

The discharge coefficient curve for the exemplar spray ball is shown in Fig. 3.10.

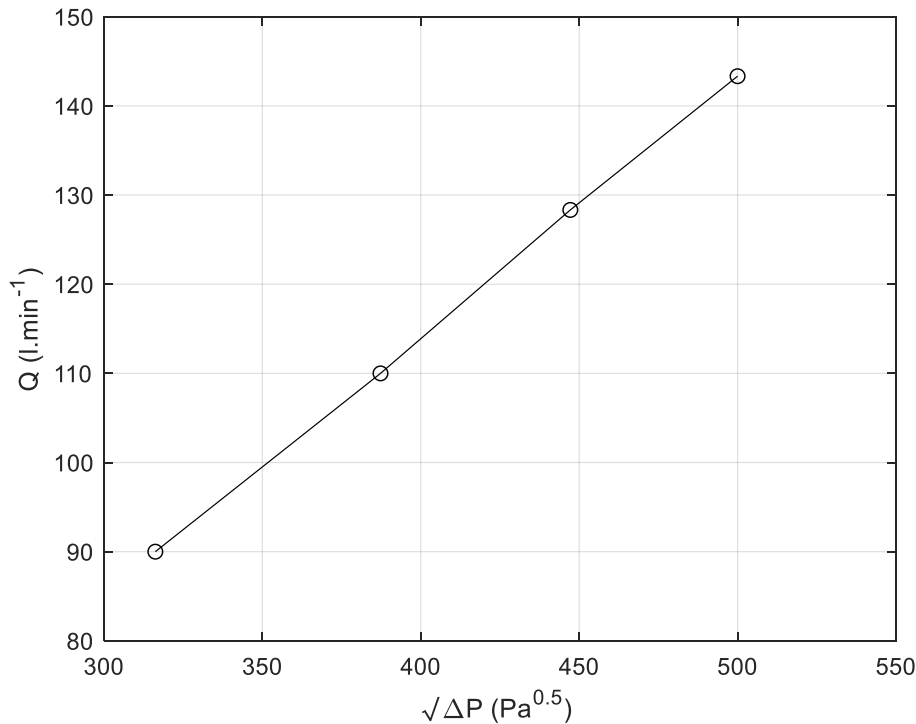


Fig. 3. 10: Flow rate Q vs square root of pressure drop $\sqrt{\Delta P}$ from spray ball interior to atmosphere. The gradient of the line represents the discharge coefficient for the spray ball. Data accessed from Delta Stainless Steel Ltd (Accessed 5/3/19).

By taking the gradient of the line, the discharge coefficient was calculated to be $0.286 \text{ lmin}^{-1}\text{Pa}^{-0.5}$. The spray ball in question consisted of 81 holes whereas the number of holes counted on the spray balls on Rack 2 was 60. To scale the exemplar spray ball discharge coefficient to that on Rack 2, the discharge coefficient was divided by the number of holes to give the discharge coefficient for each hole and then multiplied by 60 to give the coefficient for a 60-hole spray ball. This resulted in a discharge coefficient of $0.212 \text{ lmin}^{-1}\text{Pa}^{-0.5}$.

Several of the nozzles on Rack 2 were open pipe sections that created jets. Since these were also made in house and no data was available, experiments were run by de Boer (2014) to measure the discharge coefficient for open pipes as a function of the pipe diameter. The resulting plot is shown in Fig. 3.11.

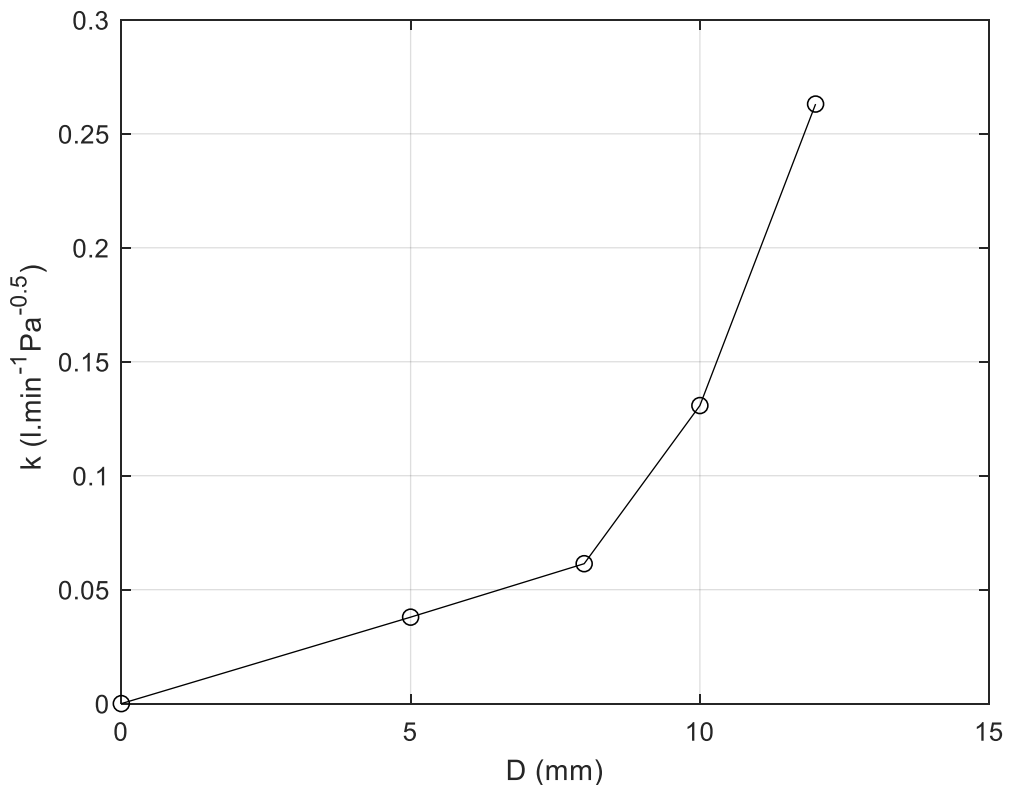


Fig. 3. 11: Nozzle discharge coefficient k for open pipe vs pipe diameter D (de Boer, 2014).

The open pipe sections were measured to have an internal diameter of 1.5mm. By interpolating from the data of de Boer (2014) the discharge coefficient for these nozzles was approximated to be $0.01 \text{ lmin}^{-1}\text{Pa}^{-0.5}$. This value was then assigned to the EPANET model for all relevant nozzles. Now that all the required data for the rack had been obtained, the rack was recreated on EPANET in the same manner as for Rack 1 and

using the same pump curve (Fig. 3.2). The flow network on EPANET is shown in Fig. 3.12. For reference, the length and diameter of the main feed was again 940 mm and 40 mm respectively, the first two branches protruding from the main feed were 22 mm in diameter and the subsequent branches downstream of the main feed were 18 mm in diameter.

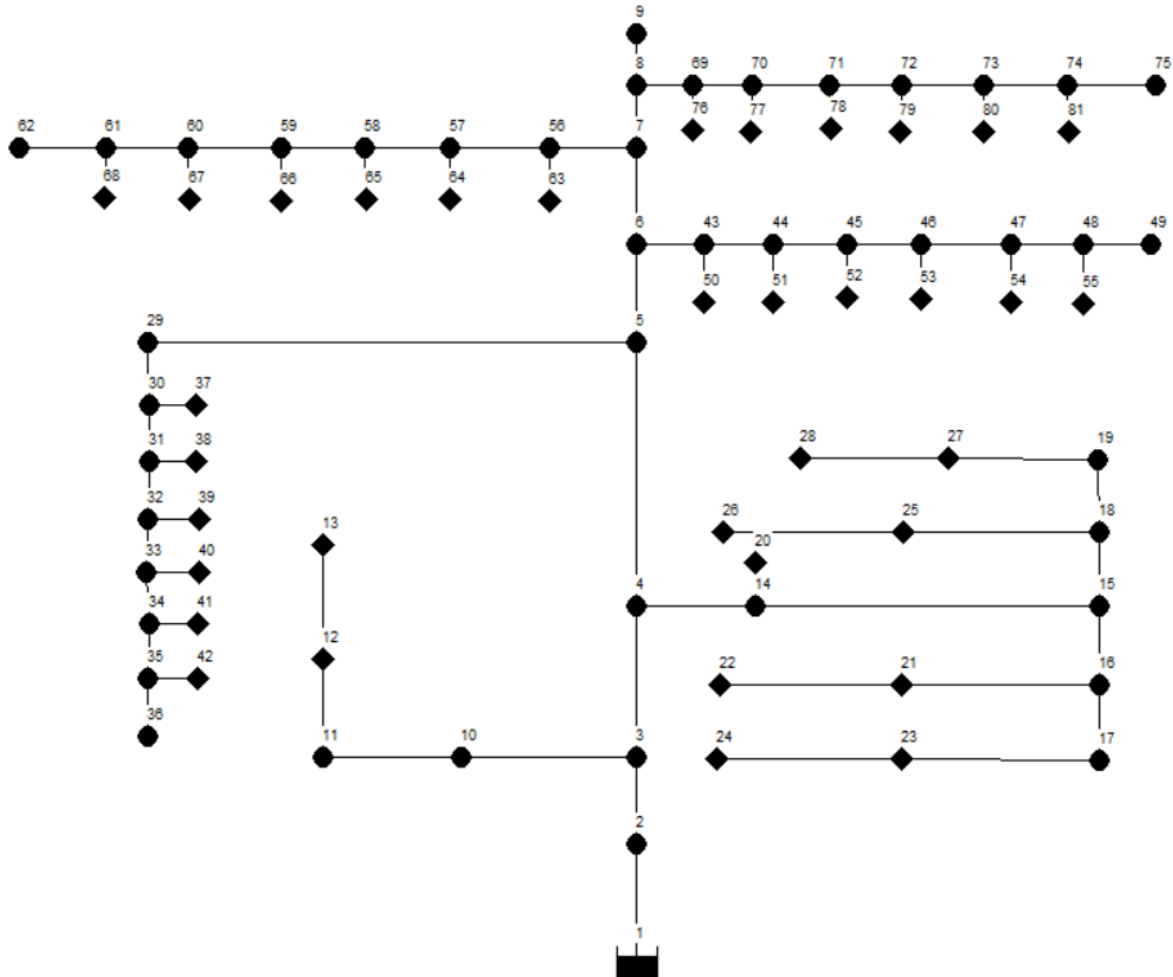


Fig. 3. 12: EPANET model of Rack 2: Lines represent pipe sections, circular nodes junctions, diamond nodes emitters, node 1 is a reservoir and the pump is that which connects nodes 1 and 2. Nozzle discharge coefficient data is available in Table A3 in Appendix A.

The subsequent bubble plot generated by EPANET is shown in Fig. 3.13.

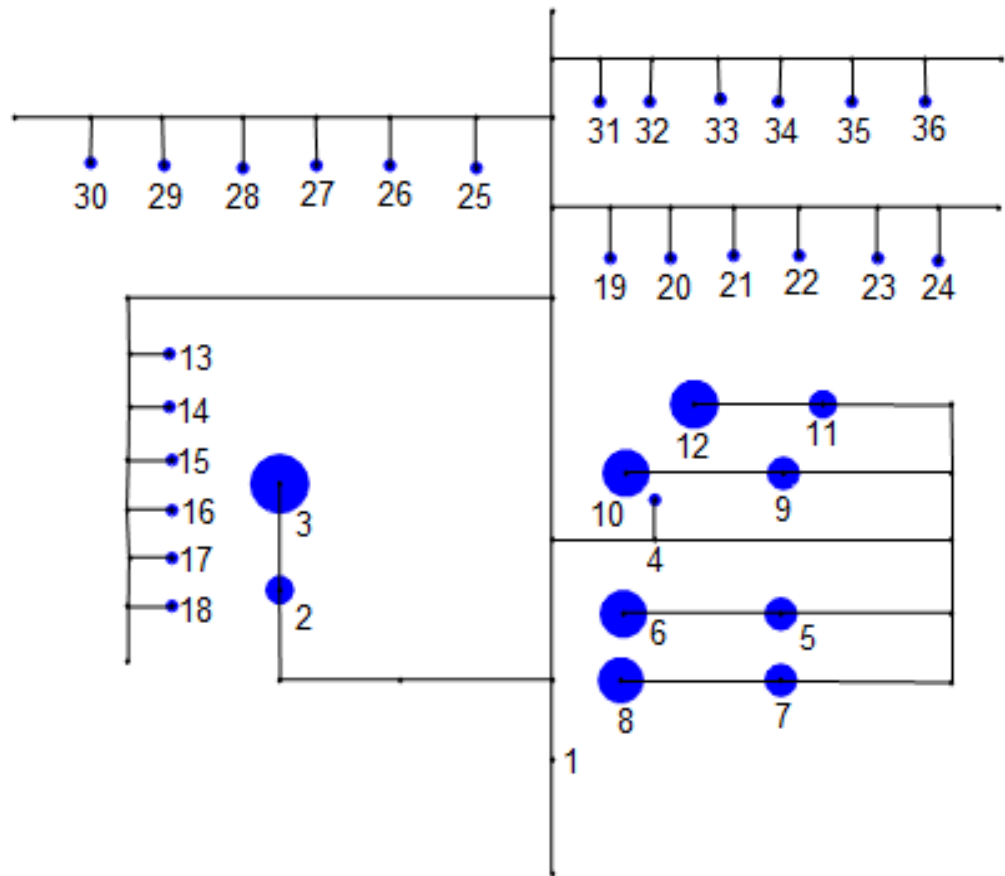


Fig. 3. 13: Bubble plot showing the distribution of flow rates in Rack 2 with each nozzle ID labelled. Flow rates proportional to nodal areas (blue), coupling left unfilled. Flow rate data and percentage distribution through nozzles can be found in Table A4 in Appendix A.

Flow rate data can be found in Table A4 of Appendix A. The flow rate extracted from this for the vertical jet experiments will later be discussed in 3.4.2.

3.3 Horizontal jet apparatus

3.3.1 Test rig design

To investigate the cleaning characteristics of the jets on Rack 1, a coherent horizontal jet was visualised on a test apparatus. This was designed and built where a stationary coherent jet was positioned to impact perpendicular to a transparent wall made from Perspex. The nozzle was made in house, using a brass barb fitting with a $\frac{1}{4}$ " BSP thread and a 4 mm hole drilled through the centre. Fig. 3.14a shows the jet nozzle and Fig. 3.14b shows the footprint of the jet on the Perspex wall.

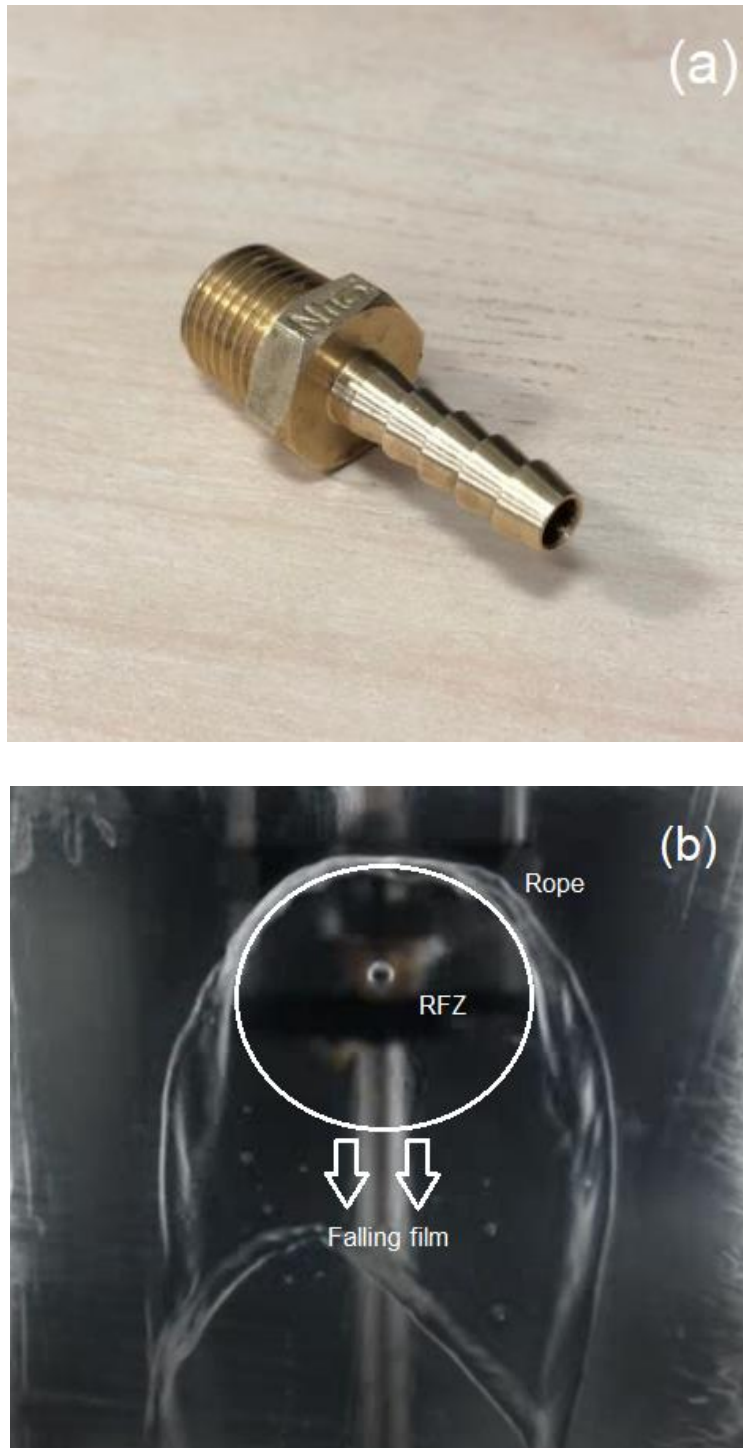


Fig. 3. 14: Top: Jet nozzle, bottom: footprint of horizontal 1 lmin^{-1} jet impinging on vertical Perspex wall. Key regions observed by Wilson et al. (2018) highlighted: rope, RFZ and falling film

In Fig. 3.14b the three regions observed by Wilson et al. (2014) can be clearly seen. The RFZ around the impingement point where a thin layer of fast-moving fluid moves radially outward from the impingement point. A rope like boundary then forms around the RFZ where the thickness in the water film increases. A falling film then forms due to gravity

and drains the fluid from the rope and RFZ down the surface. The nozzle used was made in house and was 4 mm in diameter with a discharge coefficient, measured using the method outlined in 3.2.3.1, of $0.032 \text{ l min}^{-1} \text{ Pa}^{-0.5}$. Fig. 3.15 shows the graph of flow rate versus the square root of pressure drop across the nozzle. The data was obtained by connecting the nozzle to a hydraulics bench and varying the flow rate delivered to the nozzle, taking measurements of the pressure downstream and upstream of the nozzle using a digital manometer. The difference in the pressure downstream and upstream was then plotted for each flow rate. Three repeat experiments were conducted, and the average gradient was taken to give the nozzle discharge coefficient.

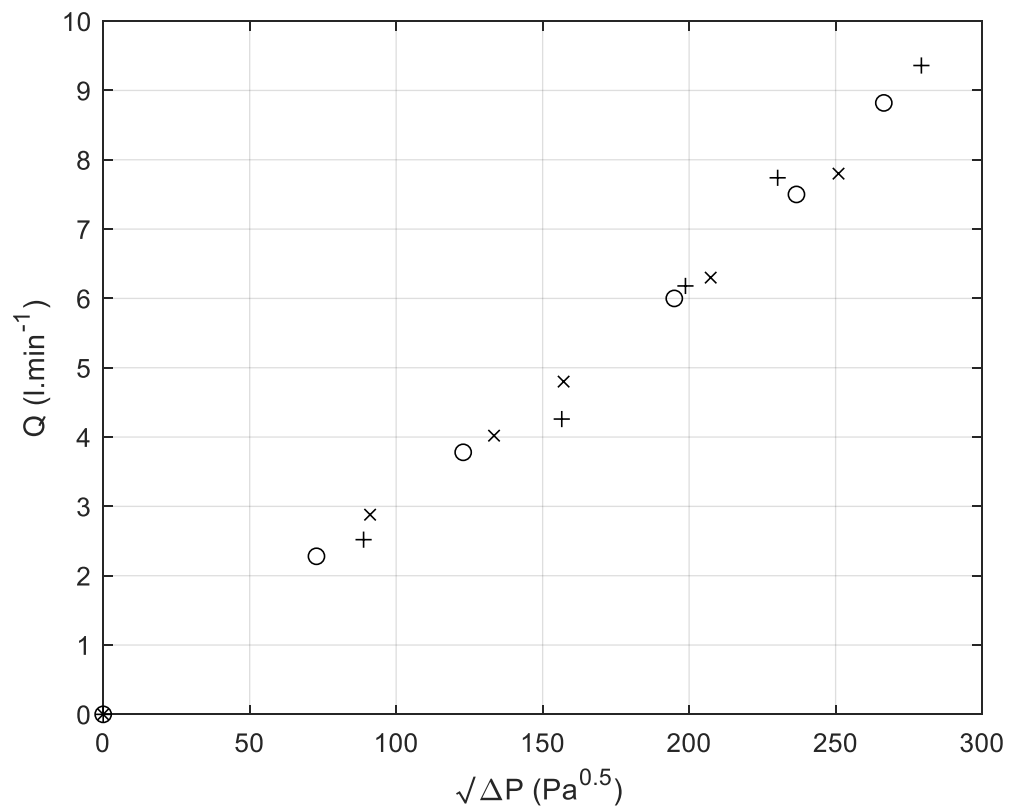


Fig. 3. 15: Flow rate, Q , vs square root of pressure drop across the nozzle, $\sqrt{\Delta P}$ for three repeat experiments.

The standoff distance of the nozzle from the wall was set to a specified value, d . Behind the transparent wall a Logitech C920 web camera was positioned so that the cleaning process could be observed and recorded. The flow of water, measured using a rotameter, was recycled through a collection tank. To ensure the water was not contaminated it was replaced at regular intervals. The tank was covered with a nitrile rubber thermal insulating sheet of 25 mm thickness and a thermal conductivity of $0.034 \text{ Wm}^{-1}\text{K}^{-1}$ to ensure that the water remained a stable temperature during heated

experiments. Fig. 3.16a shows a schematic diagram of the test rig and Fig. 3.16b shows a photograph of the experimental apparatus.

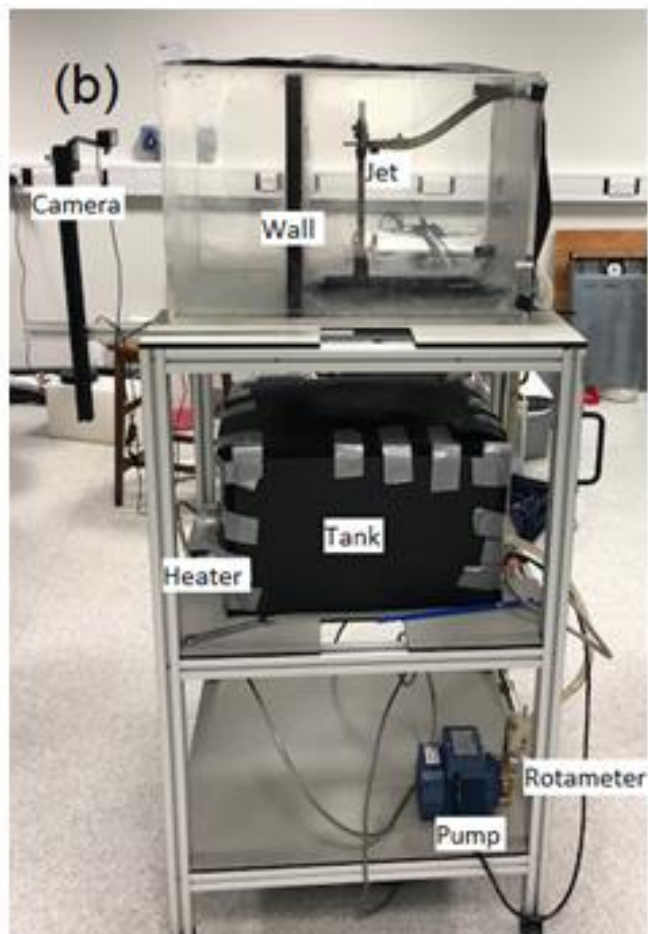
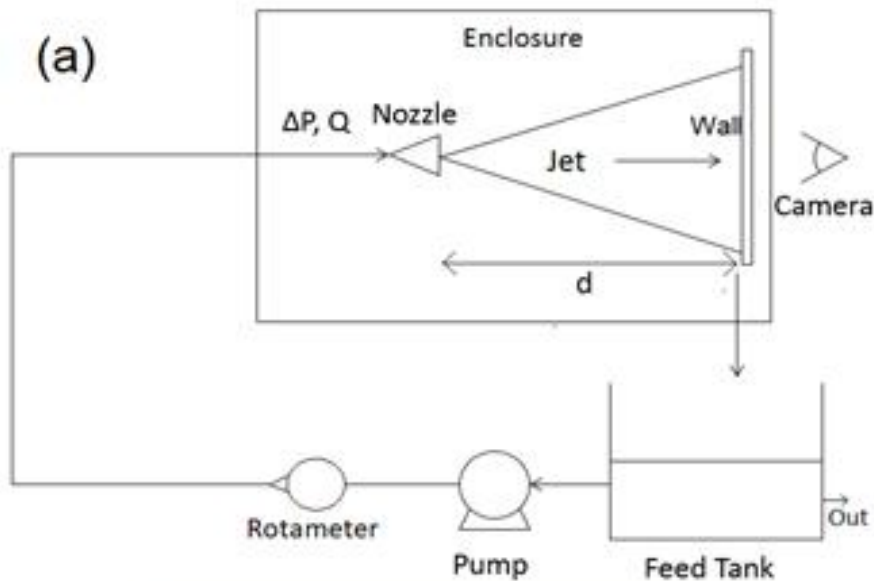


Fig. 3. 16: a) Test rig schematic; the arrows represent the flow of water. The enclosure and wall are both made of Perspex to allow for easy observation and imaging from the camera. ΔP and Q represent pressure drop across the nozzle and flow rate respectively. b) Photograph of test apparatus with main components identified.

It is important to note that the test apparatus assumes a flat surface perpendicular to the jet and located vertically to allow drainage, however frequently on the wash racks there is curvature of the surfaces loaded on to them. In addition to this, jets do not always impinge perpendicular to the surfaces being cleaned; there can often be an angle of incidence. In this work these factors have not been studied in order to simplify the problem. The use of Perspex as the surface material is also a simplification of the cleaning process observed on the wash racks since most production equipment used in the pharmaceutical industry is stainless steel. Perspex has a significantly lower surface energy of approximately 0.041 Nm^{-1} (Hild, accessed: 17/1/19) compared to that of stainless steel which has a surface energy of between $0.65 - 1.2 \text{ Nm}^{-1}$ depending on what grade is used (Bartholomew, Accessed: 10/11/18). Stainless steel therefore has much greater adhesive properties than Perspex and a stainless-steel substrate is more difficult to clean. Perspex was chosen for its transparency thus allowing for relative ease of filming the cleaning process. Water with no added surfactant was also used as a simplification of the cleaning process as surfactant is often used on wash racks. This decision was made to study the cleaning process from a purely hydrodynamic and thermal perspective. The addition of surfactants and other avenues for future work, based on the simplifications in this study, are discussed in chapter 8.

3.3.2 Design of experiments (DOE)

The experiments were designed such that the variables to be studied were flow rate, standoff distance of the nozzle, soil thickness and water temperature. In order to operate on the test rig under conditions that match those experienced on the wash racks as closely as possible, typical distances from the surface to the jet were to be determined. This was achieved by examining a range of cleaning racks on a pharmaceutical manufacturing site. By looking closely at the racks it was possible to identify the typical size of the components that are loaded on to them and measure the distance between the surface being cleaned and the nozzle. The parts loaded on to the racks varied from small diameter pipes to larger components such as filling machine pressurised header tanks. Typical standoff distances varied between approximately 50 mm to 200 mm.

To efficiently fill the design space a Box Behnken design for the remaining three variables was used (Box et al., 1960). Three points were used to fill the design space for each variable. Flow rates were matched to those on Rack 1 using the data generated by EPANET. Flow rates on the rack varied between 2 and 40 l min^{-1} . The mean, median and mode flow rates respectively on the wash rack are 10.4 l min^{-1} , 5.4 l min^{-1} and 4.2 l min^{-1} , respectively. The pump used on the rig was selected to study flow rates in proximity to the modal nozzle flow rate. This research focused mainly on the cleaning of smaller

components and not larger components which demanded the higher flow rates seen on the rack, the lower boundary of the flow rates was thus explored. Operating flow rates on the test rig were 1, 2.5 and 4 $\text{l}\cdot\text{min}^{-1}$. Water temperatures were selected as 20 °C, 40 °C and 60 °C, the latter two of which encompass the melting point of the soil under study. The Box Behnken parameter space used in the experiments is shown in Fig. 3.17.

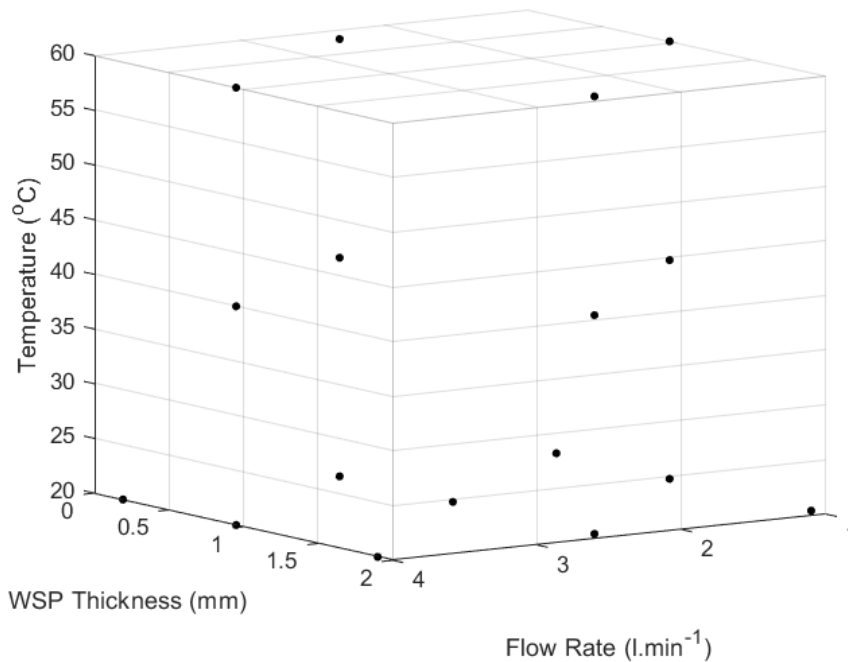


Fig. 3. 17: Box Behnken DOE for 3 design variables: temperature, WSP thickness and flow rate.

Each point in Fig. 3.17 represents an experiment that was conducted on the test rig. For example, the point in the extreme bottom left of the 3D grid represents an experiment run at 20 °C, a 0.19 mm film thickness and 4 $\text{l}\cdot\text{min}^{-1}$ flow rate. At room temperature (20 °C) the grid was filled with 3 x 3 experiments. For the two higher temperature cases, 40 °C and 60 °C, the Box Behnken design was employed, whereby a point was situated at the midpoint of each side of the box on that plane. For each of the elevated temperatures, the coordinates for each experiment were (4 $\text{l}\cdot\text{min}^{-1}$, 0.95 mm), (2.5 $\text{l}\cdot\text{min}^{-1}$, 0.19 mm), (2.5 $\text{l}\cdot\text{min}^{-1}$, 1.9 mm) and (1 $\text{l}\cdot\text{min}^{-1}$, 0.95 mm).

3.3.3 Material characterisation

The soil material chosen for the horizontal jet experiments was white soft paraffin (WSP), an excipient extensively used in pharmaceutical creams and ointments. WSP is commonly used in the manufacture of ointments which are applied to the body for dermatological use. The WSP was applied to the Perspex wall by drawing down an excess of WSP with a straight edge, using tape of thickness t either side of the wall to meter the thickness. The thickness of the WSP could then be controlled through using

multiple layers of tape. It is reasonable to assume that the error in applied thickness is small enough to be considered negligible. The typical area of WSP applied to the Perspex wall for each experiment was approximately 35000 mm². Residual soil thicknesses in batch cleaning can vary, depending on operation and whether excess material is manually removed before loading onto the wash rack. Based on observation, a range of WSP thicknesses were selected for study, these were 0.19 mm (t), 0.95 mm ($5t$) and 1.9 mm ($10t$), where t represents the thickness of each piece of tape.

3.3.3.1 Penetration tests

To characterise the WSP used for cleaning, penetration tests were conducted. The penetration test indicates the force required to penetrate the sample. It is commonly used in the pharmaceutical industry to test WSP and is part of standardised quality testing for WSP (Pharmacopoeia, 2005). The tests were conducted on a TA-XT Plus texture analyser (Stable Micro Systems, UK). A flat metallic probe of 10mm diameter was positioned above the sample and lowered at a constant speed of 0.5 mms⁻¹ to a depth of 2 mm below the surface of the WSP. Once the penetration distance had been reached, the probe was withdrawn at a constant speed of 5 mms⁻¹. This test was then repeated in 4 different locations on the sample and an average force – distance curve plotted. The test was conducted at room temperature 20 °C. The resulting plot is shown in Fig. 3.18.

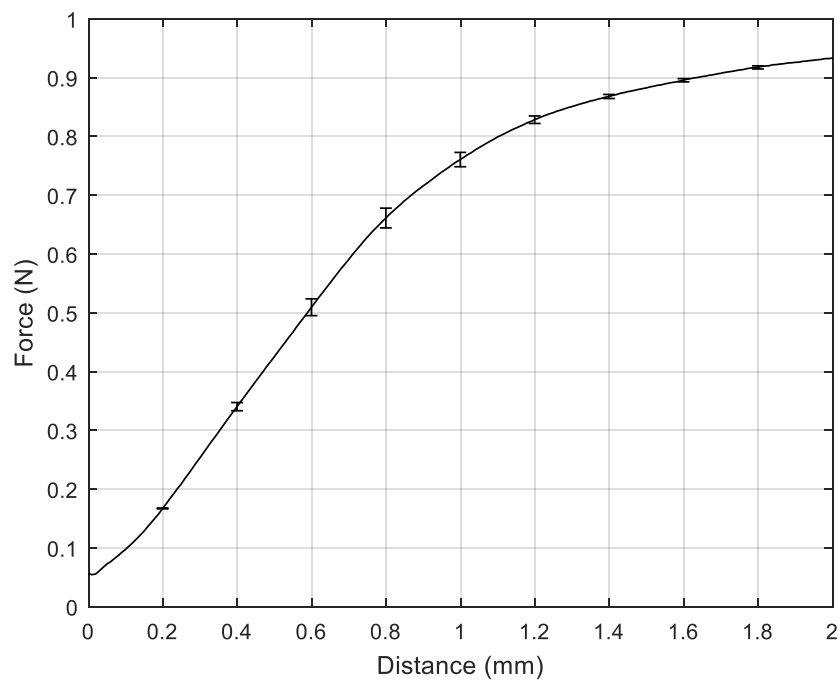


Fig. 3. 18: Penetration test Force versus Distance plot (measured at 20°C) Error bars plotted using standard deviation.

Fig. 3.18 shows how the gradient of the Force vs Distance curve decreases with increasing depth of penetration under the WSP. Using this curve, the force required to penetrate the WSP to the surface of the wall can be extrapolated for each WSP thickness. An initial force of approximately 0.06N is required for the WSP to yield and penetration to occur. For the 0.19 mm, 0.95 mm and 1.9 mm WSP thicknesses respectively, and assuming no interaction of the solid support surface the forces required to penetrate the entire soil layer are approximately 0.16 N, 0.74 N and 0.93 N. The drop point temperature range of the WSP was given on a manufacturer's data sheet as between 35 - 70 °C, but DSC analysis by Bentley (2017) shows a large melting peak at 30-40°C.

3.3.3.2 Contact angle measurement

A further characterisation of the WSP was conducted whereby the contact angle of water on WSP was measured. This was done by applying a thin layer of WSP to a stainless-steel coupon and positioning it on an Attension Theta Flex optical tensiometer. A single droplet of water was applied to the surface using a pipette and a high-resolution camera in line with the surface of the coupon measured the contact angle between the water and WSP. Three measurements were taken, resulting in an average contact angle of 83°, suggesting the WSP is hydrophilic.

3.4 Vertical jet apparatus

3.4.1 Test rig design

For analysis of Rack 2, a vertical jet alignment was considered to replicate the cleaning of needles commonly used in filling. These components are significantly different from the external components considered by the design of the test rig of Fig. 3.3. The setup on the rack is shown in Fig. 3.19.



Fig. 3. 19: Rack 2 position of filling needles (b) cleaned by vertically aligned impinging jets (a).

To replicate this experimentally, the geometry of the filling needles was obtained from site and steel tubing of the same dimensions was ordered from an online supplier. The test rig of Fig. 3.16b was then modified to accommodate for a vertically aligned jet. A different jet was used for this set of experiments, as measurements of the jets shown in Fig. 3.19 on site showed that the nozzle orifice was of a smaller diameter, 1.5 mm. Using the method outlined in 3.2.3.4 the discharge coefficient for this nozzle was estimated to be $0.01 \text{ l min}^{-1} \text{ Pa}^{-0.5}$. The Perspex wall was removed and replaced with a clamp stand that would hold the tubing in place. Measurements were taken on site to determine the standoff distance between the nozzle and the filling needle and the jet was then positioned to this height above the tubing. A funnel was placed beneath the tube to collect water from the exit of the tube and this was channelled to a beaker that was placed on a scale so that the mass flow rate of water could be recorded throughout the experiments. To ensure that no water that missed the entrance to the tube was collected, a protective shroud was placed on the exterior of the tube to divert water away from the funnel. The experimental set up is shown in Fig. 3.20.

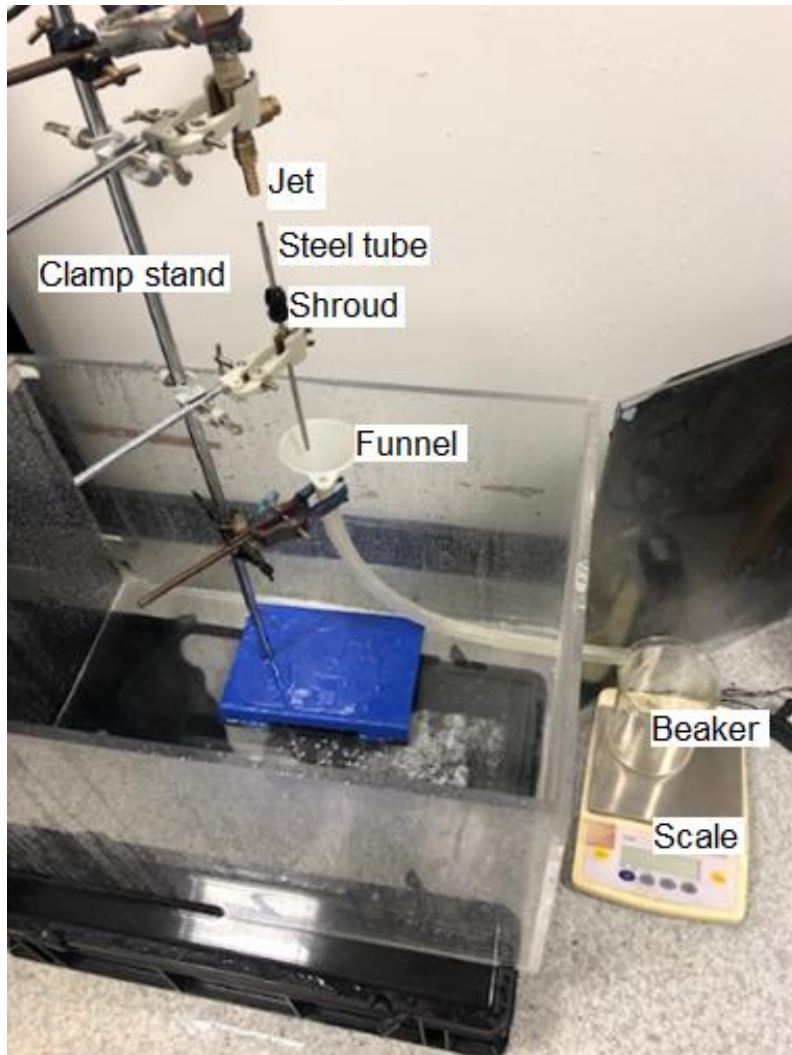


Fig. 3. 20: Vertically aligned jet test rig with key elements labelled.

3.4.2 Design of experiments

For the vertically aligned jet experiments, the flow rate for the jet was again obtained from EPANET to match the flow to that delivered to the relevant nozzles on Rack 2. The flow rate delivered to the relevant nozzle on Rack 2 was calculated on EPANET to be 0.6 lmin^{-1} . Unlike the horizontal jet experiments, the flow rate remained constant, as did the water temperature (room temperature 20°C). In this case the variables in the experiments were the state of the soil in the tube (discussed in 3.4.3) and the alignment of the jet relative to the tube. For the misaligned case, the tube was rotated through an angle whilst keeping the jet in a fixed position. The measure of cleaning performance in the vertically aligned experiments was the time taken for the mass flow rate collected from the exit to the tube to equal that of the impinging jet, i.e. indicating that all the bulk soil in the tube had been removed.

3.4.3 Material characterisation

The soil material for the vertical jet experiments was a gel which the equipment loaded on to Rack 2 was exclusively used to manufacture. The gel was supplied from site and subsequently used to fill each steel tube. The gel consisted of Chlorhexidine Gluconate. As aforementioned, the gel was studied in different states. Three states were considered; fresh, dried and baked at 85 °C. For the fresh state, the gel was simply inserted into the tube and cleaned immediately. For the dried gel it was inserted into the tube, left for five days to dry and then cleaned. For the baked gel it was heated at 85 °C in an oven for 45 minutes, left to cool to room temperature and then cleaned. To characterise the rheology of the gel, a shear stress sweep was conducted on a Malvern Kinexus rheometer. The shear stress on the sample was increased from 1 – 1000 Pa, raising a decade every 5 s. Shear viscosity was measured at each shear stress, three measurements were taken and an average plotted. The rheometer test was repeated three times and the average curve plotted, which is shown in Fig. 3.21.

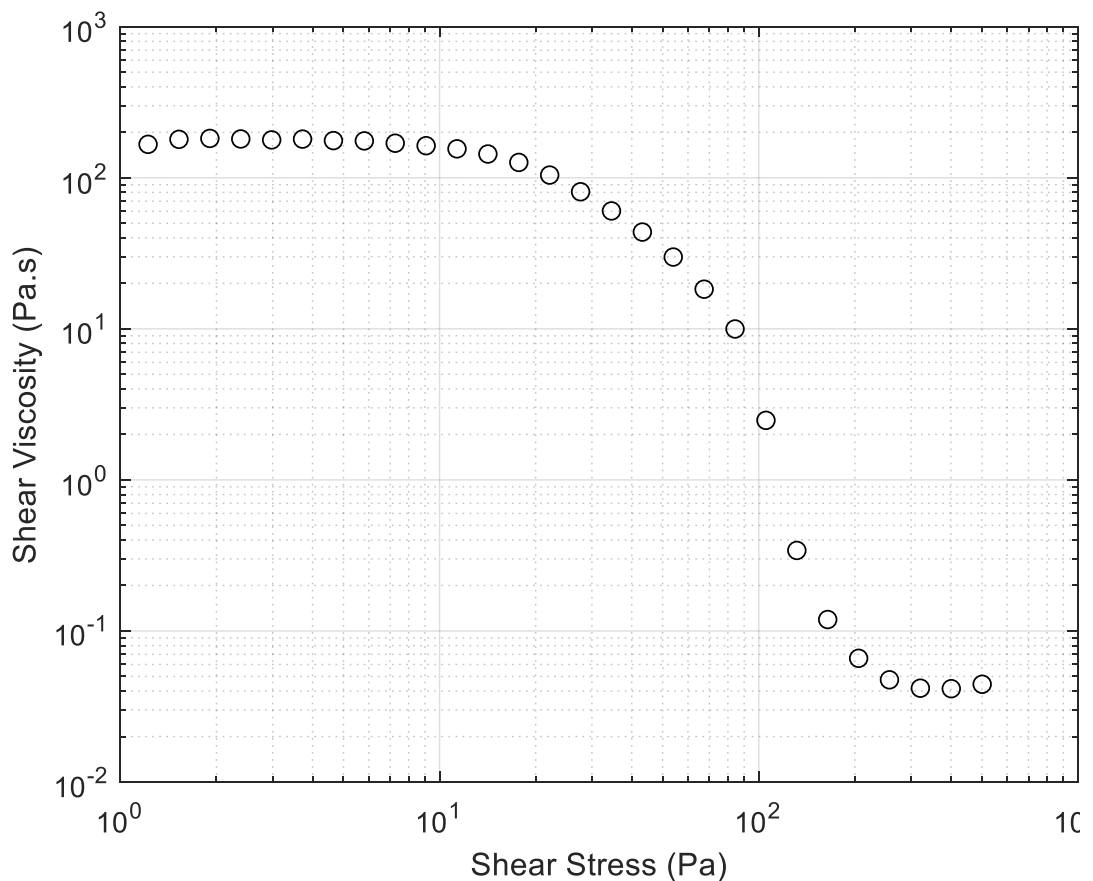


Fig. 3. 21: Shear Viscosity vs Shear Stress for gel (20 °C).

Fig. 3.21 shows how initially for shear stress < 10 Pa, the shear viscosity is independent of an increase in shear stress, the viscosity is constant at approximately 200 Pa.s.

Between 10 – 100 Pa however there is a sharp decrease in the viscosity of the gel where shear thinning of the gel occurs, the yield stress of the gel is in this region which can be estimated to be 20 Pa, where the gradient of the curve begins to decrease rapidly. For shear stress > 100 Pa the curve eventually plateaus to the infinite shear viscosity value of approximately 0.04 Pa.s. Any further shear applied to the gel will have no effect on the viscosity beyond this point.

3.5 Spray apparatus

To investigate the cleaning characteristics of the sprays on the wash racks, the same test rig used for the horizontal jet experiments was used (Fig. 3.14b). The only modification was changing the nozzle from that of the jet to a spray. A full cone PNR BCQ-1740-B1 spray nozzle (PNR, online) was used, which closely matched those typically used on the wash racks. The nozzle is depicted in Fig. 3.22 and its spray distribution is shown in Fig. 3.23.



Fig. 3. 22: cone PNR BCQ-1740-B1 spray nozzle (PNR, Accessed: 4/4/18).

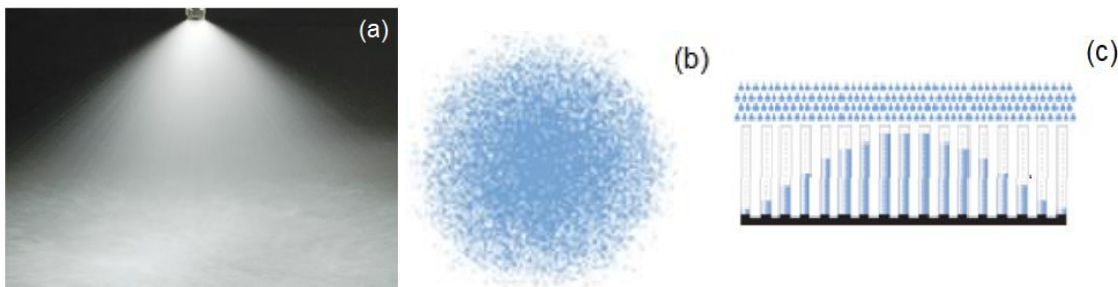


Fig. 3. 23: (a) Photograph of spray distribution from nozzle (b) surface droplet distribution (c) convex distribution of droplets on surface (PNR, Access: 4/4/18).

As Fig. 3.23b and 3.23c show the droplet distribution is convex, whereby the droplets are more densely populated in the centre of the cone, with the droplet density decreasing with radial distance from the centre. The nozzle of Fig. 3.22 has an X-vane configuration, which are widely used in steelworks. They comprise two sloping flat surfaces which induce a rotation of the liquid going through the nozzle and two small slots on each flat part to produce a full cone pattern. From the manufacturer's data sheet of the nozzle (PNR, online), the nozzle discharge coefficient, k , for the spray nozzle was calculated to be $0.014 \text{ lmin}^{-1}\text{Pa}^{-0.5}$. This is 44% of the discharge coefficient for the jet, described in section 3.2.3.1. This means that for a given pressure, the spray delivers 44% of the flow in accordance with equation 3.1. Side-on images were taken of the spray at each flow rate and using ImageJ each spray angle induced by the nozzle was approximated. For the 4 lmin^{-1} , 2.5 lmin^{-1} and 1 lmin^{-1} flow rates, the respective spray angles were 64° , 56° and 40° .

3.6 Image processing

The recordings from the camera positioned behind the Perspex were used to calculate the area of WSP removed as a function of time. This was done using ImageJ, an open source image processing software (Rasband, 1997). Still images were taken from the videos at specified time points. The images were scaled in ImageJ to a known distance which was the distance between the pieces of tape described in 3.3.3. Each pixel was thus assigned a scale and each clean area could be measured using an analysis tool in ImageJ. The tool allows the user to draw freehand around the shape of the clean area and subsequently measure the size of the enclosed area. This was then plotted against its corresponding time.

3.7 Energy input calculations

The power input, W , across the nozzle is given by the product of pressure drop and flow rate, given by equation 3.21 (Massey, 2006).

$$W = Q\Delta P \quad (3.21)$$

Substituting 3.1 into this gives the power input in terms of two known quantities, Q and k , given by equation 3.22

$$W = Q^3 k^{-2} \quad (3.22)$$

where ΔP is the pressure drop across the nozzle (Pa) and Q is the flow rate (m^3s^{-1}). The energy input was then calculated by taking the product of power and time. Calculating the energy input with respect to time allowed for the WSP removal to be plotted against energy input and this subsequently gauged the efficiency of each experiment.

3.8 Computational droplet simulations

To study the soil removal mechanism of a spray, a single droplet impingement on to a surface was considered. The droplet impingement was modelled computationally using COMSOL, a computational fluid dynamics (CFD) package. A domain was created in which a single water droplet was suspended in air with initial zero velocity. The simulation was computed using the level set method.

3.8.1 Level set method

The level set method is a technique to represent moving interfaces or boundaries using a fixed mesh, first introduced by Osher and Sethian (1988). The method is particularly useful for problems where the computational domain can be divided into two separate domains separated by an interface. The main advantage of this method is the ability to naturally handle changes in topology for moving interfaces (Gibou et al., 2018). The interface is represented by a certain level set or iso-contour of a globally defined function, the level set function Φ . In COMSOL, Φ is a smooth step function that equals 0 in a domain and 1 in the other. Across the interface there is a smooth transition between 0 and 1. The interface is defined by $\Phi = 0.5$. An example domain is shown in Fig. 3.24.

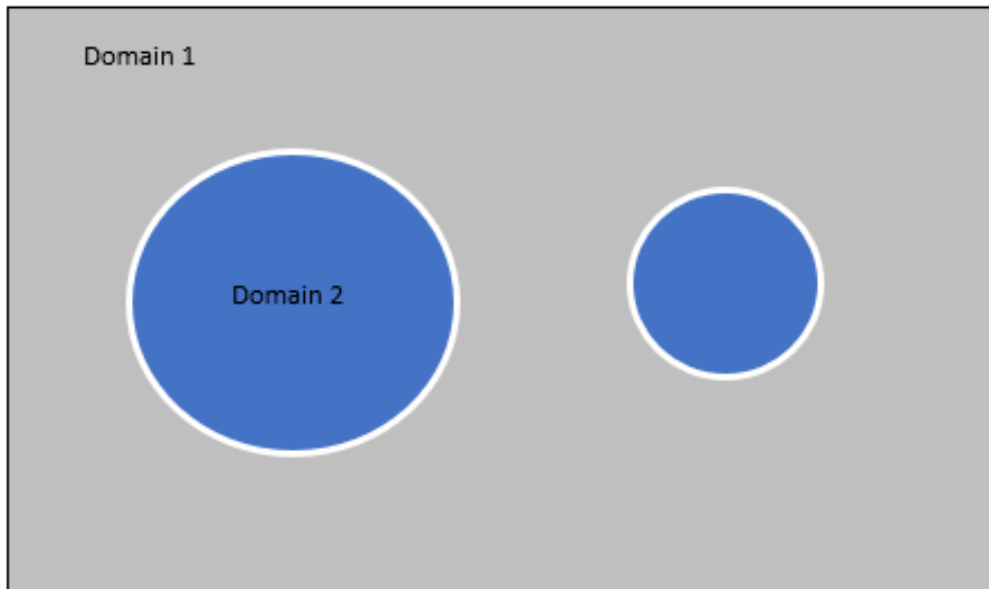


Fig. 3. 24: Example computational domain consisting of two phases, domain 1 and domain 2. The grey domain 1 is represented by $\Phi = 1$, the blue domain 2 is represented by $\Phi = 0$, the white interface is represented by $\Phi = 0.5$.

The modelling interface solves the following equation, 3.23, in order to move the interface with the velocity field \mathbf{u} (COMSOL, 2012).

$$\frac{\partial \phi}{\partial t} + \mathbf{u} \cdot \nabla \phi = \beta \nabla \cdot \left(\varepsilon \nabla \phi - \phi(1 - \phi) \frac{\nabla \phi}{|\nabla \phi|} \right) \quad (3.23)$$

The LHS of 3.23 gives the motion of the interface, and the RHS is included for numerical stability. The parameter, ε , determines the thickness of the region where Φ goes smoothly from 0 to 1 and is typically of the same order as the size of the elements of the mesh. By default, ε is constant in each domain and equals the mesh element size within the domain. The parameter β determines the amount of reinitialization or stabilisation of the level set function. It can be fine-tuned for each problem, however a suitable value to use is the maximum magnitude of the velocity field, \mathbf{u} (COMSOL, 2012).

3.8.1.1 Conservative and non-conservative form

In the simulations of this thesis the flow is modelled as incompressible and satisfies the continuity equation given by 3.24.

$$\nabla \cdot \mathbf{u} = 0 \quad (3.24)$$

In a 2D domain the area bounded by the interface should be conserved if there is no inflow or outflow through the boundaries. To obtain exact numerical conservation, the conservative form of 3.25 can be used.

$$\frac{\partial \phi}{\partial t} + \nabla \cdot (\mathbf{u}\phi) = \beta \nabla \cdot \left(\varepsilon \nabla \phi - \phi(1 - \phi) \frac{\nabla \phi}{|\nabla \phi|} \right) \quad (3.25)$$

Using the conservative level set form the exact numerical conservation of the integral of Φ is obtained (COMSOL, 2012). Note all the equations presented in 3.8.1 are referenced from COMSOL, 2012.

3.8.1.2 Initialising the level set function

Before solving 3.23 or 3.25 the level set function must be initialised in order for it to smoothly transition from 0 to 1 across the interface. This is done by setting $\Phi = 0$ on one side of the interface and $\Phi = 1$ on the other. Equation 3.26 is then solved.

$$\frac{\partial \phi}{\partial t} = \beta \nabla \cdot \left(\varepsilon \nabla \phi - \phi(1 - \phi) \frac{\nabla \phi}{|\nabla \phi|} \right) \quad (3.26)$$

Φ_0 is the initial condition from $t = 0$ to $t \sim 5\varepsilon/\beta$. The resulting Φ is smooth across the interface and provides a suitable initial condition for the level set equation.

3.8.1.3 Variables for geometric properties of the interface

The interfacial geometric properties are required in order to solve the level set equation. The unit normal to the interface is given by 3.27.

$$\mathbf{n} = \frac{\nabla \phi}{|\nabla \phi|_{\phi=0.5}} \quad (3.27)$$

The curvature is then defined as 3.28.

$$\kappa = -\nabla \cdot \mathbf{n}_{\phi=0.5} \quad (3.28)$$

3.8.1.4 Volume Force

The volume force feature is used, for example, to incorporate gravity into a model. The volume force is specified on the RHS of the incompressible flow equation, given by 3.29.

$$\rho \frac{\partial \mathbf{u}}{\partial t} + \rho(\mathbf{u} \cdot \nabla)\mathbf{u} = \nabla \cdot [-\rho \mathbf{I} + \mu(\nabla \mathbf{u} + (\nabla \mathbf{u})^T)] + \mathbf{F} \quad (3.29)$$

3.8.1.5 Fluid properties

The fluid properties are assigned to the model for each domain, these are density and dynamic viscosity. Each fluid in the domain must then be assigned $\Phi = 0$ and $\Phi = 1$.

3.8.1.6 Boundary conditions

The level set interface contains the following boundary conditions.

Wall

The wall feature describes the flow conditions at a wall, two primary cases will be considered:

- No slip, the default condition for a stationary solid wall. The condition prescribes that $\mathbf{u} = 0$, i.e. the fluid at the wall is not moving.
- Slip, where it is assumed there are no viscous effects at the slip wall and hence, no boundary layer develops. There is a no-penetration condition that dictates that $\mathbf{u} \cdot \mathbf{n} = 0$.

Outlet

The outlet boundary describes the flow conditions at a boundary in a domain. The pressure condition is the default, whereby a reference pressure is assigned at the boundary, and was used in this study. The alternatives are velocity, normal stress, pressure and no viscous stress.

Symmetry

The symmetry boundary condition describes symmetry boundaries in a simulation. No penetration of the boundary is permitted and shear stress vanishes at the boundary. The boundary condition is a combination of the Dirichlet condition and a Neumann condition (Cheng and Cheng, 2005), given by 3.30 and 3.31.

$$\mathbf{u} \cdot \mathbf{n} = 0, \quad \left(-\rho \mathbf{I} + \left(\mu(\nabla \mathbf{u} + (\nabla \mathbf{u})^T) - \frac{2}{3} \mu(\nabla \cdot \mathbf{u}) \mathbf{I} \right) \right) \mathbf{n} = \mathbf{0} \quad (3.30)$$

$$\mathbf{u} \cdot \mathbf{n} = 0, \quad \left(-\rho \mathbf{I} + (\eta(\nabla \mathbf{u} + (\nabla \mathbf{u})^T)) \right) \mathbf{n} = \mathbf{0} \quad (3.31)$$

For the compressible and incompressible formulation respectively.

No flow

The no flow condition is the default boundary condition and represents boundaries where there is no flow across the boundary.

Pressure point constraint

The pressure point constraint feature adds a pressure constraint at a point used as a reference point for calculating pressure throughout the rest of the domain.

3.8.2 Finite element method

In COMSOL the finite element method is used to discretise the equations used in the level set method. The partial differential equations (PDEs) are difficult and computationally expensive to solve, so instead an approximation of the equations is formed based upon different types of discretisation. The finite element is a numerical method for solving the PDEs (COMSOL, 2016). By dividing the domain into a series of finite elements, forming a mesh, the solution becomes easier. The $|\nabla\phi|$ term in the level set method is approximated at a vertex in the mesh by taking the average over a patch of elements that surround the vertex. Time discretisation is applied with a time step, given by 3.32.

$$\Delta t = t^{n+1} - t^n \quad (3.32)$$

The time step can change in COMSOL throughout the simulation depending on the complexity of the solution at each accumulated time. The level set function can then be discretised using 3.33.

$$\phi_i^{n+1} = \phi_i^n - \Delta t(\mathbf{u} \cdot \mathbf{n})_i |\nabla\phi|_i \quad (3.33)$$

The level set function can then be solved throughout the domain at each time step in the simulation (Shopples, 2009). For a liquid air system, the density and viscosity of each element can be obtained using the level set function in equations 3.34 and 3.35 respectively (Hu et al., 2014).

$$\rho_i = \rho_a + (\rho_l - \rho_a)\phi_i \quad (3.34)$$

$$\eta_i = \eta_a + (\eta_l - \eta_a)\phi_i \quad (3.35)$$

Where the subscripts a and l represent air and liquid respectively.

3.8.2 Droplet impingement model setup

A droplet impinging on to a surface was setup in COMSOL to study the soil removal mechanism of the spray from the interaction of a single droplet in the spray with the surface being cleaned. A droplet of water ($\Phi = 1$) was given an initial zero velocity, suspended in air ($\Phi = 0$). The droplet was given a diameter $d = 0.5$ mm, a typical size for a water spray similar to that used introduced in 3.5 (Sulaiman and Daud, 2013). The centre of the droplet was positioned height $z_1 = 1.5$ mm above the wall on to which it impinges. This was chosen arbitrarily to allow sufficient space upstream of the wall for the droplet to reach a steady state. The top boundary of the domain was 2.5 mm above the wall. The wall itself was assigned a length of 3 mm, six droplet diameters, to allow for spreading of the droplet on the wall after impact. Interfacial tension was applied to the liquid/air interface and given the value for water and air, 0.07 Nm^{-1} . Two cases were considered, one where the wall which the droplet impinges is a wetted wall in COMSOL, given the contact angle of water and WSP, derived in 3.3.3 to be 83° . Note that the wall is actually dry in this case and not wetted as its name would suggest. This is how it is denoted in COMSOL and will be used throughout this thesis. A parametric study of contact angle was conducted where the contact angle was lowered in 20° increments to 0° to simulate further wetting of the wall due to continual droplet impingement. The other case was where a film of water was present on the surface, building up from continual spraying assuming no drainage, to see how this affected the shear stress distribution of the droplet on the wall and the subsequent effect on cleaning performance. The domain setup for the wetted wall case in COMSOL is shown in Fig. 3.25.

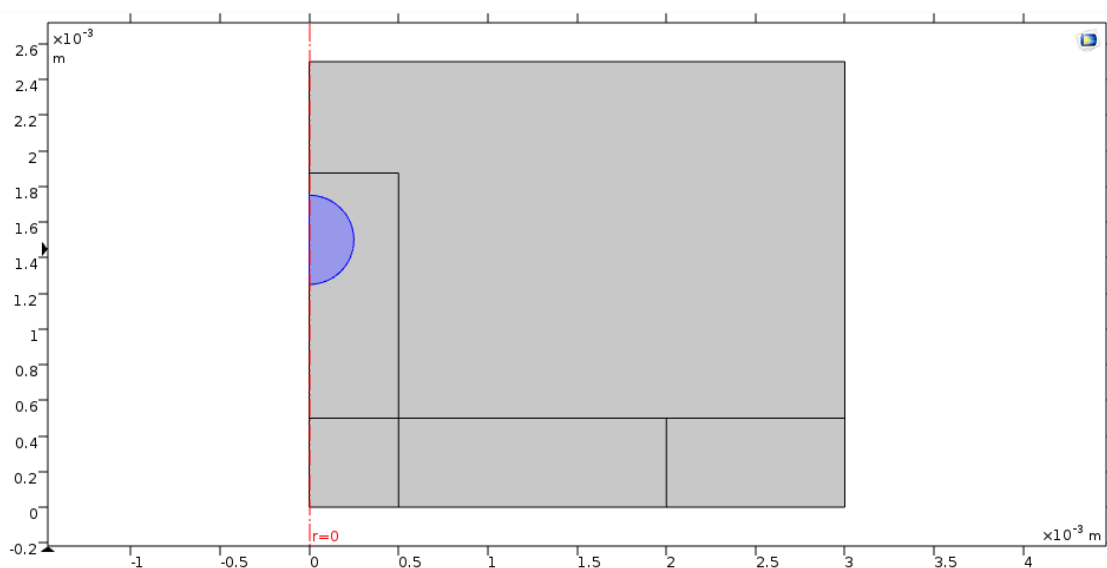


Fig. 3. 25: COMSOL domain setup, wetted wall case.

The droplet is shown as the purple semi-circle, which represents water ($\Phi = 1$). The grey parts of the domain ($\Phi = 0$) represent air. The line of axial symmetry means that the entire domain is revolved 360° about the left-hand boundary and a spherical droplet is created. The initial values assigned to the domain were that initial velocity $u_d = 0 \text{ ms}^{-1}$. Above the horizontal line at $z = 0.5 \text{ mm}$, the acceleration is such that the droplet reaches a velocity $v_d = -1 \text{ ms}^{-1}$ at that line, given by 3.36.

$$a_1 = \frac{v_d^2 - u_d^2}{2(z_2 - z_1)} \quad (3.36)$$

$$a_1 = \frac{-1^2 - 0^2}{2(0.5 - 1.5) \times 10^{-3}} = -1000 \text{ ms}^{-2}$$

Below the line $z_2 = 0.5 \text{ mm}$, the acceleration is that due to gravity, $a_2 = -9.81 \text{ ms}^{-2}$. A volume force, F (Nm^{-3}), is applied to the droplet, defined by 3.37.

$$F = -\rho \times a \quad (3.37)$$

Where ρ_w is the density of the droplet, 1000 kgm^{-3} , and a is the acceleration.

The alternative case of the water film present on the surface is shown in Fig. 3.26.

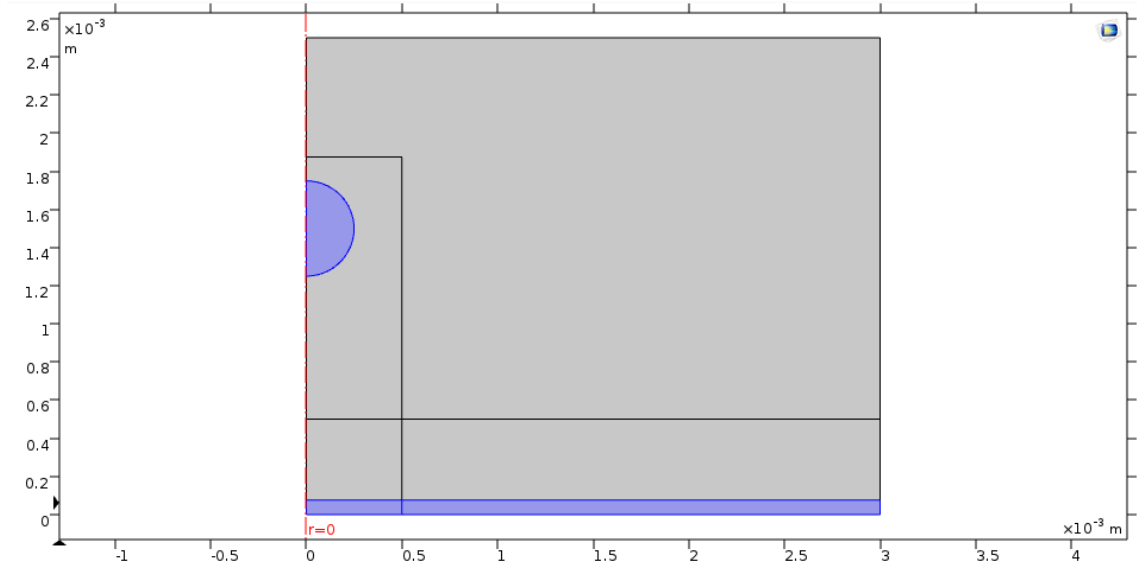


Fig. 3. 26: Droplet impingement model with water film on the surface (0.15d film thickness).

The film was also assigned $\Phi = 1$ and given the properties of water. A parametric study of the film thickness was conducted to observe how the thickness of the film on the surface affects the shear stress distribution on the wall. The thickness was varied from $h_0 = 0.05d$ to $h_0 = d$ and the shear stress on the wall measured for each thickness. The

total time for the simulation was 0.015 s. This was approximately five times greater than the time taken for the droplet to impact the surface and was chosen to allow the droplet and film to come to a steady state. The time for this to occur was gleaned from running preliminary simulations. A summary of the parameter space used in the model is shown in Table 3.1.

Table 3.1: COMSOL model parameters

Parameter	Value
Droplet diameter, d	0.5 mm
Initial droplet velocity, u_d	0 ms ⁻¹
Velocity ($z = 0.5$ mm), v_d	-1 ms ⁻¹
Acceleration, a_1	-1000 ms ⁻²
Acceleration, a_2	-9.81 ms ⁻²
Interfacial tension (water/air), σ	0.07 Nm ⁻¹
Time, t_0	0.015 s
Water film thickness, h_0	0 – 0.5 mm
Water density, ρ_w	1000 kgm ⁻³
Air density, ρ_a	1.23 kgm ⁻³
Water dynamic viscosity, η_w	1 x 10 ⁻³ Pa.s
Air dynamic viscosity, η_a	1.8 x 10 ⁻⁵ Pa.s
Wall contact angle, θ	0 – 83°

3.8.2.1 Meshing the model

When meshing the models in COMSOL, it was important to concentrate the density of mesh elements in areas of importance where complexity of the solution is highest. For these simulations the mesh density was concentrated in the droplet, the path of the droplet and the wall to capture the spreading of the droplet and the shear on the surface

more accurately. Two rectangles were created in the domain, one vertically capturing the path of the droplet and one horizontally capturing the spreading on the wall and any movement in the film. Elements were concentrated with a high density in these rectangles, setting a maximum cell size inside and a coarser mesh outside in the surrounding air where nothing of significance occurs. The vertically aligned rectangle was 0.5 mm in width and 1.9 mm in height. The horizontally aligned rectangle was 0.5 mm in height and 3 mm in width, covering the width of the domain to capture the entire wall.

3.8.2.2 *Boundary conditions*

The domain was 2D axisymmetric, whereby a line of axial symmetry was assigned to the left-hand boundary. This had the effect of revolving the 2D domain 360° around the left-hand boundary, creating a cylindrical domain. The top boundary, above the droplet, was assigned an outlet. Here the default pressure setting was used, where the pressure applied to the top boundary was set to atmospheric conditions, 1 bar. No flow was also assigned to the top boundary, in which no flow crosses the boundary. The right-hand boundary was assigned a symmetry condition and no flow, whereby there is again no flow permitted to cross the boundary and the domain is mirrored about the right-hand boundary. A pressure point constraint, where the pressure was set to 1 bar in the top right-hand corner of the domain, was applied. This was to act as a reference point from which the pressure throughout the domain could be solved. Finally, the wall on to which the droplet impinged was assigned a wetted wall with no slip. The contact angle was applied for each case. For the simulations with a liquid film on the surface, this was set to 0°.

3.8.2.3 *Interfacial thickness*

The final parameter required for input to COMSOL was that controlling interfacial thickness, ϵ , as aforementioned in 3.8.1. For preliminary simulations ϵ was assigned its default value which COMSOL sets as the same order as the maximum cell size in the mesh domain. As will be discussed later in 3.8.2.5, the cell size varies across the domain with a relatively coarse mesh in areas upstream of the droplet and a much finer mesh density downstream, where solving the simulation was of higher complexity. As such the default interfacial thickness was very diffuse and this was found to have a significant effect on the shear stress calculations on the wall. It was observed that a value of $\epsilon = 1 \times 10^{-5}$ m provided a sharp interface such that hi-fidelity solution of shear stress on the wall could be obtained. The solution time was very sensitive to further decreases in ϵ , so this was carried forward for future simulations. A comparison of the smoothing of the

interface is shown in Fig. 3.27, with the default setting of ϵ presented in 3.27a and the sharpened value of 1×10^{-5} m presented in 3.27b.

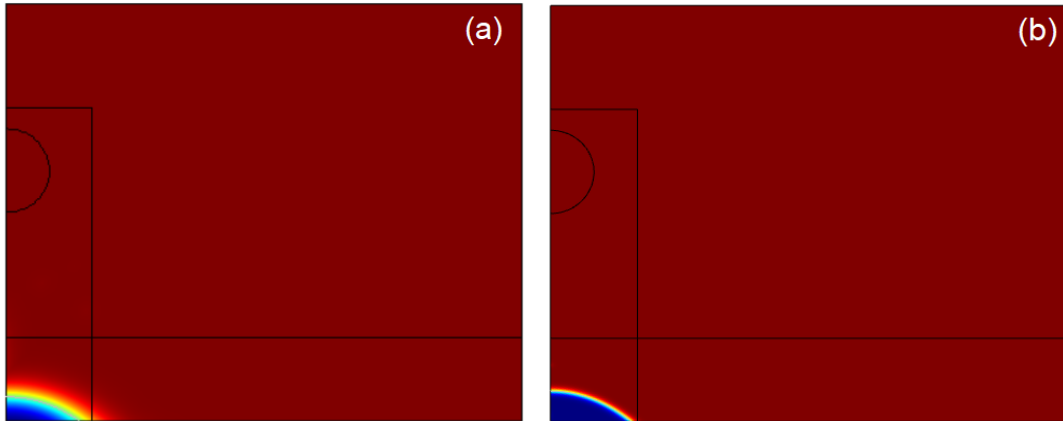


Fig. 3. 27: Interfacial thickness parameter, ϵ , control study: **a)** Default **b)** $\epsilon = 1 \times 10^{-5}$ m

The comparison of Fig. 3.27 shows the significance of the smoothing parameter ϵ . In Fig. 3.27a the interface between the two phases is very diffuse with a gradual transition occurring from the blue representing water, across the spectrum of colours to red, representing air. On the other hand when ϵ is altered to sharpen the interface, for a more realistic representation, the transition across the interface occurs over a much smaller distance.

3.8.2.4 Processing results

Once the simulations had been computed, post processing of the results was done in COMSOL to extract the information of relevance and importance to the research. Since from a cleaning perspective, the shear stress exerted on the wall by the impinging droplet was of most importance, this was calculated along the distance of the wall. The equation used to calculate this is given by equation 3.38.

$$\tau_{wall} = \gamma \cdot \eta \quad (3.38)$$

Where τ_{wall} is the shear stress on the wall, γ is the shear rate and η is the dynamic viscosity of water. Since the simulation was transient and the shear stress on the wall was a function of time, the shear on the wall was measured at different times in the simulation. Contours of time were plotted, with wall shear stress on the y-axis and distance along the wall on the x-axis. An example plot is shown in Fig. 3.27.

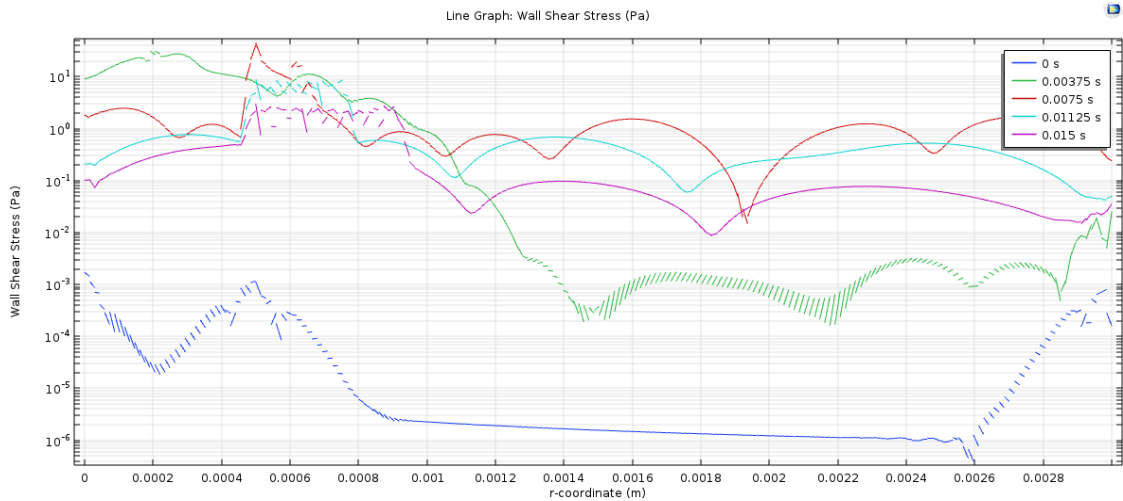


Fig. 3. 28: Wall shear stress vs Position on the wall (Film thickness 0.15d).

Time contours were plotted, from $t = 0 - 0.015$ s, in equal intervals of 0.00375 s. As it is shown in Fig. 3.28 there is some noise in the response, particularly in the 0.00375 s contour, displayed by the green curve. Instead of taking the maximum value of each curve, where spikes in the curves can give unreliable values, the time and space averaged shear stress was taken. Firstly, each curve was integrated with respect to the position on the wall, r_{wall} . This was then divided by the total length of the wall, R , to give the space averaged shear stress. This was done using equation 3.39.

$$\tau_{avg,r_{wall}} = \frac{\int_0^R \tau_{wall} dr_{wall}}{R} \quad (3.39)$$

Where $\tau_{avg,r_{wall}}$ is the space averaged shear stress and R is the maximum length of the wall. The space averaged shear stress was then plotted against time, an example plot is shown in Fig. 3.29.

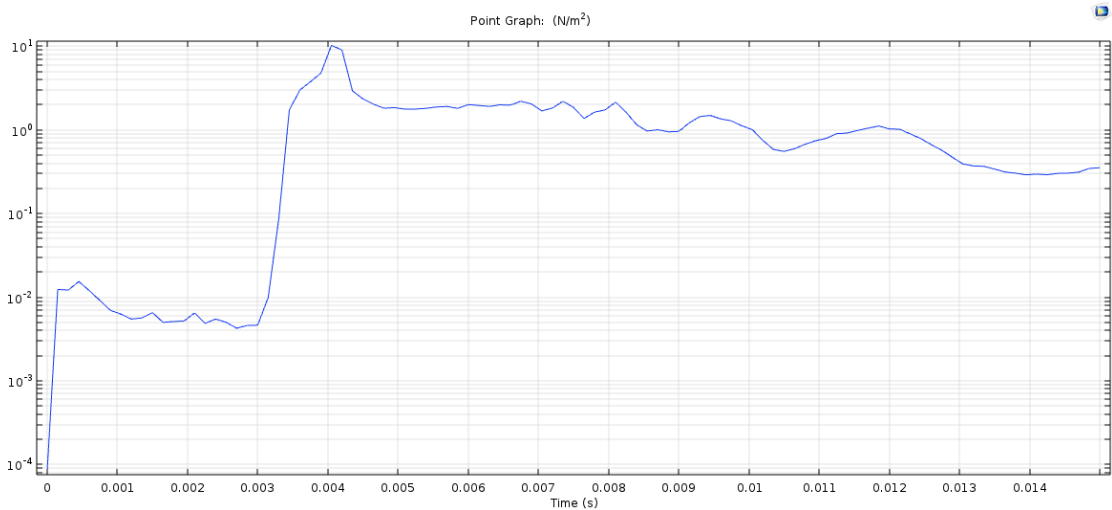


Fig. 3. 29: Space averaged shear stress vs time (0.15d film thickness).

The time averaged shear stress was then calculated by integrating the curve of Fig. 3.29, using equation 3.40.

$$\tau_{avg,t} = \frac{\int_0^t \tau_{avg,r_{wall}} dt}{t_0} \quad (3.40)$$

Where t_0 is the total simulation time, 0.015 s.

3.8.2.5 Mesh convergence

To select an appropriate mesh density and number of mesh elements to capture the droplet behaviour to a sufficient degree of accuracy, a mesh convergence study was conducted. This was important to select a mesh whereby increasing the density any further would see no improvement in the accuracy of the computation; thus the selected mesh would provide accurate results for a reduction in computational solution time. The initial, most coarse, mesh is shown in Fig. 3.30.

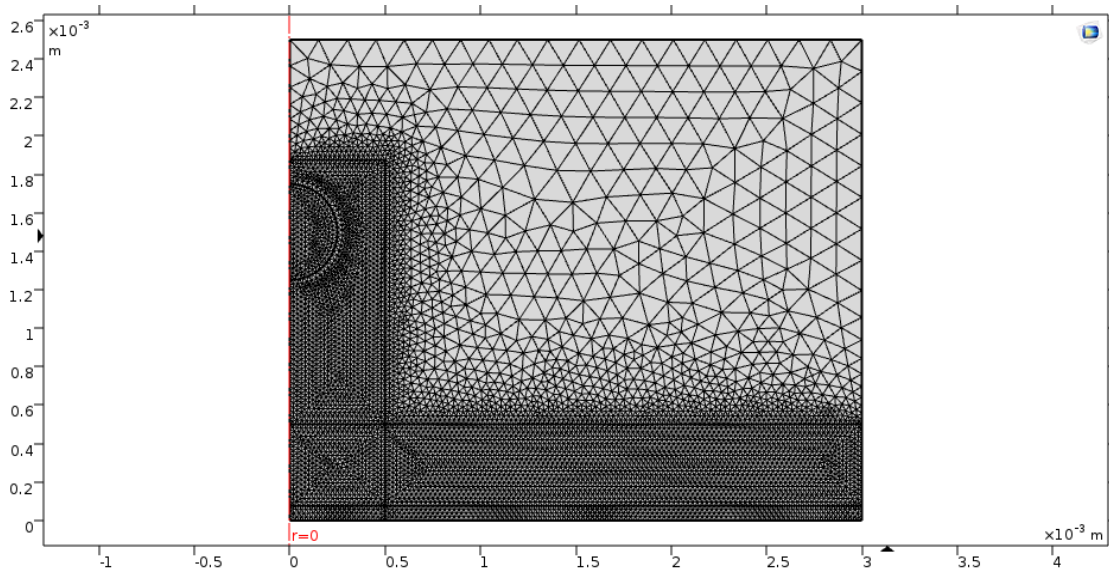


Fig. 3. 30: Mesh convergence study: coarse mesh (0.15d film thickness).

For the coarse mesh, the maximum element size in the two rectangles was set to 25 μm and a 'normal' mesh density throughout the rest of the domain selected. For the most refined density mesh, the maximum element size inside the two rectangles was set to 10 μm and the density throughout the rest of the domain set to 'fine', the mesh is shown in Fig. 3.31.

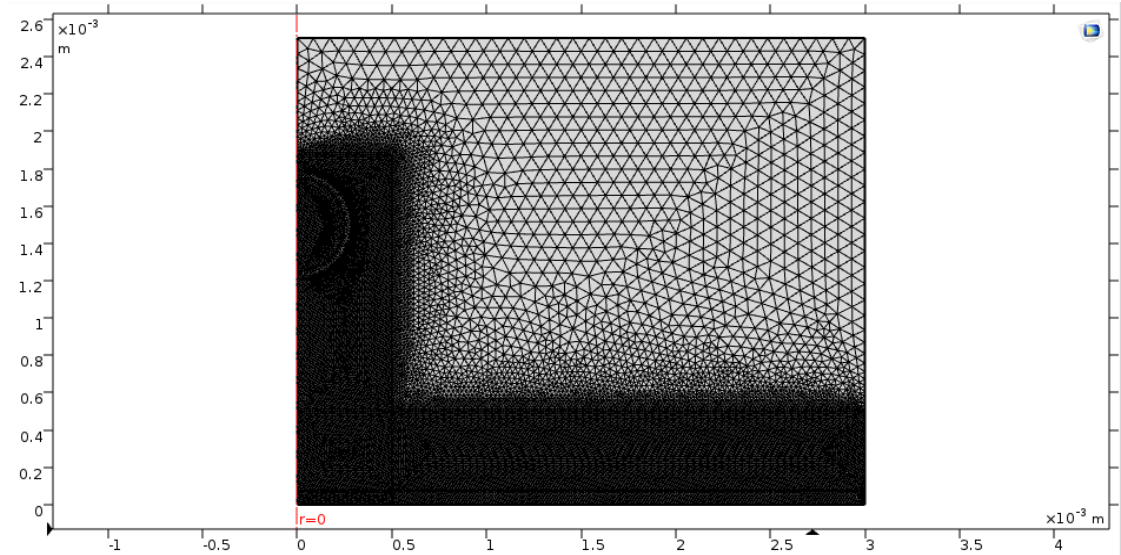


Fig. 3. 31: Mesh convergence study: most refined mesh (0.15d film thickness).

Two intermediary mesh densities between Figs. 3.30 and 3.31 were also created. Table 3.2 summarises the four mesh densities and their number of mesh elements.

Table 3. 2: Mesh convergence study: Mesh IDs and number of elements.

Mesh ID	Number of elements
1	12013
2	19218
3	32706
4	67967

For each mesh, the value of $\tau_{avg,t}$ was calculated and this was plotted against the number of elements to indicate when the value converged and which mesh could be carried forward for future simulations. The resulting mesh convergence plot is shown in Fig. 3.32.

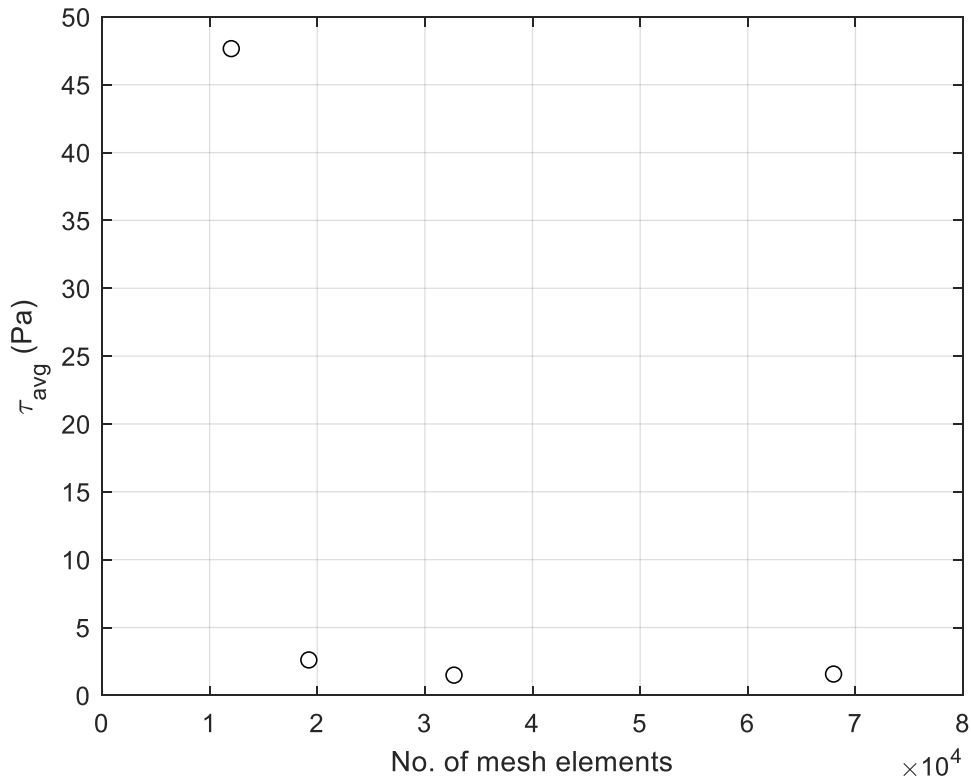


Fig. 3. 32: Mesh convergence study. Space and time averaged shear stress versus number of mesh elements.

Fig. 3.32 shows how there was a large spike in the average wall shear stress in the case of Mesh 1, the coarsest mesh under study. The value then drops off sharply and shows an asymptotic relationship with increasing mesh density. From this study Mesh 2 would be appropriate to take forward but for further reliability other parameters were considered for mesh convergence. The level set function, φ , was measured along the centre line of the domain, the path on which the droplet descends to the wall. The time taken for the droplet to reach the wall and spread such that its height was half its diameter was compared for each mesh density. This was done by finding the time that the level set function, $\varphi = 0.5$, at the position on the centre line. $\varphi = 0.5$ represents the interface between water and air, i.e. the top of the droplet, where $z = d/2$. To do this, contours of time were plotted on a graph of φ on the centre line versus height, z , on the centre line.

An example plot for Mesh 1 is shown in Fig. 3.33.

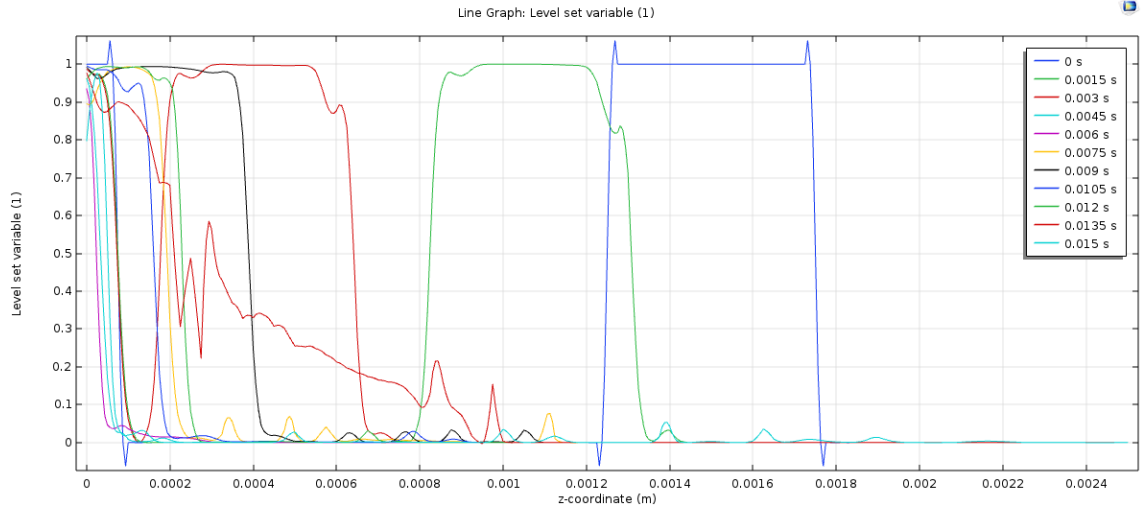


Fig. 3.33: Mesh 1: Level set function, Φ , along centre line ($r_{\text{wall}} = 0$), vs height along centre line, z (m). (Film thickness = $0.15d$).

Fig. 3.33 shows eleven contours of time, from time $t = 0$ to the final time in the simulation ($t = 0.015$ s). The very first contour, $t = 0$ (represented by the blue line), show peaks of $\Phi \sim 1$. This is where the droplet and the water film on the surface are at the start of the simulation. The film thickness for this case ($0.15d = 0.075$ mm). It can be observed that Φ decreases from the peak to 0 at this point on the x -axis. Note how the peaks and troughs at $t = 0$ dip below 0 and above 1. Since Φ is bounded by the lower and upper limits of 0 and 1 respectively, this can be attributed to numerical rounding errors. Φ then peaks again from $z = 0.00125 - 0.00175$ m, this represents the location of the droplet. The point ($z = 0.25$, $\Phi = 0.5$) was then located by zooming in on the plot of Fig. 3.33 and reading off the axes. This is shown in Fig. 3.34.

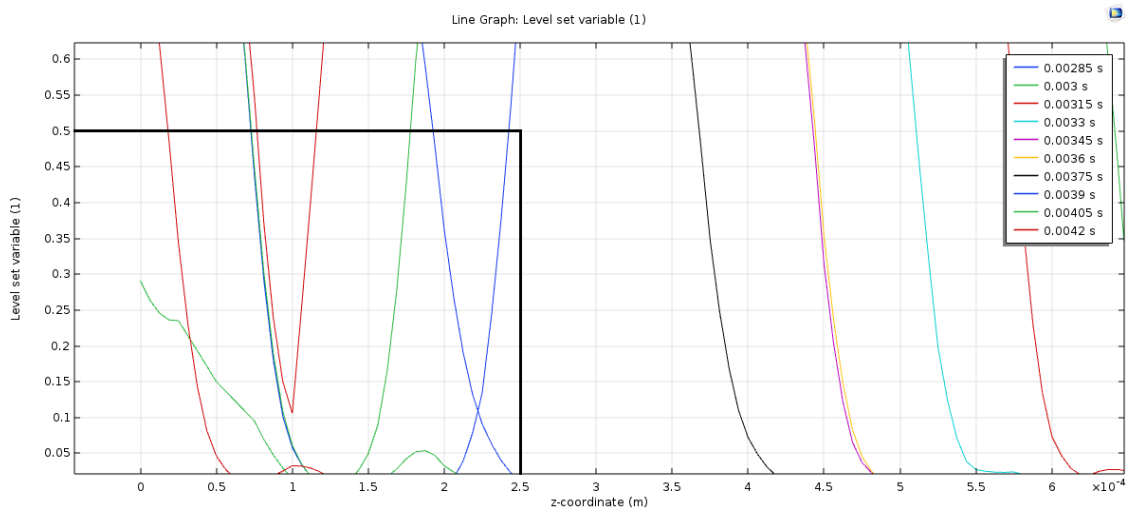


Fig. 3.34: Zoomed in image of Fig. 3.33, with the location of $z = 0.25$ mm and $\Phi = 0.5$ highlighted. (Film thickness = $0.15d$).

Once the point was located, the time contours which bound it were identified. The black contour to the right of the point ($t = 0.00375$ s) and the second blue contour to left of the point, representing the top of the droplet ($t = 0.0039$ s) were the two respective contours of interest. To estimate the time at which the point $z = 0.25$ mm and $\Phi = 0.5$ was reached, interpolation of the two contours was performed. Firstly, the horizontal distance separating the two contours was measured and then the distance from the first contour to the point was measured. The time at this point was calculated using the interpolation of 3.41.

$$t_{(0.25,0.5)} = t_1 + \frac{0.25 - z_{t_1}}{z_{t_2} - z_{t_1}} (t_2 - t_1) \quad (3.41)$$

Where $t_{(0.25, 0.5)}$ is the time representing the point where $\Phi = 0.5$ at z -coordinate 0.25 mm on the centre line of the domain, t_1 and t_2 are the lower and upper time contours bounding the point respectively and z_{t_1} and z_{t_2} are the z coordinates of the two time contours. For the case presented in Fig. 3.34, $t_{(0.25, 0.5)}$ was calculated from the interpolation of 3.41 to be 0.00385 s. The same process was repeated for the three higher mesh densities and the times were plotted against number of mesh elements, as shown in Fig. 3.35.

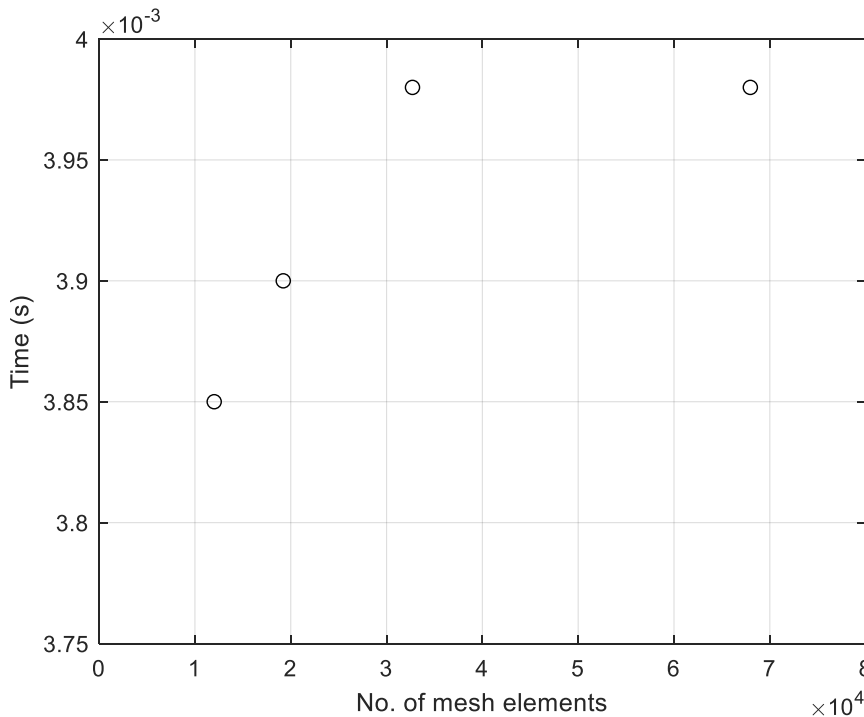
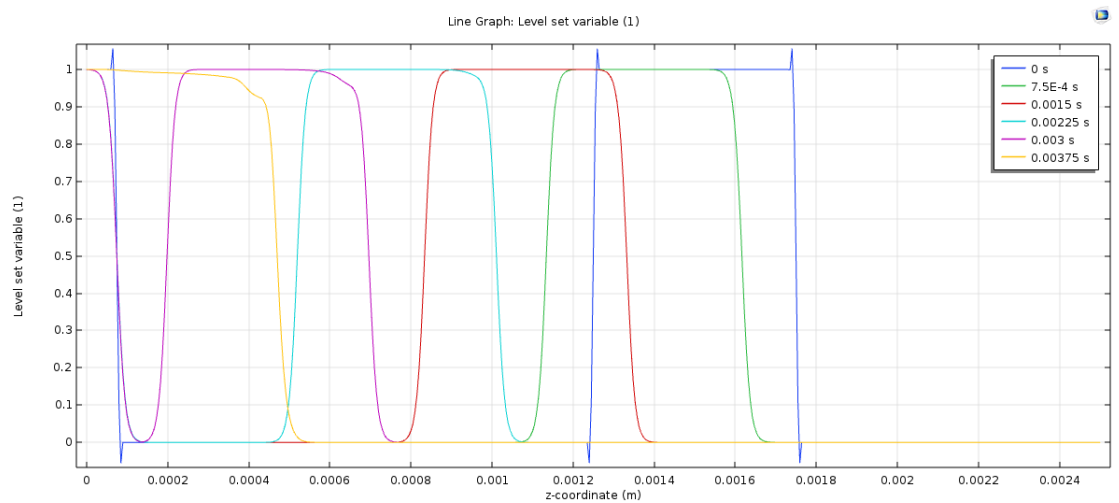
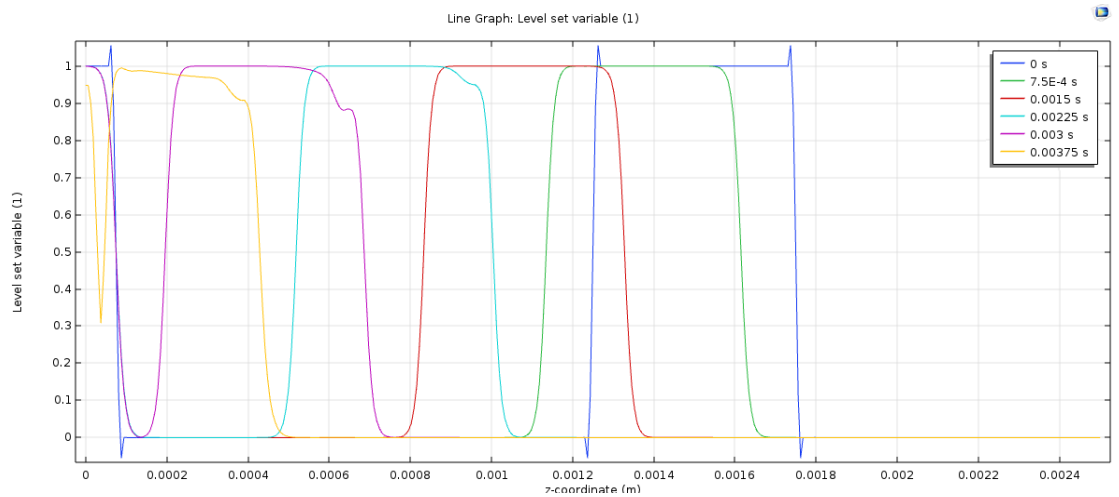
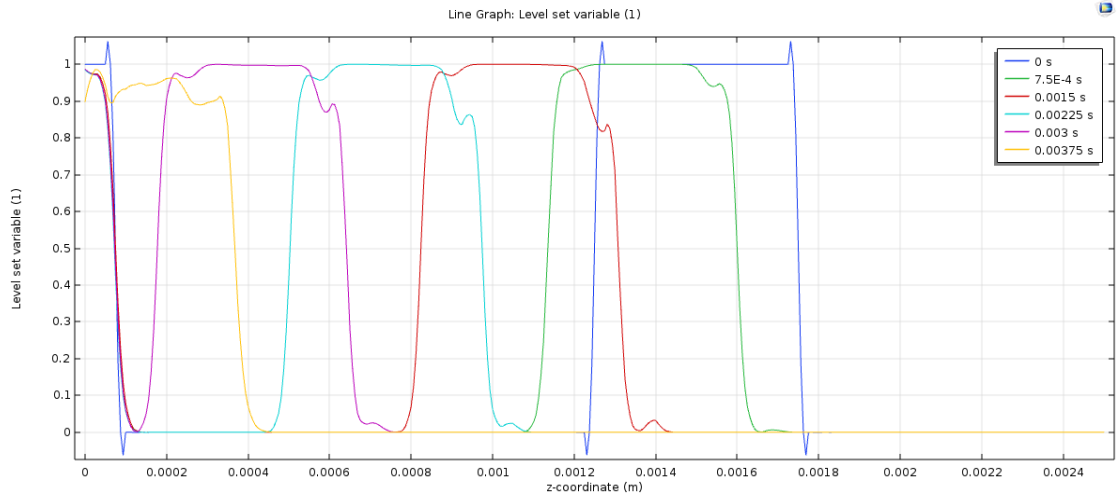


Fig. 3.35: Mesh convergence: time corresponding to $z = 0.25$ mm, $\Phi = 0.5$, versus number of mesh elements (Film thickness = 0.15d).

Fig. 3.35 shows how there is an approximately linear increase in the time taken for the top of the droplet to reach the height above the wall, $z = 0.25$ mm, as the mesh density is increased from Mesh 1 to Mesh 3. The time then reaches a plateau as the mesh

density is increased from Mesh 3 to Mesh 4, showing that the solution has converged. To view the effect on droplet behaviour as it descends towards the wall, the plot of Fig. 3.33 was repeated for each mesh density, focusing on before the droplet has impacted the film. The resulting plots are shown in Fig. 3.36.



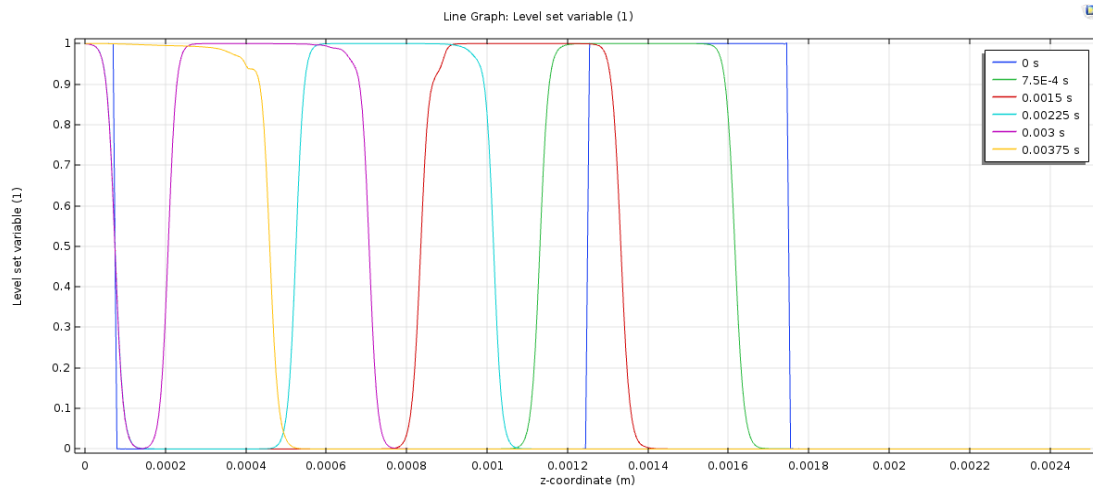


Fig. 3. 36: Φ versus z : five contours before droplet impact to measure droplet diameter for convergence. From top to bottom: Mesh 1, Mesh 2, Mesh 3, Mesh 4.

As the mesh density is increased (top to bottom in Fig. 3.36) the transition of Φ as the droplet approaches the wall becomes noticeably smoother, in the two coarsest meshes (Mesh 1 and Mesh 2) there are kinks in each contour suggesting slight deformations in the droplet geometry as it approaches the wall. The two highest density meshes (Mesh 3 and Mesh 4) show the retention of a spherical droplet. The peaks and troughs of Φ tend towards 1 and 0 respectively as the mesh density is increased, with no rounding error observed in the plot of Mesh 4. For each mesh, fluctuations in droplet diameter are negligible. One final convergence parameter was considered, the shear stress at a specific point on the wall plotted as a function of time for each mesh density. The point on the wall where $r_{\text{wall}} = 2d$ was the point of interest to capture a point downstream of the droplet impact. This is the point on the wall two droplet diameters to the right of the centre line of the domain. The plot of shear stress at this point against time is shown in Fig. 3.37 for the two highest mesh densities, Mesh 3 and Mesh 4. Note that Mesh 1 and Mesh 2 have been omitted as previous convergence studies in this chapter have shown they can be disregarded.

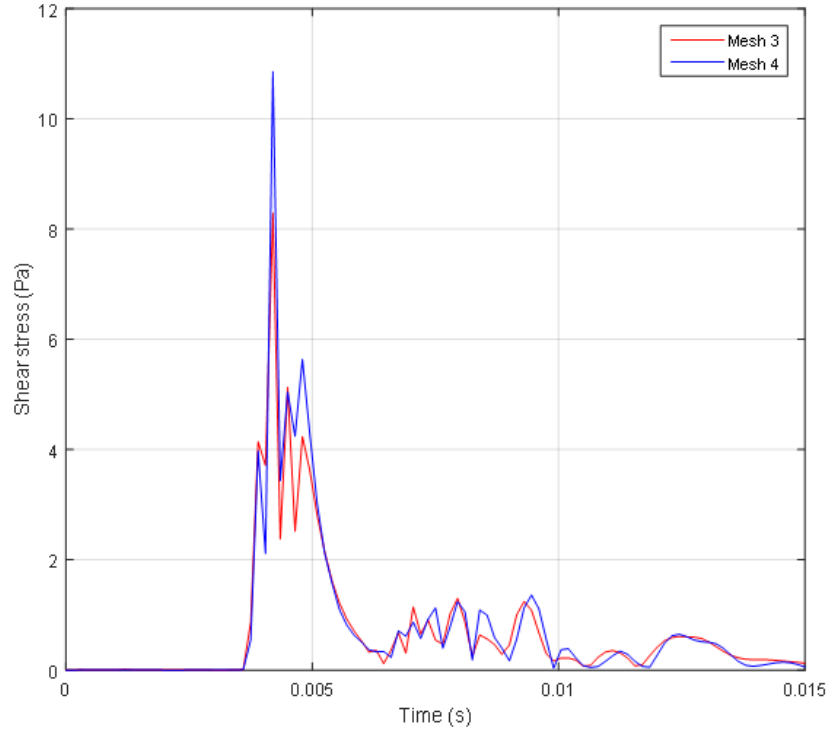


Fig. 3. 37: Shear stress at $r_{\text{wall}} = 2d$ vs time (Mesh 3 and Mesh 4).

Fig. 3.37 shows there is a good visual agreement between the two curves as they approximately overlap each other. The respective peaks for Mesh 3 and Mesh 4 occur at approximately 8 and 11 Pa respectively, a 27% disparity. Since the two curves show such an agreement and the computational solving time for Mesh 3 was considerably lower than that of Mesh 4 (~24 hours versus ~48 hours) it was decided that Mesh 3 would be used for all subsequent simulations. The other convergence parameters considered, namely the time taken for the droplet to reach a specific height and the space and time averaged shear stress on the wall, also showed a good agreement between the two meshes. The expensive time consumption of Mesh 4 justified its exclusion in future simulations.

3.9 Computational jet simulations

In addition to the computational work conducted on droplet impingement, it was decided to conduct a computational study of an impinging jet. Predictions of shear stress on the wall generated in COMSOL could then be compared to existing models from the literature as a way of validating the computational methods. This study could also then be used to support experimental work and help understand the cleaning mechanisms observed in more detail.

3.9.1 Impinging jet model setup

For the impinging jet case the model was setup as a single-phase stationary simulation in COMSOL, which is used for steady state cases. Unlike the droplet case presented earlier which required a transient simulation, since the droplet's shape and velocity changed over time, the jet remains static and the shear stress profile on the wall does not vary with time so it could be modelled as steady state. This significantly simplifies the simulation and requires far less solution time than the transient cases. The simplification of modelling a single phase and omitting air in the domain also significantly reduced solution time as the interface between the two phases could be ignored. This was of little importance to the shear stress exerted on the wall, so it was fair to ignore. Similar to the droplet case, the domain was made 2D axisymmetric.

To begin with the jet was drawn out in COMSOL using the diameter of that used in the experiments, 4 mm. The half width of this was drawn using the axis of symmetry on the centre line of the domain. Beyond the point of impingement, as was discussed in the literature, the jet forms a thin radial film on the surface (RFZ). To accurately predict the shear behaviour on the wall, it was important to draw the profile of this film in COMSOL such that it represented the film observed for a jet of the same flow conditions. For each jet Reynolds number, Re_{jet} , the profile of the film in the RFZ could be accurately drawn in COMSOL using the expressions of Bhagat and Wilson (2016) given by equations 2.5, 2.6 and 2.7 in Chapter 2. Subsequently the wall shear stress distribution on the wall could be solved in COMSOL. Fig. 3.38 shows the domain drawn in COMSOL for the 1 lmin^{-1} jet. Note that each domain was redrawn to capture the correct film profile for each jet Reynolds number.

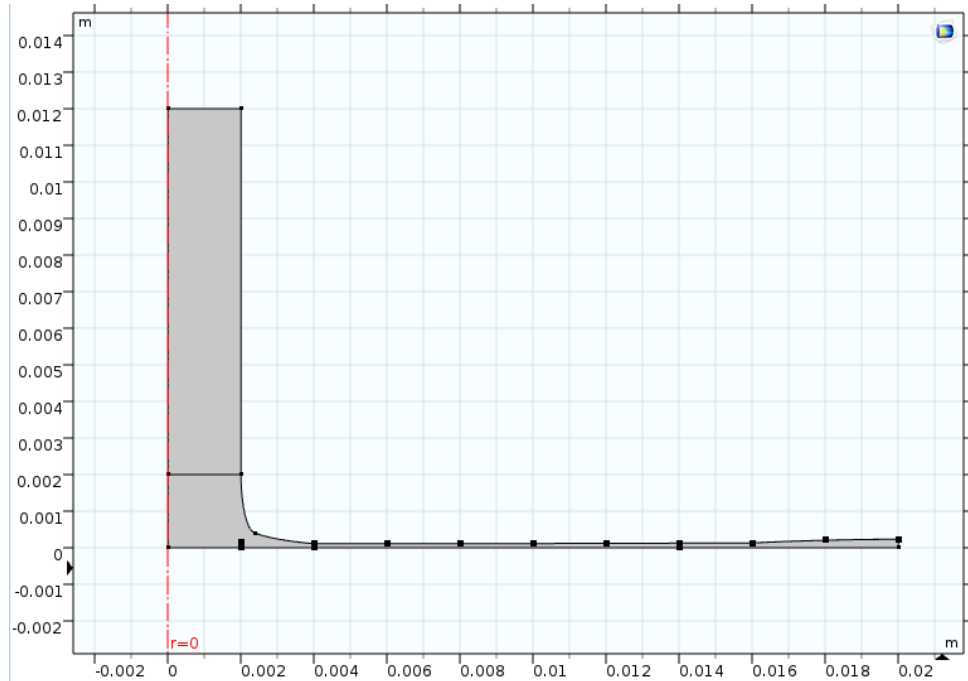


Fig. 3. 38: Single phase domain drawn in COMSOL, using coordinates of the film in the RFZ obtained from the equations of Bhagat and Wilson (2016).

The top of the jet was assigned a velocity inlet boundary, which in this case the normal inflow velocity was set to 1.33 ms^{-1} , the velocity of the 1 lmin^{-1} jet. The left-hand boundary was given a line of axial symmetry, such that the domain was revolved 360° around this axis. The bottom boundary was assigned a no-slip wall and the rest of the liquid boundary was assigned a slip wall. Given this was a steady-state simulation the solution time was considerably less than a transient simulation (<10 mins), as such a very dense mesh was used with the domain being populated with cells of a maximum size of $10 \text{ }\mu\text{m}$. A mesh convergence study was conducted and decreasing the maximum cell size beyond this had a negligible effect on the shear stress values predicted. Each flow rate used in the experiments, 1 lmin^{-1} , 2.5 lmin^{-1} and 4 lmin^{-1} , corresponded to respective Re_{jet} values of 5305, 13263 and 21221. As such each jet was turbulent and so a turbulence model was applied to COMSOL. In each case a k - ϵ turbulence model was used as this was found to give the best agreement with the predictions obtained from the literature. The k - ϵ is a two-equation model commonly used in CFD modelling of turbulent flows, first introduced by Launder and Spalding (1974). Turbulence in this model is described by two transport equations; the first transported variable is the turbulent kinetic energy (k) and the second is the dissipation rate of turbulent kinetic energy (ϵ). The two equations for k and ϵ can be written as 3.41 and 3.42 respectively.

$$\rho(\mathbf{u} \cdot \nabla)k = \nabla \cdot \left[\left(\mu + \frac{\mu_T}{\sigma_k} \right) \nabla k \right] + P_k - \rho \varepsilon \quad (3.41)$$

$$\rho(\mathbf{u} \cdot \nabla)\varepsilon = \nabla \cdot \left[\left(\mu + \frac{\mu_T}{\sigma_\varepsilon} \right) \nabla \varepsilon \right] + C_{\varepsilon 1} \frac{\varepsilon}{k} P_k - C_{\varepsilon 2} \rho \frac{\varepsilon}{k} \quad (3.42)$$

Where μ_T is the turbulent viscosity, given by $\rho C_\mu k^2/\varepsilon$, P_k is the turbulent kinetic energy production and $C_{\varepsilon 1}$, $C_{\varepsilon 2}$, σ_ε , σ_k and C_μ are all constants in the model. Respectively these are 1.44, 1.92, 1.3, 1 and 0.09. These were fine tuned by Launder and Spalding (1974) when developing the model by studying various turbulent flow regimes. Note that for the computational study of jets these constants were not altered.

3.10 Summary

This chapter has outlined the methodology in completing the research; both computationally in the analysis of the flow distribution through the wash racks and the droplet simulations on COMSOL to study the mechanisms involved in spray cleaning, and experimentally in the design of a test rig for both the jet and spray experiments. The materials used for cleaning were also discussed and characterised. The next chapter will present the results obtained experimentally using the liquid jet.

Chapter 4

Jet Results

4.1 Introduction

This chapter presents the results obtained using a jet of water to remove a soil layer in the absence of surfactant. The cleaning performance of the jet was of primary interest and an energy framework was adopted to gauge the efficiency of each process under a range of flow conditions. Cleaning performance was measured by the area of WSP transported by the jet. The soil removal mechanisms were also under study. Two cases were studied, (i) a horizontal jet impinging on to a vertical Perspex wall coated with WSP and (ii) a vertically aligned jet cleaning a pipe filled with a gel. For the case of the horizontal jet, three variables were studied; flow rate, WSP thickness and water temperature. For the internal removal of soil from a vertical pipe, the experimental variables were the initial state of the gel and the alignment of the jet relative to the pipe with flow rate held constant. The gel was prepared under a range of conditions to represent different histories; fresh, dried for 5 days and baked at 85°C for 45 minutes. Two alignments were studied, perfectly aligned normal to the centre of the pipe and misaligned by an angular displacement of 2°.

4.2 Horizontal jet impingement

For the horizontal jet study, a coherent jet was set up to impinge perpendicularly on to a vertical Perspex wall. The wall was coated with WSP at three different thicknesses; 0.19, 0.95 and 1.9 mm. Three temperatures were under study; 20, 40 and 60 °C and three flow rates; 1, 2.5 and 4 lmin⁻¹. A study of standoff distance of the jet nozzle from the wall was also conducted. Cleaning performance was measured by the area of material transported by the jet, which was measured using an image processing software (as was discussed in 3.6). Each process was filmed using a camera positioned behind the Perspex wall.

4.2.1 Visualisation of soil removal

The following section presents time lapse images of each cleaning process conducted with 20 °C water.

4.2.1.1 High flow, thin WSP layer

A time lapse of the cleaning process recorded from the camera placed behind the Perspex wall is shown in Fig. 4.1, for the 4 lmin^{-1} jet on a 0.19 mm WSP thickness, at $20 \text{ }^\circ\text{C}$.

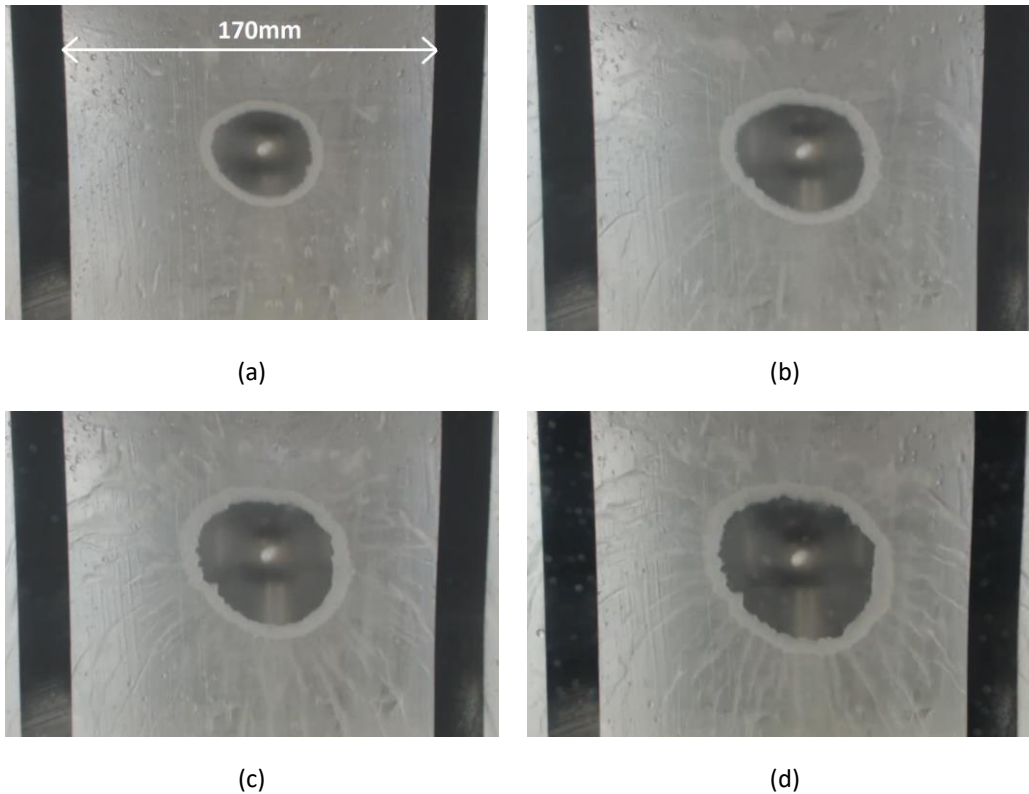


Fig. 4. 1: Time lapse removal for 4 lmin^{-1} jet, 0.19 mm WSP thickness. Water temperature $20 \text{ }^\circ\text{C}$ (a) 3 s (b) 10s (c) 30 s (d) 300 s.

Fig. 4.1 shows how as the jet impinges in the centre of the surface, the WSP is pushed radially outward forming a clean zone that grows with time. It is clear from the time lapse photographs that the rate of change of the clean area is much higher at the start of the process and decreases with time. It can also be observed that as the process develops the ridge of WSP on the perimeter of the clean zone increases in thickness both normal and parallel to the wall. Parallel to the wall the thickness of the ridge approximately doubles in size between 3 s and 300 s of cleaning, from 5 mm to 11 mm. This is captured qualitatively from 4.2 onwards. Streaks of fluid can be observed outside the ridge where fluid from the radial flow zone (RFZ) has flown over the ridge and on to the surrounding film.

4.2.1.2 Medium flow, thin WSP layer

Fig. 4.2 shows a time lapse of the soil removal for the same WSP thickness at $20 \text{ }^\circ\text{C}$ (0.19 mm) for a 2.5 lmin^{-1} flow rate of water.

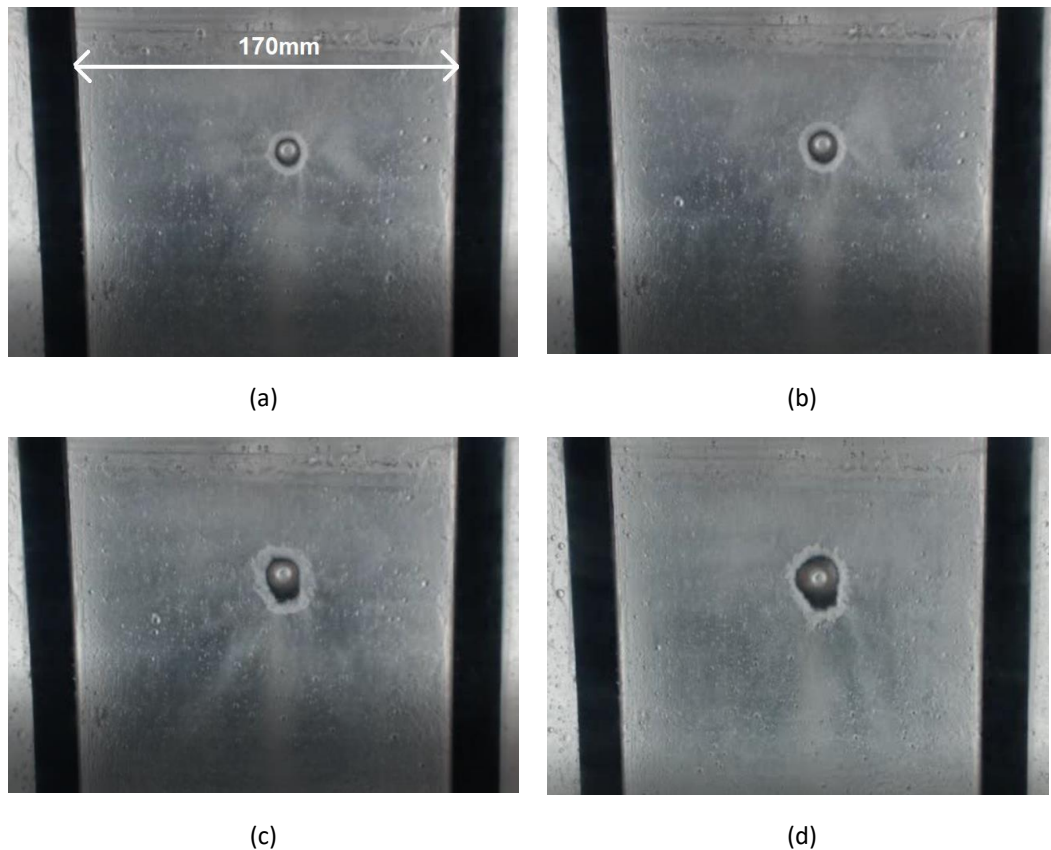


Fig. 4. 2: Time lapse removal for 2.5 lmin^{-1} jet, 0.19 mm WSP thickness, water temperature $20 \text{ }^{\circ}\text{C}$ (a) 3 s (b) 10s (c) 30 s (d) 300 s.

In this case, for a lower flow rate, the removal of WSP is far less rapid in the first 300 s of cleaning when comparing to Fig. 4.1. Due to the lack of material removed in this time, there is no discernible increase in the size of the ridge. The shape of the cleaned area also becomes less circular than the areas of Fig. 4.1. This could be due to errors in the experiment, for example when looking at Fig. 4.2d the area is slightly elongated below the impingement point of the jet. Any deviation from a true horizontal line which causes the jet to impinge at an angle could cause the RFZ to become more elongated, like that presented in Fig. 2.3. This would cause the clean area to be elongated as it is in Fig. 4.2d. Another possible explanation for this phenomenon is any non-uniformity in the application of the WSP to the Perspex which could cause the thickness on parts of the surface to be higher than others. However, to the naked eye the WSP looked to be evenly applied throughout and any fluctuations in thickness were sufficiently small to assume that they would have no discernible effect on the shape of the area cleaned, certainly none as exaggerated as in Fig. 4.2. The complex nature of WSP, consisting of a blend of oil and wax, could mean that the viscosity in certain areas was higher as the blend was not a perfectly uniform consistency throughout. These areas would prove harder to clean and thus could be plausible cause of the cleaned area showing a peculiar shape, particularly at lower flow rates.

4.2.1.3 Low flow, thin WSP layer

Meanwhile the clean area after 300 s for a 1 lmin^{-1} jet on a 0.19 mm WSP thickness is shown in Fig. 4.3.

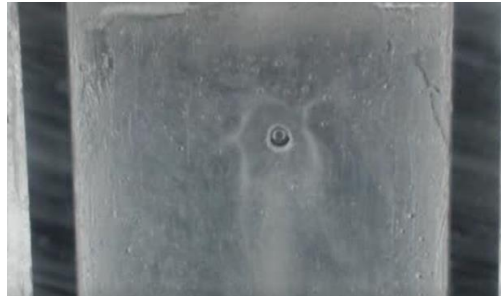


Fig. 4. 3: 300 s cleaning, 1 lmin^{-1} jet, 0.19 mm WSP thickness, water temperature $20 \text{ }^{\circ}\text{C}$.

After 300 s the material removed is only marginally greater than that of the area of the impinging jet on the surface. The shear stress exerted on the surface by the liquid in the RFZ is inadequate for rapid removal of the WSP.

4.2.1.4 High flow, medium WSP layer

Increasing the WSP thickness to 0.95 mm, the time lapse of soil removal for a 4 lmin^{-1} jet is shown in Fig. 5.4.

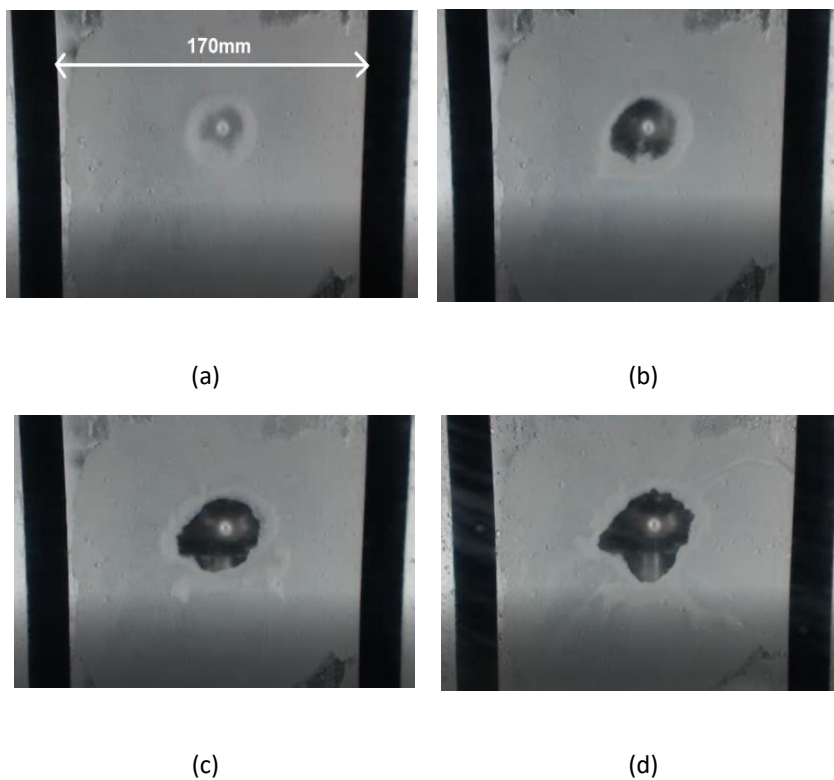


Fig. 4. 4: Time lapse removal for 4 lmin^{-1} jet, 0.95 mm WSP thickness, water temperature $20 \text{ }^{\circ}\text{C}$ (a) 3 s (b) 10s (c) 30 s (d) 300 s.

The increased thickness of WSP causes a delay in the initial cohesive removal of the WSP and the adhesive removal is also slowed down due to the increased shear required to displace the greater volume of material in the ridge. After 300 s it can be observed that large slugs of WSP detach from the ridge due to the thickness normal to the wall increasing to such that the stability of the structure of the ridge is compromised. When the thickness of the ridge reaches a certain height the peaks of the ridge are vulnerable to detaching from the surface under gravity. The shape of the clean area is also not a uniform circle as it was in the previous case of the 0.19 mm film. The causes of this were discussed for Fig. 4.2 and the same apply in this case.

4.2.1.5 Medium flow, medium WSP layer

For the same thickness and a 2.5 lmin^{-1} jet the time lapse of removal is shown in Fig. 4.5.

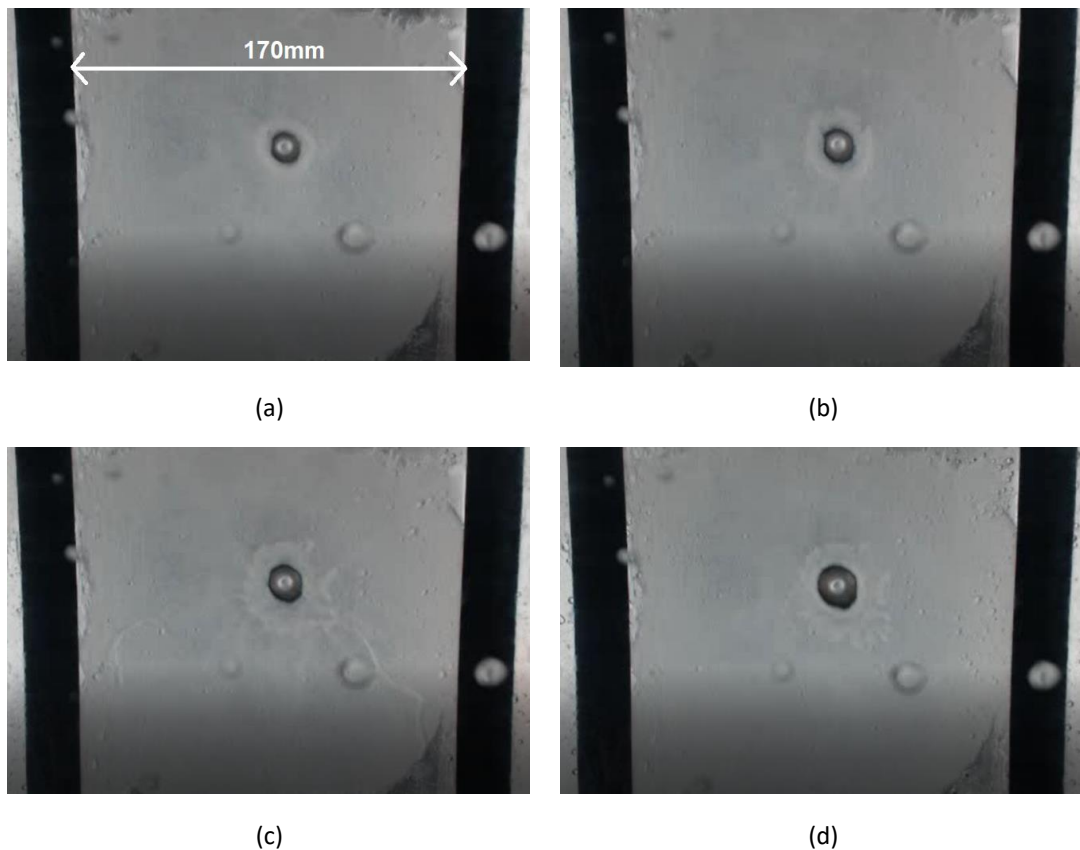


Fig. 4. 5: Time lapse removal for 2.5 lmin^{-1} jet, 0.95 mm WSP thickness, water temperature $20 \text{ }^{\circ}\text{C}$ (a) 3 s (b) 10s (c) 30 s (d) 300 s.

The restriction in clean area growth at a higher film thickness is exaggerated for the lower flow rate of 2.5 lmin^{-1} as shown in Fig. 4.5.

4.2.1.6 Low flow, medium WSP layer

When the flow rate is further decreased to 1 lmin^{-1} , the clean area after 300 s is shown in Fig 4.6.



Fig. 4. 6: 300 s cleaning, 1 lmin^{-1} jet, 0.95 mm WSP thickness, water temperature $20 \text{ }^{\circ}\text{C}$.

The clean area is restricted to just 52 mm^2 after 300 s of cleaning using the 1 lmin^{-1} jet. The effect of increasing the WSP thickness becomes more discernible at the lower flow rates.

4.2.1.7 Thick WSP layer

Increasing further still to 1.9 mm, the time lapses of soil removal for the 4 lmin^{-1} , 2.5 lmin^{-1} and 1 lmin^{-1} jets are shown in Fig. 4.7, 4.8 and 4.9. The cleaning performance is reduced at the higher WSP thicknesses due to the increased volume of material having to be displaced by the impinging jet. The clean areas become noticeably smaller for the lower flow rates. At 4 lmin^{-1} the area is slightly decreased, this will be discussed in further detail in 4.2.5, and the irregular shape of the clean area is observed with slugs of WSP detaching from the ridge similar to that shown in Fig. 4.4. At the two lower flow rates, 2.5 lmin^{-1} and 1 lmin^{-1} , the clean areas after 300 s are only marginally greater than that of the impinging jet's footprint on the surface, the lower shear stress in the RFZ causes a significant decrease in the rate of adhesive removal of the WSP layer.

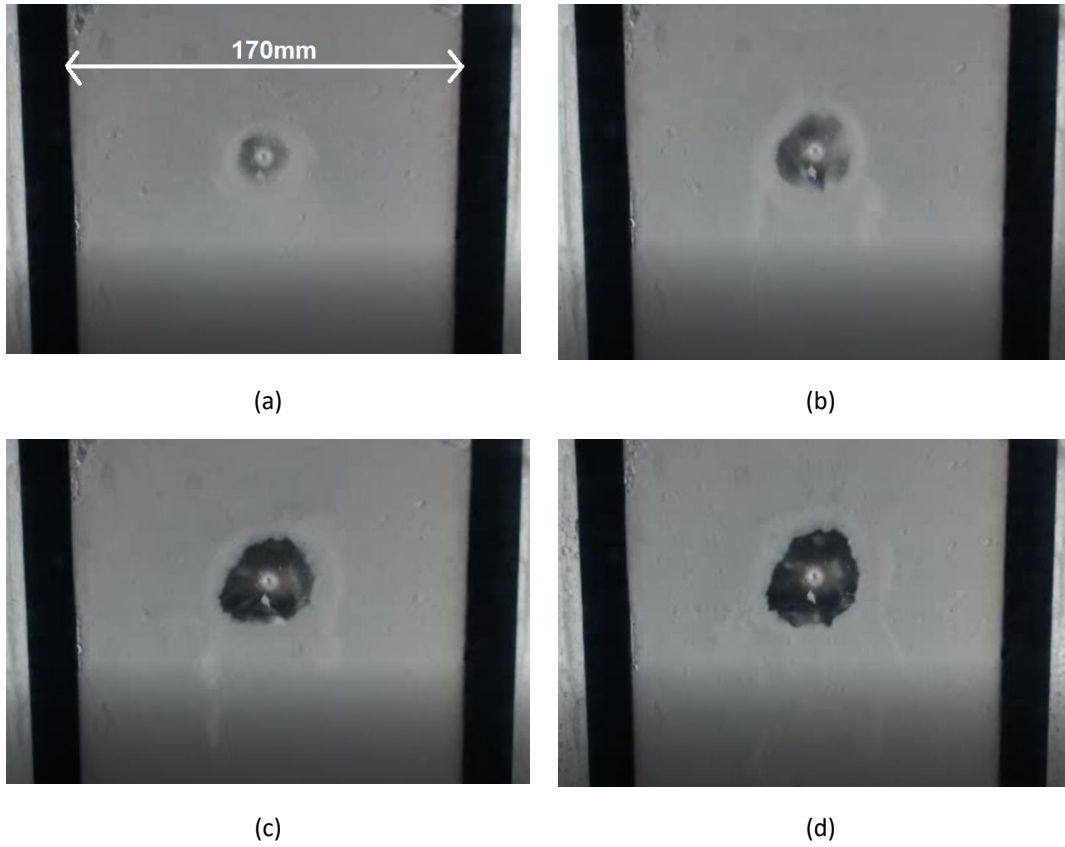


Fig. 4. 7: Time lapse removal for 4 lmin^{-1} jet and 1.9 mm WSP thickness (a) 3 s (b) 10s (c) 30 s (d) 300 s, water temperature 20°C .

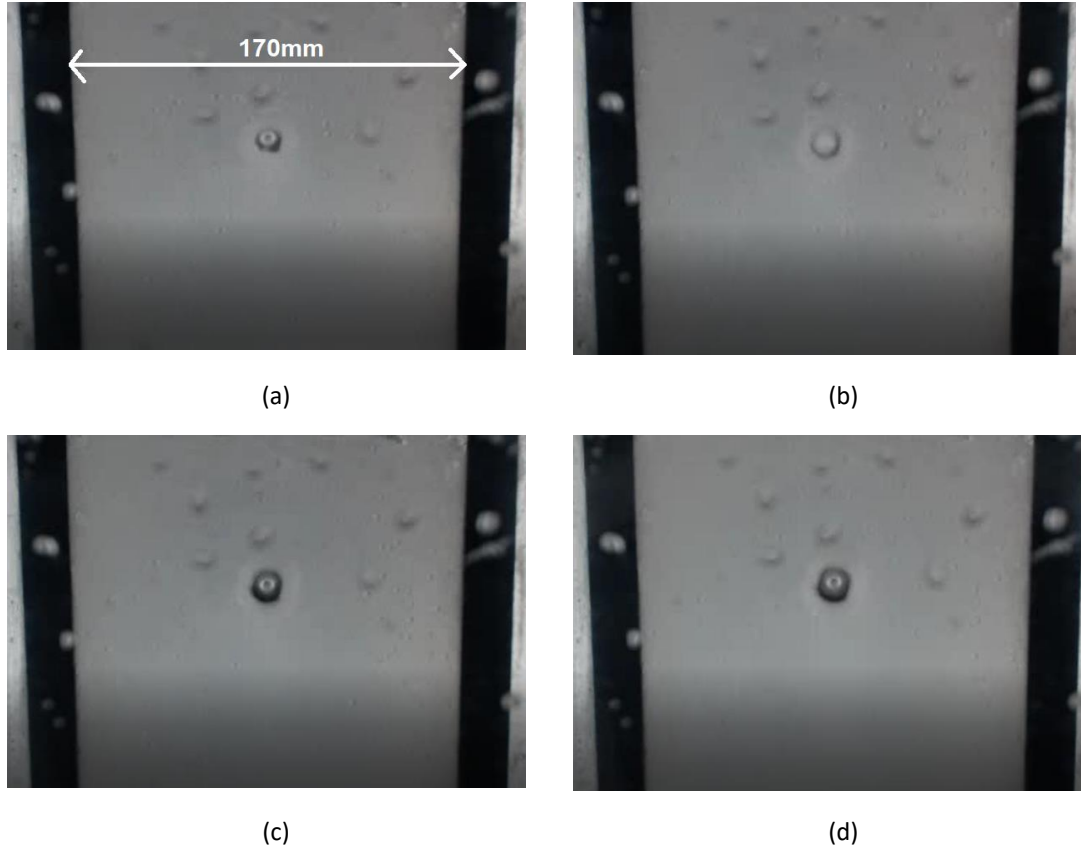


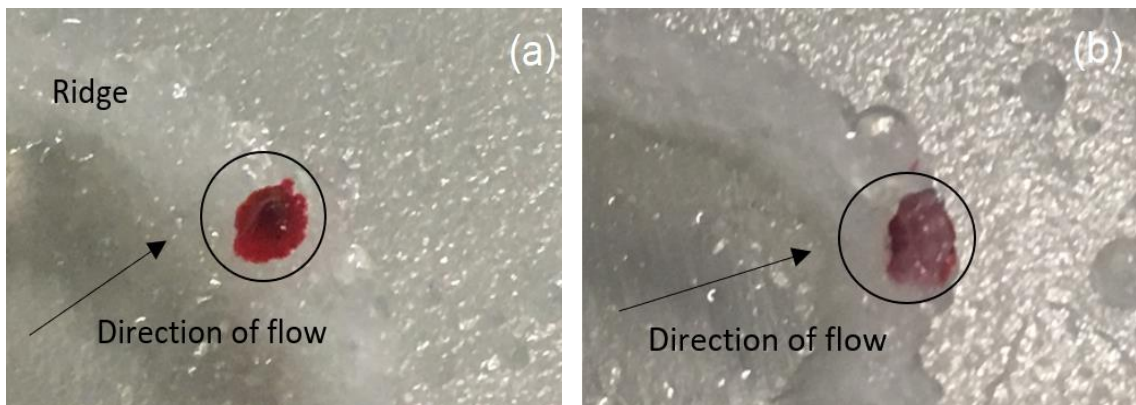
Fig. 4. 8: Time lapse removal for 2.5 lmin^{-1} jet and 1.9 mm WSP thickness (a) 3 s (b) 10s (c) 30 s (d) 300 s, water temperature 20°C .



Fig. 4. 9: 300 s cleaning, 1 lmin^{-1} jet, 1.9 mm WSP thickness, water temperature 20°C .

4.2.2 Soil removal mechanism study

To elucidate the soil removal mechanism, a study was conducted whereby an experiment was run for approximately 1 minute, before being paused, and then the base of the ridge dyed with an oil soluble dye. The experiment was then continued for two more minutes to see where the dye had been displaced to, thus showing its path and the mechanism of its removal. This is shown in Fig. 4.10a and 4.10b.



It can be observed that the dye has been pushed to the back of the ridge and submerged under the ridge by the WSP. This suggests a rolling mechanism takes place, where the WSP at the edge closest to the radiating water film is pushed up and over to the back of the ridge. This process happens continuously, submerging the dye – shown schematically in Fig. 4.10c.

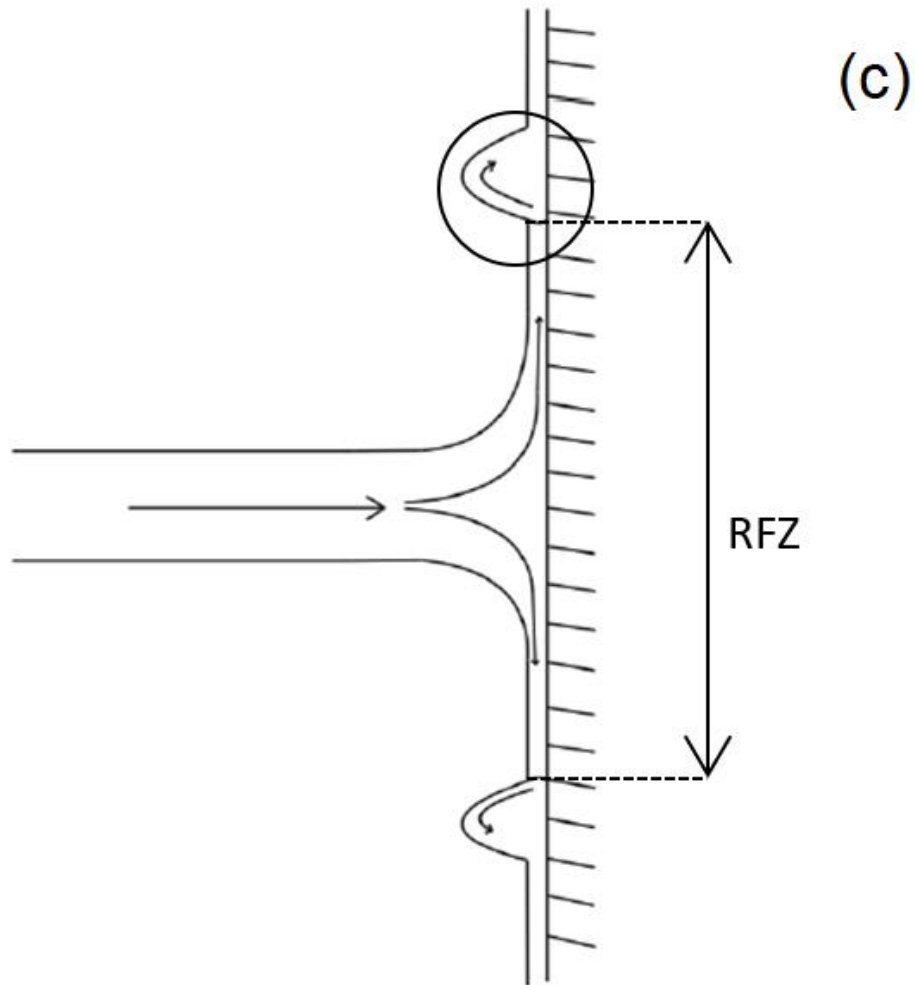


Fig. 4. 10: a) WSP ridge dye @ $t = 1$ min. b) Position of dye @ $t = 3$ min. c) Adhesive soil removal and build-up of the ridge of WSP on the perimeter of the clean area.

It can be observed that the dye has been pushed to the back of the ridge and submerged under the ridge by the WSP. This suggests a rolling mechanism takes place, where the WSP at the edge closest to the radiating water film is pushed up and over to the back of the ridge. This process happens continuously, submerging the dye – shown schematically in Fig. 4.10. The mechanism is continuous as the ridge builds in size and acts as a resistance to the radial flow produced by the jet which eventually restricts the final clean area, reducing the area theoretically derived on a clean surface by Wilson et al. (2014). Since the shear stresses exerted on the layer decrease with increasing distance from the impingement point, they are no longer large enough to overcome the adhesive force between the layer and the surface. At this point no adhesive removal can occur and the growth of the clean area reaches a standstill. A mass balance before and after the cleaning process revealed that only 17% of material had been removed from the surface, showing that most of the WSP is simply transported to the ridge. For material to be fully removed additional heat and/or surfactant need to be added to the system.

4.2.3 Effect of standoff distance

The first variable under consideration was the standoff distance of the jet nozzle, D , to the vertical Perspex wall being cleaned. Observations of typical industrial wash racks identified the typical size of the components that are loaded on to them and estimates of the standoff distance between the nozzles and the surfaces being cleaned were made. The parts loaded on to the racks varied from small diameter pipes to larger components such as filling machine pressurised header tanks. Typical standoff distances varied between approximately 50 mm to 200 mm. A study was conducted whereby the standoff distance between the jet nozzle and the wall was increased from 50 mm to 200 mm in increments of 50 mm, to gauge the importance of standoff distance on cleaning performance within this range. Three experiments were run for each flow rate and an average value of clean area plotted. For a 4 lmin^{-1} jet and a 0.19 mm WSP thickness, the results are shown in Fig. 4.11.

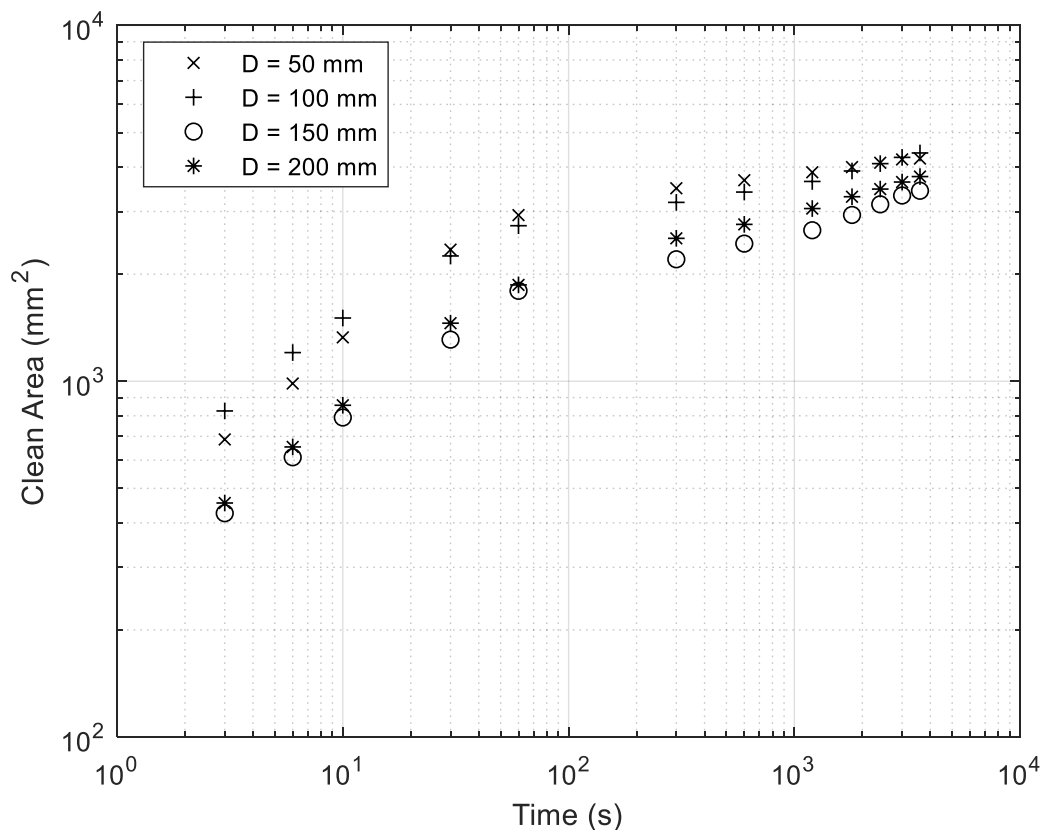


Fig. 4. 11: Clean area versus time for each standoff distance, D (0.19 mm WSP thickness, 4 lmin^{-1} jet, water temperature 20°C).

Fig. 4.11 shows there is no direct correlation between the standoff distance of the nozzle and the cleaning performance of the jet. Whilst the two jets closest to the wall ($D = 50, 100 \text{ mm}$) exhibit a higher clean area in the first 100 s of cleaning, all the jets begin to

converge as the cleaning process continues and tends to the long-time of one hour. For each clean area, the average diameter of the area assuming a uniform circle, d_{avg} , is introduced. It is the 100 mm jet that yields the highest final clean area of 4382 mm² ($d_{avg} = 75$ mm) and the lowest clean area is that of the 150 mm jet at 3332 mm² ($d_{avg} = 65$ mm), a 32% difference encompassing all four jets. In the range studied, 50 – 200 mm, the jet remained coherent and there was no breakup or droop observed (e.g. Fig. 2.4). As such the jet footprint on the surface was relatively independent of the standoff distance of the nozzle, thus the independence of cleaning performance. Since there was no direct correlation, the standoff distance was held constant for all further experiments and the midpoint of those observed on the wash racks was used, 125mm.

4.2.4 Effect of flow rate

Three flow rates were used which were in the typical range of those delivered to the nozzles on Rack 1. These were 4 lmin⁻¹, 2.5 lmin⁻¹ and 1 lmin⁻¹. Each flow rate was used to clean WSP thicknesses of 0.19 mm, 0.95 mm and 1.9 mm. The resulting plot of clean area versus time for each flow rate on a 0.19 mm WSP thickness is shown in Fig. 4.12.

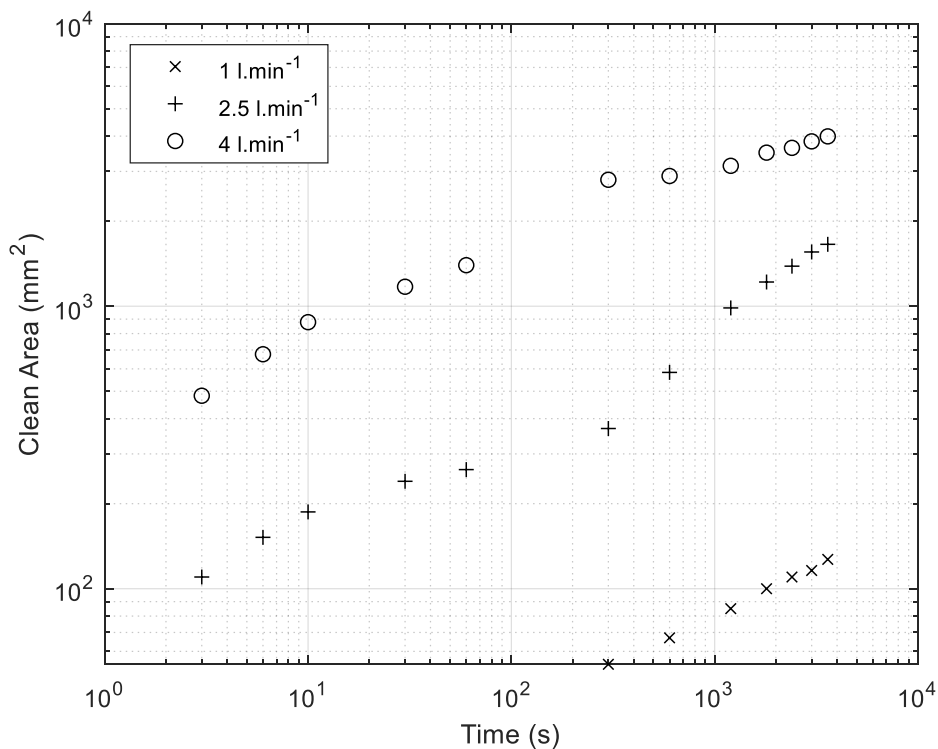


Fig. 4. 12: Clean Area versus Time for each flow rate (0.19 mm WSP thickness, water temperature 20 °C).

For each jet the soil is first removed cohesively as the jet has to break down the layer by the force exerted normal to the surface. The schematic of a jet impinging horizontally on a vertical surface is shown in Fig. 4.13.

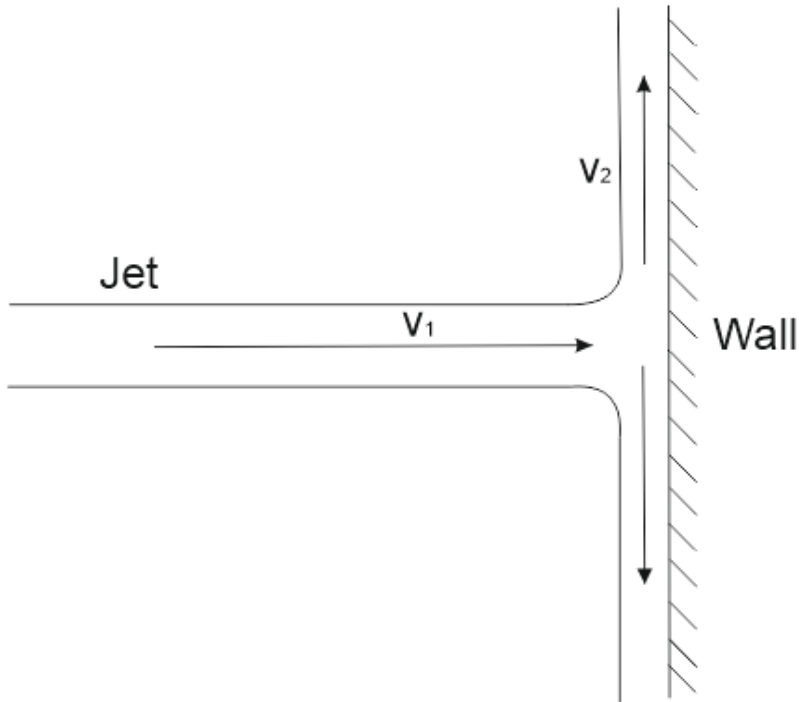


Fig. 4. 13: Horizontal jet impingement on vertical wall schematic.

The horizontal jet impinges with velocity v_1 and is turned through 90° upon hitting the wall and moves radially outwards with velocity v_2 . The impingement force can be derived by calculating the rate of change of momentum of the jet, given by equation 4.1.

$$F_x = \frac{dp}{dt} = \frac{p_1 - p_2}{dt} \quad (4.1)$$

Where F_x is the horizontal jet impingement force, p_1 is the initial jet momentum and p_2 is the final jet momentum. Since momentum is the product of mass and velocity, 4.1 can be rewritten as 4.2.

$$F_x = \frac{dm}{dt} (v_1 - v_2) \quad (4.2)$$

Where dm/dt is the mass flow rate (kgm^{-3}), which is the product of volumetric flow rate and fluid density. As there is a stagnation point where the jet impinges on the wall, the horizontal component of v_2 is zero. 4.2 can then be rewritten as 4.3.

$$F_x = Q\rho v_1 \quad (4.3)$$

Substituting $v_1 = Q/A$, where A is the cross-sectional area of the impinging jet, 4.3 can be written as 4.4.

$$F_x = \frac{Q^2 \rho}{A} \quad (4.4)$$

The area of the impinging jet was calculated to be $1.257 \times 10^{-5} \text{ m}^2$. Substituting this and the fluid density, ρ (1000 kgm^{-3}), the impingement force for each jet could be calculated. The values are summarised in Table 4.1.

Table 4.1: Jet flow rate and corresponding impingement force.

Q (lmin ⁻¹)	Impingement Force (N)
1	0.022
2.5	0.138
4	0.354

Table 4.1 can be related to the data presented in section 3.3, where the penetration force required for each WSP thickness was measured. To recall; for the 0.19, 0.95 and 1.9 mm thicknesses the impingement forces required to reach the underlying surface were 0.16, 0.74 and 0.93 N respectively. Relating to Table 4.1 the only jet that satisfies any of these criteria is the 4 lmin⁻¹ jet and that is only that required to penetrate the 0.19 mm layer. This is reflected in the cleaning performance as 482 mm² ($d_{\text{avg}} = 25 \text{ mm}$) of WSP is removed in 3 s. The jet instantaneously breaks down the 0.19 mm layer cohesively and adhesive removal occurs. The cohesive removal also occurs rapidly with the 2.5 lmin⁻¹ jet, since 110 mm² ($d_{\text{avg}} = 12 \text{ mm}$) is removed after 3 s. The gap between the impingement force of the jet and that required to penetrate the layer is bridged by soaking of the layer occurring, contact with the jet changes the microstructure of the WSP and promotes its removal. The removal takes considerably longer for the 1 lmin⁻¹ jet due to the impingement force being small and much less than that required to penetrate each later. In fact, for the 0.19 mm layer there is 300 s of cleaning before any discernible clean area is produced. Once the jet in each case has reached the surface a liquid film is created that moves radially outwards and the removal mechanism becomes adhesive, where the soil is rolled over the surrounding material via the mechanism shown in Fig. 4.10c. The 4 lmin⁻¹ jet shows a very sharp increase in clean area during the first minute of cleaning. Close to the impingement point the shear stress exerted on the wall is at a maximum, consequently the adhesive removal occurs very rapidly. The 2.5 lmin⁻¹ jet shows a similar behaviour, but with a much more gradual rate of removal over the remainder of the process and not the sharp plateau that is observed in the 4 lmin⁻¹ case.

The clean area after one hour of cleaning is now denoted by A^* , this is a time significantly greater than the time of a single cleaning step experienced on the wash racks (one hour as opposed to a cleaning cycle of <10 min). These are estimated to be 3992 mm^2 ($d_{\text{avg}} = 71 \text{ mm}$), 1656 mm^2 ($d_{\text{avg}} = 46 \text{ mm}$) and 127 mm^2 ($d_{\text{avg}} = 13 \text{ mm}$) for the 4 lmin^{-1} , 2.5 lmin^{-1} and 1 lmin^{-1} jets on a 0.19 mm film respectively. The areas of the RFZ created by the three flow rates on a clean Perspex wall were measured to be 13591 mm^2 ($d_{\text{avg}} = 132 \text{ mm}$), 8092 mm^2 ($d_{\text{avg}} = 102 \text{ mm}$) and 2893 mm^2 ($d_{\text{avg}} = 61 \text{ mm}$) respectively. For a 0.19 mm WSP thickness the 1 lmin^{-1} , 2.5 lmin^{-1} and 4 lmin^{-1} clean 4%, 20% and 29% of the area covered by their RFZ on a clean surface respectively. The restriction therefore becomes more discernible at lower flow rates.

4.2.5 Effect of WSP layer thickness

To view the effect of WSP thickness on cleaning performance, the WSP thickness was varied between 0.19 mm and 1.9 mm .

4.2.5.1 High flow

The resulting clean area versus time graph for the 4 lmin^{-1} flow rate is shown in Fig. 4.14.

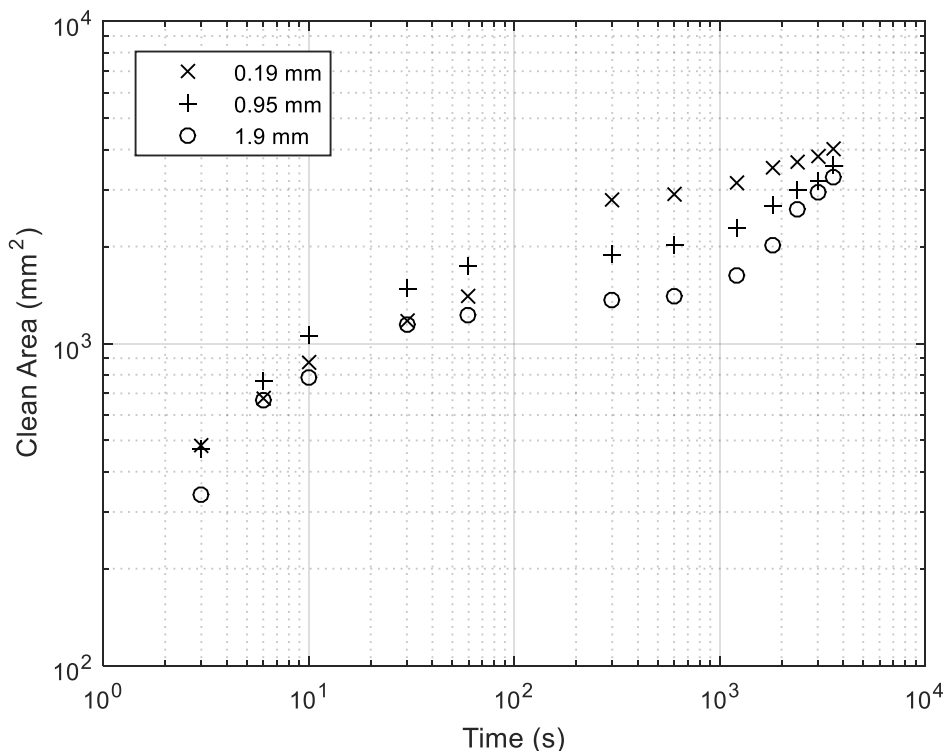


Fig. 4.14: Clean area versus time (4 lmin^{-1} flow rate, water temperature $20 \text{ }^\circ\text{C}$).

For the 4 lmin^{-1} flow rate, the cleaning performance during the first minute of operation is very similar for each WSP thickness with all the curves lying close to each other and

with a very steep gradient. The curves begin to deviate from one another as the process continues with the lowest WSP thickness showing a higher rate of removal. Ultimately however the final clean areas, A^* , reached for each thickness are relatively close together and there is only a 17% discrepancy between the A^* value of the 0.19 mm and 1.9 mm WSP thicknesses.

4.2.5.2 Medium flow

The discrepancy in A^* between each thickness becomes more discernible when the flow rate is lowered to 2.5 lmin^{-1} (see Fig. 4.15). Once again the clean area curves adhere to a similar gradient in the first minute of cleaning. This is in the region close to the impingement of the jet where shear stresses are such that the thickness of the WSP being cleaned has very little effect on the cleaning performance. However as the radial distance from impingement increases the effect becomes more discernible and the lower flow rates show a notably lower efficiency of removal. There is a 67% reduction in A^* when increasing the WSP thickness from 0.19 mm to 1.9 mm.

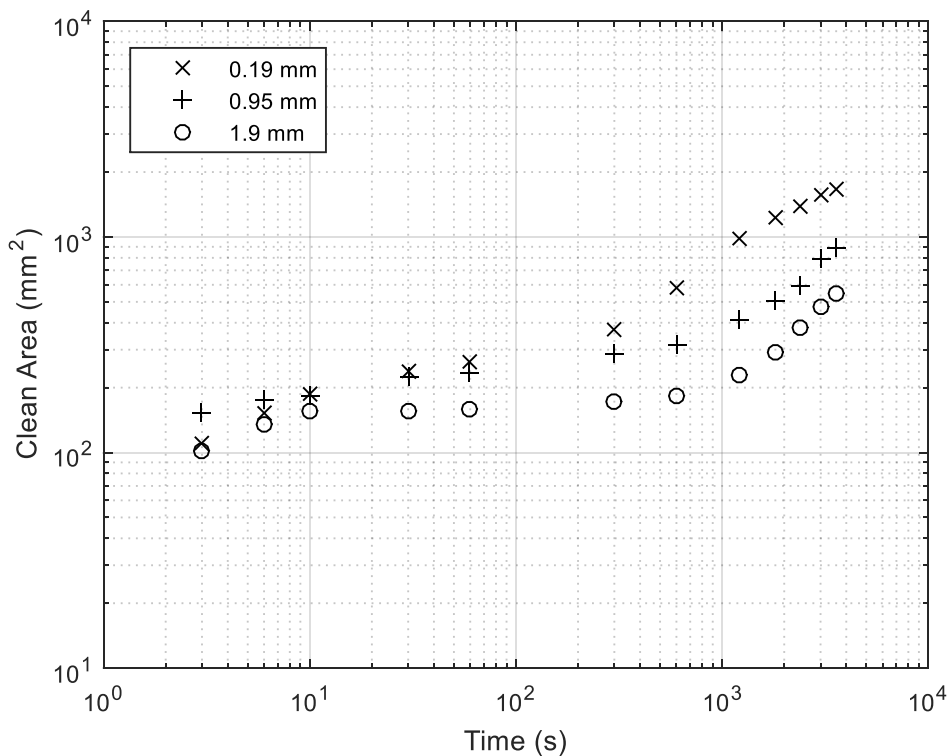


Fig. 4. 15: Clean area versus time (2.5 lmin^{-1} flow rate, water temperature $20 \text{ }^\circ\text{C}$).

4.2.5.3 Low flow

For the 1 lmin^{-1} jet (Fig. 4.16), the breakdown of the soil layer took longer to occur than the higher flow rates due to the force exerted on the layer being lower and taking longer

to penetrate to the surface of the wall. As such there are no data points in the first minute of cleaning and the clean area only becomes apparent after 5 minutes. In this case there is a 36% decrease in A^* between the 0.19 mm and 1.9 mm WSP thicknesses.

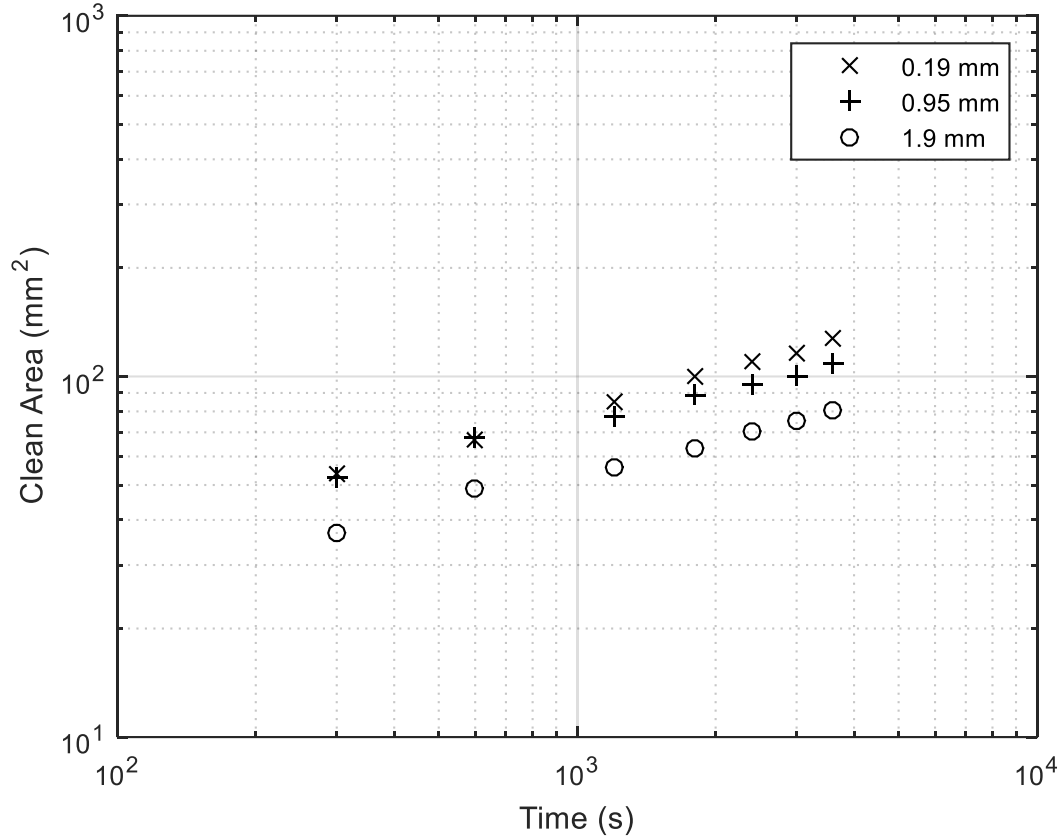


Fig. 4. 16: Clean area versus time (1 lmin^{-1} flow rate, water temperature $20 \text{ }^\circ\text{C}$).

4.2.6 Energy efficiency

Through plotting the ratio A/A^* , the removal expressed as a fraction of the maximum removal for a given flow-rate can be examined. This can be expressed in an energy context, through use of equation 3.22 (with energy being the product of power and time). Fig. 4.17 illustrates that for a given amount of energy, the jet operating at 1 lmin^{-1} approaches its long-time area quicker than for the higher flow rates.

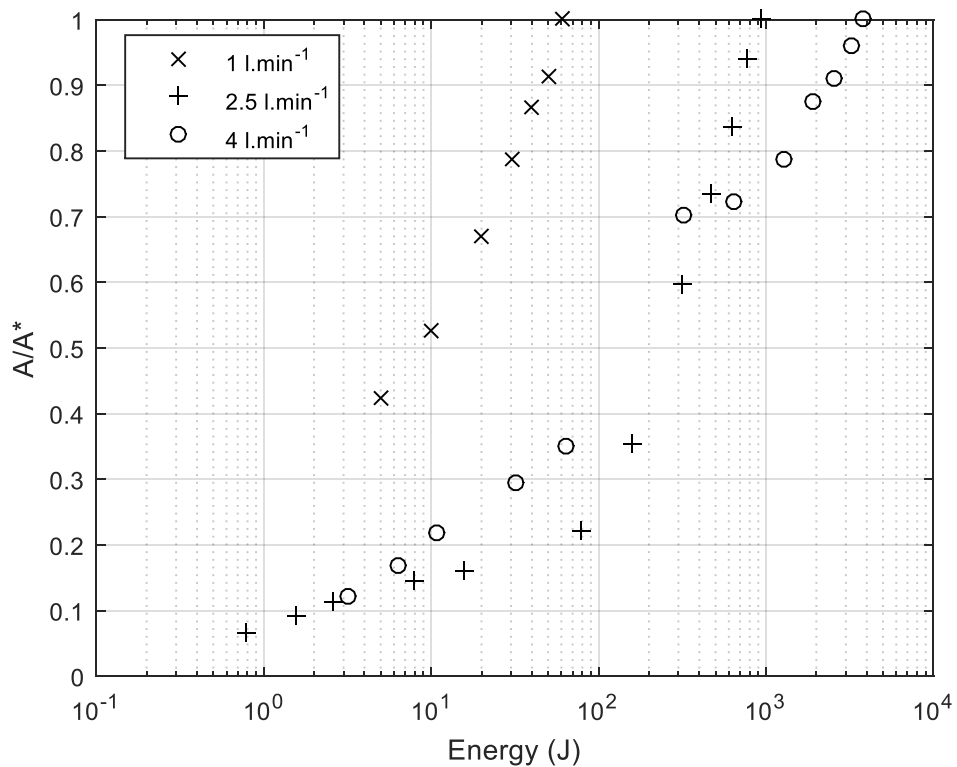


Fig. 4. 17: Area relative to final value at each time interval plotted against energy input to the cleaning process (0.19 mm WSP thickness, water temperature 20 °C).

A similar approach can be used to give a measure of efficiency defined as cleaned area per unit of energy. This is shown in Fig. 4.18. At short times the removal per unit of energy for the three flow rates is very similar, with efficiencies of material removal being much higher than at longer times. At longer times, jets of a lower flow rate show a greater efficiency in material removal. This is likely due to the difference in the rate of material removal at long times (the gradient of the curves shown in Fig. 4.12), which is lower for the higher flow rates. What can be gleaned from these results is that cleaning should be done in very short bursts as that is when the efficiency of removal is at its greatest. At short times, cleaning is done in proximity to the impingement point of the jet. In this region shear stresses are at their highest and cleaning is more efficient. As the radial distance from impingement increases the cleaning efficiency reduces since shear stresses on the surface are lower and the ridge of WSP being greater means there is more resistance to clean area growth. This suggests that the use of a cluster of jets for a short burst of time whose clean areas coalesce would be more efficient than running a single jet for a prolonged time that eventually reaches the same area as the combined area from the cluster. For instance, take the 4 lmin⁻¹ jet for example. After 300 s on the 0.19 mm soil layer, the area cleaned is 2803 mm² ($d_{avg} = 60$ mm) at the expense of 321 J of energy.

After 30 s, each 4 lmin⁻¹ jet cleans 1172 mm² ($d_{avg} = 39$ mm) at the expense of 32 J of energy. This is in the region closer to the impingement point where shear stress exerted on the layer is higher and the ridge is smaller. After 30 s the area cleaned per joule is 36.56 Jmm⁻², compared to 8.74 Jmm⁻² after 300s. If the three jets ran for 30 s were superimposed so that their perimeters touched one another, the combined area cleaned would be 3516 mm² ($d_{avg} = 67$ mm) at the expense of just 96 J and a cycle time of 30 s. Whereas one 4 lmin⁻¹ jet running for 300 s cleans 20% less area at the expense of 230% more energy consumption. Plus, on a manufacturing facility where time is money, the 10 times greater cycle time is inefficient.

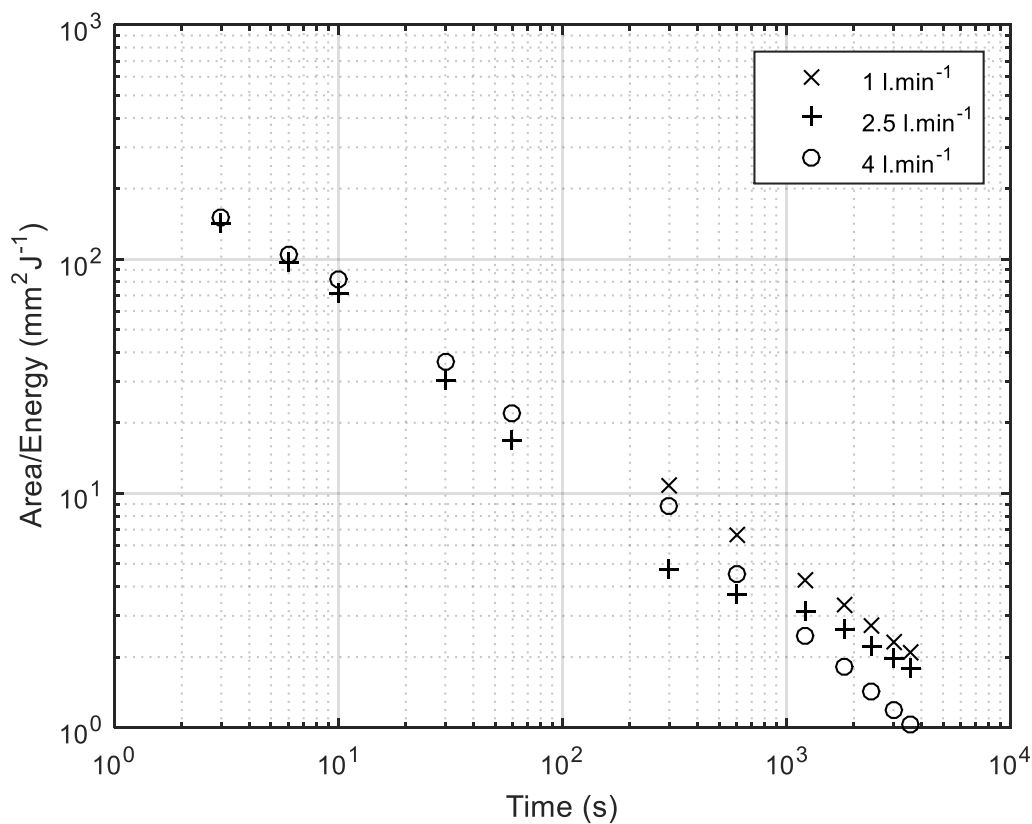


Fig. 4. 18: Efficiency of WSP removal from surfaces expressed as clean area per energy (0.19 mm WSP thickness, water temperature 20 °C).

4.2.7 Effect of water temperature

The effect of increasing the temperature of the water from 20 °C to 40 °C and 60 °C was now studied. 60 °C represented the physical limit of temperature for the equipment used. These experiments were run for 5 minutes as at higher temperatures the majority of cleaning is achieved in this time and this represents a typical cycle duration on a wash rack.

4.2.7.1 High flow, medium WSP layer

Fig. 4.19 shows the response of clean area versus time for the 4 lmin^{-1} jet and 0.95 mm WSP thickness.

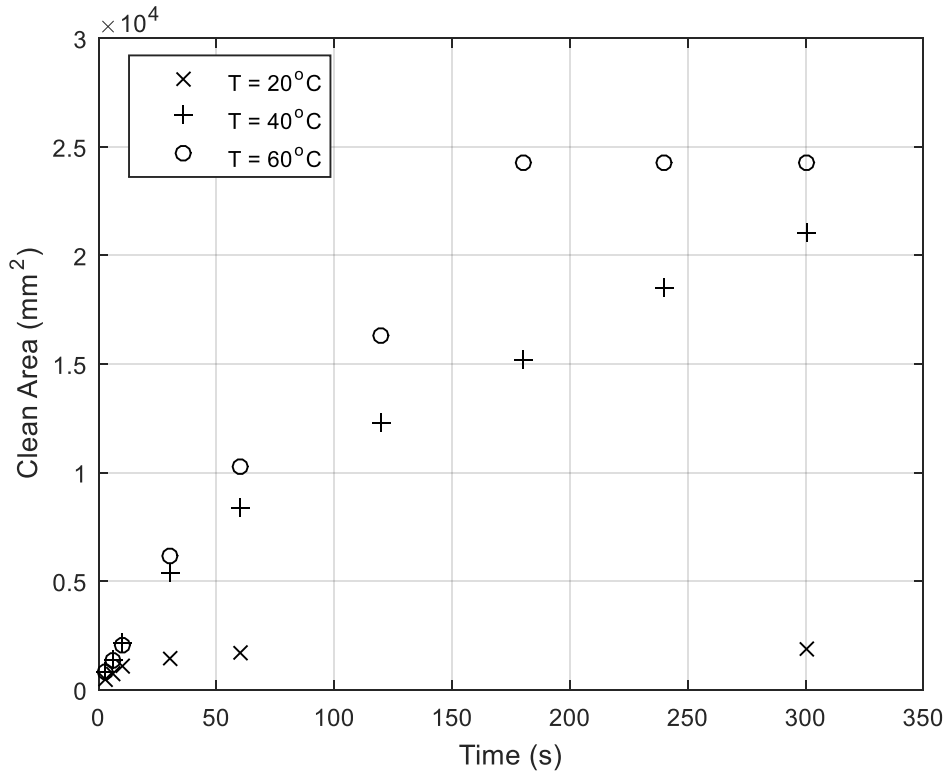


Fig. 4. 19: Clean area versus time (4 lmin^{-1} flow rate, 0.95 mm WSP thickness).

As the temperature is increased, the cleaning rate increases dramatically, with the clean area reaching a steady value inside 5 minutes of cleaning at 60°C . For the first 30 s, the cleaning performance is very similar at 40°C and 60°C . Beyond this time, the effect of temperature becomes discernible and the rate of cleaning increases. After 3 minutes, the clean area at 60°C has reached its maximum value equating to 24300 mm^2 . As discussed in 4.2.4, the RFZ for a 4 lmin^{-1} jet is 13591 mm^2 so this shows the extent of the material removed in the falling film at higher temperatures. This is approximately a 500% increase over the value of A^* for the 20°C case. 3 minutes of cleaning at 60°C sees any WSP on the surface in contact with the hot water is removed as the temperature is above the drop point of the WSP and at this point the material begins to behave more like a liquid than a semi-solid. As such the material is washed away by the falling film created by the jet since the viscosity of the WSP is significantly reduced. At 40°C the time taken to reach its maximum clean area is greater however the final value reached is only slightly smaller than at 60°C , measured to be 21000 mm^2 , 13% lower than at 60°C . Given the energy input to raise the temperature of water by 40°C as opposed to 20°C

°C is an increase of 100%, this is a poor yield in cleaning performance relative to the additional energy to the system. For 5 minutes of cleaning at 4 lmin^{-1} , the energy required to raise the required 20 litres of water by $20 \text{ }^{\circ}\text{C}$ is 1.674 MJ, which makes the 320 J of running the jet negligible. The clean areas both exceed the RFZ created by a 4 lmin^{-1} jet on a clean surface by greater than 50%. This can be explained by the material removed by the falling film. Whilst the melting point of a given WSP is reported across a range of temperatures, reflecting the complexity of the material and multiple phase transitions occurring during heating, targeting the lower end of this range may be appropriate from an energy efficiency perspective since this appears to be sufficient to cause the phase transition to a mobile phase. The loss in structure at this temperature is also observed through rheological measurements by Bentley (2017).

4.2.7.2 Medium flow, high WSP layer

Clean area versus time is plotted for the 2.5 lmin^{-1} jet on a 1.9 mm thick layer of WSP for the range of temperatures under study in Fig. 4.20.

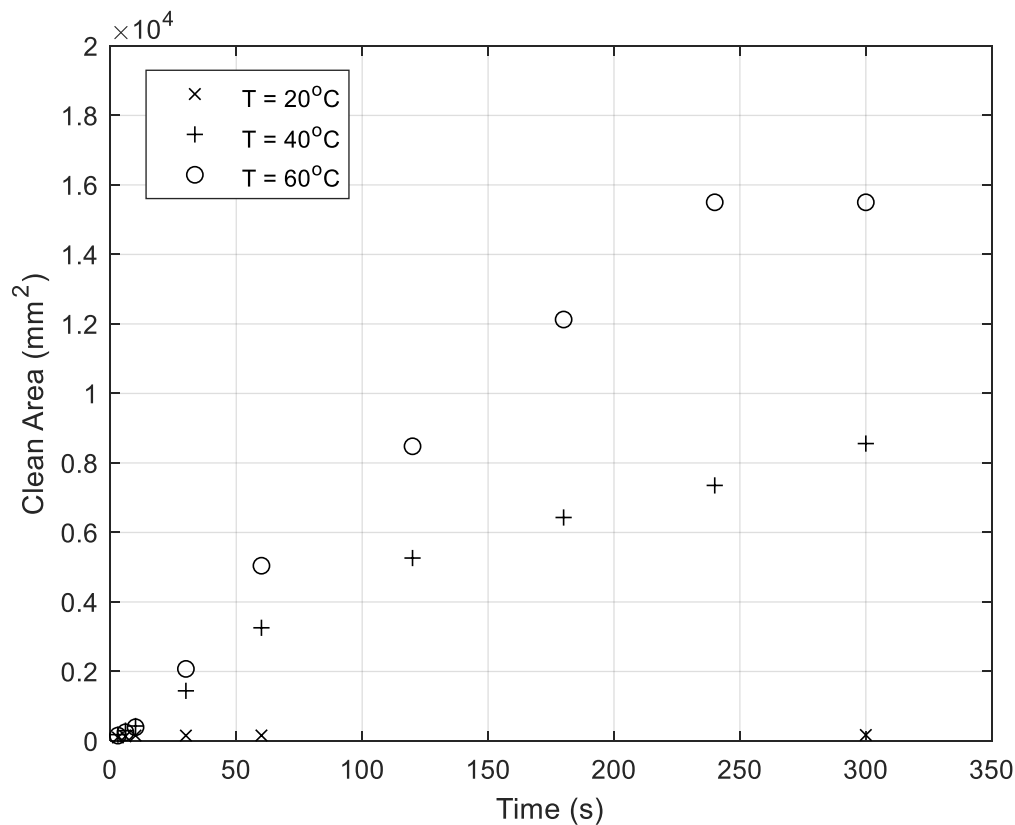


Fig. 4. 20: Clean area versus time (2.5 lmin^{-1} jet, 1.9 mm WSP thickness).

Fig. 4.20 shows again the dramatic effect of raising the temperature of the water above the drop point of the WSP. The respective clean areas after 5 minutes of cleaning for the $20 \text{ }^{\circ}\text{C}$, $40 \text{ }^{\circ}\text{C}$ and $60 \text{ }^{\circ}\text{C}$ jets are 172 mm^2 , 8558 mm^2 and 15500 mm^2 . In contrast, for the

4 lmin⁻¹ jet on a 0.95 mm layer of WSP, there is a significant increase of 81% in clean area between the 40 °C and 60 °C jets. The improved yield in clean area almost merits the 100% increase in energy input raising to 60 °C instead of 40 °C. As the study of 4.2.5 showed, WSP thickness has a greater effect on cleaning performance for lower flow rates and this is partly why the difference in cleaning performance is more discernible between the different temperatures in this case. Whereas in Fig. 4.19 the time taken to reach the final clean area value was approximately 3 minutes for the 60 °C jet, in this case it took an additional minute. The melting process is prolonged due to the increased volume of material in the thicker layer. The heat transfer in the 40 °C jet is further prolonged which explains the substantial difference in clean areas after 5 minutes cleaning. It can be observed that the 40 °C curve has shown no plateau after 5 minutes and once the layer has fully melted the area cleaned would increase to closer to the 60 °C case, as was observed in Fig. 4.19. For 5 minutes cleaning at 2.5 lmin⁻¹, each rise in 20 °C comes at the expense of 1.047 MJ, again making the running of the jet negligible from an energy perspective. Therefore, increasing the cycle time to accommodate for the prolonged time to reach A* at 40 °C is justified.

4.2.7.3 Soil removal mechanism

At elevated temperatures there is a change in the mechanism by which soil is removed from the Perspex wall. Fig. 4.21 shows a time lapse series of images of the removal process for the 1 lmin⁻¹ jet on a 0.95 mm WSP thickness at 60 °C. It can be observed there is no formation of a ridge of WSP on the perimeter of the clean area, unlike the case for cleaning below the melting point of WSP (e.g. Fig. 4.1). After 10 s a very thin layer of material exists between the clean area and the film jump and after 30 s this has been displaced. The growth of the clean area does not significantly increase in width beyond this time, however WSP in the falling film begins to be removed. All material in contact with the jetted fluid is removed from the surface and washed downstream of the flow. Due to the phase transition of the WSP at 60 °C, the removal of the layer is more easily achieved, and the shear stress exerted on the wall by the falling film is sufficient to displace the melted WSP.

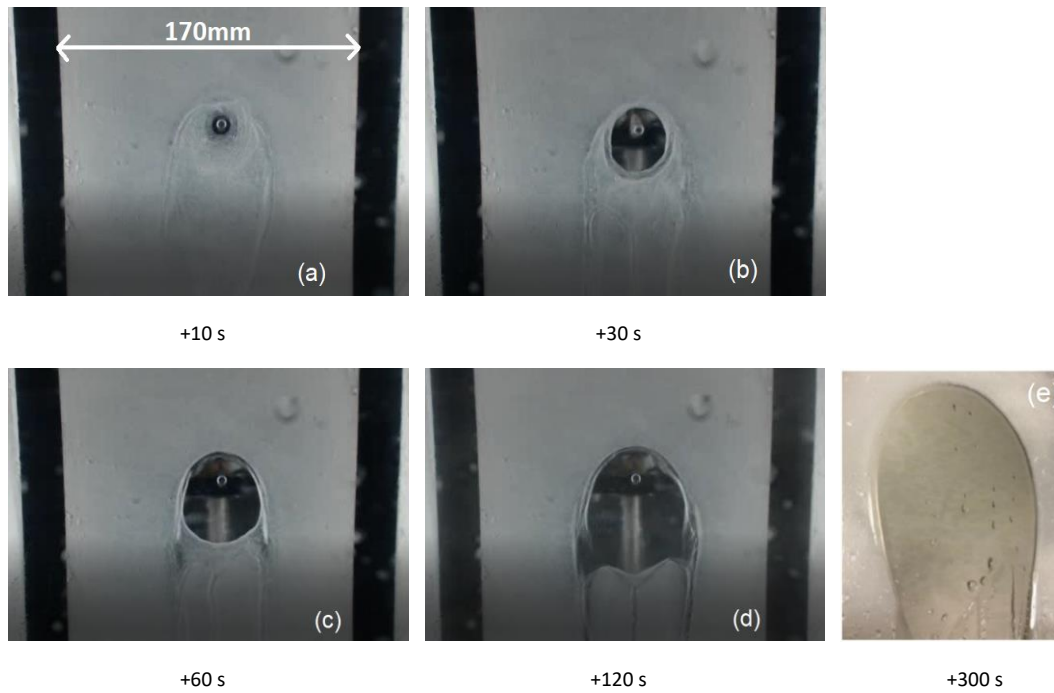


Fig. 4. 21: Time lapse of removal 1 lmin^{-1} jet, 0.95 mm WSP thickness, water temperature $60 \text{ }^{\circ}\text{C}$. (a) 10 s. (b) 30 s. (c) 60 s. (d) 120 s. (e) Zoomed in region of clean area at long time 300 s.

Fig. 4.22 shows the time lapse of soil removal for a 1 lmin^{-1} jet on a 0.95 mm WSP thickness at $40 \text{ }^{\circ}\text{C}$.

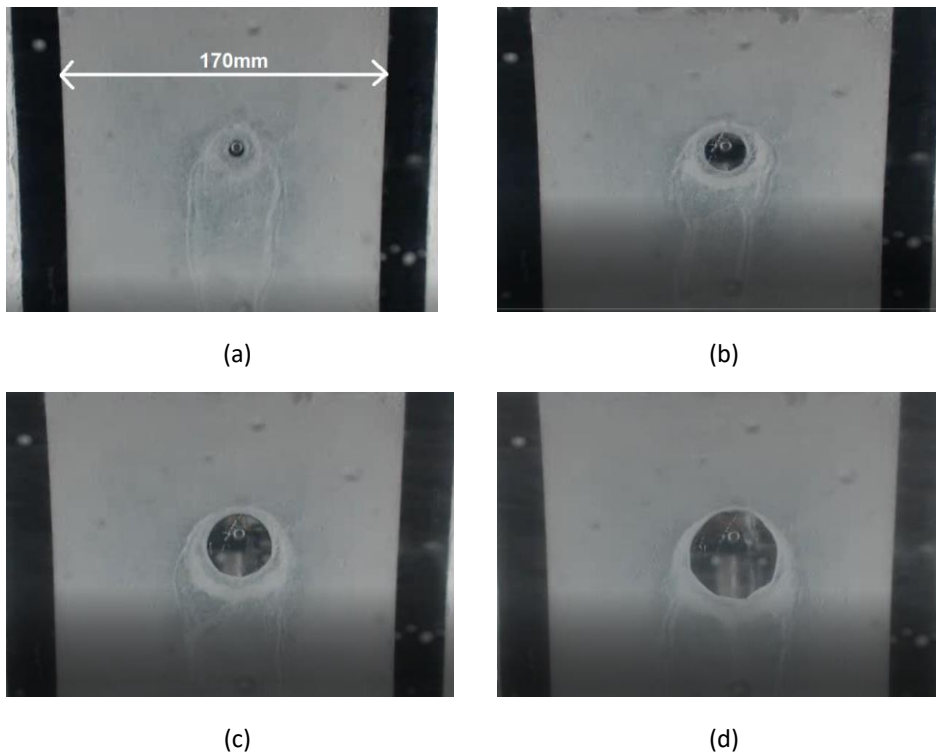


Fig. 4. 22: Time lapse removal for 1 lmin^{-1} jet, 0.95 mm WSP thickness, water temperature $40 \text{ }^{\circ}\text{C}$ (a) 3 s (b) 10s (c) 30 s (d) 120 s.

When compared to the time lapse of Fig. 4.21, the soil removal at 40 °C does not occur at the same rate as the 60 °C, due to the slower heat transfer to the soil and the longer time taken to melt the surrounding WSP. There is a discernible lower clean area produced at 120 s, however once the melting occurs any WSP in contact with the flow from the jet is removed from the surface, this is demonstrated in the time lapse for the 2.5 lmin⁻¹ jet at 40 °C on a 0.19 mm WSP thickness (see Fig. 4.23), where at 120 s the area cleaned is equivalent to that of the RFZ and falling film of the impinging jet.

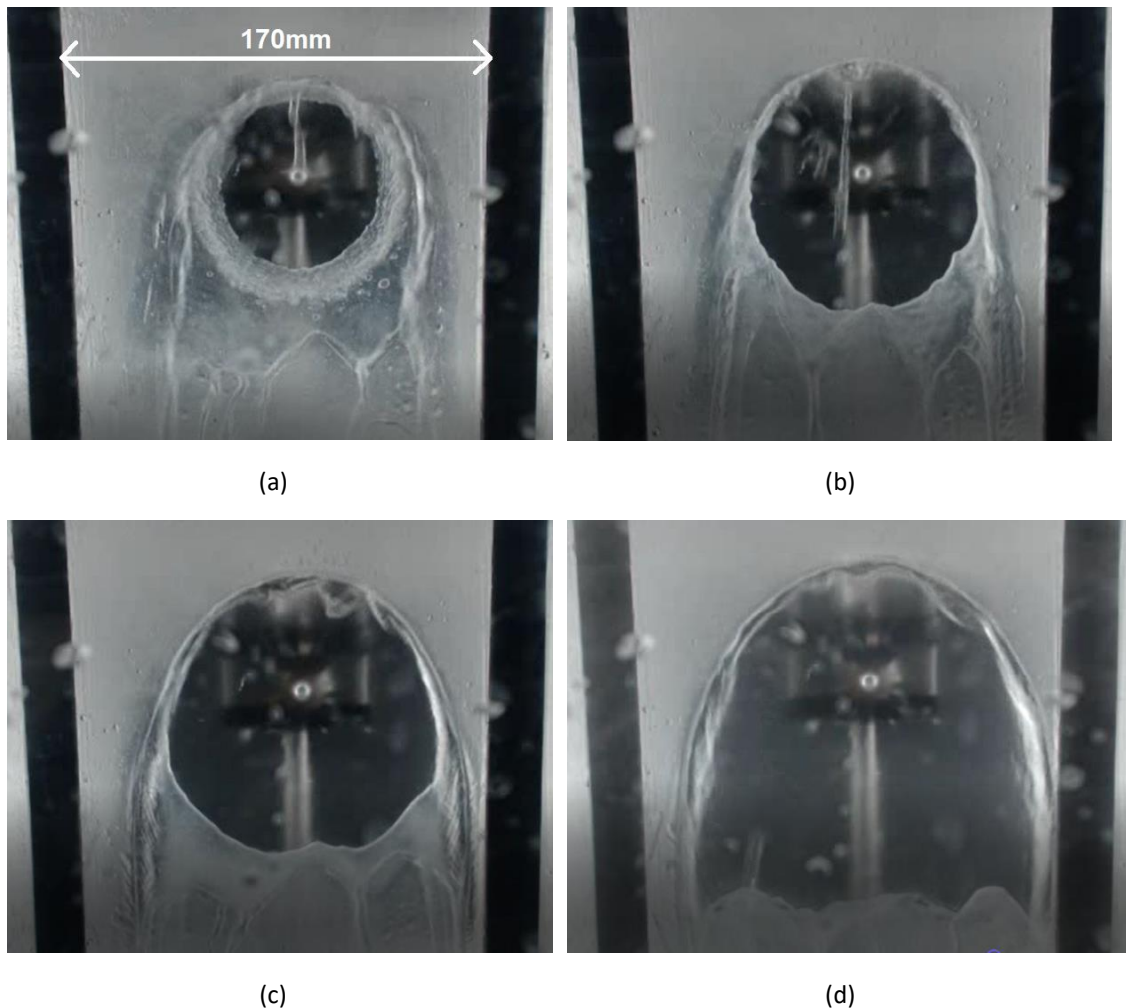


Fig. 4. 23: Time lapse removal for 2.5 lmin⁻¹ jet, 0.19 mm WSP thickness, water temperature 40 °C (a) 3 s (b) 10s (c) 30 s (d) 120 s.

4.3 Vertical jet impingement through pipe

In addition to the case of a jet impinging horizontally on to a Perspex wall, a case of a jet flowing vertically down a pipe was also considered. Filling needles are commonly used in pouch filling and cleaned with jets impinging on to the top surface. The needles were replicated using steel piping as described in 3.4.1 and filled with gel, characterised in 3.4.3. The flow conditions were matched to those obtained from EPANET using room

temperature water with no surfactant. Water was collected from the exit of the pipe and was deemed clean once the flow rate collected from the exit was equivalent to that of the impinging jet. Two jet scenarios were considered for a constant flow rate (0.6 lmin^{-1}); a perfectly aligned case where the jet is positioned to impinge in the centre of the pipe and a misaligned case, where the jet was offset by an angle relative to the length of pipe.

4.3.1 Perfectly aligned jet

For the perfectly aligned jet, the mass of water collected from the exit to the pipe was plotted against time and the resulting graph is shown in Fig. 4.24.

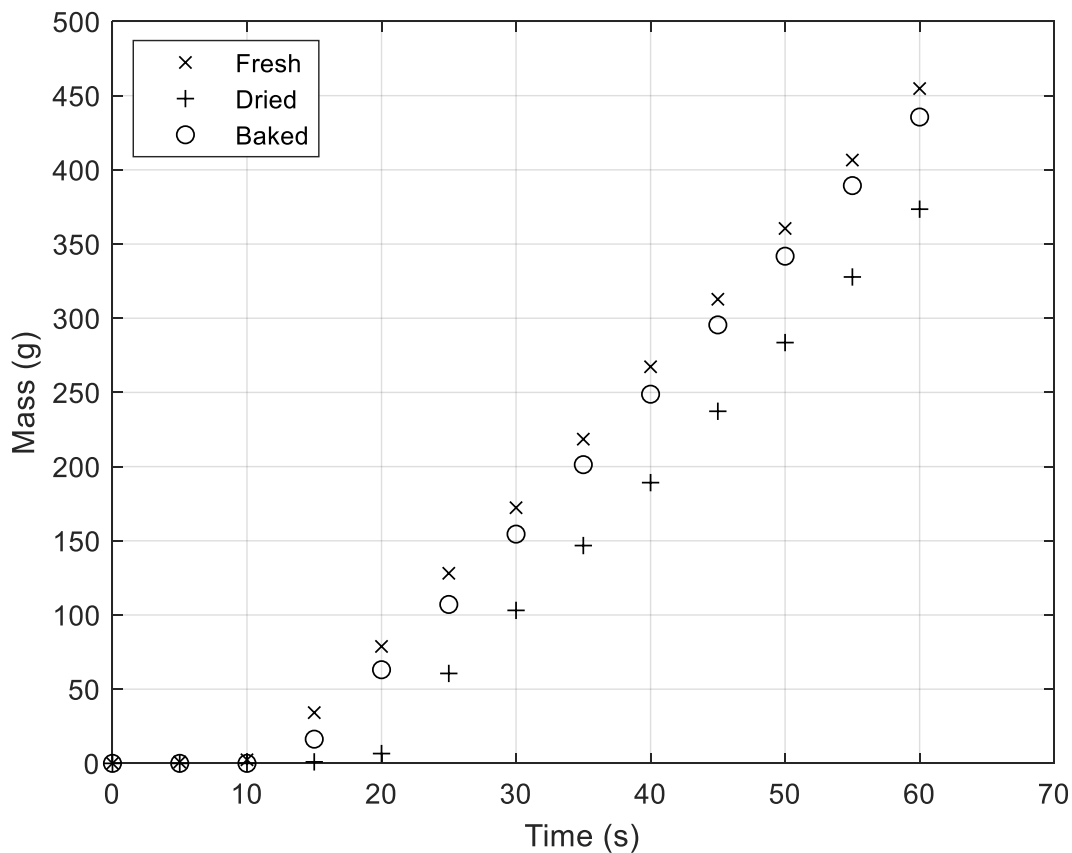


Fig. 4. 24: Mass of water collected from exit to pipe versus time, perfectly aligned jet; fresh, baked and dried gel samples.

For all three states of gel there is an initial delay between time zero, the moment the jet is initiated, and water being collected from the exit of the pipe. Whilst there is a section of pipe connecting the funnel to the beaker that is weighed during the experiment, the time taken for the water to pass through this is approximately 1 s. Fig. 4.24 shows there is a minimum time elapsed of 10 s for water to enter the beaker, so the delay is attributed to the time taken for the jet to push through the gel that fills the pipe. Palabiyik et al. (2018) described the removal of a fouling deposit in a pipe using water in three stages; rapid removal of deposit in the core, thinning of the residual film on the interior wall of

the pipe and patch removal, where patches of the deposit left on the interior wall are gradually eroded with further rinsing. The first two stages are pictured schematically in Fig. 4.25.

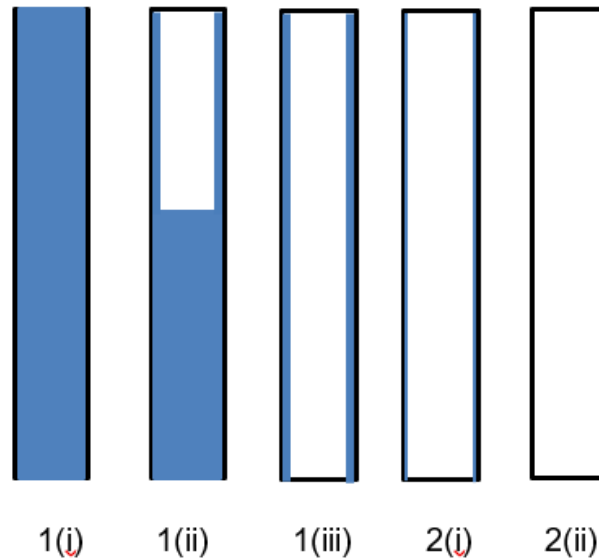


Fig. 4. 25: Removal of fouling deposit in pipe in 2 stages: 1(i) Needle initially full with gel ; 1(ii) water impinging on top of gel pushes fluid from pipe; 1(iii) water flow through pipe established; 2(i) residual film on wall surface which needs to be removed under shear to give clean walls 2(ii).

The bulk of the gel in the core is gradually pushed downward through the pipe by the jet impingement central to the top of the bulk in the perfectly aligned case. This process continues until the jet pushes through the other side of the pipe, Fig. 4.25 (1(iii)), and the fully developed flow is collected by the funnel and channelled to the beaker. The bulk gel is also collected by the beaker, however the full pipe consisted of only 3.1 g of gel. This was sufficiently small relative to the total mass collected in the beaker (~500 g) to be considered negligible. Fig. 4.24 shows how the water begins to collect in the beaker for the fresh and baked gel after approximately 12 s. A constant mass flow rate is achieved immediately, taking the gradient of both curves the mass flow rate is approximately 9.5 gs^{-1} . The graph of mass flow rate in the beaker versus time is shown in Fig. 4.26.

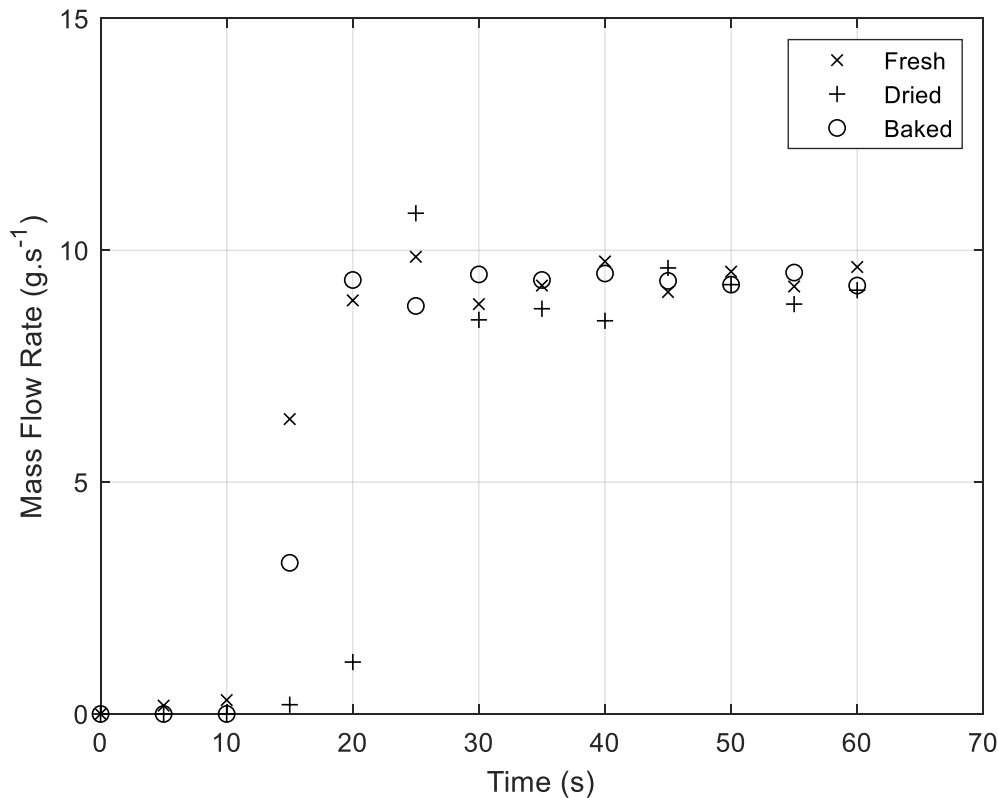


Fig. 4. 26: Mass flow rate versus Time for fresh, dried and baked samples.

Assuming the combined gel and water mixture density is equal to that of water, a reasonable assumption considering the density of the gel was 1061 kgm^{-3} , this equates to a flow rate to the beaker of 0.56 lmin^{-1} . This is equivalent to that of the impinging jet, taking into account the errors in the experiment and potential losses in the connecting tube from the pipe to the beaker.

Fig. 4.24 also shows there is an extended induction time for flow to be established through the needle containing dried gel. For drying, the pipes were filled with gel and left to dry for 5 days. This was done to imitate if, for example, there was a delay between the machine being stripped and cleaning taking place. Exposure to the air for a prolonged time causes the rheology of the gel to change to a more solid state and the yield stress increases, causing a delay in phase 1. Under the same flow conditions as the fresh and baked gel, the mass begins to collect in the beaker approximately 20 s after initiation of the jet. Despite this, the delay is less than 10 s compared to the undried gel and is negligible relative to the cycle times experienced on Rack 2 ($\sim 5 \text{ mins}$). This indicates that a perfectly aligned jet is capable of initiating phase 1 of the mechanism.

To establish the efficiency of phase 2 of the removal mechanism, the pipes were weighed both clean and after the soiled pipes had been cleaned. Post cleaning the pipes were

left to dry to ensure no water residue was included in the weight. It was found that for the fresh and dried gel, the residual gel on the walls was negligible. The mass of the residue was measured to be approximately 0.01 g for both cases, ~0.3% of the initial mass of gel. In its fresh and dried state, the shear stress exerted on the interior walls of the pipe are great enough to initiate 2(i). However the residue present after cleaning of the baked gel was measured to be approximately 0.3g, 10% of the initial mass. This is a significant amount of residue. This suggests parts being heated to 85 °C where gel bakes on to the interior walls of the filling needles can cause extended cycles and more challenging conditions for cleaning. The flow conditions on Rack 2 delivered to these needles are no longer capable of supplying the necessary shear stress required to achieve phase 2(ii), a fully clean interior wall.

4.3.2 Misaligned jet

The effect of misalignment of the jet relative to the pipe was also studied. An angular displacement was applied to the pipe, with the jet remaining in a fixed position. The standoff distance of the nozzle to the entrance to the pipe was measured on site to be 35 mm and given the internal diameter of the pipe (4.36 mm), trigonometry shows that a misalignment of 3.5° is enough for the jet to completely miss the pipe interior, or a horizontal displacement of 2.18 mm from the centre of the pipe. Fig. 4.27 shows the perfectly aligned jet on the left and a misalignment of approximately 2° on the right, such that approximately half the flow rate of the impinging jet is delivered to the pipe interior.

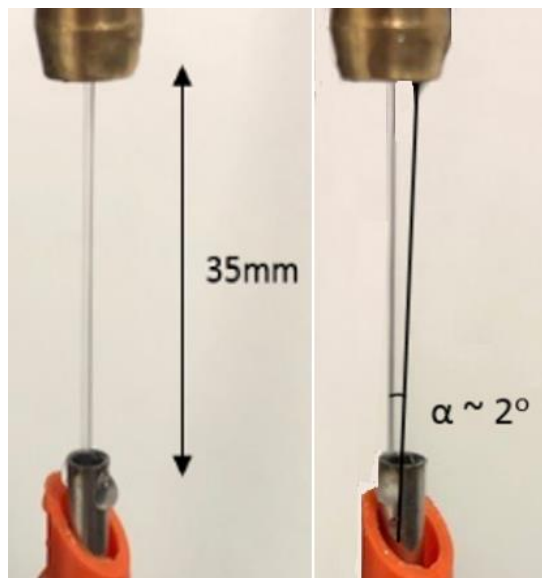


Fig. 4. 27: Left: perfectly aligned jet, Right: misaligned jet (~2° angular displacement).

The same set of experiments were run for the misaligned jet as the perfectly aligned jet and the resulting mass flow rate through the pipe versus time curves are plotted in Fig. 4.28.

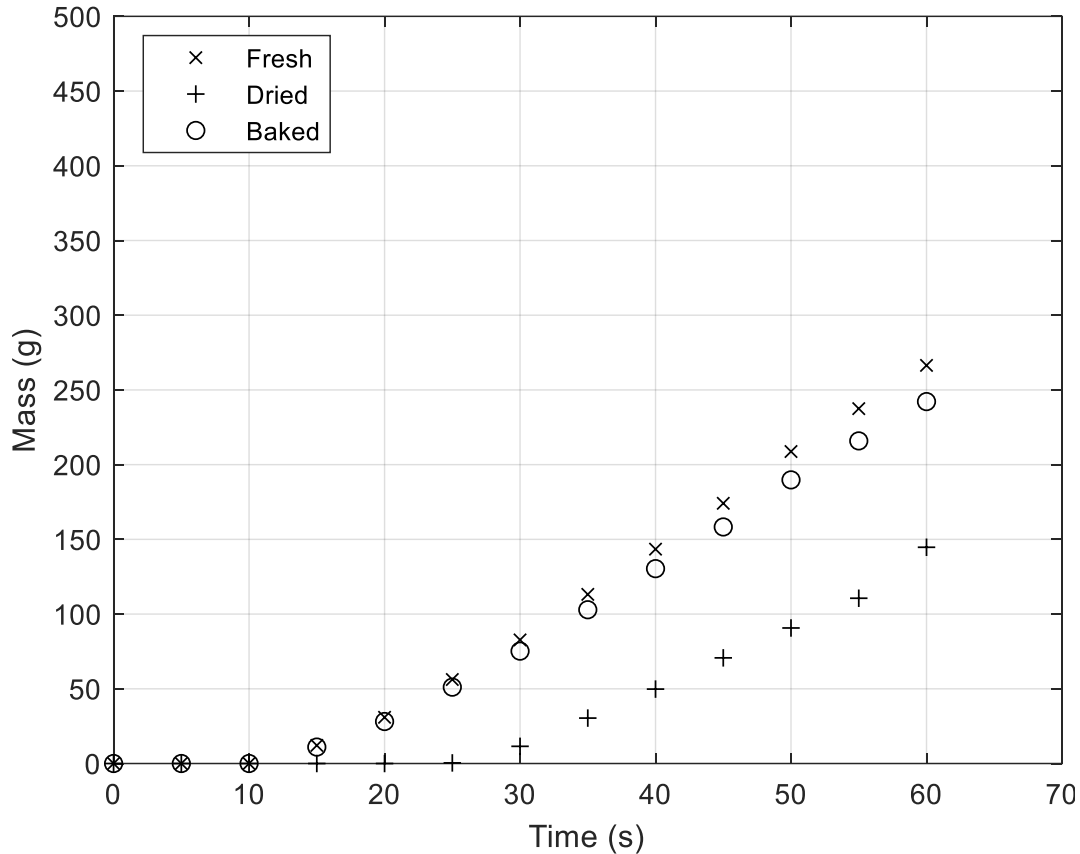


Fig. 4. 28: Mass of water collected from exit to pipe versus time, misaligned jet; fresh, baked and dried gel samples.

For the fresh and baked samples of gel, the flow from the exit to the pipe is established after approximately 14 s, a delay of approximately 2 s compared to the perfectly aligned jet. A delay for the dried gel is again observed, however for the misalignment the delay is slightly exaggerated by a further 5 s, with flow being established through the exit of the pipe after approximately 25 s. This is still however negligible in respect to the length of a cycle time on the rack. For the fresh, dried and baked gel the established flow rates are 0.35 lmin^{-1} , 0.26 lmin^{-1} , 0.33 lmin^{-1} respectively. For the 2° misalignment, approximately half the flow rate of the impinging jet is delivered to the pipe interior, so for the 0.6 lmin^{-1} jet these are as expected, accounting for the errors in the experiment and the possible deviation from an exact 2° misalignment. The flow rate through the pipe is noticeably lower for the dried gel case, suggesting that there is a restriction in the flow through the dried gel at the reduced flow rate. Due to the angle of the jet impinging on

one side of the pipe interior, one side is subject to high shear and the efficiency of soil removal on this side is much higher. Equally the other side experiences considerably less shear than the perfectly aligned case and the extent of the residual film is higher. However, a mass balance showed that due to one side being cleaned to a greater efficacy, the mass of residue after cleaning in all cases was similar to that of the perfectly aligned case. For the fresh and dried gels, the residue was approximately 0.5% of the initial gel mass, and a residue of approximately 13% was present after cleaning of the baked samples. This suggests that the principal failure mechanism in this setup is the baking of gel on the interior walls of the filling needles when they are heated before cleaning. Significant residues are present after cleaning, such that would fail cleaning validation procedures, irrespective of jet alignment ($< 3.5^\circ$). Misalignment however becomes a significant issue greater than 3.5° as the fluid completely misses the entrance to the filling needles, equally a horizontal misalignment of 2.18 mm from the centre of the filling needle is sufficient for the fluid to miss the needle. When setting up the preliminary experiments for the vertical jet, it became clear how easy it is for the misalignment to exceed these limits.

4.4 Rack optimisation study

The bubble plots of Fig. 3.5 and 3.13 were a powerful visualisation of the wash rack flow rates because it allows the user to observe the nozzles which are either over or under supplied with fluid. For instance, if parts loaded on to particular nozzles are requiring long times to clean, the relevant nozzles can be identified in Fig. 3.5 to see if this is due to the nozzle being under-supplied. This then allows for an iterative approach to be made in-silico by optimising the nozzle selection for improved flow distribution.

For one study, the total flow available was up to as 2000 l min^{-1} , and this with a range of zero-flow pressures, was used to evaluate possible losses through the coupling. The analysis for the pump curve considered (Fig. 3.2) showed that the discharged flow through the coupling was as high as 1610 l min^{-1} and the total flow through the wash rack given as 2000 l min^{-1} (82.0 % of the total flow). The pressure upstream of the coupling was such that for the pressure downstream of the coupling to match that which was measured in-situ (140 kPa) the discharge coefficient required for the coupling was $4.312 \text{ l min}^{-1} \text{ Pa}^{-0.5}$. Visual observations showed this is significantly greater than that seen in practice. By lowering the zero-flow pressure in the pump closer to the value measured downstream of the coupling, it was possible to lower the discharge coefficient of the coupling to a more realistic value. For example, a zero-flow pressure in the pump of 147 kPa (50% of the initial value) gives a significant reduction in total flow through the rack to 824 l min^{-1} and now 57% of the flow (470 l min^{-1}) discharged through the coupling.

Although this still appears rather excessive, it does show the potential to include coupling loss if the full pump curve is available. It is important to note that the rest of the flow through the rack is independent of the pump/coupling, so long as the pressure downstream of the coupling is known and applied to the EPANET model. Thus, the bubble plot of Fig. 3.5 is fully representative of the flow distribution of the wash rack under study.

The bubble plot of Fig. 3.13 shows there is a significantly uneven distribution of the flow through Rack 2. This is primarily due to the discharge coefficients of the spray balls and perforated pipe sections being much larger than that of the open pipe jets and spray nozzles on the branches downstream on the main feed. The spray balls and perforated pipes thus demand more flow than the jets and sprays elsewhere on the rack. For instance, nozzle 3 (a spray ball) demands a flow rate of 16.2 lmin^{-1} , in comparison to the open pipe jets (e.g. nozzle 25) which demand 0.6 lmin^{-1} , approximately $1/30^{\text{th}}$ of the spray ball. It is likely that parts loaded on to the spray balls are being overcleaned and the flow delivered to them exceeds that which is required. In contrast parts being cleaned by the open pipe jets may be receiving lower flow, and thus to achieve the required acceptance criteria for cleanliness the cycle time becomes longer. Therefore, there is grounds for optimisation of Rack 2 to more equally distribute the flow about the rack. A study was conducted where the discharge coefficient of the spray balls was lowered such that they demanded less flow and the excess flow available from this could be distributed to the other branches on the rack. The coefficient of the perforated pipes was left the same as this would involve much greater modifications to the rack in practice. Modifications to the spray balls would simply involve removing those currently in place and replacing with a new spray ball. The 60-hole spray ball on the rack could for example be replaced by a spray ball of 10 holes, such that the discharge coefficient would be reduced by a factor of 6 since it is proportional to the number of holes on the ball. Changing the discharge coefficient of the spray balls from $0.212 \text{ lmin}^{-1}\text{Pa}^{-0.5}$ as was deduced in 4.3.2, to $0.035 \text{ lmin}^{-1}\text{Pa}^{-0.5}$ and leaving everything else on the rack unchanged has the following effect on the distribution of flow in the rack (see Fig. 4.29).

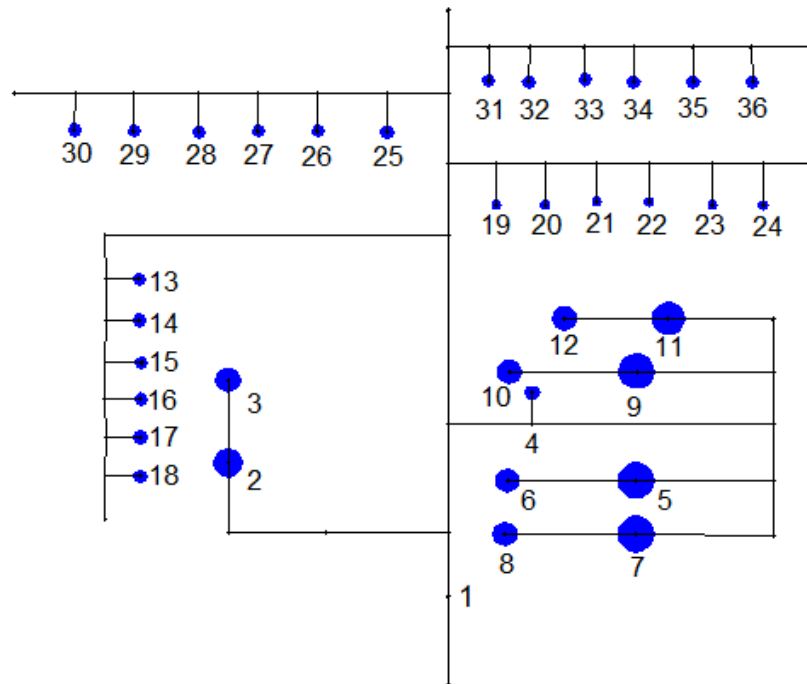


Fig. 4. 29: Bubble plot of flow distribution in Rack 2 after altering spray ball coefficients for improved flow distribution through the rack, coupling left unfilled.

The bubble plot of Fig. 4.29 shows a more even distribution of flow through the wash rack than that shown in Fig. 3.13. Whilst there is still a considerably larger flow delivered to the perforated pipes and spray balls on the first two branches off the main feed, this is a necessity for the larger disassembled parts that are positioned on these branches. Consider the spray ball represented by node 3, reducing the number of holes in the spray ball to 10 from 60, as aforementioned, lowers the flow rate delivered to it from 16.2 lmin^{-1} to 4.8 lmin^{-1} . Consider also the open pipe jet represented by nozzle 25, whilst the discharge coefficient of this nozzle has not been changed the flow delivered to it increases from 0.6 lmin^{-1} to 1.2 lmin^{-1} . The excess flow from the reduction of that to the spray ball has been able to be rerouted elsewhere on the rack to the nozzles which were previously being undersupplied. Validation tests for the parts loaded on to the spray balls would be required on site to ensure that these parts are still being cleaned to an acceptable level, but this could have the net effect of reducing the overall cycle time. This study shows that an iterative approach can be taken for rack optimisation, changing the spray balls on the rack to fully optimise the flow rate distribution. Ultimately the time to clean the rack is the slowest time for any one part to reach acceptance criterion.

4.5 Summary

This chapter has presented the results obtained experimentally using a liquid jet. Two cleaning scenarios were studied, a horizontal jet impinging on to a vertical Perspex wall coated with WSP, and a vertical jet cleaning a vertically aligned pipe filled with gel. For

the horizontal jet, the cleaning process was filmed to observe cleaning performance against time and an energy framework was adopted to gauge the efficiency of each cleaning process. It was discovered that cleaning efficiency is at its best in the early stages of cleaning, where removal occurs close to the impingement point of the jet. In this region shear stresses exerted on the wall by the RFZ are at a maximum and adhesive removal of the soil is thus at its optimum. Beyond this region, as the cleaning radius increases, efficiency decreases rapidly. A soil removal mechanism study was conducted to observe how the material in the ridge is transported and the study showed that a rolling mechanism occurs, where material rolls over the boundary and is submerged by more material as the process repeats itself. The ridge builds in size over time and ultimately acts as a resistance to clean area growth. A final clean area, A^* , is eventually reached where shear stress at the boundary is insufficient to push this ridge any further radially. A temperature study was also conducted and this showed that for the soil under study, WSP, the melting point is exceeded by temperatures at 40 °C or higher. Whilst the removal is accelerated at 60 °C, results suggest that 40 °C is sufficient to remove any material in contact with the flow once melting has occurred. This allows an upper temperature limit to be established which then could ensure the design of an energy efficient process.

For the vertical jet flow through the pipe, three gel states were under consideration; fresh, dried and baked. Two jet alignments were also studied, perfectly aligned normal to the centre of the pipe and misaligned by an angular displacement of the pipe of approximately 2°. It was shown that flow through the exit of pipe was established in approximately 12 s for the fresh and baked gel and 20 s for the dried gel with a perfectly aligned jet. Meanwhile for the misaligned jet, flow was established through the exit after approximately 14 s for the fresh and baked gel and 25 s for the dried gel. Despite the delays in flow through the needle being established, the cleaning time is well within typical cycle times used on racks (~5 mins). The main failure modes were discovered to be the residue found on the baked samples, where up to 13% of the initial gel mass was residual. Trigonometry showed that a misalignment of just 3.5° was enough for jetted fluid to entirely miss the pipe and setting up of the experiments showed the ease at which this could occur. Under these conditions no cleaning would take place.

Finally, the opportunity for wash rack optimisation was discussed as the uneven distribution of flow throughout the racks, observed in Chapter 3, could be a potential source of cleaning validation failure. If certain parts were being cleaned by nozzles that were under-supplied with fluid, simple modifications to the rack could be made to alter the distribution of flow and supply more fluid to these nozzles.

Chapter 5

Spray Results

5.1 Introduction

This chapter will present the results obtained using a water spray with no surfactant present. The same test rig of Fig. 3.16 was used, changing the nozzle to a spray (see Fig. 3.22). For the spray only one horizontal impingement, on to a vertical wall, case was considered. The experimental variables for the spray experiments were chosen the same as for the jet and in the same range; flow rate ($1 - 4 \text{ lmin}^{-1}$), WSP thickness ($0.19 - 1.9 \text{ mm}$), water temperature ($20 - 60 \text{ }^\circ\text{C}$), two standoff distances were also studied, 50 and 125 mm.

5.2 Visualisation of soil removal

Videos of each cleaning process were recorded via a camera positioned behind the Perspex wall on to which the spray impinged. The following section will present time lapse images of each process.

5.2.1 High flow, thin WSP layer

A time lapse of the soil removal for the 4 lmin^{-1} spray at room temperature, 0.19 mm WSP thickness and 50 mm standoff distance is shown in Fig. 5.1.

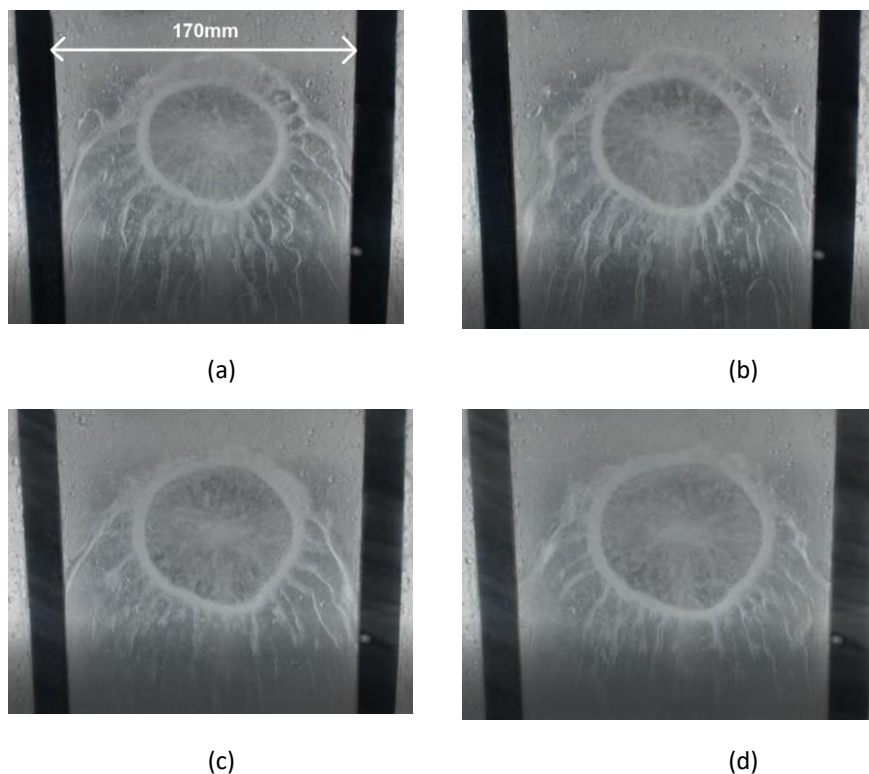


Fig. 5. 1: Time lapse removal for 4 lmin^{-1} spray, 0.19 mm WSP thickness, water temperature $20 \text{ }^\circ\text{C}$, 50 mm standoff (a) 30 s (b) 60s (c) 300 s (d) 600 s .

When compared to the jet under the same conditions (see Fig. 4.1), the growth in the area cleaned with time is less discernible. With the spray, unlike the jet, the area cleaned often contained a residual film and was not visually clean. As such, all areas presented at 20 °C in this chapter represent the area bound by the ridge of WSP on the perimeter of each area. Between 30 s (a) and 600 s (d), the area cleaned by the spray increases from 3832 mm² ($d_{\text{avg}} = 70$ mm) to 5631 mm² ($d_{\text{avg}} = 85$ mm), an increase of 47%. In the same time period, the jet area cleaned increased by 147%. The spray after 1 hour of cleaning reached a final cleaned area of 7032 mm² ($d_{\text{avg}} = 95$ mm), compared to the jet under the same conditions of 3846 mm² ($d_{\text{avg}} = 70$ mm). Fig. 5.2a shows a close-up of the cleaned area by the spray after an hour of cleaning.

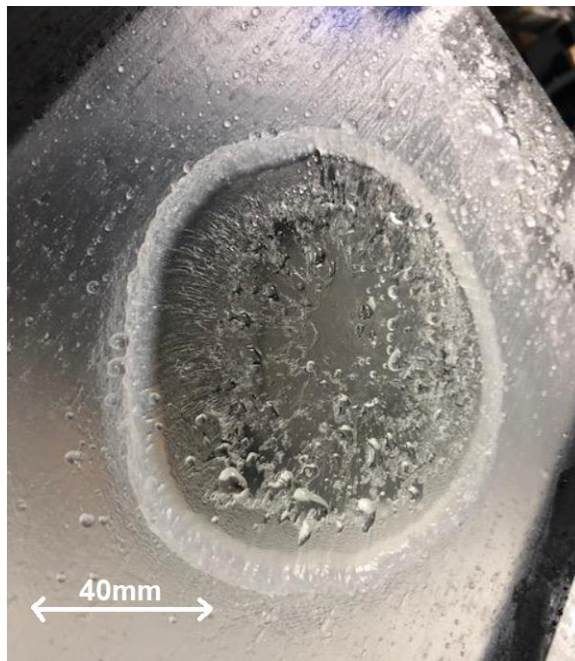


Fig. 5. 2a: Cleaned area close-up after one hour of cleaning: 4 lmin⁻¹ spray, 0.19 mm WSP thickness, water temperature 20 °C, 50 mm standoff

Fig. 5.2a shows how despite the cleaned area being far greater than the jet under the same conditions there is the presence of a residual film in the cleaned region where the WSP has not been removed. It can also be observed that the ridge of WSP forms around the perimeter of the cleaned area suggesting there is adhesive removal of WSP as it is pushed outwards by the impinging cone of the spray. At 4 lmin⁻¹ the spray angle discharged from the nozzle is 64°, measured using ImageJ. This results in an impingement zone, from a 50 mm standoff, with a diameter of 62 mm and area of 3067 mm². The superimposed impingement zone on the cleaned area shown in Fig. 5.1d is shown in Fig. 5.2b.

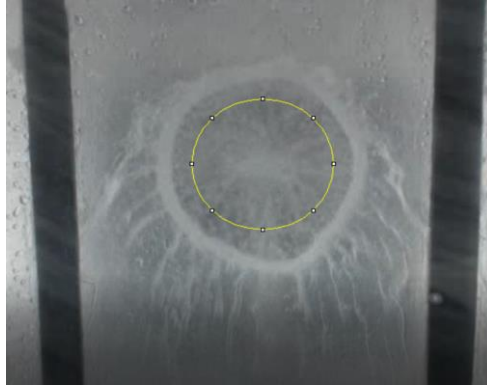


Fig. 5. 2b: Superimposed spray impingement area on cleaned area. (4 lmin^{-1} spray, 0.19 mm WSP thickness, water temperature $20 \text{ }^{\circ}\text{C}$, 50 mm standoff).

This shows that fluid from the cone is transported radially outwards, adhesively removing WSP until the ridge is large enough to prevent any further removal. Inside the cone the soil layer is broken down cohesively, by progressive impingement of droplets. The convex distribution of droplets can be observed in the impingement zone superimposed. In the centre of the area, there is a clear dense concentration of droplets, whilst close to the circumference of the area the droplet distribution appears far sparser.

5.2.2 Medium flow, thin WSP layer

The removal time lapse for a 2.5 lmin^{-1} spray, again on a 0.19 mm film is shown in Fig. 5.3.

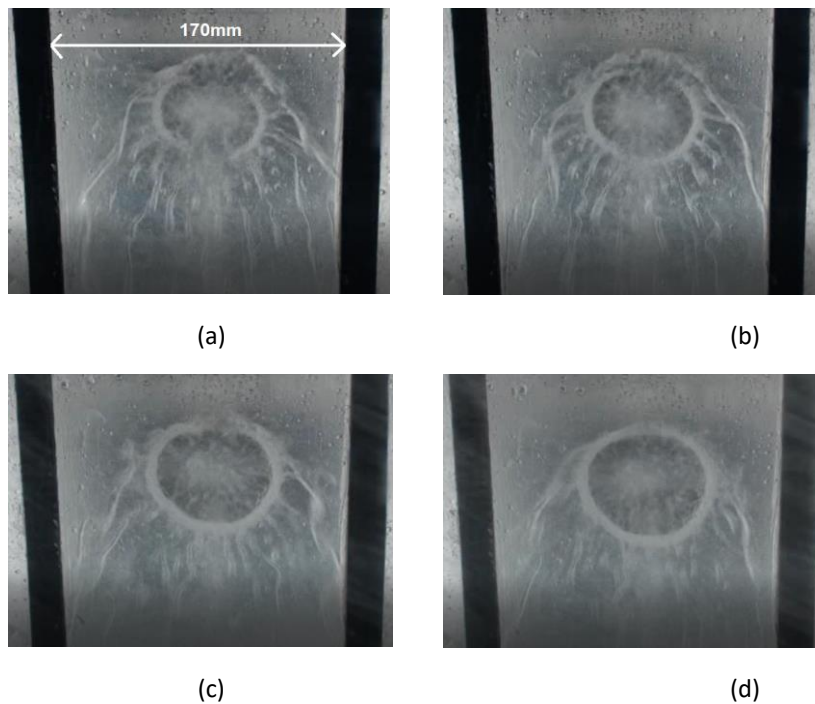


Fig. 5. 3: Time lapse removal for 2.5 lmin^{-1} spray, 0.19 mm WSP thickness, water temperature $20 \text{ }^{\circ}\text{C}$, 50 mm standoff (a) 30 s (b) 60s (c) 300 s (d) 600 s.

For the lower flow rate of 2.5 lmin^{-1} the area cleaned increases from 1980 mm^2 ($d_{\text{avg}} = 50 \text{ mm}$) at 30 s to 3539 mm^2 ($d_{\text{avg}} = 67 \text{ mm}$) at 600 s. This represents a 79% increase in area, compared to 47% in the same time frame at 4 lmin^{-1} . Due to the rate of droplet impingement being lower in this case, the cohesive removal rate of WSP is subsequently lower inside the cone of the spray. The spray angle produced at 2.5 lmin^{-1} is 56° , resulting in an impingement zone area of 2220 mm^2 and diameter of 53 mm. So, in 30 s, the ridge is located within the impingement zone whereas at 4 lmin^{-1} the impingement zone had been cleared of the bulk of the layer at 30 s, with the ridge location being outside of the cone. A close-up of the cleaned area after one hour is shown in Fig. 5.4.

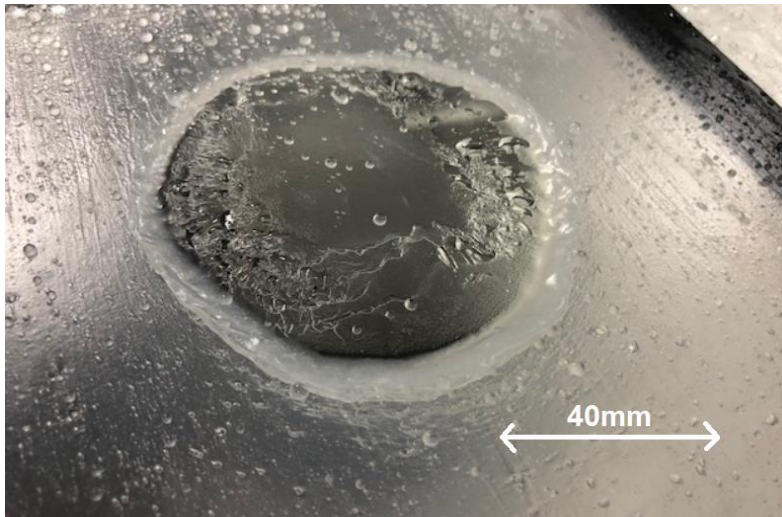


Fig. 5. 4: Cleaned area close-up after one hour of cleaning: 2.5 lmin^{-1} spray, 0.19 mm WSP thickness, water temperature 20°C , 50 mm standoff.

Similar to the 4 lmin^{-1} spray a large residual film is present in the centre of the cone. There are regions that have been cleaned more effectively outside the cone, where the Perspex appears clear. This is in the region where adhesive removal takes place. Again, the ridge can be observed where the material from inside the cone has been displaced radially outward.

5.2.3 Low flow, thin WSP layer

After an hour of cleaning, a close-up of the soil cleaned by the 1 lmin^{-1} spray is shown in Fig. 5.5.

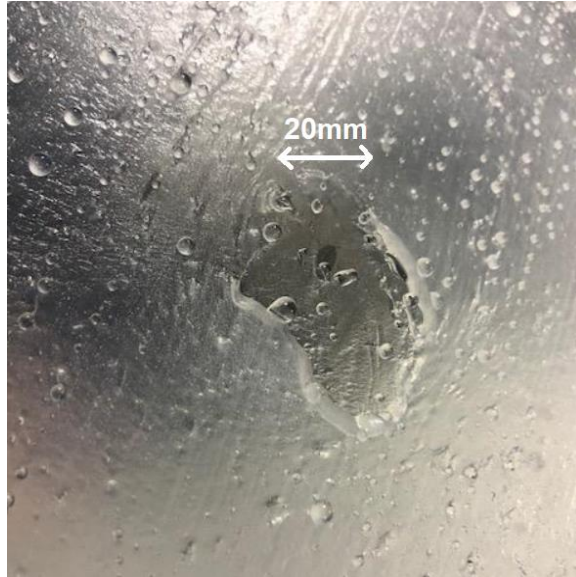


Fig. 5. 5: Cleaned area close-up after one hour of cleaning: 1 lmin^{-1} spray, 0.19 mm WSP thickness, water temperature 20°C , 50 mm standoff.

The spray angle of the 1 lmin^{-1} spray is 40° , at a 50 mm standoff this produces an impingement zone area of 1040 mm^2 and diameter of 36 mm. In this case the area cleaned after one hour is 1681 mm^2 ($d_{\text{avg}} = 46 \text{ mm}$), although as Fig. 5.5 shows there are no parts where the Perspex appears fully clean and there is a residual film covering the entire cleaned region. Also, the ridge is very small suggesting a small amount of WSP has been displaced. Due to the frequency and force of droplet impingement being lower than the higher flow rate cases, the efficacy of the cohesive removal is significantly reduced.

5.2.4 High flow, medium WSP layer

Increasing the WSP thickness to 0.95 mm, the time lapse removal for the 4 lmin^{-1} spray is shown in Fig. 5.6.

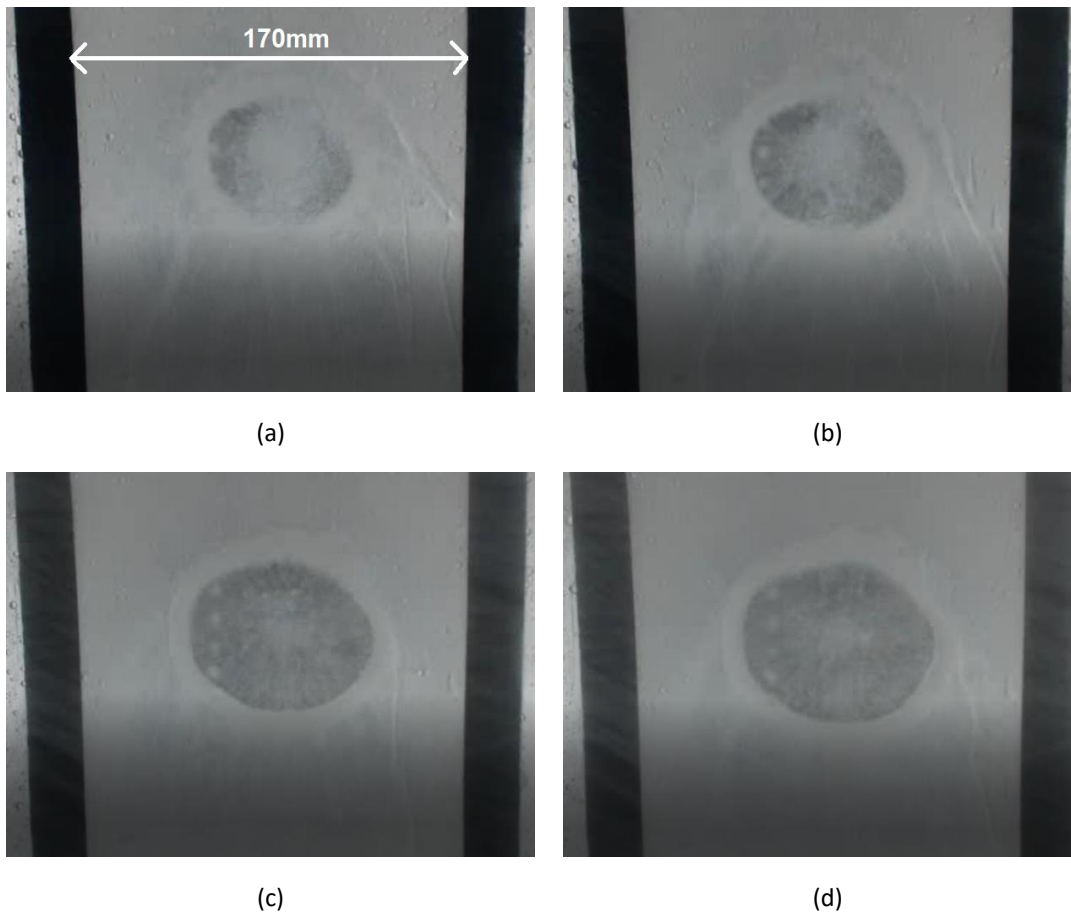


Fig. 5. 6: Time lapse removal for 4 lmin^{-1} spray, 0.95 mm WSP thickness, water temperature $20 \text{ }^{\circ}\text{C}$, 50 mm standoff (a) 30 s (b) 60s (c) 300 s (d) 600 s.

When compared to Fig. 5.1, the cleaned areas at each time interval are noticeably smaller for the thicker WSP layer. The increase to a 0.95 mm WSP layer sees a final cleaned area reduction from 7032 mm^2 ($d_{\text{avg}} = 95 \text{ mm}$) to 6545 mm^2 ($d_{\text{avg}} = 91 \text{ mm}$) after one hour of cleaning. The ridge formed on the perimeter of the cleaned area is also noticeably thicker, this can be more clearly observed in Fig. 5.7.

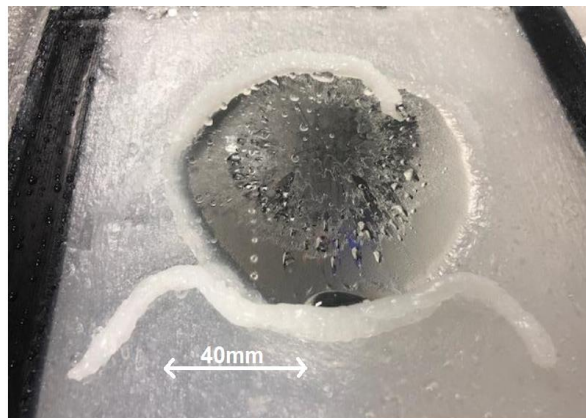


Fig. 5. 7: Cleaned area close-up after one hour of cleaning: 4 lmin^{-1} spray, 0.95 mm WSP thickness, water temperature $20 \text{ }^{\circ}\text{C}$, 50 mm standoff.

Fig. 5.7 shows the extent of the ridge of WSP built up on the 0.95 mm layer. The thickness of the ridge is such that large slugs of WSP detach from the ridge due to gravity. The residual film can also be observed inside the cleaned area. There are areas inside the cone that appear fully clean, where the Perspex is transparent, but the majority of the cleaned area exhibits a residual film.

5.2.5 Medium flow, medium WSP layer

For the WSP thickness of 0.95 mm, the time lapse for the 2.5 lmin^{-1} spray is shown in Fig. 5.8.

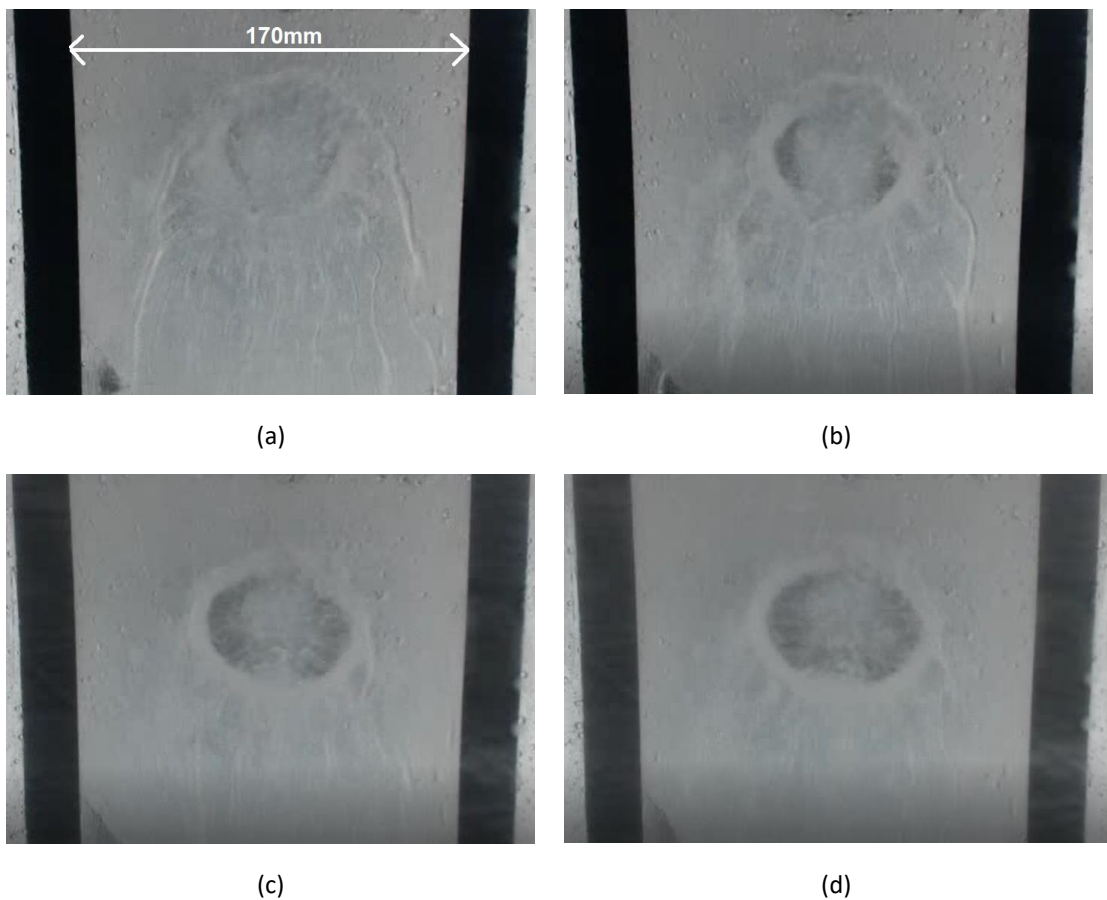


Fig. 5. 8: Time lapse removal for 2.5 lmin^{-1} spray, 0.95 mm WSP thickness, water temperature $20 \text{ }^{\circ}\text{C}$, 50 mm standoff (a) 30 s (b) 60s (c) 300 s (d) 600 s.

When compared to Fig. 5.6, there is a discernible delay in the cohesive removal that occurs. At 2.5 lmin^{-1} the frequency and force of impinging droplets on the layer is decreased and therefore breakdown of the layer takes longer. The final cleaned area produced after one hour decreases from 6545 mm^2 ($d_{\text{avg}} = 91 \text{ mm}$) to 3606 mm^2 ($d_{\text{avg}} = 68 \text{ mm}$) when decreasing the flow rate to 2.5 lmin^{-1} from 4 lmin^{-1} . A close-up of the cleaned area after one hour is shown in Fig. 5.9.

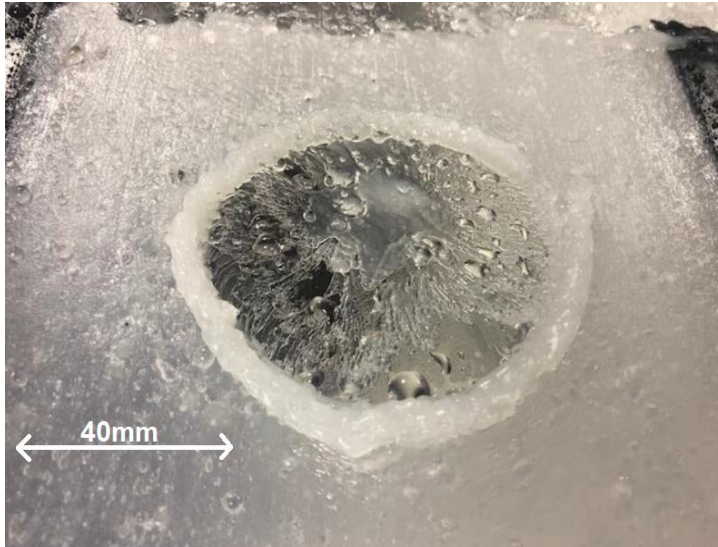
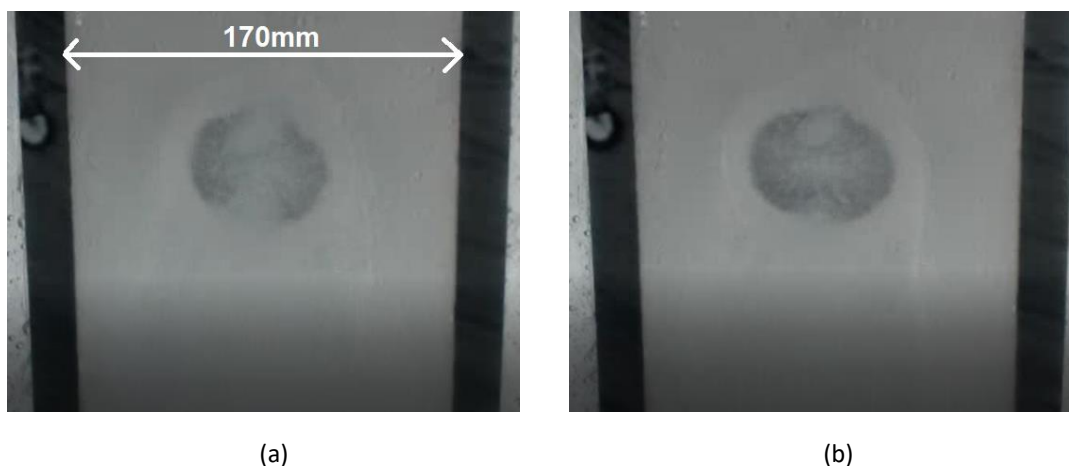


Fig. 5. 9: Cleaned area close-up after one hour of cleaning: 2.5 lmin^{-1} spray, 0.95 mm WSP thickness, water temperature $20 \text{ }^{\circ}\text{C}$, 50 mm standoff.

In this case no slugs form from the ridge as was observed in Fig. 5.7, since less material has been transported to the ridge and the ridge isn't large enough to start detaching under gravity. The residual film in the cleaned region is noticeably larger in this case, with a large mass of WSP apparent in the upper half the cone. Small areas of cleanliness can be observed, particularly on the left-hand side of the cleaned region but overall, there is a significant residual film across the entire region. For the two thicker WSP thicknesses of 0.95 mm and 1.9 mm, the 1 lmin^{-1} spray was unable to penetrate the layer to the surface and as such no clean area was produced.

5.2.6 High flow, thick WSP layer

For the 1.9 mm WSP layer, the time lapse of removal for the 4 lmin^{-1} spray is shown in Fig. 5.10.



(a)

(b)

Fig. 5. 10: Time lapse removal for 4 lmin^{-1} spray, 1.9 mm WSP thickness, water temperature $20 \text{ }^{\circ}\text{C}$, 50 mm standoff (a) 300 s (b) 600 s.

In this instance the removal only became discernible after 300 s, where it can be observed there is a large mass of WSP still uncleared in the centre of the cone. This clears slightly after 600 s but remains omnipresent. A close-up of the surface after one hour of cleaning is shown in Fig. 5.11.

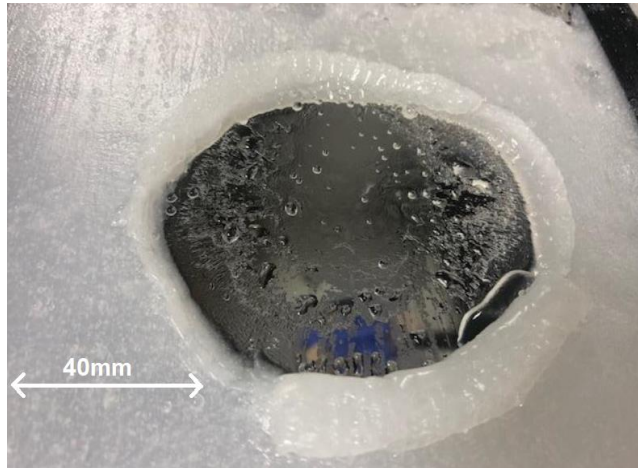


Fig. 5. 11: Cleaned area close-up after one hour of cleaning: 4 lmin^{-1} spray, 1.9 mm WSP thickness, water temperature $20 \text{ }^\circ\text{C}$, 50 mm standoff.

The close-up of Fig. 5.11 shows once again the residual film covering most of the surface cleaned. The clean area falls to just 4667 mm^2 ($d_{\text{avg}} = 77 \text{ mm}$) compared to 6545 mm^2 ($d_{\text{avg}} = 91 \text{ mm}$) for the same flow conditions on the 0.95 mm WSP layer. The ridge is noticeably larger, and it can be observed that a slug of WSP has fallen off the surface on the bottom left hand side of the cleaned area.

5.2.7 Medium flow, thick WSP layer

The time lapse removal for the 2.5 lmin^{-1} spray on the 1.9 mm WSP layer is shown in Fig. 5.12.

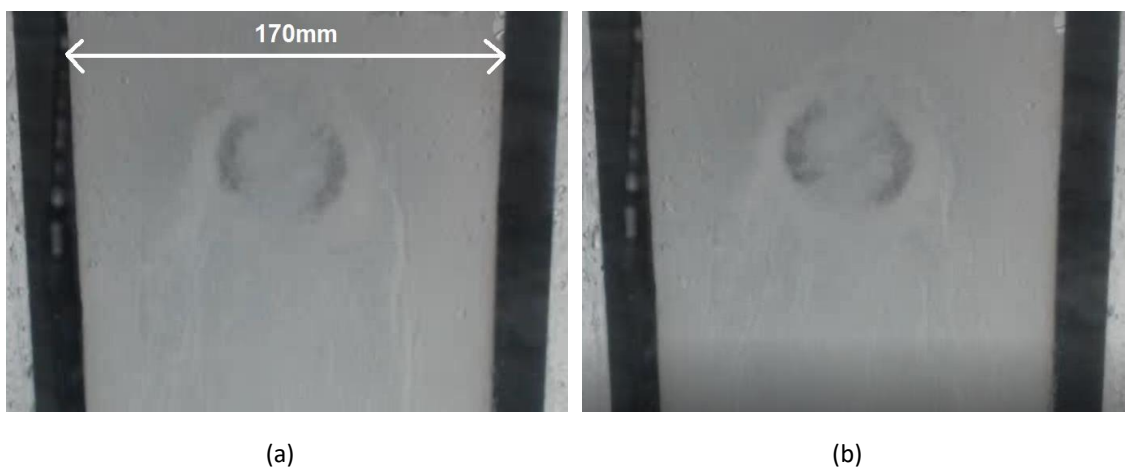


Fig. 5. 12: Time lapse removal for 2.5 lmin^{-1} spray, 1.9 mm WSP thickness, water temperature $20 \text{ }^\circ\text{C}$, 50 mm standoff (a) 300 s (b) 600 s.

Once again Fig. 5.12 shows a significant reduction in cleaned area for the highest thickness of the WSP layer, 1.9 mm. It can be observed that the centre of the cone remains virtually uncleaned at 300 s, whilst adhesive removal takes place on the perimeter and cleaned regions begin to become visible. A small but discernible decrease to this mass of WSP in the centre is observed at 600 s and the cleaned region on the perimeter slowly begins to expand. A close-up of the cleaned region after one hour of cleaning is shown in Fig. 5.13.

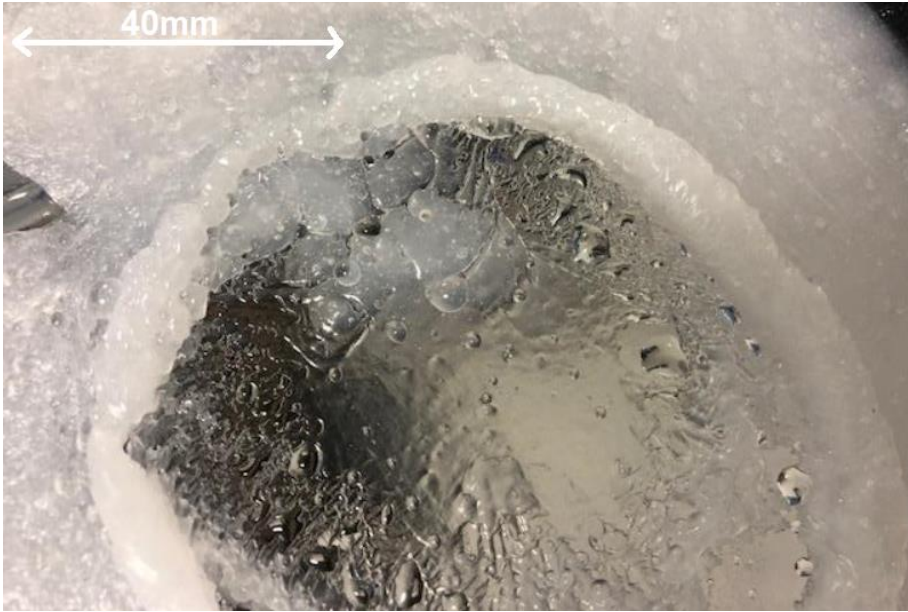


Fig. 5. 13: Cleaned area close-up after one hour of cleaning: 2.5 lmin^{-1} spray, 1.9 mm WSP thickness, water temperature $20 \text{ }^{\circ}\text{C}$, 50 mm standoff.

Fig. 5.13 shows a particularly large residual film compared to those previously observed, with large masses of WSP still present on the surface, particularly towards the top of the cleaned area. The cleaned area in this case was 2783 mm^2 ($d_{\text{avg}} = 60 \text{ mm}$) in area, compared to 3606 mm^2 ($d_{\text{avg}} = 68 \text{ mm}$) in the case of the 0.95 mm WSP layer.

5.3 Residual film measurements

A short research visit to the University of Cambridge Department of Chemical Engineering and Biotechnology was undertaken to use a confocal thickness sensor (CTS) available at the department used for measuring thin films on surfaces. The CTS focused a polychromatic white light on to the target and a specific distance to the target was assigned to each wavelength via a factory calibration. The distance to the surface being cleaned from the light source was calibrated, and any deviation from that distance represented the thickness of the film present. For the CTS to scan the surface, the sensor was fixed on a clamp that was positioned above an X-Y stepper motor table. The sample was then mounted on to this table which then moved so that the entire surface was scanned. The size of the scanned region and the step size were inputted by the user into a Python code that thereafter controlled the movement of the table. Due to limitations on the movement of the table, the sample size was restricted and therefore a different target plate was used in Leeds. The table size was 15 x 15cm and so several target plates were cut to this size so that they could be easily mounted on to the table. Fig. 5.14a and 5.14b show said plate on the test rig and mounted on to the table for CTS analysis. Note that before each sample was loaded on to the CTS table, it was first dried out to avoid any noise in the results from water droplets.

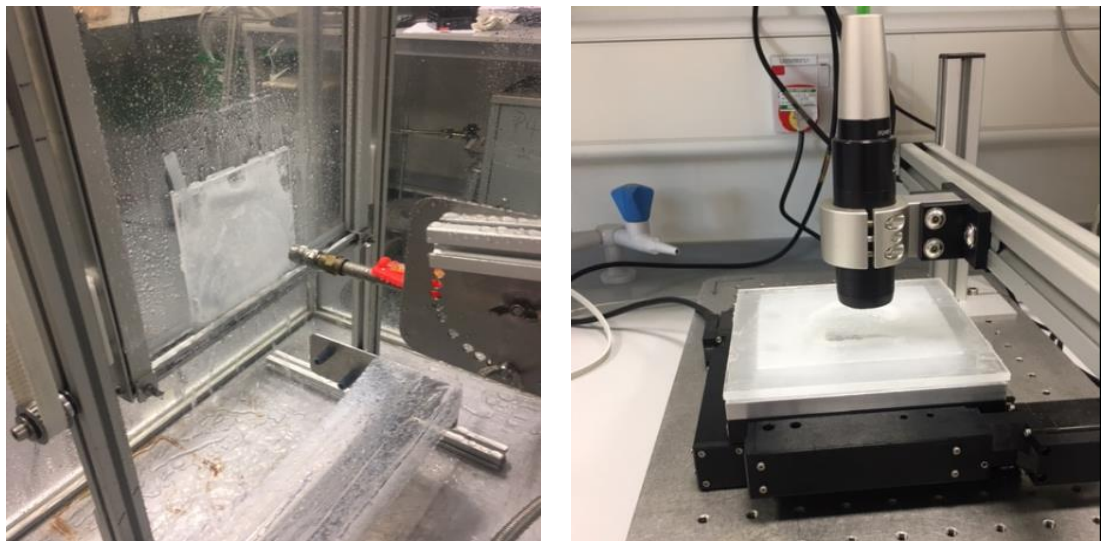


Fig. 5. 14: Left (a) Sample plate on test rig. Right (b) Sample plate mounted on to X-Y table.

Four spray experiments were conducted; for durations of 5 minutes, 15 minutes, 30 minutes and 45 minutes to monitor how the residual film on the surface varied for different cleaning times. Note that the same spray nozzle as the experiments of section 5.2 was used throughout, the same standoff of 50 mm, and the same WSP as was used in chapter 4 for the jet experiments. The WSP layer thickness was set to 1 mm and the flow rate used was 4 lmin^{-1} .

5.3.1 5 minutes cleaning

Fig. 5.15a and 5.15b show the cleaned sample after 5 minutes and the CTS scan respectively.

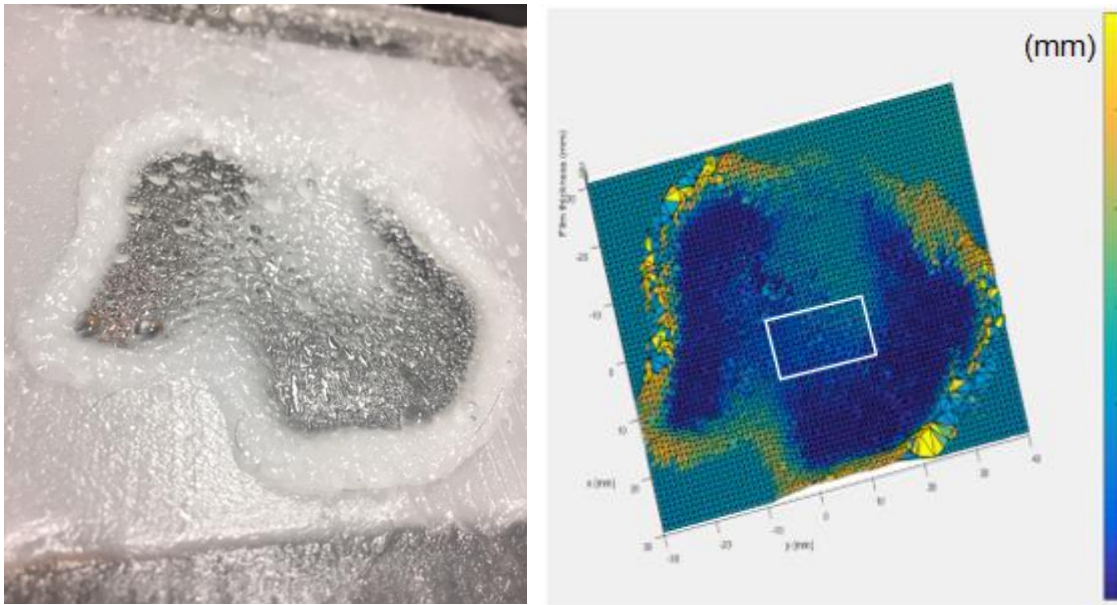


Fig. 5.15: Left (a) 5 minutes cleaning sample. Right (b) 5 minutes cleaning CTS

Firstly, it can be observed that the CTS scan provides a very good visual agreement with the cleaned sample, showing many of the same features as the sample in 5.15a. The ridge of WSP formed on the perimeter is shown by the regions of yellow, corresponding to a maximum thickness of 3mm as shown by the colour bar in Fig. 5.15b. This is where the bulk of the WSP has been displaced radially from the impingement zone of the spray and accumulated into the ridge as was observed in the case of the jet. Note that there are areas in the ridge that show a lower resolution of data points, this is due the light from the CTS going out of focus in certain areas of the ridge, since it had been calibrated to the surface of the Perspex. As such the CTS produced noisy data points which were removed when processing the data, thus the areas of low resolution. However, the characteristics of the ridge are still well represented. The central area of the cleaned region has been virtually unremoved, as the colour corresponds to that of the uncleaned area of the surrounding WSP. The areas closer to the perimeter and to the ridge appear to be far cleaner as they are represented by areas of blue in Fig. 5.15b. However, when looking at 5.15a it is clear that this is not in fact fully clean and there is an obvious residual film still present on the surface. By increasing the resolution of the colour bar and zooming in on the region enclosed by the white square in Fig. 5.15b, it can be seen in more detail the characteristics of the residual film. This is shown in Fig. 5.16.

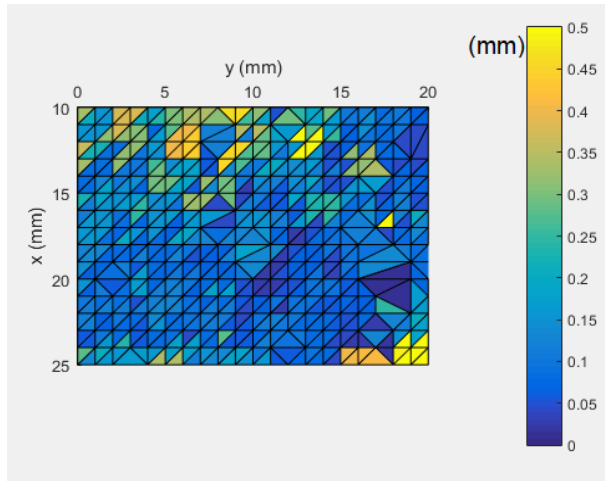


Fig. 5. 16: Close-up of highlighted region in 5.15b.

Despite the region highlighted in Fig. 5.15b appearing almost fully clean, as it is shown as blue on the larger colour scale, when increasing the resolution of the scale and looking at thicknesses from 0-0.5 mm, the extent of the residual film becomes more apparent. Very few pixels are fully clean, deep blue, in Fig. 5.16 and there is an omnipresent residual film of approximately 0.1-0.2 mm left on the surface. There are also peaks of up to 0.5 mm in this region.

5.3.2 15 minutes cleaning

A new sample was created, and it was then cleaned using the spray under the same conditions but for 15 minutes. The resulting cleaned sample and CTS scan results are shown in Fig 5.17a and 5.17b respectively.

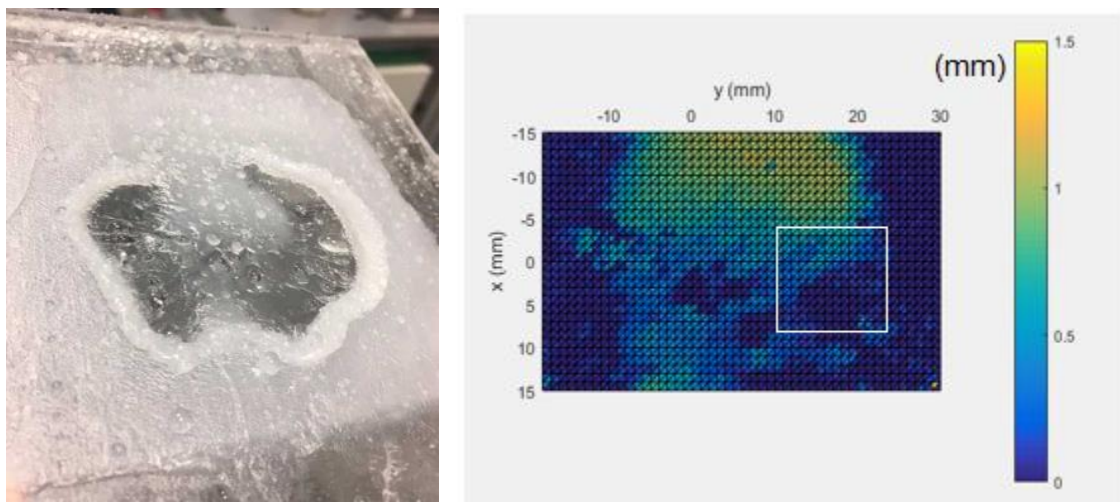


Fig. 5. 17: Left (a) 15 minutes cleaning sample. Right (b) 15 minutes cleaning CTS

In this case the CTS scan was focused inside the cleaned region as this was of primary interest. When looking at the central region it can be observed that again the CTS

provides good agreement with what can be seen from the sample. When looking at the case in 5.16b after 5 minutes, there is a larger area of deep blue in Fig. 5.17b after 15 minutes. This can be confirmed when looking at 5.17a as there are clearly more areas of apparent transparency on the surface. There is however still a large area of WSP in the centre that appears to remain uncanceled, albeit slightly reduced in size compared to the 5-minute case. By repeating the same process as the 5-minute case and zooming in on the region highlighted in Fig. 5.17b, the residual film can be viewed in more detail to see how clean the areas of deep blue really are. This is shown in Fig. 5.18.

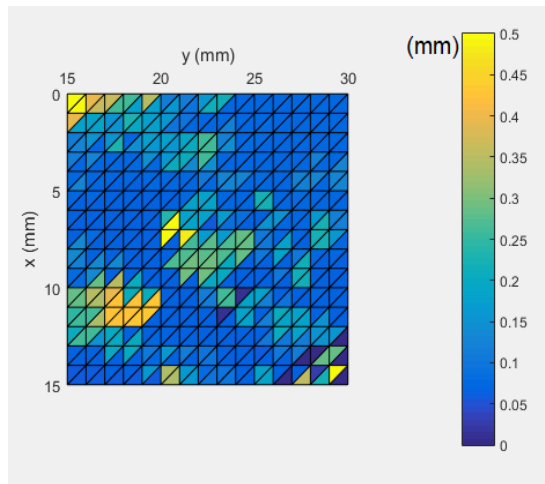


Fig. 5. 18: Close-up of highlighted region.

Again, by looking at a section of the surface that would appear clean on a greater colour scale, by increasing the resolution it becomes clear that it is not in fact clean but the surface is still mostly covered by a residual film. There are very few pixels in Fig. 5.18 that have an absolute zero value and most of the region is covered by a film of approximately 0.1 mm.

5.3.3 30 minutes cleaning

Another sample was then cleaned for 30 minutes and the results are shown in Fig 6.19a and Fig. 5.19b.

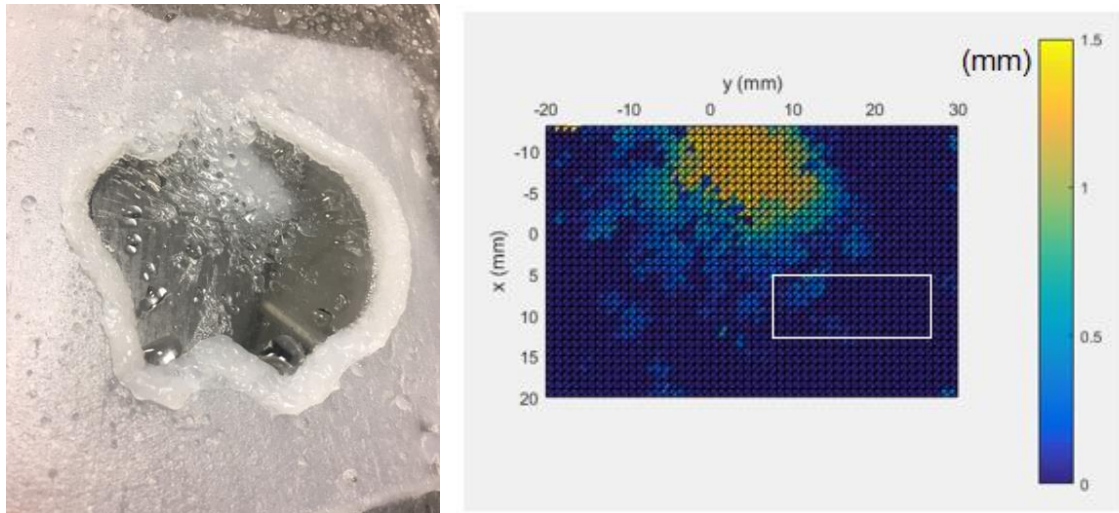


Fig. 5. 19: Left (a) 30 minutes cleaning sample. Right (b) 30 minutes cleaning CTS.

Fig. 5.19a and 5.19b show that after a further 15 minutes cleaning, the residual film on the surface becomes less apparent. In Fig. 5.19a there is a large area of transparency on the surface that to the naked eye appears clean. Once again, the CTS shows an accurate representation of the surface and there are large areas of deep blue that represent no residual film present. The limit of the resolution of the CTS is a nanometre, so whilst this appears to be a clean surface there could be the presence of a film below this scale. There is, as in previous cases, still an area in the centre of the cleaned region that has not been cleaned. This is smaller in surface area in this case, but the colour bar would suggest that in this case it is slightly thicker than in the 15-minute case. This implies that some material has been shifted to the centre, as in places the film thickness is higher than the original film thickness of 1mm. This however could also be due to an irregularity in the application of the film. The region highlighted in 5.19b is shown to a higher resolution in Fig. 5.20.

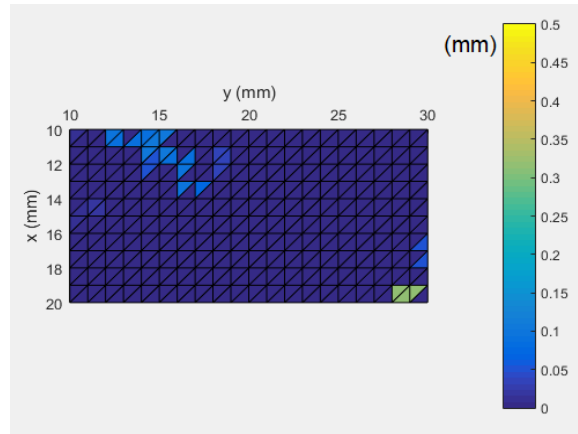


Fig. 5. 20: Close-up of highlighted region.

In this case the higher resolution image of the surface shows that the surface is genuinely clean in the regions of blue shown in Fig. 5.19b. Fig. 5.20 shows that the vast majority of the area highlighted has zero film thickness, with a low number of pixels containing any residual film at all. Prolonged exposure to the spray has removed most of the material in this region.

5.3.4 45 minutes cleaning

Finally, the spray was then run for 45 minutes, the results of which are shown in Fig. 5.21a and 5.21b.

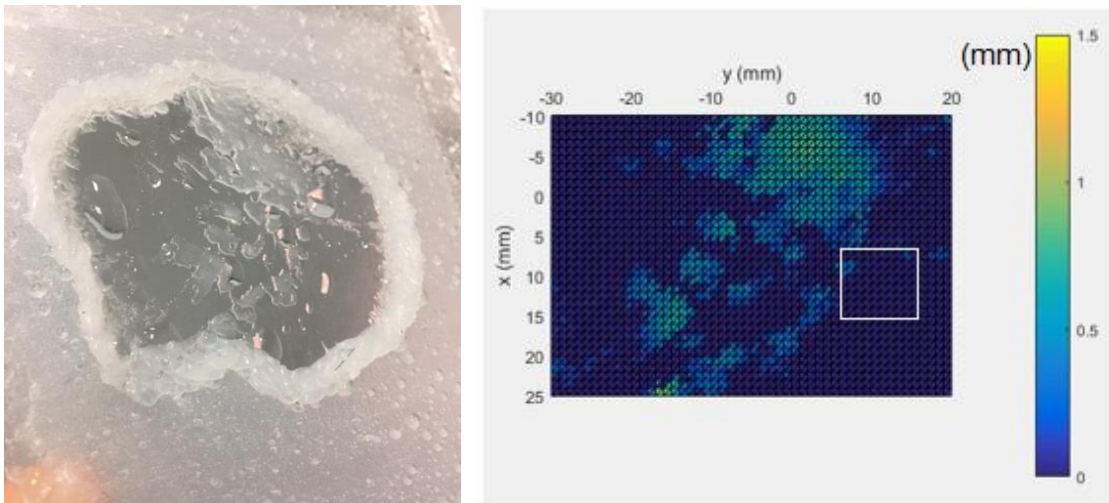


Fig. 5. 21: Left (a) 45 minutes cleaning sample. Right (b) 45 minutes CTS.

After 45 minutes cleaning, the sample again shows large areas of transparency in 5.21a and large regions of zero film thickness according to the CTS scan. There is again an area of uncleaned WSP in the centre, which in this case appears less thick than the

surrounding film unlike the case of the 30 minutes cleaning sample. This would suggest that the mechanism of soil being pushed into the centre and accumulating to a greater thickness was anomalous and more likely due to an irregularity in the application of the film. The higher resolution image of the surface is shown in Fig. 5.22.

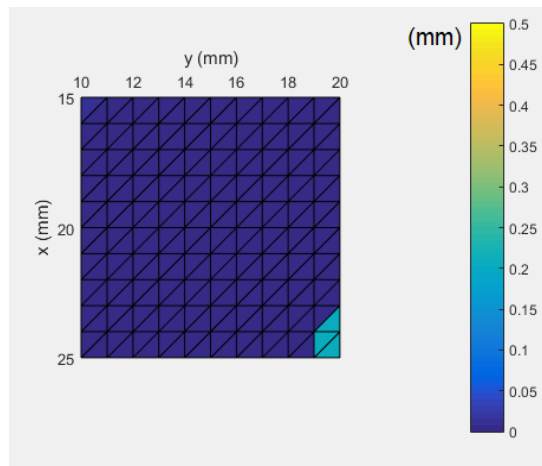


Fig. 5. 22: Close-up of highlighted region.

Fig. 5.22 shows that after 45 minutes cleaning the spray has removed most of the material in areas that appear clean. Only 3 pixels in the image contain any residual film. As aforementioned, the CTS can detect films on a nanometre scale, so the resolution could be further increased. However, from this resolution the film thickness is shown to be less than 0.05 mm which can be considered negligible. It can be observed in the clean areas of Fig. 5.15, 5.17, 5.19 and 5.21 that the area is an unusual shape relative to those seen in section 5.2. Rather than representing a circular shape, there are bulges in the shape of the ridge that encloses the cleaned area. This can be attributed to the swirl generated by the nozzle as discussed in section 3.5.

5.4 Effect of flow rate

A study on the effect of flow rate on cleaning performance using the liquid spray was conducted under the parameter space outlined in 5.1.

5.4.1 Thin WSP layer

For the 0.19 mm WSP thickness, Fig. 5.23 shows the cleaned area versus time response for the spray for each flow rate under study. Fig. 5.23 shows how there is a relatively flat response of cleaned area versus time relative to that of the jet.

For the 4 lmin⁻¹, 2.5 lmin⁻¹ and 1 lmin⁻¹ sprays respectively the final cleaned areas are 7032 mm² ($d_{\text{avg}} = 95$ mm) , 4431 mm² (75 mm) and 1681 mm² (46 mm).

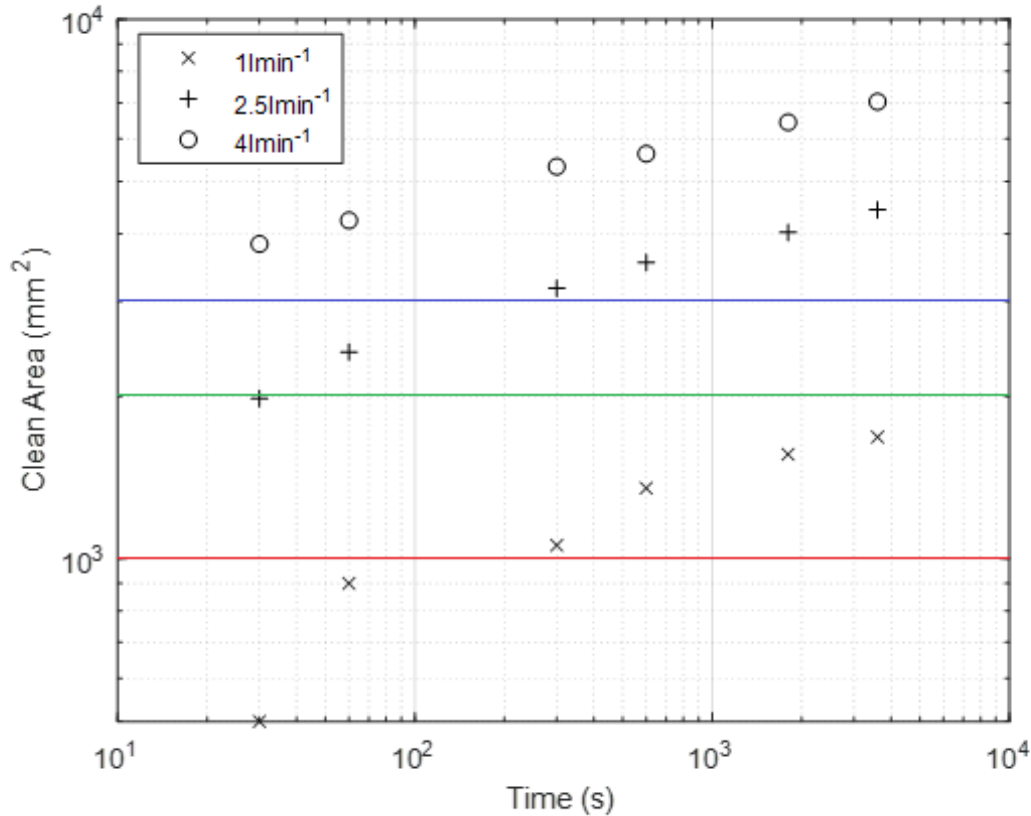


Fig. 5. 23: Cleaned Area versus Time for each flow rate (0.19 mm WSP thickness, water temperature 20 °C, 50 mm standoff) The red, green and blue lines represent the impingement areas from the cone of the spray for the 1, 2.5 and 4 lmin⁻¹ sprays respectively.

Meanwhile the respective growths in cleaned area from the first recorded time, 30 s, to the long-time of one hour are 84%, 124% and 237%. It can be observed from this that the growth in cleaned area becomes larger with decreasing flow rate. This suggests that the adhesive mechanism is predominant as a greater percentage of the material is pushed out radially with the lower flow rates, whilst at 4 lmin⁻¹ the bulk of the material is removed cohesively with progressive impingement of the droplets from the spray. Consider Fig. 5.24b, as flow rate of the spray is increased, the cone impingement area increases relative to the total area cleaned, reducing the area cleaned by the RFZ. In descending order of flow rates, the spray angles, α , of the spray are approximately 64°, 56° and 40°. From trigonometry, the corresponding impingement areas of each spray are 3066 mm² ($d_{\text{avg}} = 62$ mm), 2220 mm² ($d_{\text{avg}} = 53$ mm) and 1040 mm² ($d_{\text{avg}} = 36$ mm) respectively. These are highlighted on Fig. 5.23; with the red, green and blue lines

showing the respective impingement areas of the 1, 2.5 and 4 lmin^{-1} sprays. This shows that the cleaned areas are considerably larger than the impingement areas for each spray. Fig. 5.24 shows a schematic of the spray impinging on a clean wall from a) a side view and b) a front view.

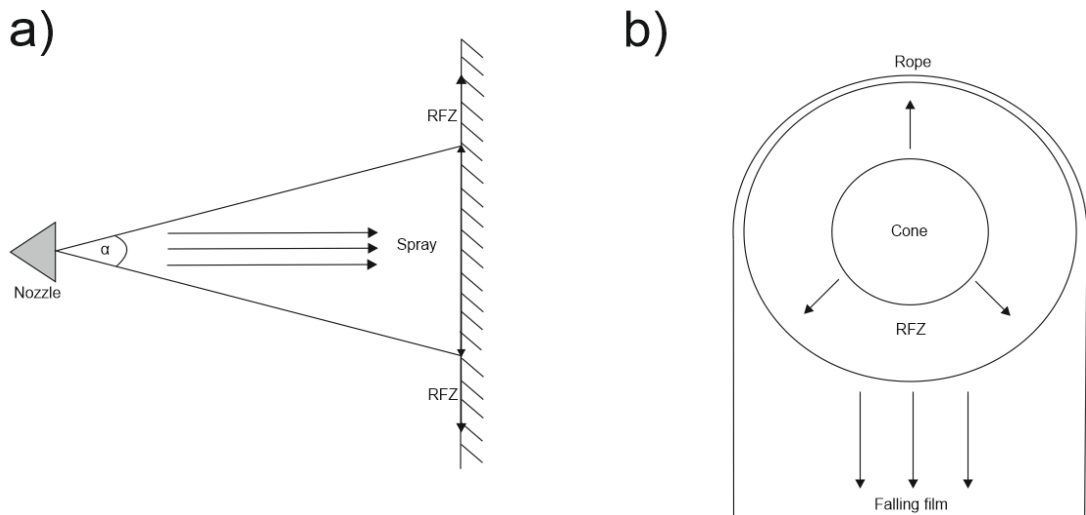


Fig. 5. 24: Full cone spray impingement on clean vertical wall a) side view b) front view.

The cone forms a circular impingement area on the wall and the fluid from the cone forms a RFZ in a similar fashion to the impinging jet. The fluid from the RFZ is then drained in the falling film (see Fig. 5.24b). The similarity with the rope-bound pattern seen in jets shows that cleaning in the RFZ is achieved via the shear stress exerted on the wall, i.e. adhesive removal. Inside the cone the cleaning is achieved by soaking of the layer and erosion from the continuous impingement of droplets. Due to the convex distribution of droplets in the spray used (see Fig. 3.21) the droplet density is concentrated in the centre of the impingement area and less concentrated towards the perimeter of the impingement area. Material in the centre of the cone would therefore be assumed to be cleaned more efficiently. However, when looking at the closeup pictures of the long-time cleaned areas (e.g. Fig. 5.9, 5.11 & 5.13) the regions in the very centre of the cleaned area appear to be covered with a residual film of WSP. Regions outside the centre appear to be cleaned most effectively where the Perspex appears transparent suggesting the presence of no film. This is particularly the case with Fig. 5.17a, 5.19a and 5.21a. Residual films were not observed with the jet, where all the cleaning is done via an adhesive mechanism, except the point at which the jet impinges. This implies this is the most efficient mechanism of soil removal. The spray however largely relies on

cohesive removal inside the cone, which can explain why such residual films are present. Despite outside the cone adhesive removal taking place, there are still large residues present on the surface, particularly in Fig. 5.9, 5.11 and 5.13. Unlike the jet where the force of impingement is concentrated in a fixed point, generating large shear on the surface around the impingement point, the force is dissipated across a much larger region on the surface and as such the shear in the RFZ will be considerably lower. Also due to the two distinct zones in the spray case, i.e. the cone impingement zone and the RFZ, there is a transport of WSP required from the cone to the RFZ and subsequently to the ridge for the area to be fully cleaned. This is shown schematically in Fig. 5.25.

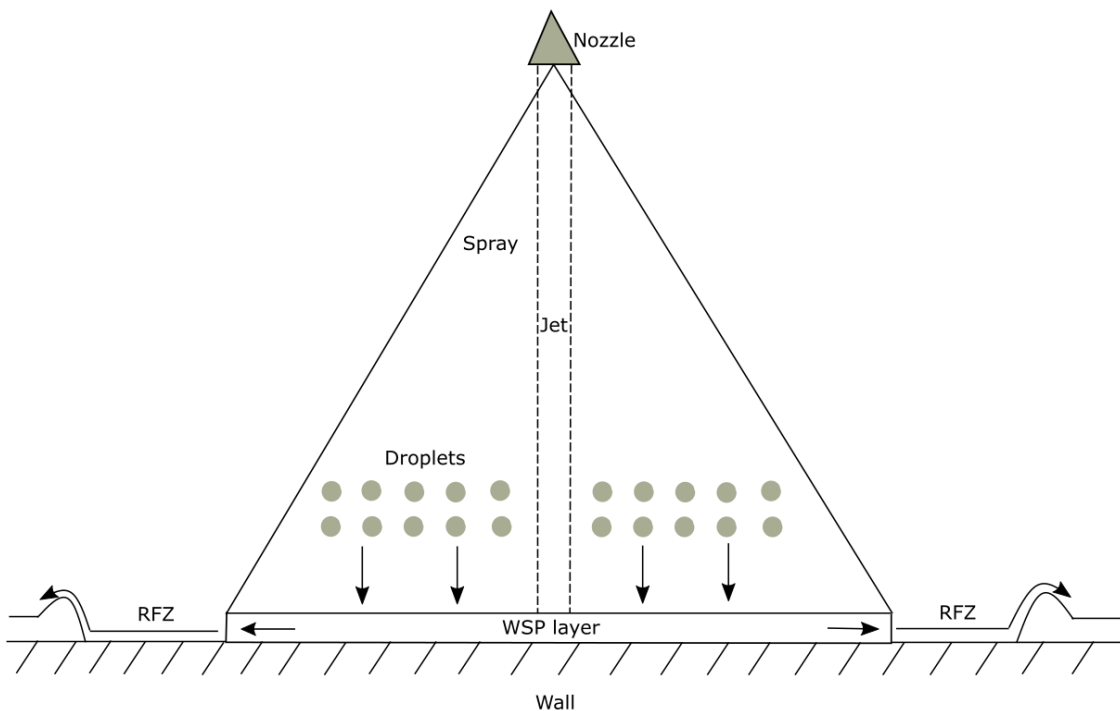


Fig. 5. 25: Spray soil removal mechanism schematic.

Fig. 5.25 shows a horizontal wall contrary to a vertical wall but the same mechanisms apply, the only difference being on a vertical wall the fluid from the RFZ is drained via a falling film. The fluid in the cone of the spray forms an impingement zone on the WSP layer where the continuous impingement of droplets promotes cohesive removal of the layer via soaking and erosion. Outside the cone, a RFZ is formed as shown in Fig. 5.24. Here the fluid moves out radially and adhesively removes the WSP. Unlike the jet which exhibits much higher shear in this region and fully penetrates the layer to the substrate, despite adhesive removal occurring there is still a thin residual layer of WSP on the surface. The adhesive removal by the spray is evident in the WSP ridge formation on the perimeter of the cleaned area. This is achieved via a roll-up mechanism, as was observed in the jet and discussed in Chapter 4. The WSP inside the cone must be

transported from the cone to the RFZ in order for the area to be cleaned and transported to the ridge. However, as there is negligible radial movement of the fluid inside the cone, there is poor transport from inside the cone to outside. As such there remains a bulk of material inside the cone that is 'trapped' and remains as the large residues that were observed in section 5.3. Consider material in the very centre of the cone, there is a large distance for the WSP to be transported from the centre to the RFZ. Contrary to the jet, which is drawn in Fig. 5.25 for comparison, the radius of the impingement zone is considerably smaller and the transport of the material cohesively removed occurs easily and rapidly. Also, as the energy is concentrated in such a small area relative to the spray, the force and shear stress exerted on the surface are much higher, increasing the efficacy of the transport.

5.5 Effect of WSP thickness

A study of the effect of WSP layer thickness on cleaning performance of the spray was conducted under the parameter space outlined in 5.1.

5.5.1 High flow

The response of clean area versus time for the 4 lmin^{-1} spray for each WSP thickness is shown in Fig. 5.26.

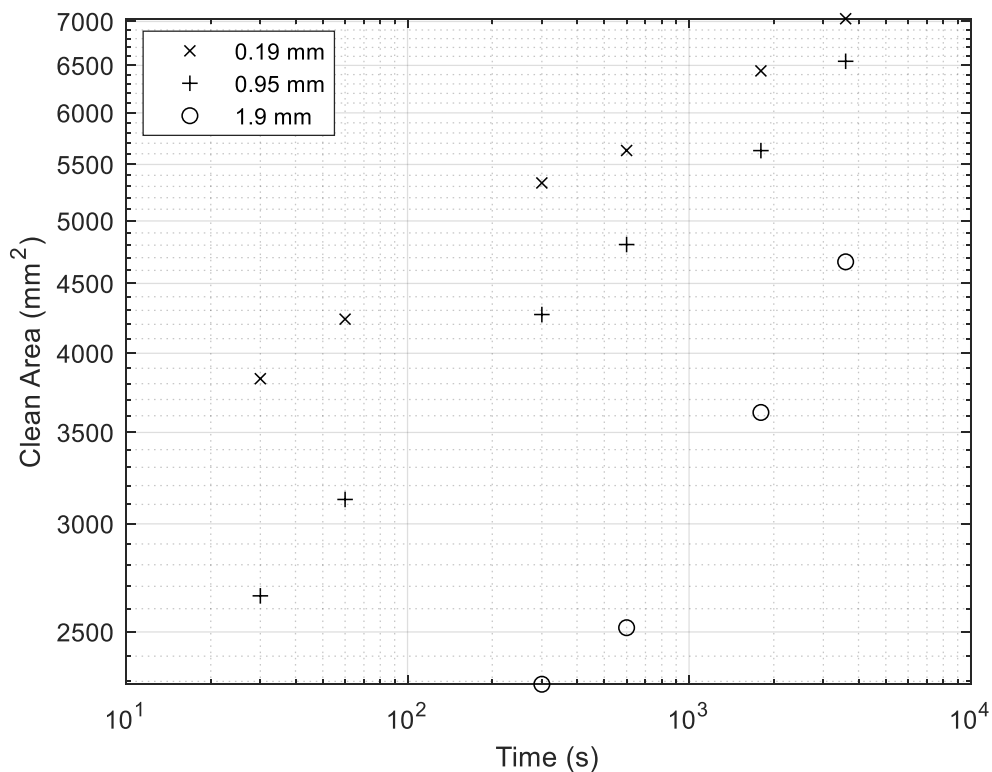


Fig. 5. 26: Cleaned area versus time (4 l min⁻¹ flow rate, water temperature 20 °C, 50 mm standoff).

When compared to Fig. 4.14, the same flow conditions for the jet, Fig. 5.26 highlights the disparity between final cleaned area values reached between WSP thicknesses for the same flow rate. In Fig. 4.14 all the curves converge to a common value after an hour of cleaning, however the spray case in Fig. 5.26 shows a large difference particularly for the thickest film of 1.9 mm. The two thinner layers of 0.95 mm and 0.19 mm show a small difference between final cleaned areas at 4 lmin⁻¹. As aforementioned, large residual films exist inside these cleaned areas and they do not represent a fully cleaned surface as the jet did.

5.5.2 Medium flow

Fig. 5.27 shows the response of cleaned area versus time for each WSP layer thickness at 2.5 lmin⁻¹.

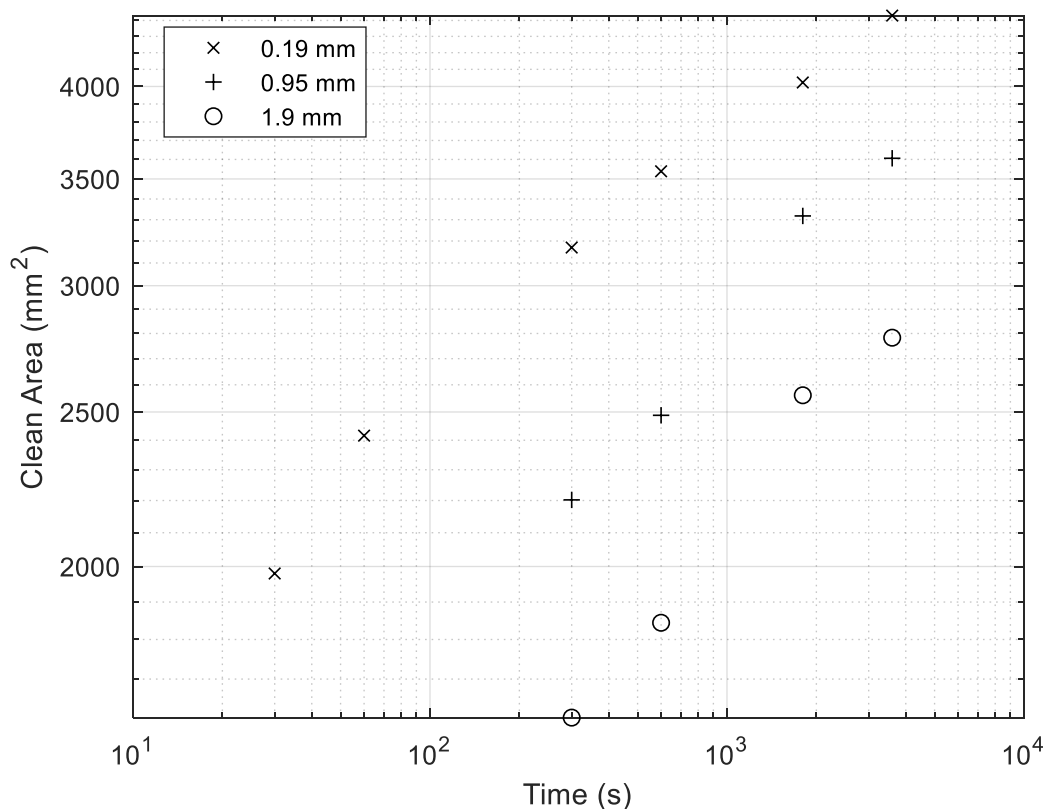


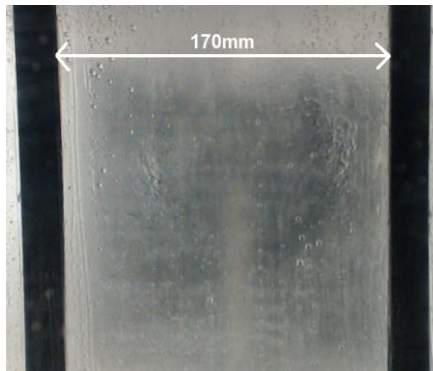
Fig. 5. 27: Cleaned area versus time (2.5 l min⁻¹ flow rate, 20 °C, 50 mm standoff).

Fig. 5.27 shows there is a smaller disparity between the 1.9 mm and 0.19 mm layers than shown in the 4 lmin⁻¹ case of Fig. 5.26. As aforementioned, a greater percentage of

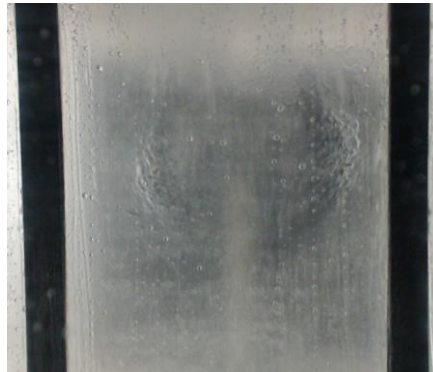
the cleaning for the lower flow rates is achieved via adhesive removal where there is a larger relative growth in the cleaned area from time 30 s to the long-time. For larger WSP layers where cohesive removal is made more difficult, adhesive removal occurs more rapidly whilst the cohesive removal inside the cone is prolonged (e.g. Fig. 5.10). This explains the cleaned areas of the highest and lowest thickness layers are closer together for the 2.5 lmin^{-1} spray. Fig. 5.13 demonstrates however there is a particularly large residual film in the region cleaned via the impinging cone where the cohesive mechanism is predominant. No cleaned area versus time graph is presented for the 1 lmin^{-1} spray since no area was cleaned for the two thicker layers. The force exerted on the surface on the higher thickness layers was unable to penetrate to the surface of the Perspex.

5.6 Effect of standoff distance

Unlike the jet, where standoff distance in the range observed on the racks (50 – 200 mm) had little to no effect on the cleaning performance, the standoff of the spray was significant. Due to the spray angle induced by the nozzle, increasing the standoff distance proportionally increased the impingement area of the spray on the surface. Whilst all previous results in this chapter have been conducted at 50 mm, a secondary standoff distance of 125 mm was studied (equivalent to the distance used for jet experiments). The time lapse for the 2.5 lmin^{-1} spray at this standoff, on a 0.19 mm WSP layer, is presented in Fig. 5.28 and the closeup of long-time cleaned area (one hour) in Fig. 5.29.



(a)



(b)

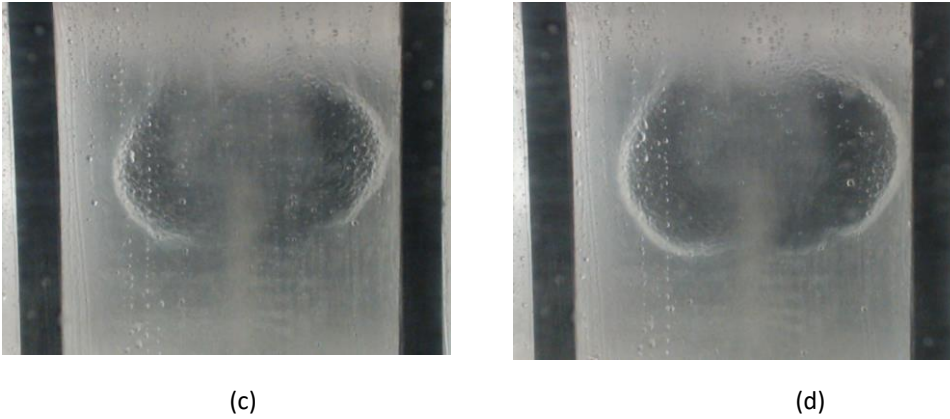


Fig. 5. 28: Time lapse removal for 2.5 lmin^{-1} spray, 0.19 mm WSP thickness, water temperature 20°C , 125 mm standoff (a) 30 s (b) 60 s (c) 300 s (d) 600 s.



Fig. 5. 29: Cleaned area close-up after one hour of cleaning: 2.5 lmin^{-1} spray, 0.19 mm WSP thickness, water temperature 20°C , 125 mm standoff.

In comparison to the same flow conditions and layer thickness (see Fig. 5.3), there is a significant difference in the cleaning performance of the 2.5 lmin^{-1} spray from the further standoff distance of 125 mm. Only after 300 s does any soil removal on the surface become apparent and this is only around the perimeter of the cone where the adhesive mechanism is predominant. Whilst it may appear cleaned from the naked eye looking through the camera behind the Perspex, the closeup of Fig. 5.29 shows that there is a residual film covering the entire cleaned region. Material has been pushed outward forming a ridge but no areas inside the ridge appear fully clean. At 50 mm, despite large areas containing residue, there were areas where the Perspex appeared transparent and fully clean. When the standoff distance is increased, the droplets in the spray are exposed more to drag force, meaning they impact the surface with a lower velocity and

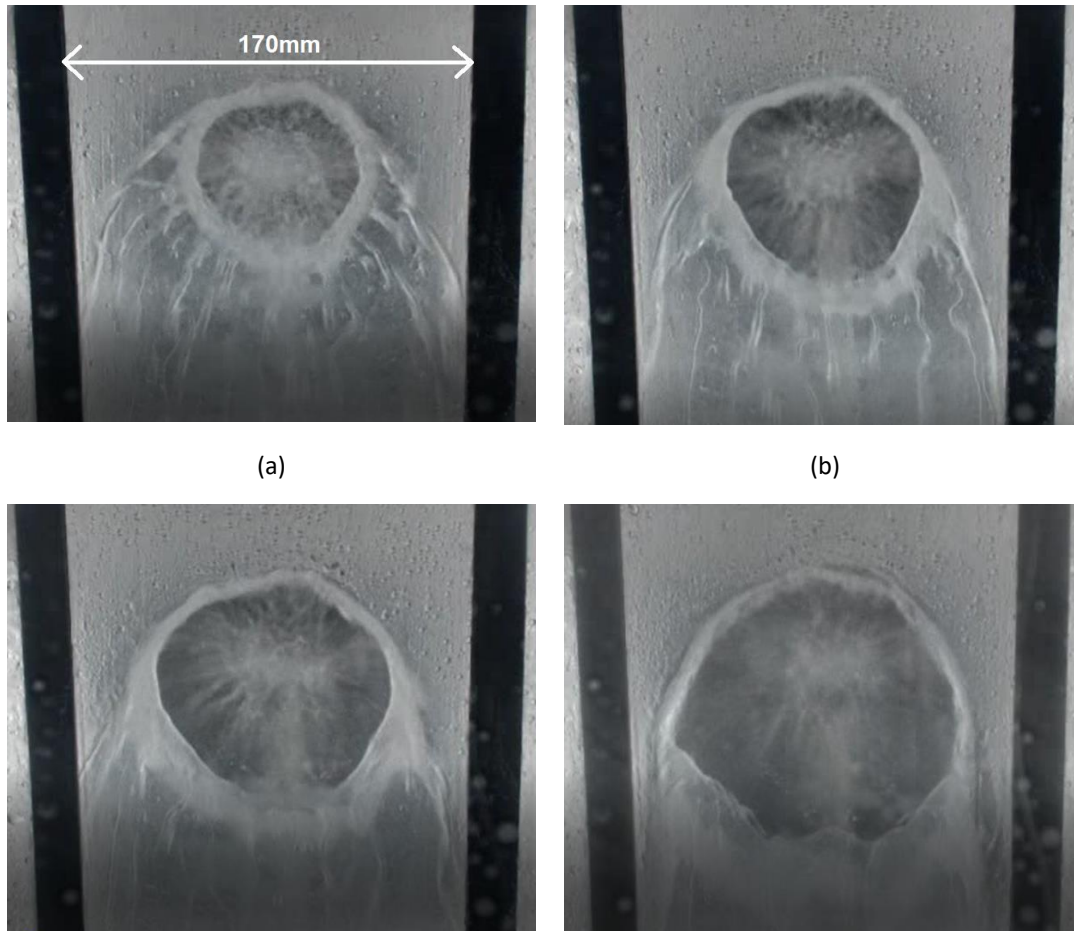
thus the impingement force exerted on the surface is lower. Energy available for cleaning is also dissipated across a larger area than at closer standoff distances, and thus the efficiency of removal per unit area is decreased. The one advantage to cleaning with sprays from larger standoff distances is the area cleaned being greater. With the addition of surfactant and/or heat, the residual film observed in Fig. 5.29 may be removed.

5.7 Effect of water temperature

A study of the effect of water temperature on cleaning performance of the spray was then conducted. The same two temperatures above 20 °C were under study as were with the jet, 40 °C and 60 °C.

5.7.1 Medium flow, thin WSP layer, medium temperature

Fig. 5.30 shows the time lapse of soil removal for the 2.5 lmin⁻¹ spray on a 0.19 mm layer of WSP at 40 °C and Fig. 5.31 shows a closeup of the long-time clean area (300 s cleaning).



(c)

(d)

Fig. 5. 30: Time lapse removal for 2.5 lmin^{-1} spray, 0.19 mm WSP thickness, water temperature $40 \text{ }^{\circ}\text{C}$, 50 mm standoff
(a) 10 s (b) 30 s (c) 60 s (d) 120 s



Fig. 5. 31: Left: long-time (300 s) clean area close-up (2.5 lmin^{-1} spray, 0.19 mm WSP thickness, water temperature $40 \text{ }^{\circ}\text{C}$), Right: long-time cleaned area close-up (2.5 lmin^{-1} spray, 0.19 mm WSP thickness, water temperature 20°C).

The image on the left of Fig. 5.31 shows there is a clear increase in cleaning performance when increasing the water temperature to $40 \text{ }^{\circ}\text{C}$ from $20 \text{ }^{\circ}\text{C}$ (right of Fig. 5.31). As was observed with cleaning at elevated temperatures with the jet, the $40 \text{ }^{\circ}\text{C}$ water exceeds the drop point of the WSP and the rheology changes such that it behaves more like a liquid. After 120 s the heat transfer from the sprayed fluid to the layer has resulted in the layer reaching the drop point temperature and most of the WSP in contact with the flow, including the falling film, is washed off the surface. Fig. 5.31, the clean area after 300 s, shows that the residual film observed with the spray at $20 \text{ }^{\circ}\text{C}$ has been completely removed to the naked eye.

5.7.2 Medium flow, thin WSP layer, high temperature

Fig. 5.32 shows the time lapse removal for the 2.5 lmin^{-1} spray on a 0.19 mm WSP layer using $60 \text{ }^\circ\text{C}$ water and 5.32 shows the closeup of the clean area

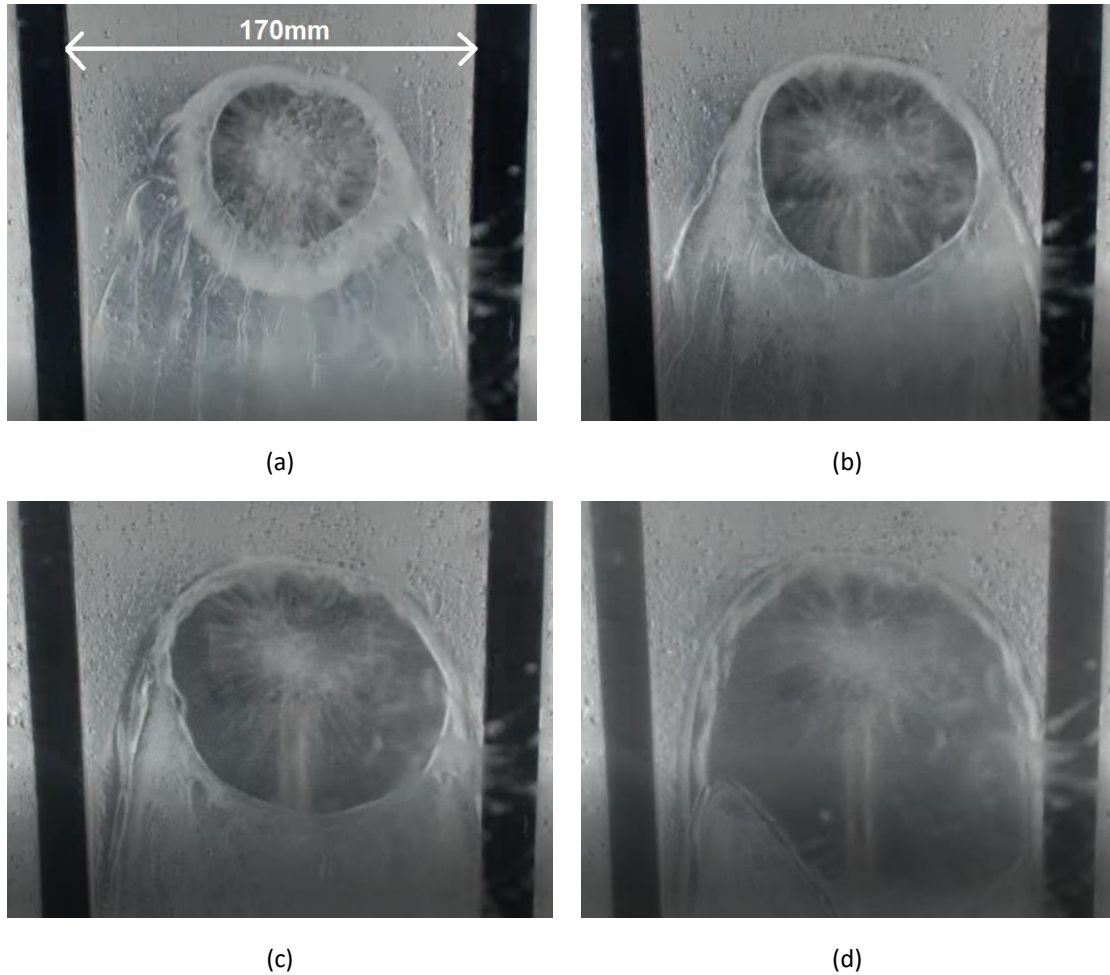


Fig. 5. 32: Time lapse removal for 2.5 lmin^{-1} spray, 0.19 mm WSP thickness, water temperature $60 \text{ }^\circ\text{C}$, 50 mm standoff
(a) 10 s (b) 30s (c) 60 s (d) 120 s.



Fig. 5. 33: Long-time (300 s) clean area close up (2.5 lmin⁻¹ spray, 0.19 mm WSP thickness, water temperature 60 °C).

When the temperature is increased further by 20 °C to 60 °C it can be observed that the heat transfer process is accelerated, and the areas cleaned are larger in Fig. 5.32 at the same points as those at 40 °C (see Fig. 5.30). Once again, the closeup of the clean area after 300 s is shown in Fig. 5.33, showing how the residual film has been completely removed, at least to the naked eye. Further CTS tests could be conducted on the higher temperature samples to check that the surface is clean on the nanoscale, this was not done due to access to the CTS technology being restricted to the research visit to Cambridge. The clean area versus time curves at 2.5 lmin⁻¹ for each temperature are presented in Fig. 5.34.

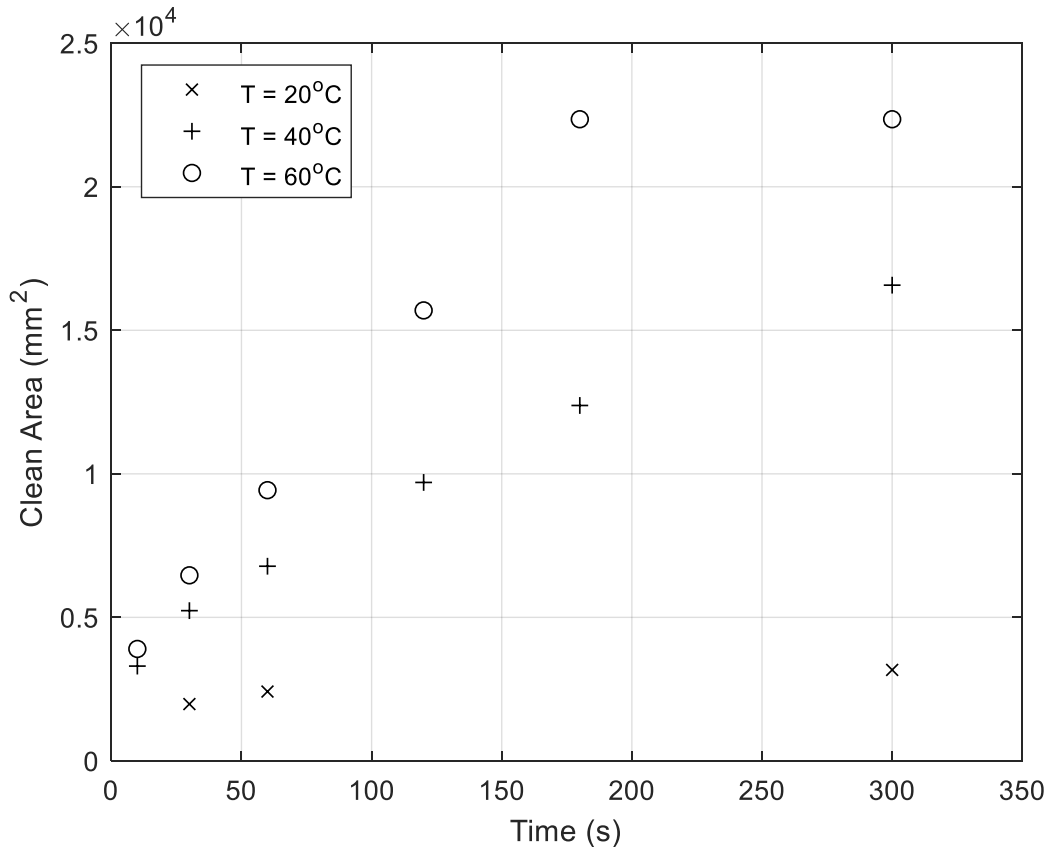


Fig. 5. 34: Clean area versus time, 2.5 lmin⁻¹ spray, 0.19 mm WSP thickness, water temperature 20 °C, 40 °C and 60 °C (50 mm standoff).

Fig. 5.34 shows the drastic effect of raising the water temperature to 40 °C and 60 °C, where the melting point of the WSP is encompassed and phase transition to a mobile phase occurs. The shear on the surface exerted by the spray is sufficient to wash all the WSP in contact with the flow from the surface at 60 °C. Fig. 5.34 shows how this curve

plateaus after 180 s. Due to the lower temperature in the 40 °C spray, the heat transfer to the WSP takes longer to cause phase transition and the rate of soil removal is lower. However, after 300 s the 40 °C curve is still rising and, given more time, it can be expected to approach a similar value as the 60 °C spray. Finally, Fig. 5.35 shows the time lapse for a 1 lmin⁻¹ spray on a 0.95 mm WSP layer at 40 °C and Fig. 5.36 the closeup after 300 s. Reiterating what was observed with the previous higher temperature experiments, the 1 lmin⁻¹ spray removes any residual WSP on the surface at 40 °C when looking at the closeup of the long-time clean area. The material in the falling film has washed the material downstream of the impingement area of the spray.

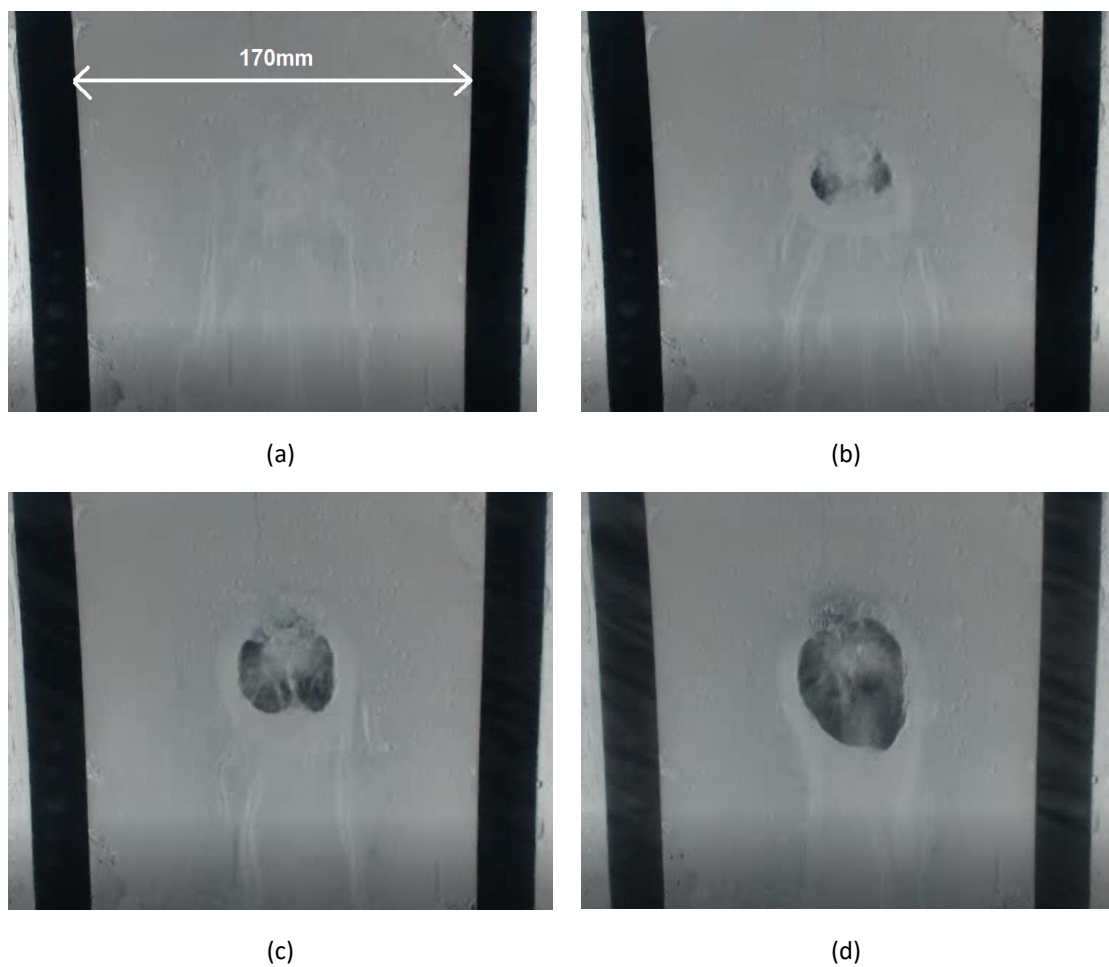


Fig. 5. 35: Time lapse removal for 1 lmin⁻¹ spray, 0.95 mm WSP thickness, water temperature 40 °C, 50 mm standoff (a) 10 s (b) 30 s (c) 60 s (d) 120 s.



Fig. 5. 36: Long-time (300 s) clean area close up (1 lmin⁻¹ spray, 0.95 mm WSP thickness, water temperature 40 °C).

5.8 Energy efficiency

As described in section 3.5, the nozzle discharge coefficient of the spray used was 0.014 lmin⁻¹Pa^{-0.5}, which was 44% of the counterpart jet. This means that, for an equivalent flow rate, the power consumption of the spray was 5.17 times greater than the jet in accordance with equation 3.22. The graph of area relative to the long-time clean area (A/A^*) versus energy for the spray on a 0.19 mm WSP layer is shown in Fig. 5.37.

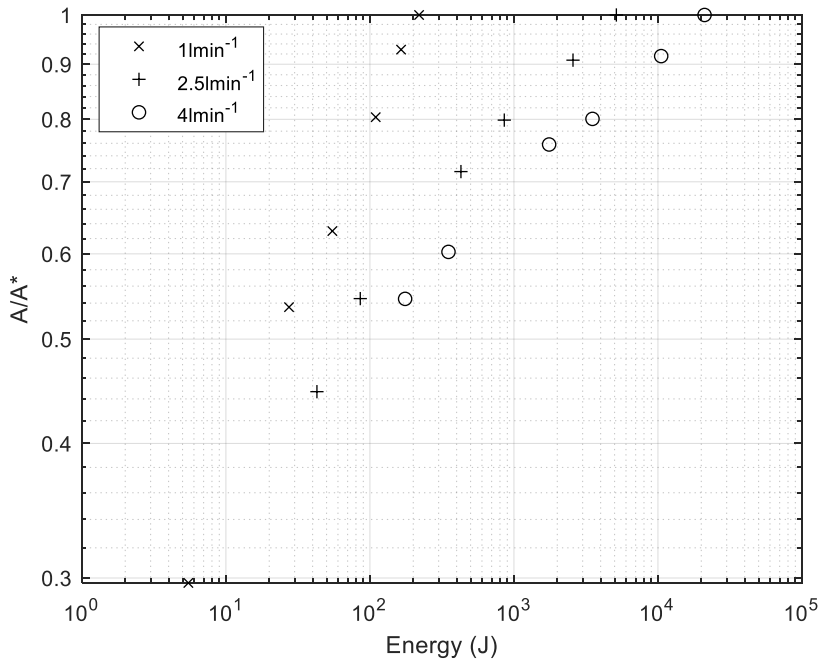


Fig. 5. 37: Area relative to long-time value at each time plotted against energy input to the cleaning process (0.19 mm WSP thickness, water temperature 20 °C).

Similar to the jet (Fig. 4.16) each spray requires less energy to reach A^* as flow rate is decreased. Due to the higher power consumption of the spray, the total energy input at long-time is 5.17 times greater for each flow rate. Due to the residual films on the surface after cleaning with the spray, the area removed displayed in the 20 °C was that which was bound by the ridge and did not represent a visually clean area as was the case with the jet. However, at temperatures above the melting point of the WSP where the residual film on the surface is negligible, the area can be considered fully clean. Fig. 5.38 shows the clean area versus time curves for both the jet and the spray on a 1.9 mm layer of WSP at 60 °C.

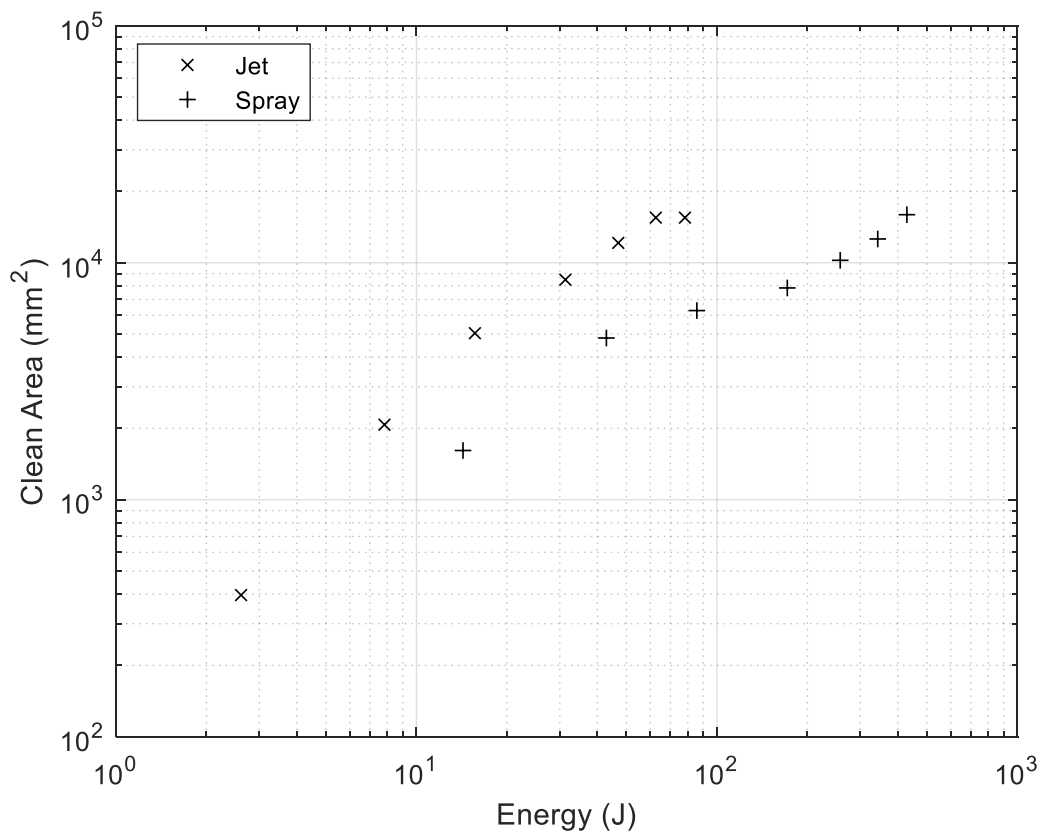


Fig. 5.38: Clean Area versus Energy, 2.5 lmin⁻¹ jet and spray, 1.9 mm WSP thickness, water temperature 60 °C.

Fig. 5.38 shows how the area cleaned by the jet increases more rapidly than the spray, however the two cleaning methods reach a very similar value after 300 s of cleaning. After 300 s the respective clean areas of the jet and spray are 15500 and 15951 mm² respectively. As previously discussed, due to the nozzle discharge coefficient of the spray being 44% that of the jet, the power and subsequent energy consumption after 300 s of cleaning is 429 J versus 78 J of the jet. Whilst the spray yields a fractionally larger clean area, the considerably higher energy input does not warrant this. For these

particular nozzles, use of the jet would be a considerably more efficient option to use for cleaning. The jet also has the advantage of cleaning the surface at room temperature and does not require additional heat to remove residual films.

5.9 Summary

In this chapter the experimental results cleaning a vertical Perspex wall coated with WSP via a liquid spray have been presented. A distinct difference in cleaning mechanisms and performance at 20 °C was observed. The spray exhibited similar characteristics to the liquid jet, i.e. the RFZ of liquid outside the impingement of the cone and a falling film on the wall, however the removal of material in the cone was very inefficient compared to the jet. Residual films were observed inside the cone whereas these were not observed with the jet. Due to the energy from the spray being dissipated across a much larger area than the jet, the efficiency of cohesive removal in the cone per unit area was considerably less. Adhesive removal outside the impingement area, where the RFZ formed, was more effective in areas but still large residual films were present in some cases. This is due to the velocity and shear in the RFZ being considerably less than the counterpart jet. Also, it was identified that a transport of material within the cone to the RFZ, in order to subsequently be transported to the ridge, was required to fully clean the area to an efficiency seen with the jet. With the jet all the flow is concentrated on the surface in an area equal to the cross-sectional area of the jet, so the velocity of the fluid in the RFZ is much higher than the spray. Unlike the jet the standoff distance of the nozzle had a big impact on cleaning performance due to the spray angle induced by the nozzle. Droplet velocities are reduced due to longer exposure to drag forces and the energy for cleaning is dissipated over even larger areas on the surface. As a result, no discernible cleaning was observed from a 125 mm standoff. This was however at 20 °C and with addition of heat and surfactant, cleaning at larger standoffs could be advantageous. If the film is removed, then the area cleaned is far greater. Similar to the jet, at temperatures above the drop point of the WSP any soil in contact with the flow was removed. Using an energy framework it was derived that, for an equivalent flow rate, the energy consumption of the spray was approximately 5 times greater than the jet for the nozzles under study. Given the greater cleaning performance of the jet at room temperature, in this case a jet would be a considerably more viable and efficient option. However, at elevated temperatures, the energy to heat a volume of water to higher temperatures far exceeds that of running the jet and spray. Referring back to section 4.2.7, the cost of heating 20 litres of water by 20 °C was 1.674 MJ, which makes the cost of running the jet for 5 minutes at 4 lmin⁻¹ (320 J) negligible. This will also apply to the spray, so given the spray offers a larger coverage and area cleaned, provided the water temperature is above the drop point of

the material being cleaned, the spray could be a more appealing option. This study has also only considered the cleaning of WSP, easier to clean soils with a lower yield may be sufficiently cleaned at room temperature by the spray and the larger coverage of the spray could again be advantageous. The next chapter reviews spray cleaning computationally, by modelling the impingement of a single droplet on a surface, in order to gain more of an understanding of the soil removal mechanisms at play.

Chapter 6

Numerical Results

6.1 Introduction

This chapter presents the results obtained numerically using the CFD software COMSOL, as outlined in 3.8 and 3.9. The numerical work focused on, firstly, the impingement of a single droplet on to both a wetted wall and a wall with a film of water on the surface. To recap, wetted wall is the terminology for a wall in COMSOL that is given a specified contact angle, the wall in this case is in fact dry. Two variables were considered, the contact angle of the wetted wall and the thickness of the water film on the surface. The purpose of this part of the research was to try and understand the cleaning mechanisms of sprays impinging on to a soil layer by reducing the problem to that of a single droplet, which represents one of many projected by the spray on to the surface. There was little work found in the literature that considered droplet impingement from a cleaning context, so this was of particular interest. In the model setup the wetted wall represented WSP which was given the contact angle of 83° derived in 3.3.3.2. Progressive wetting by the spray, as the surface soil is removed, then lowers the contact angle and simulations were run in decreasing increments, to 0° , for the wetted wall case. In addition, as the spraying process continues, assuming there is no drainage of the liquid, the film of water builds on the surface until its thickness is equivalent to the droplet diameter. Qualitative behaviour of the droplet on the surface was recorded and the shear stress exerted on the wall measured in each simulation to gauge the impact each parameter had on cleaning performance. Secondly, jet impingement was studied as described in 3.9. For this study the only variable was the inlet velocity of the jet, which corresponded to that for each flow rate studied in the experimental work of Chapter 4.

6.2 Dry wall

The first case under study was that of a dry wall with no water film present, represented by the model shown in Fig. 3.23. The initial contact angle of water and the WSP used for the experiments was measured in 3.3.3.2 to be 83° . With the continuous impingement of droplets, the WSP surface is wetted and the contact angle lowers to that of water-water, 0° . Simulations were run for four contact angles; 83° , 60° , 40° , 20° and 0° .

6.2.1 Volume fraction of fluid time lapse images

Animations of the droplet impinging on to the surface were exported from COMSOL, plotting the volume fraction of fluid using the level set function, Φ . Water ($\Phi = 1$) is

represented by blue whilst air ($\Phi = 0$) is represented by red. Images were taken from these animations for various points of interest throughout the time of study.

6.2.1.1 0° contact angle

The volume fraction time lapse for the 0° case is shown in Fig. 6.1.

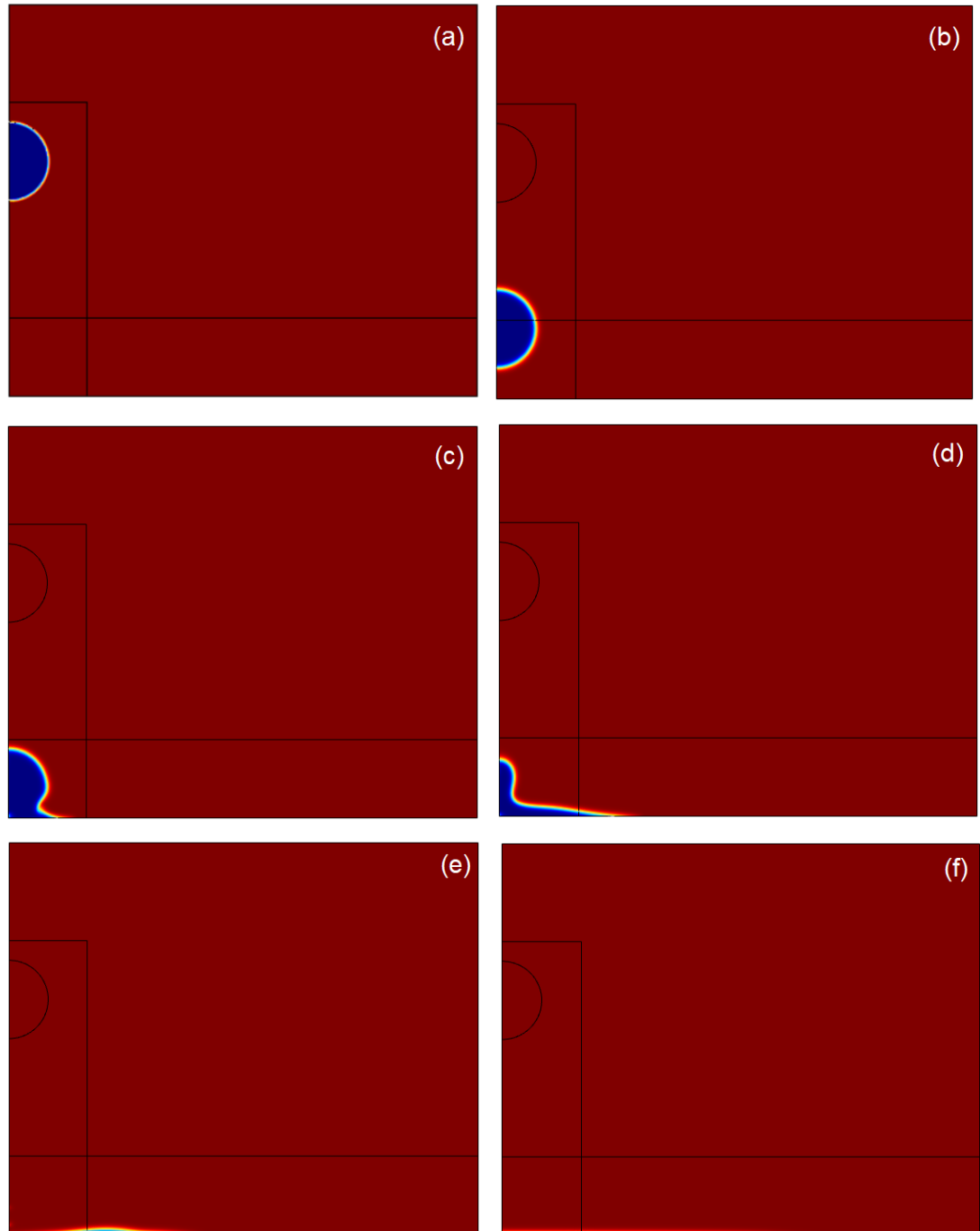


Fig. 6. 1: Volume fraction of fluid time lapse, 0° wetted wall. (a) $t = 0$ ms, (b) $t = 3$ ms, (c) $t = 3.6$ ms, (d) $t = 4.1$ ms. (e) $t = 4.7$ ms and (f) $t = 15$ ms.

Fig. 6.1 shows the droplet descend from its initial static position above the surface. To recap, the acceleration is such that the droplet reaches a velocity of 1 ms^{-1} at the first

line above the surface, $z = 0.5$ mm, and then descends under gravity. Upon impact with the surface at $t = 3.6$ ms, the droplet deforms and the lower part of the droplet in contact with the surface begins to spread as the contact angle is set to 0° . The spreading of the droplet continues into the next frame at $t = 4.1$ ms and a central jet of liquid forms as was observed in the literature. The jet then collapses and the droplet spreads into a very thin film on the surface with a contact angle tending to 0° . Referring back to the splash criterion proposed by Moreira et al. (2010) in Chapter 2, prompt splash was said to occur when inertial forces exceed capillary effects. This criterion was written as equation 2.18, to recap see 6.1.

$$\rho v_d^2 > \frac{\sigma}{d\sqrt{Re}} \quad (6.1)$$

Using the parameters of the droplet simulation outlined in Table 3.1, the LHS of 6.1 was calculated to be 1000 Nm^{-2} , whilst the RHS was calculated to be 6.26 Nm^{-2} i.e. the threshold is exceeded, and splash occurs which is supported by the results shown in Fig. 6.1.

6.2.1.2 40° contact angle

The volume fraction time lapse for the 40° contact angle is shown in Fig. 6.2.

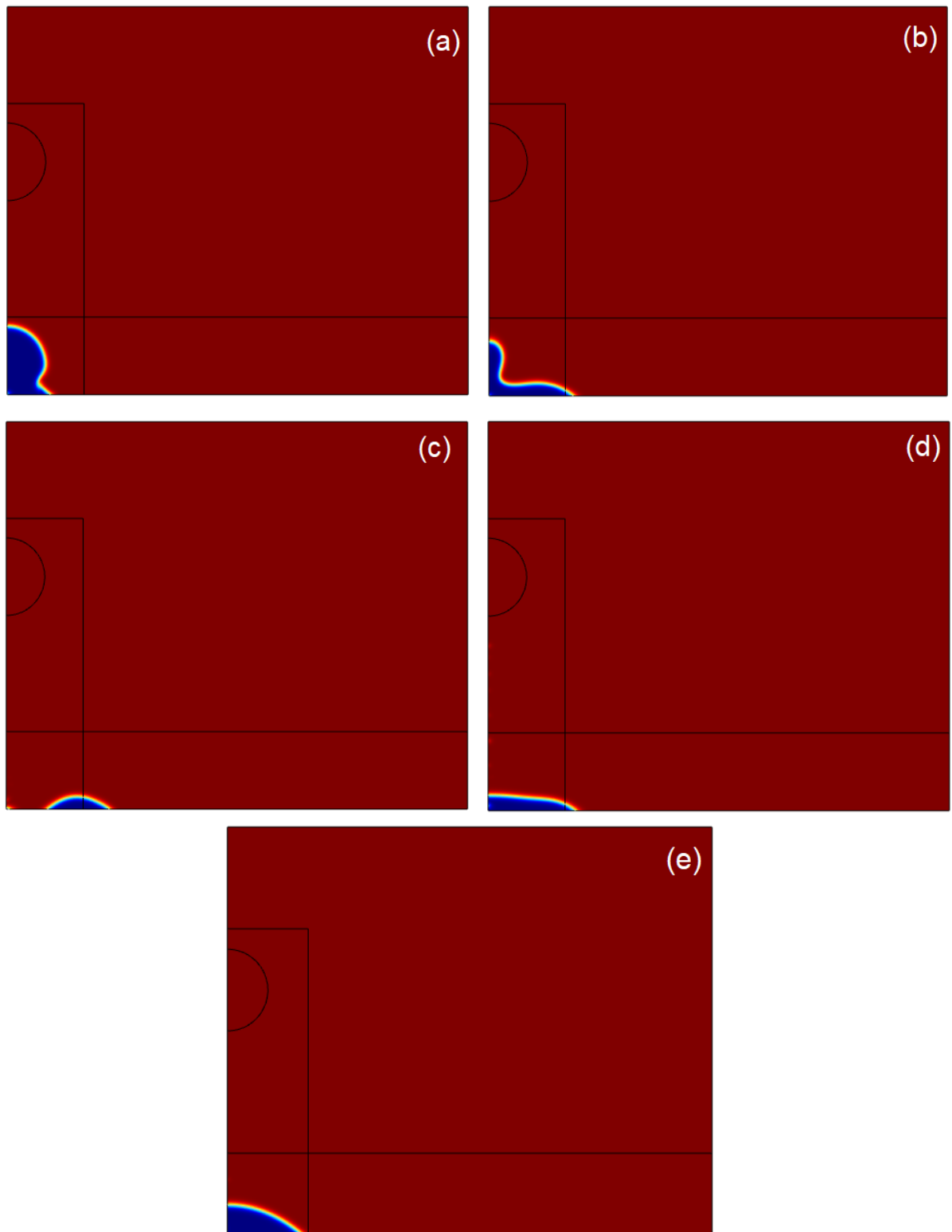


Fig. 6. 2: Volume fraction of fluid time lapse, 40° wetted wall. (a) $t = 3.6$ ms, (b) $t = 4.1$ ms, (c) $t = 4.7$ ms, (d) $t = 7.2$ ms and (e) $t = 15$ ms.

Fig. 6.2 shows the droplet impact under the same flow conditions as Fig. 6.1 but the higher contact angle of 40° . Given the flow conditions are the same, the criterion of 6.1 is again satisfied. At the point in frame (b) just after impact at $t = 4.1$ ms, a jet in the centre of the droplet rises as was observed in Fig. 6.1. In this case the part of the droplet in contact with the surface has not spread to the same extent due to the higher contact angle. A difference in behaviour is then observed as the droplet divides into two smaller droplets that slide radially outwards, as shown in frame (c) where the droplet has beaded up on the surface downstream of the impingement point. The droplet then retracts back to the centre of the domain and eventually comes to rest in frame (e), after some oscillatory movement, at the 40° contact angle.

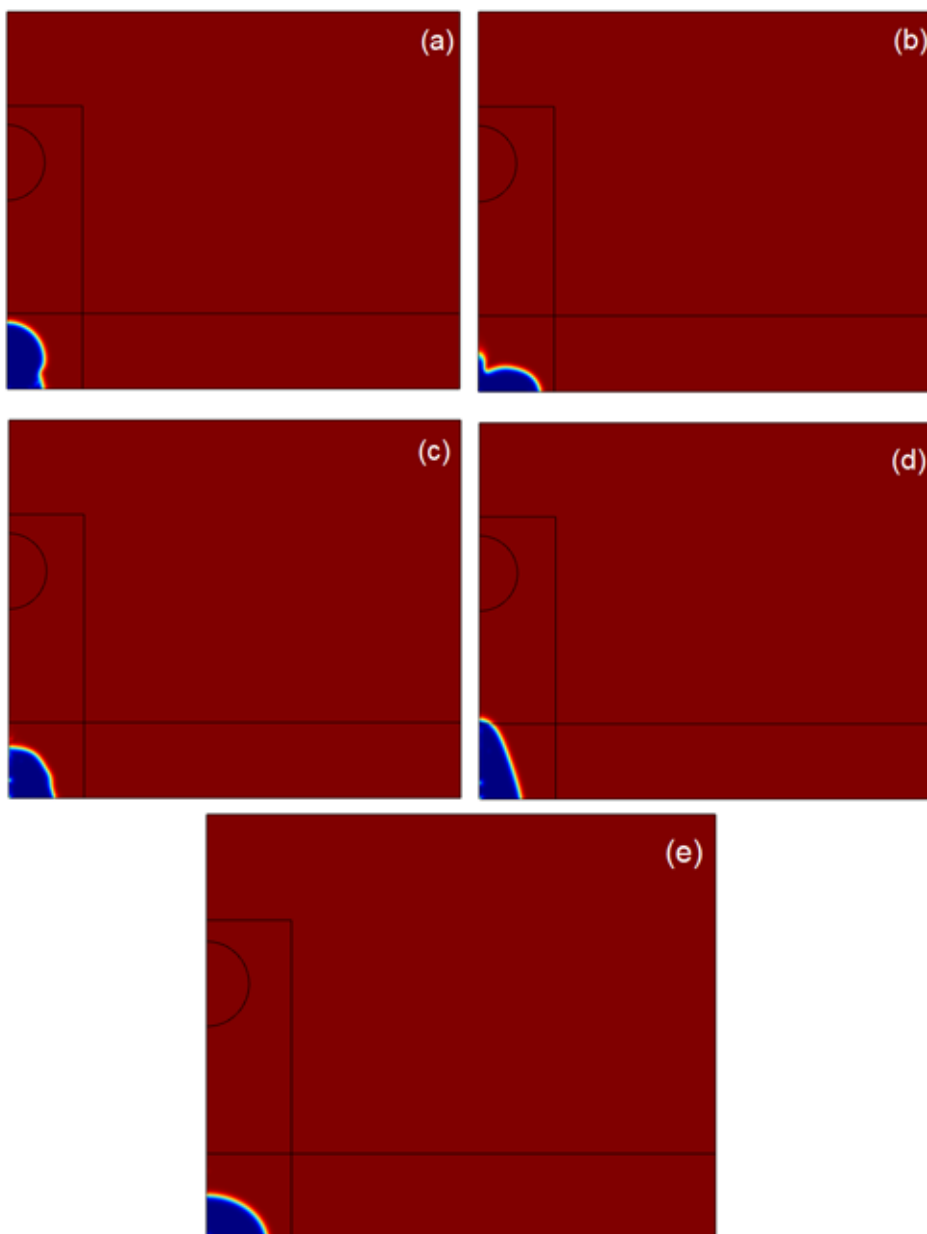


Fig. 6. 3: Volume fraction of fluid time lapse, 40° wetted wall. (a) $t = 3.6$ ms, (b) $t = 4.1$ ms, (c) $t = 4.7$ ms, (d) $t = 5.1$ ms and (e) $t = 15$ ms.

Fig. 6.3 shows the volume fraction of fluid time lapse for the higher contact angle of 83° , which was representative of the WSP under study. When the droplet impacts in the first frame, 3.6 ms into the simulation, it deforms and spreads to approximately $r_{\text{wall}} = 0.8d$ in the subsequent frame (b). The spreading was significantly less due to the wall being more hydrophobic than the previous two cases. After impact in the second frame, a central jet of liquid from the droplet can be observed but, in this case, much smaller than the two lower contact angles presented in Fig. 6.1 and 6.2. In the third frame, the droplet retracts back towards the centre of the domain and then this momentum causes the droplet to stretch upwards to a height of approximately $z = d$ in frame (d). The droplet then oscillates and comes to rest at the 83° contact angle. The droplet comes to rest earlier than in the previous two cases which were more unstable due to the lower contact angles.

6.2.2 Wall shear stress

The shear stress exerted on the surface by the impinging droplet was measured on the wall at various distances from the centre of the domain, where $r_{\text{wall}} = 0$. Four points in total were probed to measure the shear stress at that point as a function of time throughout the simulation, these were $r = 0, d, 2d$ and $3d$ and thus no shear was exerted further along the wall. Note that no distances further than this were probed because the droplet did not spread to that extent for the wetted wall case. A comparison of the shear on the wall at $r_{\text{wall}} = 0$ for the contact angles of $20^\circ, 40^\circ$ and 83° is shown in Fig. 6.4.

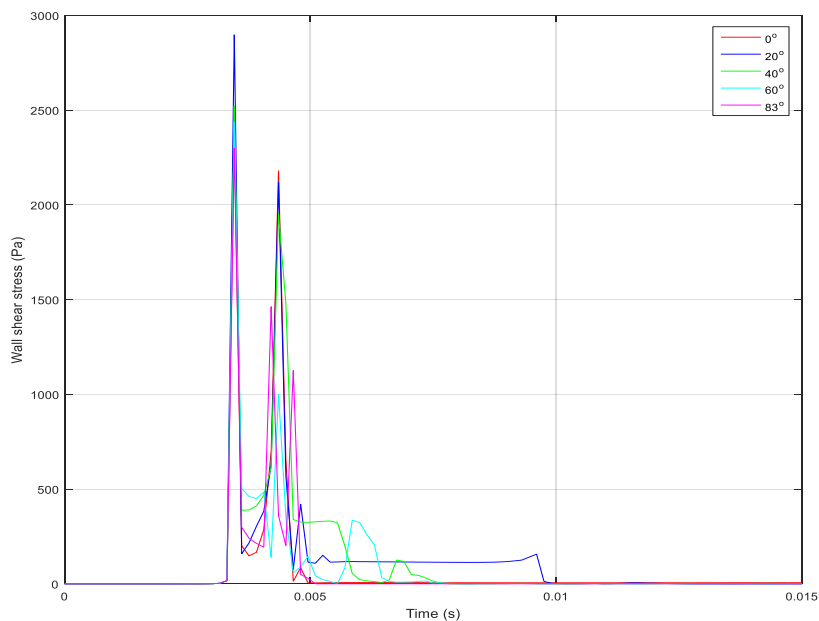


Fig. 6. 4: Wall shear stress for each $\theta = 0^\circ, 20^\circ, 40^\circ, 60^\circ$ and 83° , $r_{\text{wall}} = 0$.

At the point of impact, approximately 3 ms into the simulation, the shear on the wall shows spikes of shear stress at $r_{\text{wall}} = 0$. The initial spikes are approximately equivalent in magnitude for all the contact angles at ~ 2400 Pa. This is with the exception of the 20° contact angle which exhibits a slightly higher peak shear stress at approximately 2900 Pa. There is then a fall in the shear followed by another spike for each contact angle at approximately 4 ms. In this instance the two highest contact angles exhibit the lowest peaks. The highest contact angle, 83° , shows two spikes with peaks of 1400 Pa and 1200 Pa in quick succession suggesting an oscillatory movement of the droplet. This was supported by the animations presented in 6.2.1. The 60° contact angle however shows a solitary peak of approximately 1000 Pa. For the three lowest contact angles, the second spike in the shear stress versus time graph show a mutual peak of approximately 2200 Pa. This is higher than that shown by the higher contact angles due to the rate of spreading of the droplet on the surface being higher. After the two spikes in shear shown after droplet impact, the response comes to rest after approximately 0.005 s. Moving one droplet diameter downstream of the impingement point, $r_{\text{wall}} = d$, the shear stress versus time curves are plotted in Fig. 6.5.

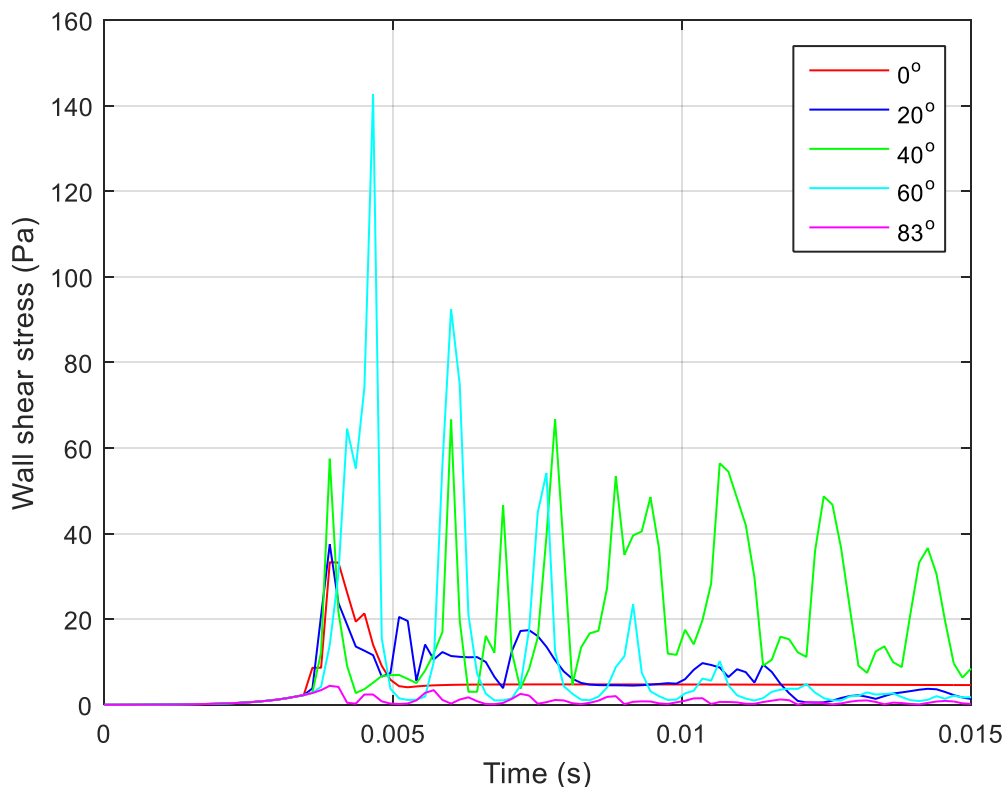


Fig. 6. 5: Wall shear stress for each contact angle, $\theta = 0^\circ, 20^\circ, 40^\circ, 60^\circ, 83^\circ$, $r_{\text{wall}} = d$.

At the point a droplet diameter downstream of the impingement point, the 83° contact angle shows a negligible shear stress throughout the simulation as the droplet does not spread beyond this point, which is shown in Fig. 6.3. The 60° and 40° show an oscillatory response as the droplet wobbles on the surface and comes to rest. The 60° shows the highest amplitude of shear at this point, with a peak of approximately 140 Pa whilst the 40° exhibits a maximum peak of approximately 70 Pa. Meanwhile the 0° and 20° contact angles both show a peak shear stress of approximately 35 Pa and a much flatter response as the droplet spreads past the point being probed and does not show any oscillation. For a further droplet diameter downstream (i.e. away from the centre point), the response is shown in Fig. 6.6.

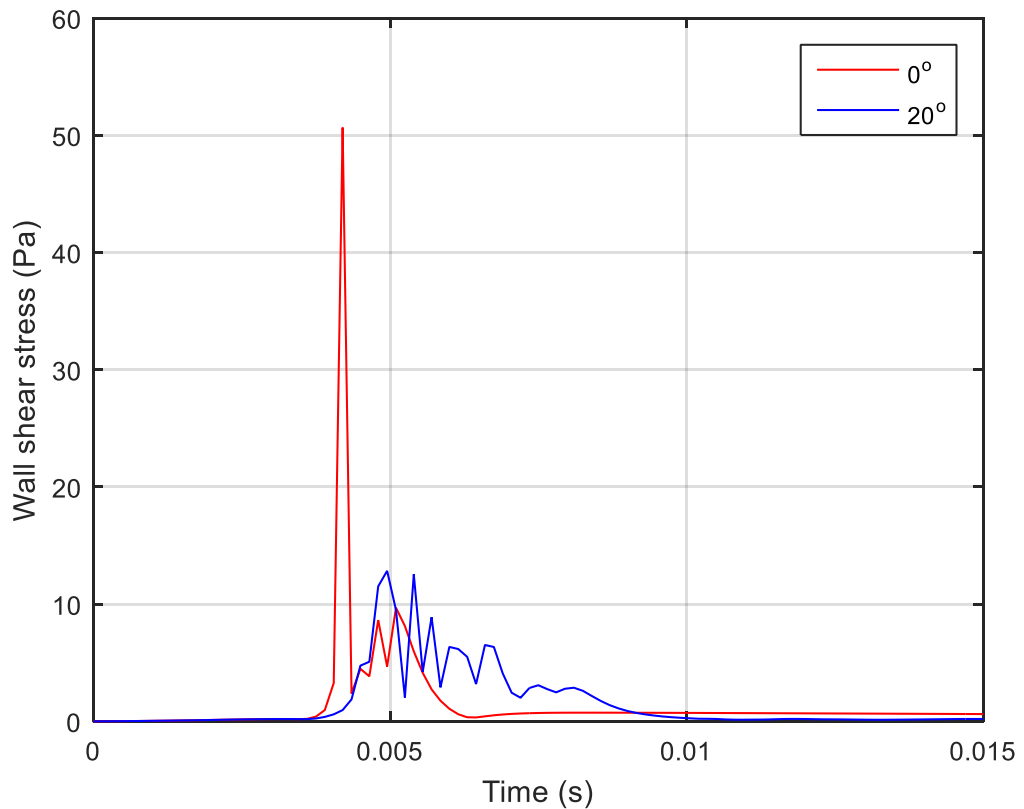


Fig. 6. 6: Wall shear stress for the $\theta = 0^\circ, 20^\circ$. $r_{\text{wall}} = 2d$.

Two droplet diameters downstream of impingement, the shear on the surface is approximately 50 Pa at the contact angle of 0° and 12 Pa for the contact angle of 20° . The two lower contact angle droplets did not spread this far and thus no shear was exerted. It can be noted that as the distance along the wall is increased, the peaks in shear stress are reduced as was also observed in the work of Cense et al. (2006).

6.3 Film on surface

The second case was to represent later in the spraying process when a liquid film had formed on the surface being cleaned, assuming no drainage. Five film thicknesses were simulated in COMSOL, increasing from $0.05d - d$ (where d is the droplet diameter) shown in the model setup of Fig. 3.24.

6.3.1 Volume fraction of fluid time lapse images

In the same manner as section 6.2.1, volume fraction time lapses were taken from animations exported in COMSOL.

6.3.1.1 Film thickness $h_0 = 0.05d$

The volume fraction time lapse for the film thickness of $0.05d$ is shown in Fig. 6.7.

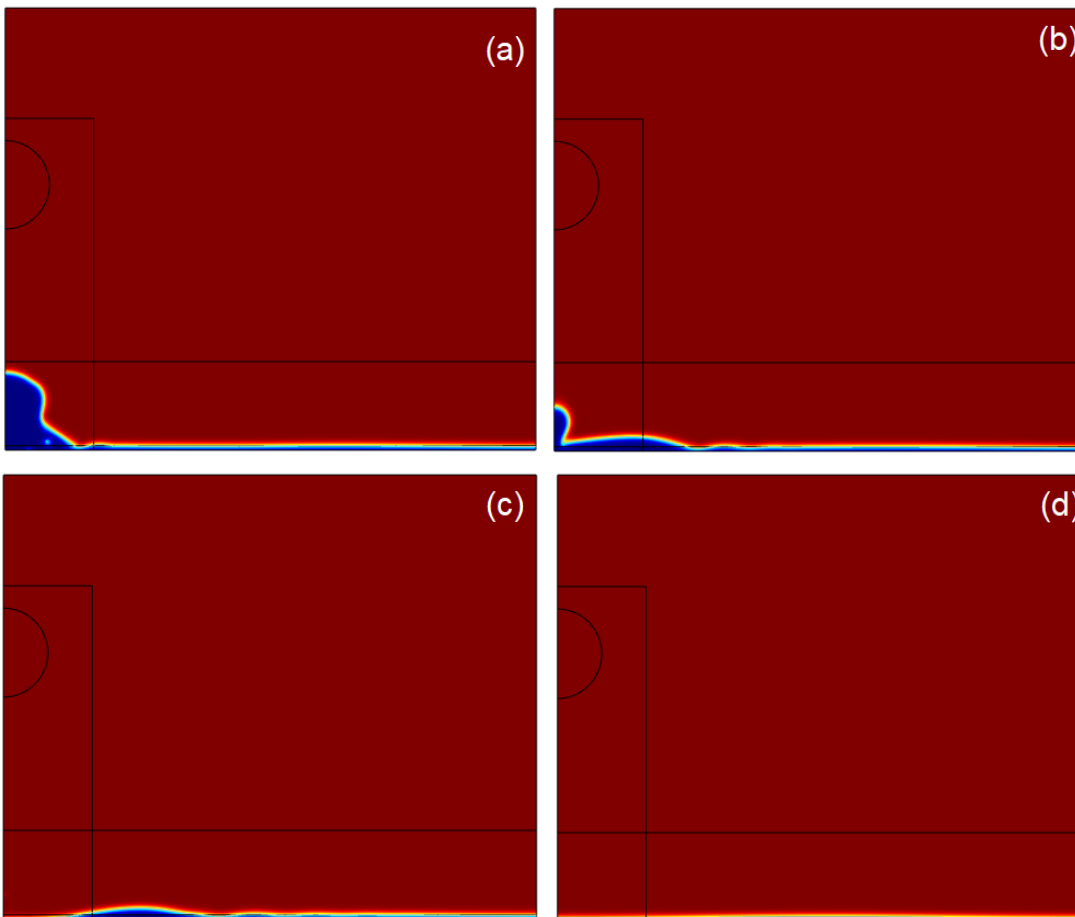


Fig. 6. 7: Volume fraction of fluid time lapse, film thickness = $0.05d$ (a) $t = 3.6$ ms, (b) $t = 4.1$ ms, (c) $t = 4.7$ ms and (d) $t = 15$ ms.

Immediately after impact of the droplet with the film, in the second frame ($t = 4.1$ ms), the droplet spreads on the surface of film. There appears to be some splash in the form of a secondary droplet emerging from the film at $r_{\text{wall}} = 0$. The droplet then is absorbed by the film and a ripple moves downstream from the impingement point in the third frame. Finally, the film on the surface comes to rest in the final frame at $t = 15$ ms, the volume

of the droplet has been absorbed. In the literature review of chapter 2, a critical threshold parameter for droplet disintegration on a surface with a film of liquid present was introduced, $K_{c,wet}$. The critical threshold parameter for $\delta_f \leq 0.1$ was defined by Wang et al. (2002) as 6.2.

$$K_{c,wet} = We_c = 450 \quad (6.2)$$

This can then be rearranged to find the critical impact velocity, v_c , by rearranging the equation for We , given by 2.8. The critical impact velocity, v_c , can then be calculated using 6.4.

$$v_c = \sqrt{\frac{We_c \sigma}{\rho d}} \quad (6.3)$$

Using the parameters outlined in 3.8.2 gives a critical impact velocity of 7.94 ms^{-1} . Since the impact velocity was 1 ms^{-1} there should theoretically be no droplet disintegration. The droplet does show no initial disintegration when impacting the film as it spread across the surface, but a secondary droplet was seen to form later on in the process as the film was displaced outwards. This was however insignificant in comparison to the wetted wall cases where significant disintegration could be observed. The small secondary droplet seen at $t = 4.1 \text{ ms}$ could also be attributed to the splash from the film.

6.3.1.2 Film thickness $h_0 = 0.15d$

The volume fraction time lapse for the film thickness of $0.15d$ is shown in Fig. 6.8.

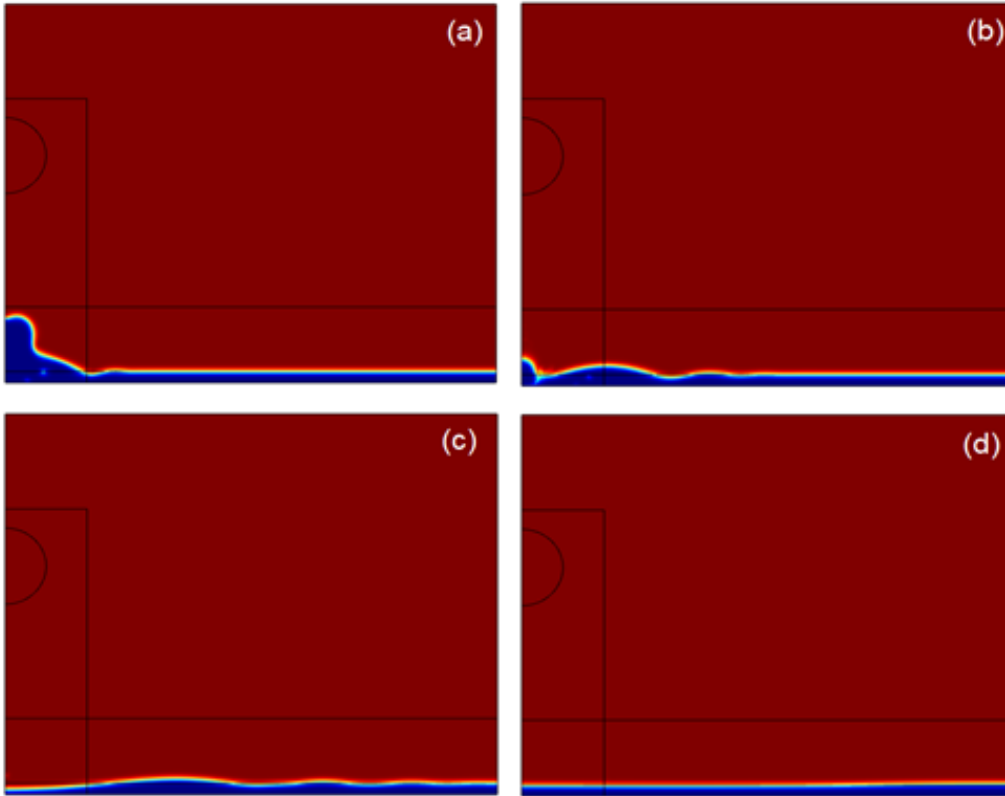


Fig. 6. 8: Volume fraction of fluid time lapse, film thickness = 0.15d. (a) $t = 3.6$ ms, (b) $t = 4.1$ ms, (c) $t = 5.1$ ms, (d) $t = 15$ ms.

Fig. 6.8 shows how at the point of impact with the film ($t = 3.6$ ms), the formation of a crown can be observed around the perimeter of the droplet where it meets the film, as was observed in the literature (e.g. see Fig. 2.15b). As the droplet continues to move downwards, it is absorbed by the film and the film moves radially outwards. There is no disintegration or splash of the droplet and no secondary droplets or jets are formed. Referring back to the set of equations given by 2.23, proposed by Wang et al. (2002), which calculates $K_{c,wet}$ for varying film thicknesses. In this case, the film thickness relative to droplet diameter $\delta_f = 0.15$, so the threshold for $0.1 < \delta_f < 1$ is used, given by 6.4.

$$K_{wet} = We_c = 1043.8 + 232.6\delta_f^{-1} \quad \text{for } 0.1 < \delta_f \leq 1 \quad (6.4)$$

Which yields 6.5.

$$K_{c,wet} = We_c = 2594 \quad (6.5)$$

Using the parameters previously described for the droplet simulations and $We_c = 2594$ from 6.5 and solving for 6.3, this gives a critical impact velocity of 19 ms^{-1} . Given the droplet impacts the film with a velocity of 1 ms^{-1} , this is well below the critical value required for disintegration and explains why none is observed. At $t = 4.1 \text{ ms}$, at the point where $r_{\text{wall}} = 0$, the droplet has coalesced with the film. A ripple can be seen in the next time frame at $t = 5.1 \text{ ms}$ and the film finally comes to rest on the surface at 15 ms as it was before the droplet impact, with the additional volume of the impinging droplet. The volume fraction time lapse for a film thickness of $h_0 = 0.5d$ is shown in Fig. 6.9.

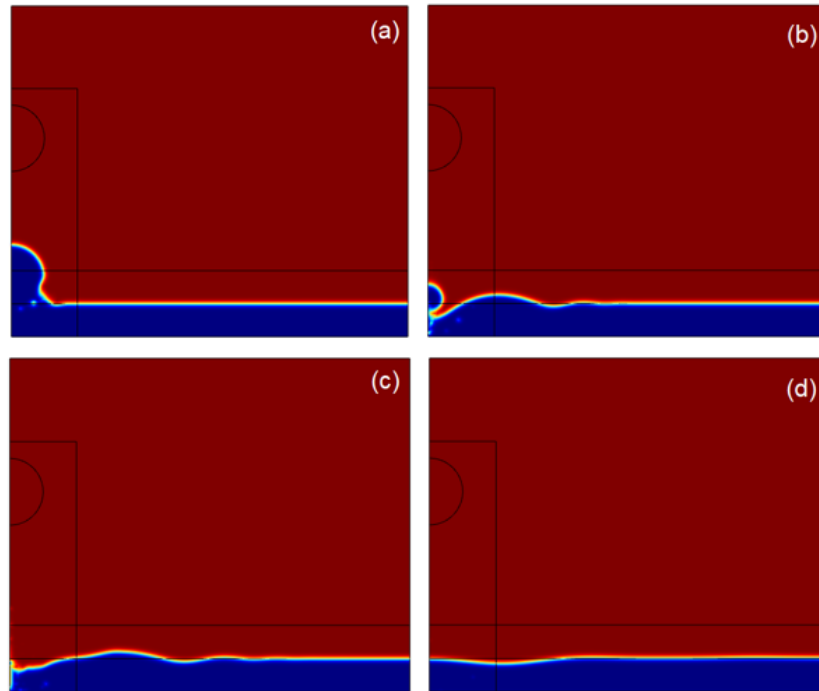


Fig. 6. 9: Volume fraction of fluid time lapse, film thickness = d . (a) $t = 3 \text{ ms}$, (b) $t = 3.6 \text{ ms}$, (c) $t = 4.1 \text{ ms}$, (d) $t = 15 \text{ ms}$

The droplet first touches the surface of the liquid film at 3 ms and then in the subsequent frame ($t = 3.6 \text{ ms}$) forms a crater in the film, from which a secondary droplet can be seen to emerge. A wave is formed where the thickness of the film increases above its initial value as the volume of the droplet is absorbed and disperses throughout the film. The film then retracts due to the symmetry condition on the right-hand boundary and has not quite come to rest after 15 ms , unlike the two previous cases of thinner films.

6.3.2 Wall shear stress

Following the same procedure as 6.2.2, different points on the wall were probed to measure the shear stress as a function of time on the wall for each film thickness. The 0° contact angle has been included for comparison in each plot. Fig. 6.10 shows the response at $r_{\text{wall}} = 0$ for each case.

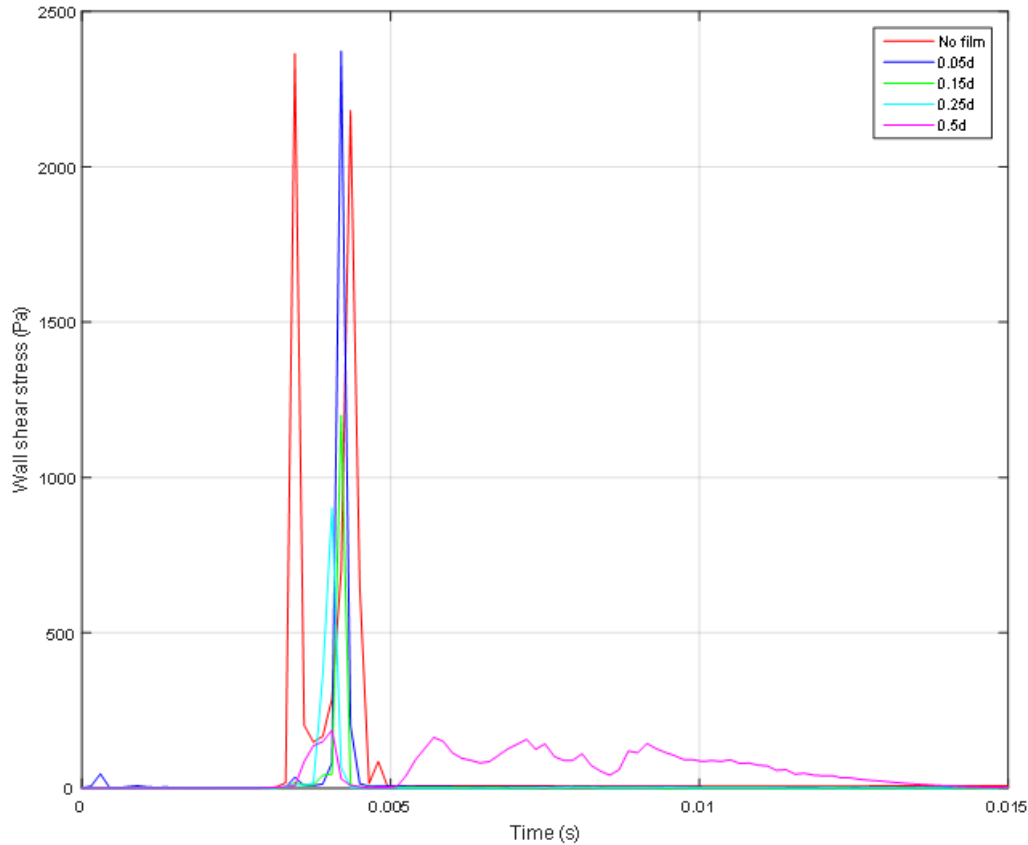


Fig. 6. 10: Wall shear stress versus time: no film (0° contact angle), film thickness $h_0 = 0.05d$, $0.15d$, $0.25d$ and $0.5d$.
 $r_{\text{wall}} = 0$

The red curve representing the 0° wetted wall, shows two spikes as was presented in 6.2.2. For the film of $h_0 = 0.05d$, there is negligible effect on the shear stress exerted on the centre point in the domain and the peak has a very similar value of approximately 2400 Pa. For the film thickness of $0.15d$ there is a significant reduction in the initial spike in shear stress at $r_{\text{wall}} = 0$. There is then a further reduction in maximum shear for the thicker film of $0.25d$ and another significant reduction is observed with the $h_0 = 0.5d$ case. This shows how as the film of water on the surface on which the droplet impinging is increased in thickness, the shear exerted on the wall is decreased as the film absorbs the energy of the droplet on impact to a greater extent. Fig. 6.11 shows the shear stress versus time curves at $r_{\text{wall}} = d$.

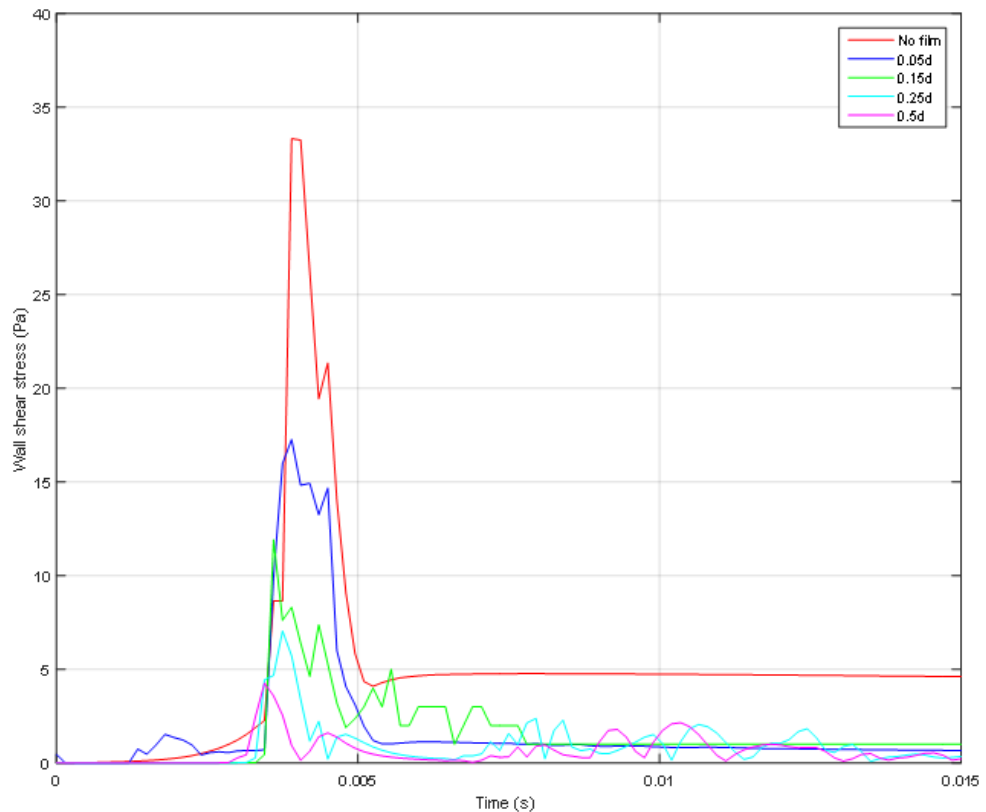


Fig. 6. 11: Wall shear stress versus time: no film (0° contact angle), film thickness $h_0 = 0.05d$, $0.15d$, $0.25d$ and $0.5d$. $r_{\text{wall}} = d$.

A droplet diameter downstream of the impingement point, there is a clear drop in the shear stress exerted on the wall as the thickness of the film is increased. The presence of a $0.05d$ film on the surface sees an approximate 50% reduction in the wall shear stress compared to the wetted wall of 0° . The same trend can be observed as the film thickness is increased to $0.15d$, as the peak shear stress drops from approximately to 17 Pa to 12 Pa. Finally, when the film thickness is $0.5d$, there is very low shear on the surface with a peak of approximately 5 Pa. As a film builds up on the surface, when the droplet impinges on to this film the energy from the impingement is absorbed on impact and dissipated throughout the film. As a result, there is less shear exerted on the wall and less energy available for soil removal. The same phenomenon was presented in Chapter 2 in the work by Cense et al. (2006). Moving a further droplet diameter along the wall, $r_{\text{wall}} = 2d$, the shear stress versus time response is shown in Fig. 6.12.

A very similar response can be observed as at $r_{\text{wall}} = d$. The maximum shear is considerably greater when there is no film on the surface than when a film has developed. Once again, the energy from the droplet is absorbed by the film meaning significantly reduced shear stress downstream of the impingement point is exerted on the wall. The final case of $r_{\text{wall}} = 3d$ is shown in Fig. 6.13.

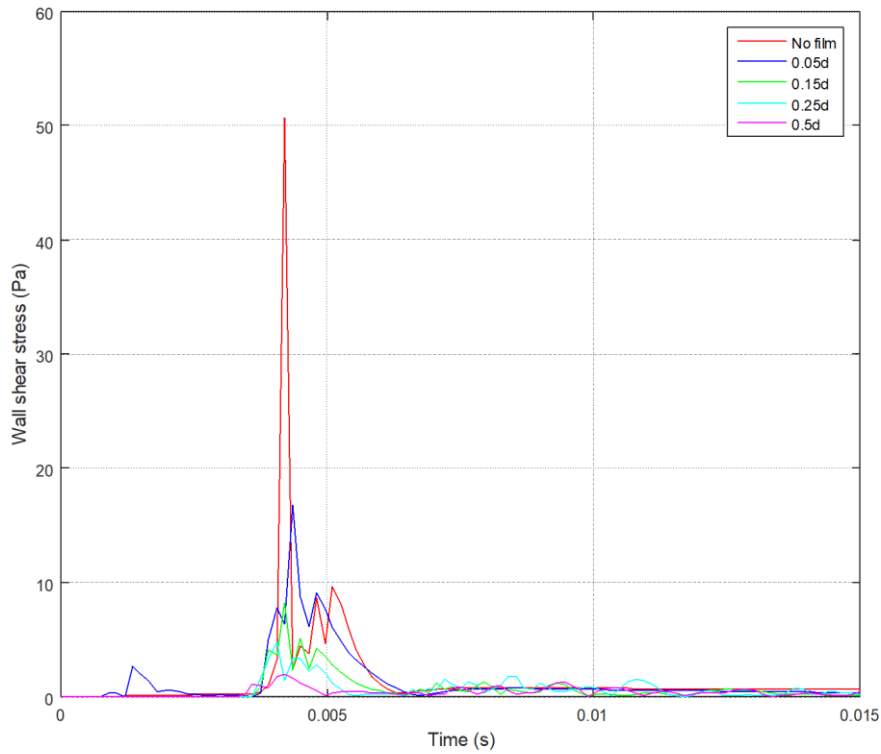


Fig. 6.12: Wall shear stress versus time: no film (0° contact angle), film thickness $h_0 = 0.05d, 0.15d, 0.25d$ and $0.5d$. $r_{\text{wall}} = 2d$.

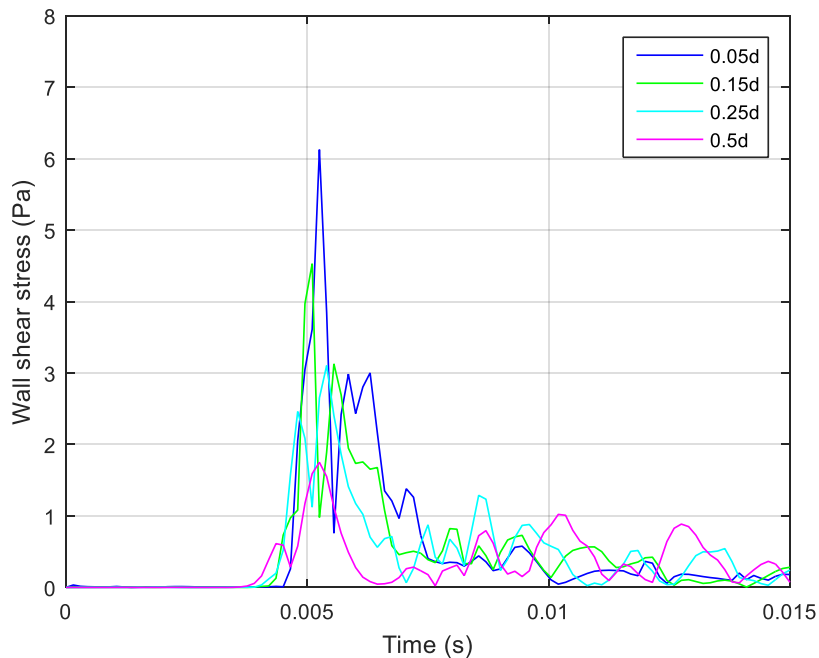


Fig. 6.13: Wall shear stress versus time: film thickness $h_0 = 0.05d, 0.15d, 0.25d$ and $0.5d$. $r_{\text{wall}} = 3d$.

Since in the 0° case the droplet did not spread to $r_{\text{wall}} = 3d$ no curve has been plotted in Fig. 6.13. The volume of the droplet was insufficient to spread to this distance on the wall. However, a similar behaviour for the film cases is shown, with the peaks of wall

shear stress decreasing with increasing film thickness. The values are also considerably lower than closer to the droplet impingement with a maximum shear for the $0.05d$ case of approximately 6 Pa.

6.4 Jet impingement

Each jet was drawn in COMSOL, using the coordinates of the film in the RFZ obtained from equations 2.5, 2.6 and 2.7. The simulations were then solved for each inflow velocity.

6.4.1 Jet velocity plots

A surface plot of velocity magnitude was created in COMSOL for the 1 lmin^{-1} jet, displayed in Fig. 6.14.

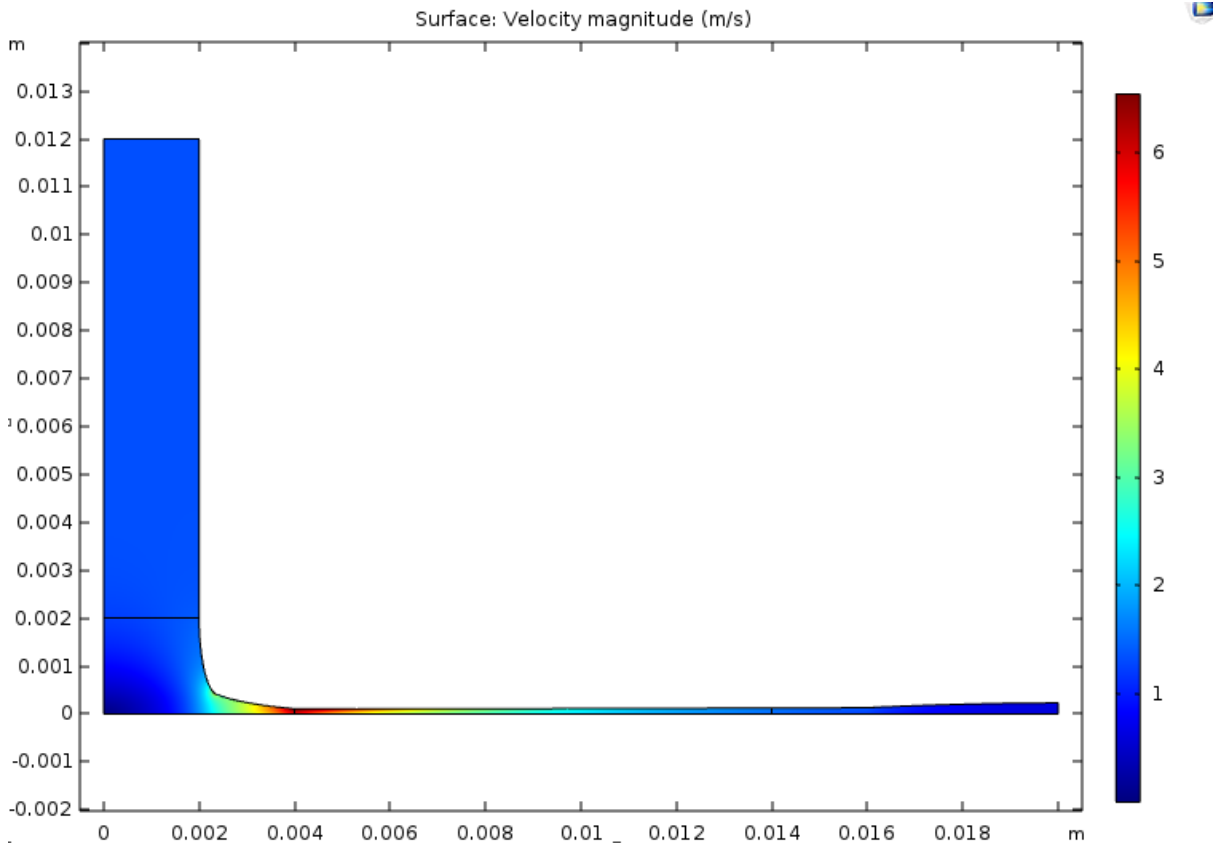


Fig. 6. 14: Jet impingement COMSOL model: Surface velocity magnitude.

Fig. 6.14 shows how the jet impinges perpendicularly to the wall with a velocity of 1.33 ms^{-1} . As it impacts the surface the flow stagnates and the velocity falls to zero. The flow is then turned through 90° and flows radially outwards. The film is at a minimum thickness at approximately $r_{\text{wall}} = 4 \text{ mm}$, at this point the velocity is a maximum of approximately 6 ms^{-1} . The thickness of the film slowly increases with distance along the wall as the flow in the film transitions from laminar to turbulent. The velocity in the RFZ subsequently

decreases and at $r_{\text{wall}} = 20$ mm, the velocity is approximately equal to that of the impinging jet, 1 ms^{-1} . A 3D surface velocity magnitude plot was created in COMSOL to show the profile of velocity in the jet and throughout the RFZ. The resultant plot is shown in Fig. 6.15.

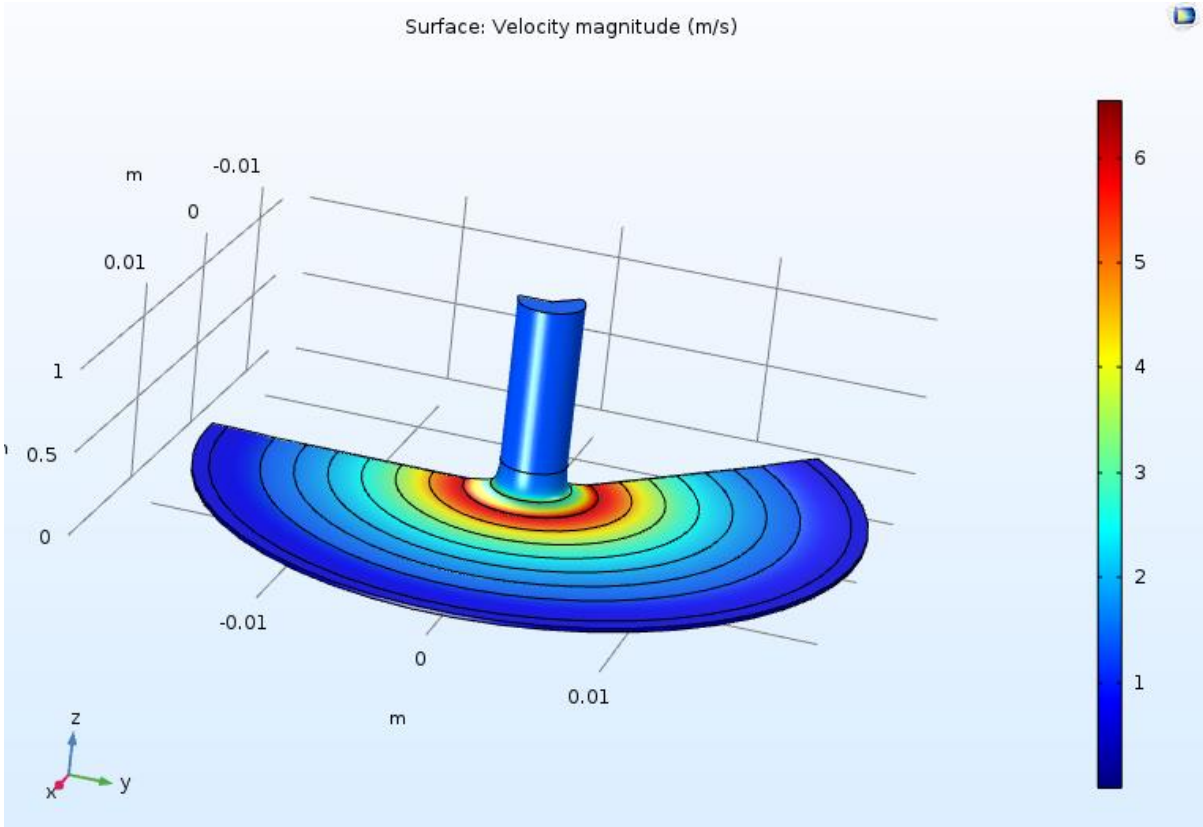


Fig. 6. 15: Jet impingement: 3D Surface velocity magnitude.

Once again, the colour bar displays the velocity ranging from $0 - 6 \text{ ms}^{-1}$. This helps to visualise the RFZ in 3D. Again, the flow stagnates at the impingement point, it is then turned through 90° by the wall and the flow is accelerated to the point where the film in the RFZ is at its minimum thickness (approximately $r_{\text{wall}} = 4$ mm). Here shear stress is at a maximum. As the flow then moves radially outwards, the thickness of the film increases as the flow transitions to a turbulent regime. The result velocity profile decreases and so too does the shear stress exerted on the wall.

6.4.2 Wall shear stress

The wall shear stress was then measured in COMSOL and plotted as a function of position on the wall. The theoretical models from the literature of Yeckel and Middleman (1987), Bhagat and Wilson (2016) and Liu et al. (1991) have also been plotted for comparison. Fig. 6.16 shows the comparison for the 1 lmin^{-1} flow rate.

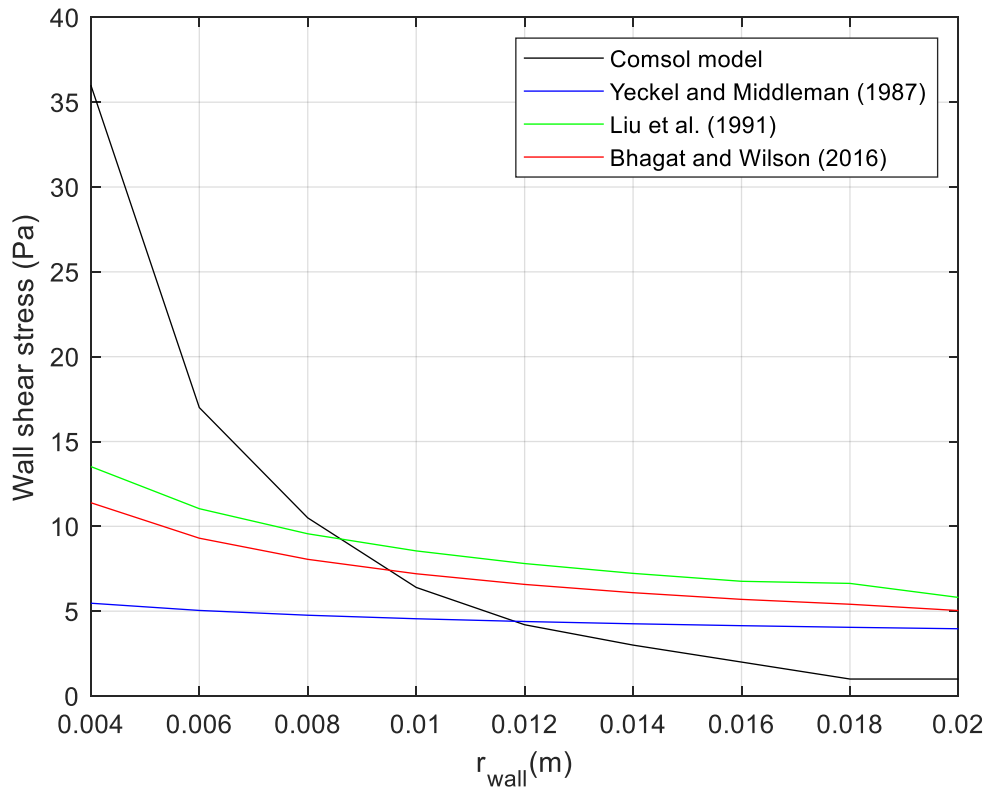


Fig. 6. 16: Wall shear stress vs radial position on wall. COMSOL model compared with literature.

Note that the first shear stress measurement on the wall has been taken at $r_{\text{wall}} = 4\text{mm}$. This is approximately where the maximum occurs, the point at which the film in the RFZ is at its minimum thickness (as shown in Fig. 6.14) and shear stress is at its peak. The shear stress at the point of impingement is zero since the flow stagnates. As the distance along the wall downstream of impingement is increased beyond 4 mm, the shear stress shows an exponential decrease and eventually reaches an asymptote at approximately 1 Pa. This demonstrates why cleaning with a jet is much more efficient close to its impingement point than further downstream, where shear stress exerted on the substrate is considerably less. In this particular case of the 1 lmin^{-1} jet, the soil removal visualisation presented earlier in section 4.2.1.3 showed only WSP within approximately one jet radius of the impingement point was removed. Fig. 6.16 shows why this is the case as beyond this the shear is insufficient for adhesive removal of the WSP to take place. There is a noticeable disparity between the results of the COMSOL model and the predictions presented in the literature, particularly close to the jet impingement point. One of the reasons for this can be attributed to the $k-\epsilon$ turbulence model used in the simulation. The flow in the RFZ film in this region of the wall is still laminar according to the zone limits proposed by Bhagat and Wilson (2016) in equations 2.3 and 2.4. For the 1 lmin^{-1} jet, the

flow in the RFZ theoretically was not turbulent until $r_{\text{wall}} = 22$ mm. Another potential reason for the disagreement with the literature is the representation of the geometry of free surface, given that it has been assumed to take the shape of that proposed by Bhagat and Wilson (2016). The geometry was assumed to simplify the problem and make the simulations easier to compute. Realistically the jet should be set up in a two-phase domain and then COMSOL could solve for the profile of the free surface. This is an avenue for future work with regards to computational simulations of a jet. Lowering the turbulent length scale and intensity in COMSOL had little effect on the shear stress profile. Assuming a laminar flow in the model also showed a greater disparity with the models in the literature due to the turbulence of the initial impinging jet. Despite the COMSOL model showing relatively poor agreement with the literature close to impingement point, as the distance along the wall is increased the difference becomes smaller.

Fig. 6.17 shows the shear stress vs coordinate on the wall for the 2.5 lmin^{-1} jet.

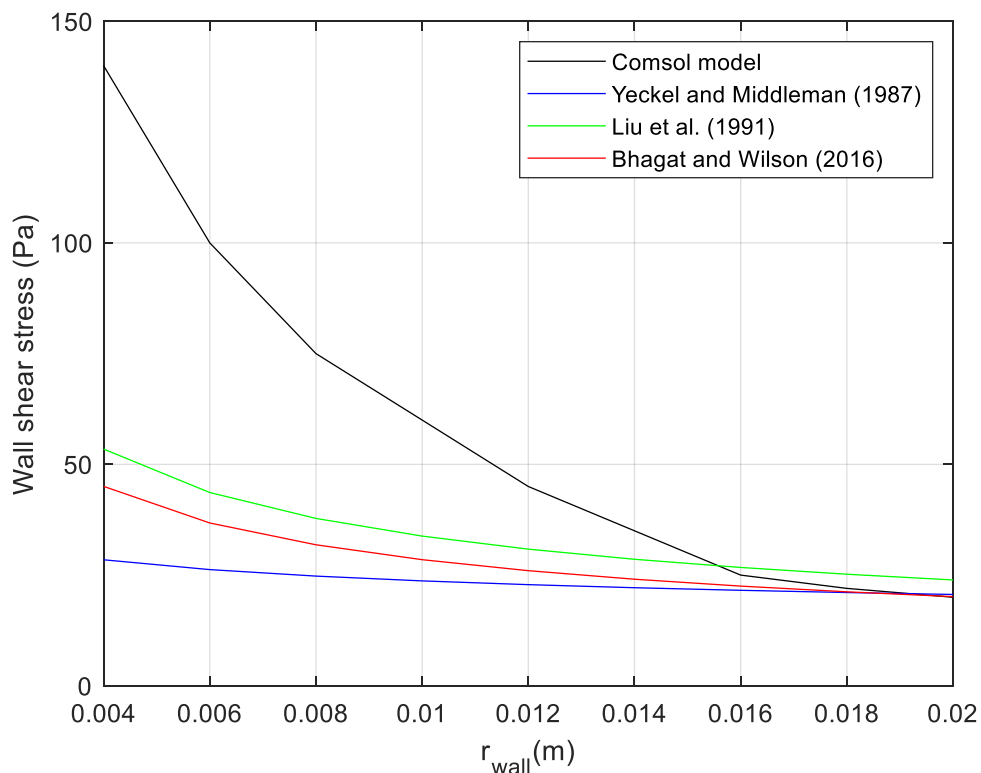


Fig. 6. 17: Wall shear stress vs radial position on wall

Once again, the shear stress on the wall shows a sharp decrease as the distance along the wall is increased. The curve reaches an asymptote at approximately 25 Pa. This demonstrates the far greater shear in the RFZ for the 2.5 lmin^{-1} jet in comparison to the 1 lmin^{-1} and this is reflected in the larger cleaned area observed in section 4.2.1.2, for

example. Again there is a considerable disparity between the COMSOL results and the predictions from the literature, but similar to the previous case of the 1 lmin^{-1} jet, the agreement downstream of impingement is much better. Here there is an excellent agreement beyond approximately $r_{\text{wall}} = 16 \text{ mm}$, particularly with the models of Bhagat and Wilson (2016) and Yeckel and Middleman (1987).

Fig. 6.18 shows the results for the 4 lmin^{-1} jet, compared to those predicted in the literature.

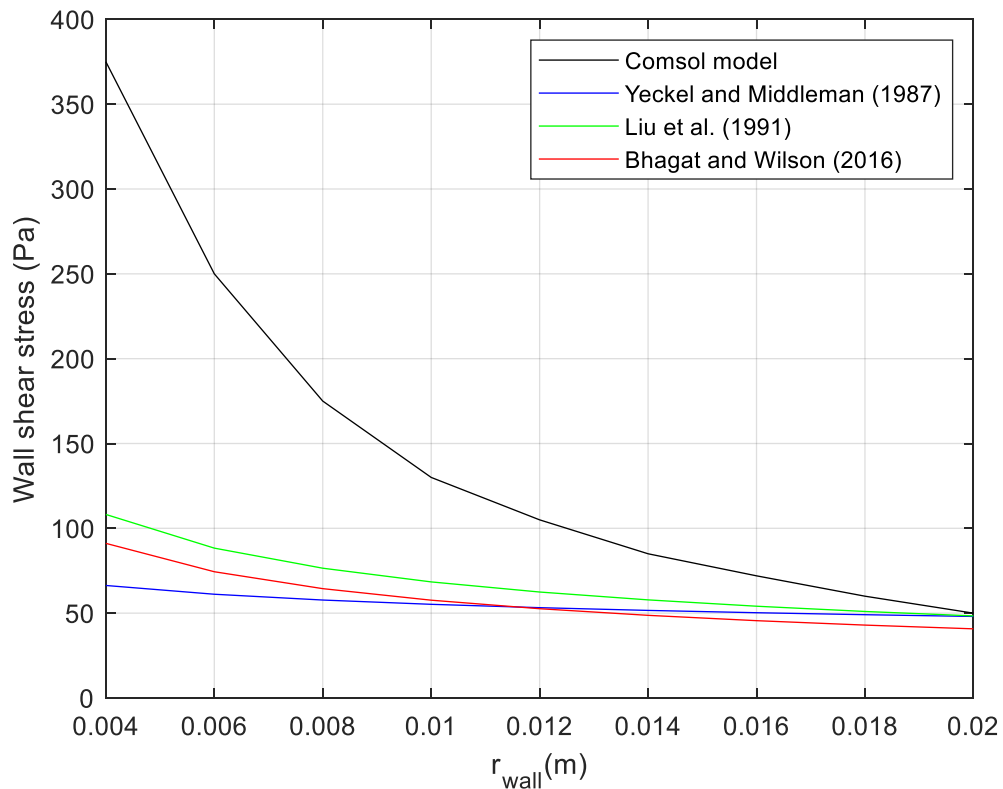


Fig. 6.18: Wall shear stress versus radial position on wall

Similar to the previous cases of Fig. 6.16 and 6.17 a large peak in shear stress is observed at $r_{\text{wall}} = 4 \text{ mm}$, in this case approximately 375 Pa . As the distance along the wall is increased the shear rapidly decreases. In this case, there is no clear asymptote as there was with the two lower flow rate jets. Also, the agreement with the literature downstream from impingement is not as good as, particularly, the 2.5 lmin^{-1} jet. For this jet Reynolds number, the RFZ does not become fully turbulent until $r_{\text{wall}} = 28 \text{ mm}$, in accordance with equation 2.4, so the application of the $k-\epsilon$ turbulence model may not be as applicable in this particular region of the wall. Once again, as was previously discussed, the assumption of the geometry of the free surface is a potential reason for this disparity. Modelling the simulation as two-phase and allowing COMSOL to predict the shape of the film could lead the results to show better agreement with those from the

literature. Despite this at the furthest point $r_{\text{wall}} = 20$ mm the solutions are beginning to converge. The shear at this point is approximately 50 Pa, this again shows why there is such disparity in the cleaning performance between each flow rate as the shear stresses exerted on the wall and RFZ areas are considerably greater as flow rate is increased.

6.4 Summary

This chapter has presented the results obtained computationally simulating the impingement of a single droplet on to a wetted wall and a wall with a film of water on the surface and a single-phase simulation of a jet impinging on to a no-slip wall. Qualitative behaviour of the droplet was observed using volume fraction of fluid animations exported from COMSOL to see the droplet's behaviour on impact with the surface. Spreading and splashing was observed in the wetted wall case. The critical threshold for droplet breakup was exceeded in the wetted wall case and duly exhibited droplet disintegration, particularly at lower contact angles, so this was in good agreement with the literature. At higher contact angles the stability of the droplet was improved upon impact with less, but still noticeable, breakup observed. With a film on the surface, the critical threshold was not exceeded. There was some breakup however observed, in the 0.05d case, as a small secondary droplet was formed. This was insignificant and none was seen in the 0.15d case, whilst there was small splash in the 0.5d case. 0.05d and 0.5d represent the lower and upper boundaries for the use of equation 6.4 so this could be the reason for them not showing ideal agreement. When a droplet spreads on a surface being cleaned, the shear stress on the wall promotes adhesive soil removal by peeling the soil, provided the shear stress exceeds the yield of the soil in question. Plotting the shear stress on the wall as a function of time at different locations on the wall showed that a film of water on the surface significantly reduced the shear exerted downstream of the impingement point. From a cleaning perspective this shows that there must be effective drainage of the fluid on a surface when being cleaned in order for a spray to clean efficiently. If a film builds up on the surface, then the impinging droplets have little chance of removing soil outside of the point on which they impinge. A drainage film could also improve cleaning performance as it would promote material removal downstream of the impingement area of the spray, similar to falling films produced by jets. This would be particularly useful at higher temperatures. There are however certain assumptions made in this study which must be considered, i.e. only single droplet impingement has been studied and not periodic or simultaneous impingements. When representing a spray, it is important to consider multiple impingements in order to replicate the fluid mechanics as accurately as possible. This is an avenue for further research, but the results from this chapter form a foundation to work from and the fundamental fluid mechanics are applicable.

Simulations of the liquid jet showed the shear stress profile of the jet exerted on the wall. A reasonable agreement with the literature was observed, particularly further downstream on the wall where the flow becomes more turbulent and the application of a turbulence model was more reasonable. A key simplification in this study was the assumption of the geometry of the free surface of the film in the RFZ, using the equations derived from Bhagat and Wilson (2016). It is important to note that this was a preliminary study and there are many more considerations such as this which can be included in future work. Whilst there are certain inaccuracies in the jet simulations, it has provided a useful visualisation of the shear stress profile throughout the RFZ and has helped estimate the order of magnitude of the shear stress exerted on a surface by a jet. This subsequently allowed comparisons to those exerted by spray droplets.

Chapter 7

Conclusions and Future Work

7.1 Introduction

This chapter summarises the findings of the research and outlines the conclusions which can be drawn, including application of the findings for improvement of current cleaning procedures used in the pharmaceutical industry at present. Future work in the field which remains to be completed as an extension on the research presented in this thesis is also discussed.

7.2 Conclusions

7.2.1 Jet experiments

The experimental work with the jet focused on two cleaning scenarios, the first being a horizontally aligned jet removing WSP from a vertical wall. This study revealed that the removal of WSP at room temperature occurs via a rolling mechanism, whereby material in the RFZ rolls over the material at the perimeter of the clean area. As the cleaning process continues the WSP forms a ridge on the perimeter where excess material has built up. This ultimately acts as a resistance to the flow and as such the area cleaned is less than the area of the RFZ of the jet on a clean surface. A different mechanism of soil removal was observed when the temperature of the water was increased. Since the drop point of the WSP used for experiments was encompassed at 40 °C, the rheology changed so that it started to behave like a liquid and mobility of the layer was increased. As such the majority of material in contact with the flow was removed at 40 °C in a 5-minute cleaning cycle. When raising the temperature to 60 °C the removal occurred in a shorter time scale but the difference in areas was not significant relative to the additional input of energy required for the surplus temperature. Using an energy framework, it was deduced that cleaning efficiency is at its highest in proximity to the jet impingement point, where the velocity of the fluid and shear force exerted on the wall is highest. Using a single jet to clean a large area becomes inefficient.

The second case considered for the jet experiments was a vertically aligned jet cleaning a gel from a pipe. This is an arrangement that is commonly found on wash racks, where a tube is positioned underneath an impinging jet on a wash rack. This arrangement allows easy loading and unloading of the jet. From these experiments a number of factors were studied and it was shown that an angular misalignment of the jet, relative to the pipe, could reduce the efficiency of the cleaning process. When perfectly aligned, the

jet flow rates derived using EPANET were sufficient to remove the gel such that negligible residues remained after cleaning in most cases. However, when the gel was preheated to 85 °C, which represented a typical drying cycle, more significant residues were observed, possibly due to drying or chemical changes in the product, which then required further cleaning efforts.

7.2.2 Spray experiments

The spray experiments showed that at room temperature, the spray was unable to fully remove the WSP from the wall. This was further supported by residual film measurements at the University of Cambridge which showed even areas which may have appeared to be clean to the naked eye still had the presence of a thin residual film. It was suggested that this was due to a poor transport of material from inside the cone of the spray to the RFZ. As a result, material was trapped in the centre of the cone, which explained the large residues in the centre of the cleaned areas observed post cleaning. Also, since the flow in the spray was dissipated over a much larger area than the jet, the velocity of the fluid and subsequent shear exerted on the wall was lower than the jet for a given flow rate.

7.2.3 Numerical modelling

The numerical study involved CFD modelling of a single droplet impinging on to a wall and a steady-state simulation of an impinging jet. The purpose of the droplet study was to represent a constituent droplet of a spray in order to gain an understanding of the soil removal mechanisms of the spray in more detail. The results from this study showed that when a liquid layer is present on the surface being cleaned, the shear exerted on the wall by the droplet is significantly dampened downstream of the impingement point. This means that cleaning efficiency is reduced, as shear of the wall by the droplet is the fundamental removal mechanism away from the impingement point, where cohesive removal is prevalent. This highlights the importance of surface drainage in cleaning procedures on site. If there is a build-up of water on the surface, then cleaning efficacy will be significantly reduced. Simple measures could be taken to ensure this, such as positioning parts so that surfaces being cleaned are inclined relative to the spray nozzle. The jet simulations exhibited the shear stress profile of the jet on the wall. At the point of impingement, the shear is zero as the flow stagnates as it is turned through 90° in to the RFZ. A large peak is then observed approximately one jet diameter downstream of the impingement point. The shear in the RFZ then decreases as the distance downstream from impingement is increased. Ultimately the shear drops to a level where adhesive removal of the WSP is prohibited and the A^* value for the particular jet is reached.

7.2.4 Comparison of findings for jet and spray

Key observations from the experimental and computational work conducted on jets and sprays are summarised and compared in Table 7.1.

Table 7. 1: Key comparisons for jet and spray

Observation	Jet	Spray
Soil removal mechanism	Cohesive at impingement Adhesive in RFZ Roll-up at ridge	Cohesive and adhesive in cone Adhesive in RFZ
Peak shear stress	~ 400 Pa	~ 3 kPa
Local impact time	Continuous (steady-state)	~ 1 ms (droplet impact)
Local zone of effect	Large ($> 10d_{jet}$)	Small ($< 3d$)
Residual film (20 °C)	Negligible	Significant

Note that the peak shear stress is considerably higher for the spray, but this is concentrated in a very small area and significantly reduces downstream from the impingement point of each droplet. The local zone of effect of each droplet was confined to less than a maximum of 3 droplet diameters downstream. This is compared to the jet which exerted a relatively high shear on the wall over a far greater area, greater than 10 jet diameters. The jet impact was also continuous compared to the spray, which was an amalgamation of single droplet impacts lasting approximately 1 ms. Soil removal inside the cone of the spray was both cohesive and adhesive, with the initial impact of each droplet eroding the soil layer and then the subsequent spreading promoting adhesive removal of the soil. Due to poor transport of the WSP from the cone to the RFZ, large residual films were observed at room temperature. Also, the comparatively low shear in the RFZ compared to the jet saw poor removal in this region, contributing to the residual films observed. Meanwhile the jet left no residual film visible to the naked eye.

7.2.5 Informing guidelines and application to site

Since the work was industrially focused and optimisation of cleaning cycles on site was the main driving force for the research, the key guidelines and recommendations for industry are outlined below.

- Cleaning via jets becomes very inefficient when a single jet is covering a large area, due to shear forces being ineffectual at large distances from the jet impingement point. Therefore, it is suggested that clusters of jets be used on wash racks for larger components. Flow rates and cycle times could be reduced for each jet and energy consumption could be improved.
- Water temperatures on site could be significantly reduced, particularly for WSP based products as this research has shown. Temperatures on wash racks can be as high as 90 °C and the temperature studies conducted showed that at 60 °C all material in contact with the flow was removed inside 5 minutes. With some products there may be other constituents that require a higher temperature, but for many as long as the drop point of the soil is exceeded, this can be reduced.
- It is important that surfaces being cleaned via sprays are effectively drained. A build-up of a water film with no drainage can have a detrimental impact on cleaning performance as the energy from the droplets in the spray are absorbed and dissipated throughout the film, meaning the droplets are unable to effectively remove the soil. This would require very simple modifications to the rack to ensure components being sprayed are positioned so that they are inclined at an angle relative to the nozzle.
- For resilient soils that are hard to clean, jets would be preferred as they have shown in this study to leave no visible residual film at room temperature. However, for soils that are easy to clean, such as low viscosity creams for example, the angle of the spray could be exploited to cover a large area by increasing the standoff distance of the nozzle.

7.3 Future work

The work presented in this thesis has provided an insight into the hydrodynamics of jet and spray cleaning, particularly in batch COP processes. However, the work has covered many aspects from a fundamental viewpoint and further research can be applied to these areas to develop their understanding further. For instance, the study has been purely hydrodynamic and has excluded the chemical effects of surfactants. Since they are used in many cleaning processes in the pharmaceutical industry this remains an important topic for further investigation. Also, work in this study has been conducted on a Perspex wall instead of stainless steel, which is most commonly associated with the internal walls of production equipment in the pharma industry. Perspex was chosen for the ease of observation of each process, but it is important to replicate the surface more accurately in future studies. Other avenues for future experimental work could include varying jet

diameter, using different types of spray nozzle (i.e. hollow cone) and investigating the effect of moving nozzles.

From a computational perspective, the study of droplet impingement in this research was preliminary in the fact that the problem was simplified to the extreme. However, there was little work on droplet impingement from a cleaning viewpoint in the literature, so it remains an important phenomenon for future research. From a numerical perspective, the use of phase-field approach with the available computational resources means there is diffuse interface, so when capturing force interactions between the droplet and the wall, these may not be well represented. Other numerical approaches could be considered with a sharper representation of this interface. Additional parameters can be added to the problem to make it more realistic. These include multiple droplet impingements (simultaneous and periodic), inclination of impingement relative to the surface, and variation of droplet diameter and velocity. There is also much work that can be done to elaborate on the jet simulations presented in this thesis, since they were also fairly preliminary in nature. A two-phase simulation whereby the geometry of the free surface could more accurately be predicted by COMSOL, changing to a 3D domain and exploring the effects of jet inclination are a few of many possible additions to the study conducted.

Bibliography

- Asadi, S., Passandideh-Fard, M. (2009) A Computational Study on Droplet Impingement onto a Thin Liquid Film, *The Arabian Journal for Science and Engineering* 34 (2B) pp.505 – 516
- Barnes, H.A., Hardalupas, Y., Taylor, A.M.K.P., Wilkins, J.H. (1999) An investigation of the interaction between two adjacent droplets, *In: ILASS-Europe'99, Toulouse, France*
- Bartholomew, E. (Accessed: 10th November 2018) Acrylic Pressure-Sensitive Adhesives. Available online: <https://www.adhesivesmag.com/articles/90226-acrylic-pressure-sensitive-adhesives>
- Bentley, P.J. (2017) *Investigation of the Functionality of White Soft Paraffin with Regards to Ointments. PhD thesis*, University of Leeds, pp.80-90
- Bhagat, R.K., Wilson, D.I. (2016) Flow in the thin film created by a coherent turbulent water jet impinging on a vertical wall, *Chemical Engineering Science* 152, pp. 606 – 623
- Bhagat, R.K., Perera, A.M., Wilson, D.I. (2017) Cleaning vessel walls by moving water jets: Simple models and supporting experiments, *Food and Bioprocess Processing* (102) pp.31 – 54
- Box, G., Behnken, D. (1960) Some new three level designs for the study of quantitative citation variables, *Technometrics* 2, pp.455 – 475
- Cense, A.W., van Dogen, M.E.H., Gottenbos, B., Nuijs, A.M., Shulepov, S.Y (2006) Removal of biofilms by impinging water droplets, *Journal of Applied Physics* 100, pp. 70 - 78
- Chateau, M-E., Galet, L., Soudais, Y., Fages, J. (2004) A New Test for Cleaning Efficiency Assessment of Cleaners for Hard Surfaces, *Journal of Surfactants and Detergents* 7 (4) pp.355 - 362
- Chee, M.W.L., Ahuja, T.V., Bhagat, R.K., Taesopapong, N., Wan, S.A., Wigmore, R.L., Wilson, D.I. (2019) Impinging jet cleaning of tank walls: Effect of jet length, wall curvature and related phenomena, *Food and Bioprocess Processing* 113, pp.142 – 153
- Cheng, A.H.-D, Cheng, D.T. (2005) Heritage and early history of the boundary element method, *Engineering Analysis with Boundary Elements* 29, pp.268-302
- Ching, B., Golay, M.W., Johnson, T.J. (1984) Droplet impacts upon liquid surfaces, *Science* 226, pp.535 – 537

COMSOL (2012) COMSOL Multiphysics User Guide, pp.493-894

COMSOL (2016) The Finite Element Method (FEM) Available online: <https://uk.comsol.com/multiphysics/finite-element-method> Accessed 19th August 2019

Cossali, G.E., Marengo, M., Santini, M. (2004) Impact of single and multiple drop array on a liquid film, *Proceeding of the 19th ILASS-Europe, Nottingham, UK (2004)*

Cox, M.F. (1986) Surfactants for hard-surface cleaning: Mechanisms of solid soil removal, *Journal of the American Oil Chemist's Society* 63 (4), pp.559 - 565

de Boer, G. (2014) [Private communication]

Delta Stainless Steel Ltd, (Accessed online: 5th March 2019) Spray balls, Available from: <https://www.deltastainless.co.uk/wp-content/uploads/2014/11/Stainless-Steel-Static-Spray-Ball.pdf>

Drosos, E.I.P., Paras, S.V., Karabelas, A.J. (2004) Characteristics of developing free falling films at intermediate Reynolds and high Kapitza numbers, *International Journal of Multiphase Flow* 30 (7-8), pp.853 - 876

Feldung Damkjaer, N., Adler-Nissen, J., Jensen, B.B.B., Wilson, D.I (2017) Flow pattern and cleaning performance of a stationary liquid jet operating at conditions relevant for industrial tank cleaning, *Food and Bioproducts Processing* 101, pp.145 - 156

Food and Drug Administration (FDA), (1993) *Guide to Inspections of Validation of Cleaning Processes*, pp.255 - 262

Fuchs, E., Kricke, S., Schöhl, E., Majschak, J-P. (2019) Effect of industrial scale stand-off distance on water jet break-up, cleaning and forces imposed on soil layers, *Food and Bioproducts Processing* 113, pp.129 – 141

Fryer, P.J., Asteriadou, K. (2009) A prototype cleaning map: A classification of industrial cleaning processes, *Trends in Food Science & Technology* 20

Gibou, F., Fedkiw, R., Osher, S. (2018) A review of level-set methods and some recent applications, *Journal of Computational Physics* 353, pp.82 – 109

Grant, R.P., Middleman, S. (1966) Newtonian jet stability, *AIChE J.* 12, pp.669 - 677

Greene, D. (2003) Practical CIP System Design, *The Official Journal of ISPE* 23 (2) pp.1 – 7

Hild, F. (Accessed online: 17th January 2019) Surface Energy of Plastics. Available online: <https://www.tstar.com/blog/bid/33845/surface-energy-of-plastics>

- Hu, J., Jia, R., Wan, K-T., Xiong, X. (2014) Simulation of Droplet Impingement on a Solid Surface by the Level Set Method, *Proceedings of the 2014 COMSOL Conference in Boston*
- Jayarathne, O.W., Mason, B.J. (1964) The coalescence and bouncing of water drops at an air/water interface, *Proceedings of the Royal Society A: Mathematical, Physical and Engineering Sciences*
- Lakshmana Prabu, S., Suriyaprakash, T.N.K. (2010) Cleaning Validation and its importance in Pharmaceutical Industry, *Pharma Times* 42 (7) pp. 21 – 25
- Lauder, B.E., Spalding, D.B. (1974) The Numerical Computation of Turbulent Flows, *Computer Methods in Applied Mechanics and Engineering* 3, pp. 269 - 289
- LeBlanc, D.A., Allison, G., Carlson, J.L., George, K., Gorsky, I., Hirsh, I.S., Osborne, J., Randall, G., Riss, P-M., Verghese, G., Walsh, J., Yankah, V. (2012) PDA Task Force on Technical Report No.29 (Revised 2012): Points to Consider for Cleaning Validation
- Lee, S.M., Lee, W.G., Kim, Y.H., Jang, H. (2012) Surface roughness and the corrosion resistance of 21Cr ferritic stainless steel, *Corrosion Science* 63, pp. 404 – 409
- Liang, G., Zhang, T., Yu, H., Chen, H., Shen, S. (2018) Simultaneous Impact of Multiple Droplets on Liquid Film, *Journal of Industrial and Engineering Chemistry* 65, pp. 51 – 61
- Liu, X., Lienhard, J.H., Lombarda, J.S. (1991) Convective heat transfer by impingement of circular liquid jets, *Journal of Heat Transfer* 113, pp. 571–582
- Lodhi, B., Padamwar, P., Patel, A. (2014) Cleaning validation for the pharmaceuticals, biopharmaceuticals, cosmetic and nutraceuticals industries, *Journal of Innovations in Pharmaceuticals and Biological Sciences* 1 (1) pp. 27 – 38
- Massey, B. (2006) *Mechanics of Fluids, 8th Edition*, p. 276
- McLaughlin, M.C., Zisman, A.S. (2005) *The Aqueous Cleaning Handbook, A Guide to Critical-Cleaning Procedures, Techniques, and Validation*, pp.105 – 139
- Mehta, N., Goenaga, J., Hernandez-Rivera, S.P., Hernandez, D., Thomson, M., Melling, P. (2002) Development of an in situ spectroscopic method for cleaning validation using mid-IR fiber optics, *Spectroscopy* 18 (4), pp.14 - 19
- Moreira, A.L.N., Moita, A.S., Panão, M.R. (2010) Advances and challenges in explaining fuel spray impingement: How much of single droplet impact research is useful? *Progress in Energy and Combustion Science* 36, pp. 554 - 580

Mundo, C., Sommerfeld, M., Tropea, C. (1998) On the Modelling of Liquid Sprays Impinging on Surfaces, *Atomisation and Sprays* 8 (6) pp.625 – 652

Osher, S., Sethian, J.A. (1988) Fronts propagating with curvature dependent speed: algorithms based on Hamilton-Jacobi formulations, *Journal of Computational Physics* 79 (1) pp.12 - 49

Palabiyik, I. Lopez-Quiroga, E., Robbins, P.T., Goode, K.R., Fryer, P.J. (2018) Removal of Yield-Stress Fluids from Pipework Using Water, *Biomolecular Engineering, Bioengineering, Biochemicals, Biofuels, and Food, AIChE Journal* 64 (5), p1517

Pharmaceutical Manufacturing Technology Centre (PMTc) (2015) Guidance for Industry: Good Cleaning Validation Practice

Pharmacopoeia, E. (2005) 2.9.9. Measurement of Consistency by Penetrometry *In: European Pharmacopoeia 5.0.*, pp.235-237

PNR (Accessed online: 27th February 2019) General Purpose Nozzles, Available from: <https://www.pnr.co.uk/browse-by-image/general-purpose-nozzles/33/>

PNR Full Cone Nozzles – Technology (Accessed: 4th April 2018) Available online: <http://www.pnr.eu/wp-content/uploads/2017/05/FULL-CONE-NOZZLES.pdf>

Quarini, J. (2002) Ice-pigging to reduce and remove fouling and to achieve clean-in-place, *Applied Thermal Engineering* 22 (7), pp.747 – 753

Raman, K.A., Jaiman, R.K., Lee, T.S., Low, H.T. (2015) On the dynamics of crown structure in simultaneous two droplets impact onto stationary and moving liquid film, *Computers & Fluids* 107, pp.285 - 300

Rasband, W.S. (1997) ImageJ, U.S. National Institutes of Health, Bethesda, Maryland, USA, Available online: <https://imagej.nih.gov.ij/>

Rayleigh (1879) On the stability, or instability, of certain fluid motions, *Proceedings of the London Mathematical Society* 1-10 (1), pp.4 - 12

Rein, M. (1993) Phenomena of liquid drop impact on solid and liquid surfaces, *Fluid Dynamics Research* 12, pp.61 – 93

Rieber, M., Frohn, A. (1999) A numerical study on the mechanism of splashing, *International Journal of Heat and Fluid Flow* 20, pp.455 - 461

Rodgers, A., Kapur, N., de Boer, G., Scott, G., Murray, B. (2019) An investigation into batch cleaning using wash racks, *Food and Bioproducts Processing* 113, pp.118 - 218

- Rodriguez, F., Mesler, R. (1985) Some drops don't splash, *Journal of Colloid Interface Science* 106 (2) pp.347 – 352
- Rosen, M.J., Kunjappu, J.T. (2012) *Surfactants and Interfacial Phenomena* 4th Edition, pp.40 – 150
- Rossmann, L.A. (2000) EPANET 2 User's Manual, p.27-47, Available from: https://cfpub.epa.gov/si/si_public_record_report.cfm?Lab=NRMRL&dirEntryId=95662
- Shewale, S.D., Chavan, M., Parekh, S.S. (2014) Pharmaceutical Product Recall: Lesson Learned, *International Pharmaceutical Industry: Regulatory and Marketplace* 6 (1), pp.16 – 23
- Shimbun, N.K. (1988) *Poka-Yoke: Improving Product Quality by Preventing Defects*, Productivity Press, p.111
- Shoppell, B. (2009) An interface-fitted finite element based level set method: algorithm, implementation, analysis and applications, *PhD thesis: University of California*, p.16
- Sinner, H. (1959) The Sinner Circle "TACT". In *Sinner's Cleaning Philosophy*, Henkel
- Simpson, A.R. and Elhay, S. (2008) "Formulating the water distribution system equations in terms of heads and velocity." 10th Annual Symposium on Water Distribution Systems Analysis, American Society of Civil Engineers, Kruger National Park, South Africa, 17-20 August.
- Sulaiman, S.A., Daud, M. (2013) Comparative study of droplet sizes of water and diesel sprays, *Asian Journal of Scientific Research* 6 (2), p.370
- Sørensen, O. (Accessed online, 7th January 2019) Controlling Hygienic Tank Cleaning – Using hygienic sensors to monitor tank cleaning, Available from: <https://www.alfalaval.com/globalassets/documents/industries/sanitary-general/thinking-ahead/new-pdfs/ese02286en-01-tank-optimization-controlling-hygienic-tank-cleaning.pdf>
- Soriano, G.E., Zhang, T., Alvarado, J.L. (2014) Study of the effects of single and multiple periodic droplet impingements on liquid film heat transfer, *International Journal of Heat and Mass Transfer* 77, pp.449 – 463
- Stow, C.D., Hadfield, M.G. (1981) An experimental investigation of fluid flow resulting from the impact of a water drop with an unyielding dry surface, *Proceedings of the Royal Society: Mathematical, Physical and Engineering Sciences*, pp.373 – 441

Tafreshi, H.V., Pourdeyhimi, B. (2003) The effects of nozzle geometry on water jet breakup at high Reynolds numbers, *Exp. Fluids* 35, pp.364 – 371

Todini, E., Pilati, S. (1988) A gradient method for the analysis of pipe networks, *In: International Conference on Computer Applications for Water Supply and Distribution, Leicester Polytechnic, UK, September 8-10.*

Tropea, C., Marengo, M. (1999) The impact of drops on walls and films. *Multi Sci Tech* 11(1), pp.19 – 36

Wang, A.B., Chen, C.C., Hwang, W.C. (2002) On some new aspects of splashing impact of drop-liquid surface interactions. In: Rein Martin, editor. Drop-surface inter-actions. Wien, New York: Springer p. 303.

Wang, T., Faria, D., Stevens, L.J., Tan, J.S.C., Davidson, J.F., Wilson, D.I. (2013) Flow patterns and draining films created by horizontal and inclined coherent water jets impinging on vertical walls, *Chemical Engineering Science* 102, pp.583 – 601

Wang, T., Davidson, J.F., Wilson, D.I. (2015) Flow patterns and cleaning behaviour of horizontal liquid jets impinging on angled walls, *Food and Bioproducts Processing* 93, pp.333 – 342

Wilkens, A. (1987) unpublished (extracted from Rein, 1993)

Wilson, D.I. (2005) Challenges in Cleaning: Recent Developments and Future Prospects, *Heat Transfer Engineering* 26 (1), pp.51 - 59

Wilson, D.I., Le, B.L., Dao, H.D.A., Lai, K.Y., Morrison, K.R., Davidson, J.F. (2012) Surface flow and drainage films created by horizontal impinging liquid jets, *Chemical Engineering Science* 68, pp.449 - 460

Wilson, D.I., Atkinson, P., Köhler, H., Mauermann, M., Stoye, H., Suddaby, K., Wang, T., Davidson, J.F., Majschak, J-P. (2014) Cleaning of soft-solid soil layers on vertical and horizontal surfaces by stationary coherent impinging liquid jets, *Chemical Engineering Science* 109, pp.183 – 196

Wilson, D.I., Köhler, H., Cai, L., Majschak, J.P., Davidson, J.F. (2015) Cleaning of a model food soil from horizontal plates by a moving water jet, *Chemical Engineering Science* 123, pp.450 – 459

Yeckel, A., Middleman, S. (1987) Removal of a viscous film from a rigid plane surface by an impinging liquid jet, *Chemical Engineering Communications* 50, pp. 165–167

Zhang, T., Muthusamy, J.P., Alvarado, J.L., Kanjirakat, A., Sadr, R. (2016) Numerical and experimental investigations of crown propagation dynamics induced by droplet train impingement, *International Journal of Heat and Fluid Flow* 57, pp.24 - 33

3M (Accessed online, 25th February 2019) 3M Novec 7100 Engineered Fluid, Available from: <http://multimedia.3m.com/mws/media/199818O/3mtm-novectm-7100-engineered-fluid.pdf>

Appendix A

Appendix A shows the nozzle discharge data for every nozzle on Rack 1 and Rack 2, introduced in section 3.2.3.

Table A.1: Nozzle discharge coefficients (Rack 1).

Node number	Discharge coefficient ($l\text{min}^{-1}\text{Pa}^{-0.5}$)
2	4.312
6	0.061
9	0.030
10	0.012
11	0.102
12	0.005
13	0.005
15	0.012
25	0.016
26	0.017
27	0.017
28	0.020
29	0.020
30	0.015
31	0.025
32	0.012
35	0.030
36	0.012
41	0.030
43	0.016
44	0.016
45	0.016
46	0.012
48	0.030
50	0.012
54	0.031
55	0.031
56	0.031
57	0.031
63	0.092
64	0.092
65	0.092
66	0.135
70	0.030
72	0.012

Table A.2: Nozzle flow rate data (Rack 1) and % total flow with/without coupling discharge.

Nozzle ID	Flow Rate (l min⁻¹)	% of Total Flow with coupling discharge	% of Total Flow without coupling discharge
1	1610	82	-
2	1.8	0.09	0.51
3	1.8	0.09	0.51
4	4.2	0.21	1.19
5	9	0.46	2.54
6	4.2	0.21	1.19
7	22.2	1.13	6.27
8	37.2	1.89	10.51
9	8.4	0.43	2.37
10	4.2	0.21	1.19
11	4.2	0.21	1.19
12	4.2	0.21	1.19
13	5.4	0.27	1.53
14	5.4	0.27	1.53
15	3.6	0.18	1.02
16	4.2	0.21	1.19
17	4.2	0.21	1.19
18	9	0.46	2.54
19	11.4	0.58	3.22
20	3	0.15	0.85
21	3	0.15	0.85
22	3.6	0.18	1.02
23	4.2	0.21	1.19
24	4.2	0.21	1.19
25	11.4	0.58	3.22
26	40.8	2.07	11.53
27	29.4	1.49	8.31
28	28.8	1.46	8.14
29	29.4	1.49	8.31
30	9.6	0.49	2.71
31	9	0.46	2.54
32	9	0.46	2.54
33	9	0.46	2.54
34	4.2	0.21	1.19
35	10.8	0.55	3.05

Table A.3: Nozzle discharge coefficients (Rack 2).

Node number	Discharge coefficient ($l \text{min}^{-1} \text{Pa}^{-0.5}$)
2	4.068
12	0.043
13	0.212
20	0.012
21	0.081
22	0.212
23	0.081
24	0.212
25	0.081
26	0.212
27	0.065
28	0.212
37	0.009
38	0.009
39	0.009
40	0.009
41	0.009
42	0.009
50	0.005
51	0.005
52	0.005
53	0.005
54	0.005
55	0.005
63	0.009
64	0.009
65	0.009
66	0.009
67	0.009
68	0.009
76	0.009
77	0.009
78	0.009
79	0.009
80	0.009
81	0.009

Table A.4: Nozzle flow rate data (Rack 2) and % total flow.

Nozzle ID	Flow Rate (l min⁻¹)	% of Total Flow
2	3.6	3.77
3	16.2	16.98
4	1.2	1.26
5	4.8	5.03
6	10.2	10.69
7	4.8	5.03
8	9.6	10.06
9	4.8	5.03
10	10.2	10.69
11	3.6	3.77
12	10.8	11.32
13	0.6	0.63
14	0.6	0.63
15	0.6	0.63
16	0.6	0.63
17	0.6	0.63
18	0.6	0.63
19	0.6	0.63
20	0.6	0.63
21	0.6	0.63
22	0.6	0.63
23	0.6	0.63
24	0.6	0.63
25	0.6	0.63
26	0.6	0.63
27	0.6	0.63
28	0.6	0.63
29	0.6	0.63
30	0.6	0.63
31	0.6	0.63
32	0.6	0.63
33	0.6	0.63
34	0.6	0.63
35	0.6	0.63
36	0.6	0.63